



TECHNISCHE UNIVERSITÄT MÜNCHEN

Fakultät für Maschinenwesen

Lehrstuhl für Leichtbau

Towards a Robust In-Situ Health Monitoring and Identification
Technique for Thin-walled Fiber Composite Structures under
Various Types of Adverse Disturbances

Liang Si

Vollständiger Abdruck den von der Fakultät für Maschinenwesen der Technischen
Universität München zur Erlangung der akademischen Grades eines

Doktor-Ingenieurs (Dr.-Ing.)

genehmigten Dissertation.

Vorsitzender: Univ.-Prof. Dr.-Ing. Klaus Drechsler

Prüfer der Dissertation: 1. Univ.-Prof. Dr.-Ing. Horst Baier

2. Univ.-Prof. Dr.-Ing. Christian Große

3. Univ.-Prof. Dr.-Ing. Michael Sinapius, TU Braunschweig

Die Dissertation wurde am 28.11.2016 bei der Technischen Universität München eingereicht
und durch die Fakultät für Maschinenwesen am 30.05.2017 angenommen.

This dissertation is dedicated to my parents for their endless loves, supports and encouragements.

Acknowledgments

I would like to thank my supervisor Professor Horst Baier, for his invaluable advice, steady guidance, strong inspiration and encouragement during this research. Without his help, this research could not be finished successfully in such a short term. I would also like to express my appreciation to Prof. Baier and China Scholarship Council for their financial supports in completing this research. Meanwhile, I appreciate Prof. Fukuo Chang (from Stanford University) much for my visiting guidance and communication with him about my research work. I also appreciate sincerely Prof. Zhanjun Wu (from DUT, China) and Prof. Zhonghui Chen (from CUMTB, China) for providing helpful advice and constructive suggestions in my research direction. Nevertheless, I need to thank Prof. Klaus Drechsler, Prof. Michael Sinapius and Prof. Christian Grosse for their dedications in my dissertation evaluation.

I would like to thank all of my colleagues in Lehrstuhl für Leichtbau. In particular, I would like to thank Manfred Bauer, Bernhard Lerch, Tanut Ungwattapanit and Josef Voetterl for their supports in my research work. I also thank Dr. Qian Wang for her selfless help and encouragement. In addition, I am thankful to the three Chinese doctors who are Longtao Xu, Shuyi Ma and Dongyue Gao from DUT, for their helpful suggestions in my research. Meanwhile, I'd like to thank my friends who are Lina Xu, Dr. Qamar Mahboob, Johannes Fischer and Dr. Simona Miraglia.

I sincerely express gratitude to all my friends wherever in Germany or in China. All of them are deeply appreciated.

I am thankful deeply to my parents. Without their strong support and warm encouragement throughout my studies in Munich, I could never reach this joyful moment. For whole my life so far, I have been in debt to them. The best thing of finishing my doctoral studies is to see my parents be so happy. I would like to dedicate this thesis to them.

Liang Si

Garching, November 16, 2015

Short Description

An Advanced Structural Health Monitoring System – Real-time Impact Monitoring and Rapid Damage Identification for Laminated Composite Structures.

Abstract

Investigations are conducted to develop a real-time automatic and robust structural health monitoring (SHM) technique for the identification and prediction of the locations, force information and possible damage state induced by foreign objects acting on composite or metallic structures. Accordingly, an in-situ ensemble structural health monitoring and identification (SHMI) technique is proposed and designed with configurable distributed sensor networks, which merges the mechanical model computations, the advanced imaging method, the proper online data processing and evaluation methods. Then, the developed structural health monitoring and identification consists of five major sequential procedures, which are the signal data preprocessing (SDP), the forward model generator (FMG), the impact positioning calculator (IPC), the inverse model operator (IMO) and the structural state evaluator (SSE) – damage assessment. In order to achieve good engineering applicability, several uncertainty factors were considered for the examined composite structures, which are diverse structure configurations, various carbon fiber prepregs layups in the CFRP specimens, sundry impact conditions, and damage (delaminations) possibly caused by adverse objects. What's more, random interfering noises resulting from inconstant mechanical vibrations were also considered as the essential disturbances. Under the different technical conditions and disturbances arising from practical structure vibration environments, the accuracy and reliability of the predictions of impact forces and locations using the SHMI technique were validated through a series of impact tests, in addition, the performance of damage identifications and predictions of the SHMI technique were also verified through a series of damage validation experiments of seeded delaminations. The errors between estimated and actually measured quantities all fall well within the satisfactorily limited range. It is concluded that the ensemble structural health monitoring and identification technique is qualified to reconstruct the input forces within sufficient precision, even due to unforeseen impact events under changeable conditions; it is also able to estimate effectively unknown impact locations in complex adverse environments and to assess the structural state such as the structural damage state rapidly.

All the studies strongly indicate that the ensemble structural health monitoring and identification technique is a good basis and potential tool of online on-board diagnosis for impact monitoring and damage identification of aerospace composite structures, even possibly of large-scale laminated composite structures.

Kurzfassung

Es werden Entwicklungen und Untersuchungen vorgenommen, um bei Stoßbelastungen (Impact) Kraftamplituden und Stoßpositionen insbesondere für dafür empfindlicheren CFK-Bauteile zu identifizieren. Dies kann dann als ein komplementäres Subsystem in einem integralen Health-Monitoring-System benutzt werden. Die impact-Identifikation soll on-line geschehen, basieren auf einer Kombination von Sensornetzwerken, Datenprozessierungen sowie Simulations- und Evaluationsmethoden. Im Einzelnen sind es die fünf Elemente Messdatenverarbeitung, Forward-model-Generator, Stoßpositionsbestimmung, der Inversmodell-Operator sowie die Bewertungsroutinen für den Bauteilzustand. Für eine sinnvolle praktische Anwendbarkeit werden verschiedene Unsicherheits- und Störeffekte berücksichtigt, die von Streuungen in Geometrie- oder Werkstoffdaten bzw. verschiedenen dynamischen Hintergrundstörungen (Schwingungen, Lärm) herrühren können. Das Verhalten des entwickelten Systems insbesondere bezüglich Genauigkeit der Kraft- und Positionsidentifikation wird an mehreren Testbauteilen auch unter Beachtung von oben genannten Unregelmäßigkeiten bzw. Störungen validiert. Dabei haben sich gute Übereinstimmungen zwischen den mit dieser Methodensequenz identifizierten Daten und den mit anderen im Labor anwendbaren Messverfahren ermittelten experimentellen Daten gezeigt. Die Methode bietet also eine gute Basis für praktische Anwendungen.

Contents

Abstract	V
Kurzfassung	VII
List of Figures	XII
List of Tables	XVII
1. Introduction	1
1.1 State of the Art and Techniques Survey	2
1.1.1 <i>Infrared and Thermographic Technique</i>	2
1.1.2 <i>Optical Fiber Sensing Technique</i>	3
1.1.3 <i>Eddy Current Technique (ECT)</i>	4
1.1.4 <i>Comparative Vacuum Monitoring (CVM) Technique</i>	4
1.1.5 <i>Vibration Based Inspection Technique – Acousto-Ultrasonic Technique</i>	5
1.2 Structural Health Monitoring (SHM) Techniques and Applications	6
1.2.1 <i>Health Monitoring Techniques for Carbon Fiber Composite Structures</i>	8
1.3 Motivation and Objectives.....	10
2. Statement of Major Tasks	15
3. Approach of Health Monitoring and Identification	21
3.1 Theoretical Development	22
3.1.1 <i>Signal Data Preprocessing</i>	23
3.1.2 <i>Forward Model for Structural Responses</i>	23
3.1.3 <i>Impulse Response Functions</i>	24
3.1.4 <i>Inverse Model Operator for Force Reconstructions</i>	24
3.1.5 <i>Structural State Assessment – Damage Identification</i>	24
3.1.6 <i>Estimation of Impact Locations</i>	25
3.1.7 <i>Sensor Calibration</i>	25
3.2 Computer Implementation	25
3.3 Experimental Verification and Accuracy Evaluation	25
3.4 Studies of Practical Engineering Issues	26
4. Signal Data Preprocessing	27
4.1 Background.....	28
4.2 Fast Empirical Mode Decomposition Module.....	28

4.2.1	<i>The Stoppage Criteria</i>	33
4.3	Filtering Processing Module.....	34
5.	Impact Monitoring and Identification	39
5.1	Forward Modeling	40
5.1.1	<i>Basic Approach</i>	40
5.1.2	<i>Determination of Model Structure</i>	42
5.1.3	<i>Predictor Formation</i>	45
5.1.4	<i>Construction of Forward Model Based on Fast Genetic Algorithm Parameters Estimation</i> 50	
5.1.5	<i>Model Order Optimization</i>	66
5.2	Inverse Model Solver.....	68
5.2.1	<i>Inverse Reconstruction Functions</i>	68
5.2.2	<i>Inverse System Model Operator for Force Reconstructions</i>	69
5.2.3	<i>Generalization of Impact Force Reconstruction</i>	72
5.3	Formation of Networks of Impulse Response Functions grids.....	75
5.4	Conclusion.....	77
6.	Structural State Awareness - Damage Identification	79
6.1	Determination of the Group Velocity of Propagating Waves.....	80
6.2	Rapid Multi-Damage Indices Algorithm Based on Multi-Functional Multi-Metrics.....	81
6.2.1	<i>Fast Ensemble Empirical Mode Decomposition (FEEMD) and Hilbert Spectral Analysis</i> ..	81
6.2.2	<i>Multi-Damage Index Parameters—Multi-functional Multi-Metrics (MFMMs) Based on HSA-FEEMD</i>	84
7.	Estimations of Multi-Impact Locations	91
7.1	Impact Region Extraction.....	92
7.2	Locating Impact Coordinates.....	93
7.2.1	<i>Updating Impact Location Using the TOF Based Quadrilateral Centroid Principle</i>	93
7.2.2	<i>Updating Impact Location Using the Mean Cost Function</i>	96
8.	Piezoelectric Sensor Modeling and Calibration	99
8.1	Sensor Selection and Design	100
8.2	Sensor Modeling.....	102
8.3	Sensor Calibration	104
8.3.1	<i>Calibration from Theoretical Calculation</i>	104
8.3.2	<i>Calibration under In-Situ Conditions</i>	108
8.4	Discussion.....	111
9.	Experimental Tests	113

9.1	Experimental Specimens	114
9.2	Experimental Setup	118
9.3	Experimental Tests	122
9.3.1	<i>Specimen 1 – A Normal Panel</i>	123
9.3.2	<i>Specimen 2 – A Stiffened Panel</i>	123
9.3.3	<i>Specimen 3 – A Cutout Panel</i>	125
9.3.4	<i>The Laminated Composite Specimens of Damage Identifications</i>	126
9.4	Validation of Forward Model of Structural Response.....	129
10.	Results and Discussion.....	133
10.1	Estimations of Impact Locations	134
10.1.1	<i>Specimen 1 – A Normal Condition</i>	134
10.1.2	<i>Specimen 2 – Structural Complexity Consideration</i>	136
10.1.3	<i>Specimen 3 – Structural Discontinuity Consideration</i>	139
10.1.4	<i>Comparison of the Location Estimation Methods</i>	141
10.2	Impact Force Reconstructions	142
10.2.1	<i>Specimen 1 – A Normal Condition</i>	143
10.2.2	<i>Specimen 2 – Structural Complexity Consideration</i>	146
10.2.3	<i>Specimen 3 – Structural Discontinuity Consideration</i>	148
10.2.4	<i>Conclusion</i>	150
10.3	Structural Condition Awareness Based on Signal Energy Distribution	151
10.4	Impact Monitoring Under Vibration Noise Contamination.....	153
10.4.1	<i>Estimations of Impact Locations</i>	153
10.4.2	<i>Impact Force Reconstructions</i>	155
10.5	Validation for Various Types of Impactors	157
10.6	Structural State Assessment – Damage Identifications	161
10.6.1	<i>Judgment of the Damage Presence by the Transient Analysis Based on FEEMD</i>	161
10.6.2	<i>Multiple Delaminations Quantification and Track by Energy Density Metric</i>	164
10.6.3	<i>Multiple Delaminations Identification and Track by Energy Time-Phase Shift Metric</i>	165
10.6.4	<i>Multiple Delaminations Identification and Track by Phase Divergence Metric</i>	167
10.7	Discussion.....	170
10.7.1	<i>Discussion for the Interval of Impulse Response Function Points</i>	171
10.7.2	<i>The Discrimination of Damage Identification Using the RMDI Approach</i>	173
10.7.3	<i>Time Resolution for the Time-Of-Flight</i>	174
11.	Conclusions and Outlook.....	177

11.1	Conclusions	177
11.2	Outlook.....	180
Bibliography		183
Appendix A. Piezoelectric Sensor Discs		191
A.1	Sensor Dynamics Theory.....	191
A.2	Design Criterion of Sensor Network	194
Appendix B. Wave Propagation in Composite Laminates		197
B.1	Basic Wave Mechanics.....	197
B.2	Propagating Wave Model	198
Appendix C. Computer Programs		203

List of Figures

Figure 1.1 Damage inspection strategy for laminated composite structures.....	2
Figure 1.2 Structural Health Monitoring (SHM) scheme of Airbus A320 airplane [26].....	8
Figure 1.3 Demonstration on the future application of a smart SHM system into the full-scale structure of a commercial airplane (the human body and aircraft parts from [64], Source: Airbus).	13
Figure 2.1 Overview of the architecture of the developed online structural health monitoring and identification system (the aircraft part from [26], Source: Airbus).....	18
Figure 2.2 Flow charts of the proposed structural health monitoring and identification technique: (a) the implementation of the SHMI technique and (b) the general computation procedure in a health monitoring and identification.	19
Figure 3.1 Overview of the systematic frame from the proposed ensemble SHMI system.....	23
Figure 4.1 Flowchart of the FEMD decomposition procedure: (a) the fast execution module, (b) the EMD [67] module.....	29
Figure 4.2 Sifting process used to illustrate an EMD [67] decomposition steps: (a)→(b)→(c)→(d)→(e)→(f)	30
Figure 4.3 FEMD for an original sensor data: (a) the sensor data with noise decomposed by FEMD, (b) an example of the 5 th IMF.	32
Figure 4.4 Flowchart of the FEMD based hybrid thresholding filtering process.	36
Figure 4.5 An original sensor data from structural response within random noises of SNR=15.	37
Figure 4.6 An original sensor data from structural response within random noises of SNR=10.	37
Figure 5.1 A complex composite structure with multi-stiffeners overlaid with a grid network of impulse response functions: (a) the monitored stiffened composite structure, (b) an adaptive-laid computation network of impulse response functions overlaying the whole structure, (c) the identification of an unknown impact through the recognized impulse response function grid.....	40
Figure 5.2 The linear relationship between an impact force and a structural response from a sensor: (a) the linear input-output relation based on the impulse response function, (b) a force signal resulting from an impact acting on the structure, (c) the corresponding structural response output from a specified sensor.	46
Figure 5.3 Demonstration for a pole-zero plot of a system model order ($n = 10, m = 4$).....	48

Figure 5.4 The layup structure of a monitored laminated composite panel	52
Figure 5.5 The modeled impulse response of the composite structure due to an impact.....	52
Figure 5.6 Model parameters estimation with the FGAPE loop.	54
Figure 5.7 The chosen structure of the input-output prediction model [78]	55
Figure 5.8 Flowchart of the prediction estimation based on minimization of error (MoE) through the fast genetic algorithm estimation method.....	59
Figure 5.9 The results of system parameters (a_i, b_j) estimation and prediction error estimation in the developed FGA Identification Interface.....	60
Figure 5.10 Comparison for the prediction estimation of a structural response using the fast genetic algorithm error estimation and least squares error estimate methods	62
Figure 5.11 Pole-zero plot of an examined system model with the model order of $(n = 4, m = 3)$	63
Figure 5.12 An example of force reconstruction under a robust prediction model and its inversion.....	64
Figure 5.13 A nonrobust demonstration of the inverse model with unstable zeros $(n = 10, m = 8)$	65
Figure 5.14 An example of force reconstruction under the nonrobust inverse model	65
Figure 5.15 A demonstration of force reconstruction of an unknown impact.	72
Figure 5.16 Generalization for an impact force acting at arbitrary location	73
Figure 5.17 Amplitude difference between real and reconstructed impact forces.....	76
Figure 6.1 Dispersion characteristics of wave group velocities c_g in a tested laminated composite: (a) in wave propagation of the 0o direction, (b) in wave propagation of the 90o direction.....	80
Figure 6.2 The fast ensemble empirical mode decomposition procedure.....	82
Figure 6.3 FEEMD processing for the sensor signals without (a), and with damage (b).	83
Figure 6.4 Energy density metrics: (a) an undamaged case, (b) a delamination case of 1.9 cm diameter with its reflected energy of 1.1007.....	85
Figure 6.5 A demonstration of the TOF definition: (a) the wave propagating path encountering a delamination in a CFRP specimen, (b) Extraction of the TOF of the delamination.....	87
Figure 6.6 Phase divergence metric used to discriminate damage existing in a laminated composite: (a) the wave propagating path encountering a delamination in a CFRP specimen, (b) the instantaneous phase variation between the undamaged and damaged cases.	89

Figure 7.1 Estimation of the initial location for an impact event.....	93
Figure 7.2 Dispersion characteristics of wave phase velocities c_p in a tested laminated composite: (a) in wave propagation of the 0o direction, (b) in wave propagation of the 90o direction.....	95
Figure 7.3 Demonstration of impact positioning procedure through updating quadrilateral...	96
Figure 7.4 Demonstration of locating the coordinates of an impact by the mean cost function using the determined triangular sensor network	97
Figure 8.1 Model diagram of sensor design: (a) the anode surface of the circular piezoelectric sensor, (b) the thickness of sensor, and (c) the cathode surface of the circular piezoelectric sensor.....	101
Figure 8.2 Piezoelectric disc sensors used to measure strain data: (a) sensors mounted on a CFRP structure, (b) sensor prototype.....	102
Figure 8.3 Flowchart of Sensor Modeling	103
Figure 8.4 A circular PZT sensor constrained by structural stiffness k_{str} [97].....	104
Figure 8.5 Impedances from different sensors	107
Figure 8.6 Piezoelectric sensors mounted on the bottom surface of a CFRP Panel: (left) undesirable adhesive layer, (right) perfect adhesive layer.....	109
Figure 8.7 Asymmetrical sensor layouts on a real aircraft panel component with multi-stiffeners: (a) a complex structure component with multi-stiffeners, (b) asymmetrical sensor layouts on the panel structure.	110
Figure 8.8 Comparison of original and calibrated sensor signals	110
Figure 9.1 Geometry of the CFRP plate (Specimen 1) and its sensor layouts.....	115
Figure 9.2 Geometry of the stiffened CFRP panel (Specimen 2) and its sensor layouts	116
Figure 9.3 Geometry of the CFRP plate (Specimen 3) and its sensor layouts.....	116
Figure 9.4 Location of layup groups for specimen 2 and the indicated axes on the rib.....	117
Figure 9.5 Demonstration of the dimensions of a laminated composite specimen used to validate damage identifications.....	117
Figure 9.6 Schematic diagram of impact tests on specimen 1	119
Figure 9.7 Experimental setup of vibration configuration on specimen 1	120
Figure 9.8 Configuration for Boundary conditions on specimen 2.....	120
Figure 9.9 Experimental setup configuration for specimen 3	121
Figure 9.10 An instrumented laminated composite specimen with three seeded-in delaminations: (a) the instrumented composite plate with the designed piezoelectric wafer	

transducer array, (b) a zoomed-in ultrasonic phased image of the multi-delaminations region.	121
Figure 9.11 Real-time visualization inspection for an unknown impact event	122
Figure 9.12 Demonstration for the formation of IRFs network on specimen 1	123
Figure 9.13 Illustration for the formation of IRFs network on specimen 2	124
Figure 9.14 Demonstration for the formation of IRFs network on specimen 3	125
Figure 9.15 Experimental validation tests for the single and multiple damage identifications: (a) the identification of single delamination in a laminated composite specimen, (b) Teflon patches used as the seeded-in delaminations, (c) the identification of multiple delaminations in another laminated composite specimen.....	127
Figure 9.16 A map of group velocity distribution varying with wave propagation angles, units: m/s.....	128
Figure 9.17 Histogram of model order selection.....	129
Figure 9.18 Forward model validations through different hammer tips: (a) three different hammer tips, (b) model validation by the plastic tip, (c) model validation by the rubber tip, (d) model validation by the steel tip.	131
Figure 10.1 Test layout demonstration for the monitored cantilever composite structure....	135
Figure 10.2 Location estimations for two unknown impact events on the structure: (a) impact FR1 localization, (b) impact FR2 localization.	135
Figure 10.3 Location estimation errors for unknown impact events on Specimen 1	136
Figure 10.4 Test layout for the monitored stiffened composite structure.	137
Figure 10.5 Location estimations for two unknown impact events on the structure: (a) impact S1 on the stiffener area, (b) impact S2 on the right bay area.	137
Figure 10.6 Location estimation errors for unknown impact events on the stiffened panel. .	138
Figure 10.7 Location estimations for two unknown impact events on Specimen 3: (a) the test layout, (b) impact C1 localization, and (c) impact C2 localization.	140
Figure 10.8 Location estimation errors for the unknown random impact events on Specimen 3	141
Figure 10.9 Comparison of the accuracies of the two impact positioning methods	142
Figure 10.10 Two unknown impact events on Specimen 1	144
Figure 10.11 Force reconstruction for an unknown impact event at point FR1.....	144
Figure 10.12 Force reconstruction for an unknown impact event at point FR2.....	145
Figure 10.13 Demonstration of random impact locations.....	146
Figure 10.14 Force reconstruction for a random impact at point A	147

Figure 10.15 Force reconstruction for a random impact at point <i>B</i>	147
Figure 10.16 Force reconstruction for a random impact at point <i>C</i>	148
Figure 10.17 Two unknown impact events on Specimen 3	149
Figure 10.18 Force reconstruction at impact location C1 on the cutout panel.....	149
Figure 10.19 Force reconstruction at impact location C2 on the cutout panel.....	150
Figure 10.20 Two random impacts on the cantilever composite structure	152
Figure 10.21 Structural condition awareness when impact at location FR1	152
Figure 10.22 Structural condition awareness when impact at location FR2	152
Figure 10.23 Original multi-sensor response signals under vibration noises contamination.	153
Figure 10.24 Location estimations for two unknown impact events under random vibration conditions: (a) the test layout, (b) impact N1 localization, and (c) impact N2 localization.	154
Figure 10.25 Force reconstruction with and without vibration noises of $SNR=20$	156
Figure 10.26 Force reconstruction with and without vibration noises of $SNR=10$	156
Figure 10.27 Validation tests at a same location for various impactors	158
Figure 10.28 Three types of impactors used to impact tests on Specimen 2	159
Figure 10.29 A force reconstruction due to impact from the rubber ball.....	159
Figure 10.30 A force reconstruction due to impact from the plastic ball.....	160
Figure 10.31 A force reconstruction due to impact from the steel ball.....	160
Figure 10.32 Comparison for the judgments of damage presence using two different baseline methods: (a) the conventional baseline method based on original response signals, (b) the new proposed baseline method based on decomposed IMF components.....	162
Figure 10.33 Judgement of damage presence using the energy density metric: (a) no reflection no damage, (b) reflection appearance damage presence.....	163
Figure 10.34 The unwrapped instantaneous phases with the delamination of 1.9 cm diameter computed from the original signal (a) and from the IMF components obtained using FEEMD (b).	163
Figure 10.35 Energy density metrics used to quantify multiple delaminations in an examined laminated composite: (a) a delamination of the 1.0 cm diameter, (b) another delamination of the 1.9 cm diameter, (c) the other delamination of the 3.0 cm diameter.	164
Figure 10.36 Damage prediction trend curve provided by the energy density metrics to trace damage growth.....	165
Figure 10.37 Energy time-phase shift metric used to quantify multiple delaminations and extract the required TOF information for locating the delaminations.	166

Figure 10.38 Damage prediction trend curve based on the TOF variables to trace the increasing damage.....	166
Figure 10.39 Phase divergence metric to identify multiple delaminations in an examined laminated composite.	167
Figure 10.40 Phase divergence metrics in different frequencies to indicate the reliability and stability of the PDM to identify multiple delaminations: (a) phase divergences due to delaminations in 160 kHz frequency, (b) phase divergences due to delaminations in 180 kHz frequency, (c) phase divergences due to delaminations in 200 kHz frequency.	168
Figure 10.41 Damage prediction trend curve constructed by the RMS phase deviation for damage growth prognosis.	169
Figure 10.42 Evaluations of impact identifications with a specified IRF interval.....	172
Figure 10.43 Variation of the average errors for impact identifications versus to the IRF intervals.....	173
Figure 10.44 Time resolution instructions for the problem of dead zones: (a) the medium overlap of the energy reflection spectra from reflected wave packets, (b) the strong overlap of the other energy reflection spectra from reflected wave packets.	175
Figure 11.1 A smart multi-functional integrative structural health monitoring and identification system	182
Figure A.1 Schematic for the electromechanical response and the coordinate system of a circular piezoelectric sensor.....	191
Figure B.1 Demonstration of a wave propagation in a stiffened CFRP panel during 8 ms ...	201
Figure C.1 Overview of the process of the developed in-situ SHMI computer program	204
Figure C.2 Computer program for the impact monitoring and identification	206
Figure C.3 Rapid computation implementation of the impact identification in real time	206

List of Tables

Table 9.1 Group layups for specimen 1	118
Table 9.2 Group layups for specimen 2	118
Table 10.1 Evaluation results for unknown impacts of FR1 and FR2	145
Table 10.2 Impact evaluation results within vibration noises of SNR=10, 15 and 20.....	157

Operators and Notational Conventions

$s(t)$	Output Sensor Signal
C_i	Intrinsic Mode Function
$e(t)$	Disturbance (Noise) at time t
A	Structural System Matrix
B	Input Matrix
C	Output Matrix
D	Feedforward Matrix
$u(t)$	Input Signal
$G(q)$	Impulse Response Function from u to s
θ	System Parameter Vector
$\hat{s}(k \theta)$	Output of Forward System Model
f	Impact Force
f_s	Sampling Rate
z_m	Zeros of Z-plane
p_n	Poles of Z-plane
$\hat{s}(k)$	Impulse Response Simulator
$\varphi(t)$	Regression Vector
$\tilde{\varepsilon}$	Prediction Residual
Ω^2	Recursive Coefficient
$H(q)$	Transfer Function from e to s
$G(q, \theta)$	IRF in a Model Structure, corresponding to system parameters θ
$v(t)$	Disturbance Variable at time t
$\det A$	Determinant of Matrix A
$\dim \theta$	Dimension of the Column Vector θ
A^{-1}	Inverse of Matrix A
A^T	Transpose of Matrix A
$I(\theta)$	Prediction Error Function
$\tilde{\theta}$	Optimized System Parameters
$H(a_n, b_m)$	Entropy in Fast Genetic Algorithm Error Estimation
$L(q)$	Stable Linear Filter for Prediction Error
$\rho(\cdot)$	Scalar Valued Positive Function
\hat{G}	Inverse Impulse Response Function
\hat{A}	Inverse of Matrix A
$\psi_i(\mu, v)$	Parameter Coordinates in Parameter Space
f_{ψ_i}	Component Force at ψ_i node in Parameter Coordinates
ΔT	Time of Flight
ε_{xx}	Strain in X direction
E	Energy of Sensor Signal
$Y(\omega)$	Electrical Admittance
Γ^2	Shear Lag Parameter
e_p	Average Positioning Error Ratio

Abbreviations and Acronyms

NDT&E	Non-Destructive Testing & Evaluation
NDI	Non-Destructive Inspection
AE	Acoustic Emission
AU	Acousto-Ultrasonic
MEMS	Micro-Electro-Mechanical Systems
FBG	Fiber Bragg Grating
CVM	Comparative Vacuum Monitoring
SHM	Structural Health Monitoring
EIMI	Ensemble Impact Monitoring and Identification
FMG	Forward Model Generator
IM	Impact Monitoring
IMI	Impact Monitoring and Identification
CFRP	Carbon-Fibre Reinforced Plastic
CF	Carbon Fibre
ADIS	Active Damage Interrogation System
SDP	Signal Data Preprocessing
EMD	Empirical Mode Decomposition
IMF	Intrinsic Mode Function
HTF	Hybrid Thresholding Filter
FEM	Finite Element Model
DSP	Digital Signal Processing
SNR	Signal-to-Noise Ratio
MOF	Multi-degree Of Freedom
SSM	Structure System Model
FSM	Forward System Model
PEM	Prediction Error Minimization
RER	Reconstruction Error Ratio
NAG	Networking And Gridding
FGA	Fast Genetic Algorithm
FGAPE	Fast Genetic Algorithm Parameters Estimation
LS	Least Squares
LSEE	Least Squares Error Estimation
IMO	Inverse Model Operator
IMP	Impact Position
IRF	Impulse Response Function
ARX	Auto-Regressive with eXternal input
SSF	State Space Formulation
MIMO	Multiple-Input Multiple-Output
TOF	Time Of Flight
TOA	Time Of Arrival
PDF	Probability Density Function
OEM	Output Error Model
MoE	Minimization of Error

FGAII	FGA Identification Interface
GUI	Graphical User Interface
LE	Location Error
IPM	Impact Positioning Method
SED	Smooth Energy Distribution
TOF-b-QCPM	Time-of-Flight based Quadrilateral Centroid Positioning Method
CF-b-PM	Cost Function based Positioning Method
PEWS	Piezo-electric Wafer Sensor
DSR	Difference in Sensor Responses
IGF	Impedance Gain Factor
APER	Average Positioning Error Ratio
RAE	Relative Average Error
SED	Signal Energy Distribution
RMDI	Rapid Multi-Damage Identification
WVC	Wave Velocity Computation
CLPT	Classical Laminated Plate Theory
MDIA	Multi-Damage Index Algorithm
FEEMD	Fast Ensemble Empirical Mode Decomposition
DIP	Damage Index Parameter
HSA	Hilbert Spectral Analysis
MFMM	Multi-Functional Multi-Metrics
EDM	Energy Density Metric
ETPSM	Energy Time-Phase Shift Metric
PDM	Phase Divergence Metric
PD	Phase Deviation
RMSE	Root-Mean-Square Error
DPTF	Damage Prediction Trend Function
COC	Compensations Of Condition
PWSA	Piezoelectric Wafer Transducer Array
DAQ	Data Acquisition
FWHM	Full Width at Half Maximum
CAD	Computer Aided Design
LLB	Lehrstuhl für Leichtbau
TUM	Technische Universität München
NASA	National Aeronautics and Space Administration
IEEE	Institute of Electrical and Electronics Engineers
ESA	European Space Agency
AIAA	American Institute of Aeronautics and Astronautics

1. Introduction

Aerospace structures whether made out of the advanced lightweight materials such as carbon fiber reinforced polymers (CFRP) or the conventional materials such as metallic alloys, can often encounter a variety of impacts over their lifetimes [1], such as runway stone-splashing as landing or takeoff and tool drop-down during maintenance. As for structural integrity, an unforeseen accidental impact is mostly a serious concern. The applications of carbon fiber composite structures are undergoing increasing growth, especially in the aeronautical industries, because of their excellent strength/stiffness-to-weight ratios and corrosion resistance. However, for conventional surface inspection approaches, structural damage in composites due to low-velocity impact events may be tiny and invisible but still can induce significant loss of the mechanical affordability of a structure, such as the extensive delaminations and/or debonds inside composite structures. Then, it is very difficult for the conventional Non-Destructive Testing and Evaluation (NDT&E) detection solutions to identify this kind of unforeseen impact event online in aerospace vehicles. Therefore, an efficient ensemble structural health monitoring (ESHM) technique was proposed and developed in this thesis, which can automatically monitor and report the events' occurrences, the locations where they occurred and force magnitudes generated by impact events, and also can recognize structural real-time condition varieties resulting from impacts, and assess structural states comprehensively including the localization and quantification of structural damage such as delaminations possibly caused by impacts and predict possible damage expansion after structural damage occurred. This developed ESHM technique would be very helpful with reducing the maintenance cost of large-scale aerospace structures [2], that means, such scheme of health monitoring and identification is able to achieve "maintenance by demand".

1.1 State of the Art and Techniques Survey

There are several inherent difficulties in detecting sudden impact events and subsequent damages induced in the inhomogeneous and anisotropic composite materials, whereas those conventional engineering materials such as alloys or metals are comparatively easy to be conducted the impact monitoring and inspection because of their uncomplicated isotropic property. Especially, the induced damage is often invisible to surface inspection, which prevents further the implementation of several detection methods. Its major reason is that aerospace laminated composite materials have an extensive variety of complicated material properties resulting from changeable fibers and fiber layups, various matrix materials and manufacturing process. These make modeling composites complex, and sometimes might even be non-linear. As a laminated composite is often a mix of diverse materials with widely different properties, such as carbon fibers of a variety of high elastic modulus in a low E -modulus matrix, which results in a significant obstacle for many detection techniques to inspect possible generated damage due to external impacts. Therefore, the significance of impact monitoring and damage identification of laminated composite structures needs to be paid more attention over that of isotropic metallic structures, as their brittleness due to damage induced by low-velocity impacts, even this damage in the struck region will be exacerbated owing to the non-visible or limited visual signature on the structural surface. In contrast with a metallic material, the mechanical property of composites is much complex and less well understood. Thus, their damage inspection strategy is not easy to be designed by general damage tolerant methodologies. However, the damage inspection strategy for composites should be hierarchical as illustrated in Figure 1.1, to prevent the catastrophe of an aero-vehicle. Therefore, the development of reliable structural health monitoring and identification systems is beneficial to preserve the integrity of aerospace vehicles. The following subsections will present overview descriptions of diverse damage inspection techniques that have been developed to detect and quantify any potential or existed damage in a structure.

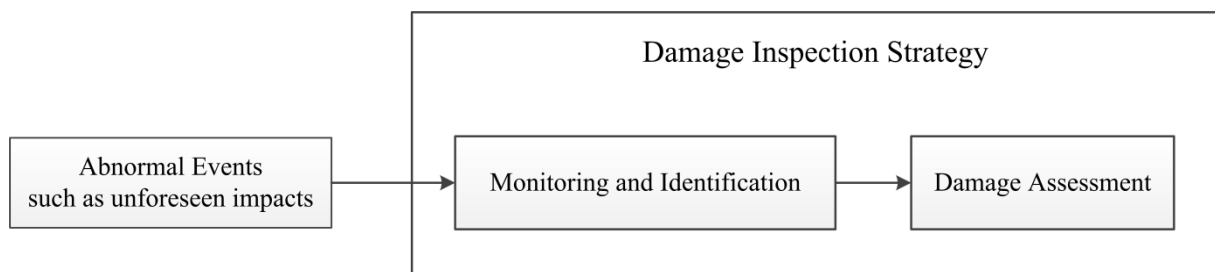


Figure 1.1 Damage inspection strategy for laminated composite structures

1.1.1 Infrared and Thermographic Technique

In contrast with other classical non-destructive testing techniques, thermography technique [3, 4] is a detection technique of non-contact, non-intrusive, high sensitive and rapid responsive,

and it can detect shallow subsurface defects in materials. If a tested object is intact or unexpected damage occur due to external events, thermography technique can be used to detect the imperfections or damage by using an external source with some energy such as flash lamps, Halogen lamps or ultrasound generator, which acts as the excitation source. A tested object generates corresponding thermal response due to the excitation source, then the set infrared camera can measure the response. Thus, to effectively inspect subsurface delaminations, defects or material inhomogeneities in a structure, a suitable thermography solution with the excitation source, infrared camera, and evaluation based imaging processing method need to be determined.

To sum up, due to the complexity of thermographic devices, thermography technique is very difficult to apply in online monitoring for aerial vehicles but doesn't act as a general NDI technique.

1.1.2 Optical Fiber Sensing Technique

Because optical fibers have many distinct advantages that are 1) lightweight, 2) anti-electromagnetic interference, 3) high corrosion resistance, 4) easy to be embedded, 5) measurements of multiple locations in a fiber, optical fiber sensing (OFS) technique has a very wide of applications in whether non-destructive testing (NDT) or structural health monitoring (SHM) systems. In OFS applications, optical fibers can be applied as sensors to measure pressure, the changes of strain and temperature, and other interesting quantities by using the modulated measurement characteristics of fibers, which are the phase, wavelength, transit time and intensity of light injected in fibers. As for optical fiber sensors [5-7], they can be multiplexed along the length of a fiber to record the demanded measurements over large structural regions. The optical fiber sensors in a fiber can sense different wavelengths of light or sense the time delays that the light passes through each sensor. In the SHM applications, the fiber Bragg grating (FBG) sensor [8-11] is actually one of the most widely deployed optical fiber sensors. It can reflect particular wavelengths of light and transmit all others, and its response alters along with the variations in temperature and/or strain. The benefits of the FBG sensor in applications are that 1) integrated easily into composites, 2) high strain measurement, 3) non-distance-dependent signals, 4) nonconductive and electrically passive, 5) easy to construct sensing network due to its multiplexing capability, etc.. However, in contrast to electrical sensors, the optical fibers have a significant drawback that is the shear lag effect, due to the quality of cohesion with a monitored host structure, etc.. This negative effect is caused by the limitation of its process technology such as the coating, cladding and adhesion layers surrounding the fiber core; thereby the optical fiber may not measure precisely any mechanical variation in the host structure. Furthermore, chirping may be caused due to severe strain gradients over gage length, and thus it will lead to loss of signals. It needs to notice that since optical fibers can be integrated into composites, they may induce feeble connections as delamination initiation sites and potential cracks in a laminated composite [12].

1.1.3 Eddy Current Technique (ECT)

The means of eddy currents is another advanced damage detection technique based on strain measurements for conductive materials such as metallic materials. Eddy current technique can provide a high sensitivity to identify material and the characterization of the microstructure state, thereby to detect physical defects such as cracks in test components through measuring the electromagnetic impedance changes in eddy current sensors, as the presence of defects can cause changes in the magnetic permeability and electrical conductivity of the test component. Therefore, eddy current technique has been invested in many applications. In the transportation field, some researchers used the eddy current technique to solve the problem of railroad safety and to trace the state of railroad track surface [13]. In high-temperature inspections, eddy current technique can detect the existed flaws at an early stage before defective materials would be manufactured. In production lines, ECT can provide early indications of random or periodic defects in product materials, in order to guarantee the quality of the products.

In contrast with a real-time structural health monitoring system, eddy current technique has own evident deficiencies, especially in aeronautical applications, such as

- 1) ECT is limited to conductive materials, because it can work based on its electrical nature. Thus, composite materials, a significant aerospace material, cannot be inspected by means of ECT, due to their insulated properties;
- 2) ECT is limited in the offline off-board work mode, because its data processing becomes complicated and time-consuming due to the presence of possible damage in a structure;
- 3) ECT is very difficult to implement the full-scale inspection solution for a large aerial vehicle.

1.1.4 Comparative Vacuum Monitoring (CVM) Technique

Comparative vacuum monitoring technique [14, 15] is a novel SHM technique developed by Ken Davey of Structural Monitoring Systems Ltd. (SMS), Australia. SMS has developed a kind of in-situ, distributed health monitoring sensor, which is known as CVM sensor, and it can overcome many inspection impediments from complex geometries, accessibility limitations [16] and the isolated regions of an examined structure. And SMS has also developed two forms of CVM sensor, which are the standard surface sensor and the through the thickness sensor. The standard surface sensor is made up of silicone with silicone pressure sensitive adhesive (SPSA) or fluorinated ethylene propylene (FEP)-coated polyimide, and it is usually applied to detect cracks in isotropic structures such as metallic structures. The through the thickness (TTT) sensor is then used for the applications of anisotropic structures, such as the detection of disbond and delamination in composite structures. For the surface CVM sensor, it consists of an adhesive silicone pad with many fine galleries into which a low

vacuum is used by a vacuum source supplier and alternating galleries at an atmospheric pressure condition. When the surface CVM sensor sticks and works to detect cracks in a structure, it needs to combine with a pressure flow meter – the Structural Integrity Monitor (SIM) and a stable supplier of low vacuum source. In case no flaw is generated in a structure, the vacuum will keep at a stable state. If a crack occurs and develops in a structure, air will flow from the channels at atmospheric pressure to the vacuum channels through the passage created by the crack. Meanwhile, the flow meter is used to measure the differential pressure between the changed galleries, and to report the information on the development of the crack. Similarly, a crack growing through the thickness of a composite structure can be detected by the CVM equipment once a low-pressure gallery is breached. The SIM can be set to trigger an alarm at a predetermined pressure, usually around 100 Pa. CVM technique is designed to provide a simple, efficient and compact solution for determining the structural integrity of a monitored structure, particularly the presence of cracks [17]. In the actual engineering environments for large commercial airplanes such as Boeing 757 and 767 [18], although the approach of comparative vacuum monitoring has demonstrated certain success in long-term operation, especially in the detection of locations of fatigue damage and hidden cracks, the CVM technique has still lots of drawbacks and deficiencies and need to be improved and perfected.

1.1.5 Vibration Based Inspection Technique – Acousto-Ultrasonic Technique

In most of the vibration-based inspection techniques for composite structures, the acousto-ultrasonic (AU) technique is a relatively new and more popular and essential NDI technique and is also a combination technique of digital signal processing and pattern recognition. It can be said that it is a complement and extension to the acoustic emission (AE) technique, because the AU technique combines the ultrasonic characterization method with the AE signal analysis to detect the presence of discontinuities such as delaminations and debonds inside a composite structure, to assess the damage conditions of a monitored structure, and to evaluate the defect states and variations of mechanical properties of an inspected structure. Meanwhile, in the AE nondestructive testing, internal sources resulting from the mechanical loading of a structure can induce a spontaneous emission of sound pulses and form a stochastic propagation phenomena, because the emission is a result of internal stresses relief in the structure, and the stress waves are produced due to the plastic deformation processes such as the slips of dislocations and grain boundaries or the generation and growth of flaws or defects in materials. In the AU nondestructive evaluation, the stress waves are generated by an external ultrasonic pulsed source which usually uses a piezo transducer. The ultrasonic source is to excite stress waves without any material disrupting, and the waves are launched periodically at a preset repetition rate. The ultrasonic source is characterized, and its location is specified depending on the practical demands. However, the AU technique can also be used to characterize the properties of the tested material. That is the major difference between the AE and AU techniques.

Every technique always possesses its own limitations, then so is the acousto-ultrasonic technique. The evaluation results of composites obtained by using the AU inspection approach may be sensitive to the following factors: 1) transducer selection and amount of the used adhesives, 2) the thickness of adhesives, 3) the surface roughness and texture of the inspected structures, 4) probe resonances and damping, and 5) boundary conditions.

However, the acousto-ultrasonic inspection technique has shown its own significant advantages to detect and access distributed flaw populations and any relevant variations of the mechanical properties of composite laminates. Thus, the AU technique can be applied to evaluate microcracks, aging, damage (e.g. delaminations, debonds, etc.) due to impacts or fatigues, and to predict composites' strength. To successfully implement an AU monitoring or detection, the transducer selection is one of critical factors, which was mentioned previously. Hence, it is very essential for structural health monitoring to fabricate AU sensors of the merited properties of extremely small, thin, stretchable and adaptive, which can also be easy to be embedded in composite materials. For instance, the SMART Layer [19-22] was developed by Prof. Chang from Stanford University.

1.2 Structural Health Monitoring (SHM) Techniques and Applications

Structural health monitoring combines the NDI principle with in situ sensing to implement rapid, onboard, and even online condition assessment. The aim of SHM techniques is to reduce inspection time and operational costs, to improve maintenance efficiency, to prolong maintenance period, and further to enhance structures' life. Therefore, the merits of SHM techniques in contrast to conventional NDT techniques have been indicated evidently as follows,

- 1) Address the demands of damage tolerance;
- 2) Overcome accessibility limitations and complex geometries restriction;
- 3) Evaluate the hidden internal damage such as delaminations, debonds and matrix fractures directly;
- 4) Reduce labor-consuming, because of automatic sensing and data analysis and assessment;
- 5) Support condition based maintenance.

In order to assure any engineering structure such as aircraft, marine, automobile and civil structures in safe and reliable conditions, structural health monitoring techniques utilize embedded and/or attached sensor network systems to real-time and autonomously monitor and identify possible structural damage in a structure. The distributed sensor networks offer the potential of online onboard monitoring and assessment and allow a SHM system to achieve the "real-time condition based maintenance" and to substitute for the conventional

“time based maintenance”, which is controlled by the flight hours of an aircraft [23]. It is worth to note that the long-term benefit of the SHM techniques to the aircraft industry is to assist the design optimization of aircraft structures, to save the design period for the engineers and to decrease the design complexity and amount, thereby to prevent the structural over-design with withstanding the activity of uninspected damage. There are reasons to believe that the effective use of reliable SHM systems can realize the objective of aircraft industries to reduce structural weights and costs and to increase flight performance and hours [24].

For a robust and comprehensive SHM system, its goal is divided into five hierarchies corresponding to the different demands. On the basis of the practical requirements from aerospace industries, they are enumerated as follows,

- 1) Level one, determining if any abnormal event such as impacts occurred and any damage was induced in structures by the external object;
- 2) Level two, diagnosing the effects to the structure due to the unknown external event. If impact events occurred, then it is essential for structural safety and reliability to estimate the impact locations, force magnitudes and impact energies;
- 3) Level three, evaluating the locations and extents of the damage caused in structures when the force magnitudes or released energies of external objects exceed the safe threshold of the structures. What’s more, it may expand to classify the type of damage;
- 4) Level four, assessing the safe states of structures based on the statistical results of the damage evaluations, and further predicting the reliable life of the structures in the light of the structural state assessment;
- 5) Level five, adaptive control and self-healing for the structural health.

Incorporating with various applications, the SHM system has extensive potentials to ensure the reliability and integrity of structures in operation. Nevertheless, the structural health monitoring (SHM) technique is divided approximately into two research directions, which are the passive and active monitoring. For the passive monitoring (PM), it is a structural monitoring method that only sensors are used directly to monitor the structural state/condition such as the variations of the strain field and temperature field in the structure. Then for the active monitoring (AM), it is an active actuation of structural monitoring method with the defined actuator mounted on the structure. The AM approach usually uses the specified actuator to excite the demanded waves through the structure, and then utilizes the laid sensor array to collect the response signals from the structure. And with some advanced signal processing and spectral analysis methods, the structural responses are processed and analyzed to obtain the information of the structural state. According to the actual applications, the PM method is mostly applied in non-damage monitoring cases such as impact monitoring

applications; whereas the AM method is normally employed for damage inspection cases such as the detections of cracks, corrosion, delaminations and debonds.

Many aerospace manufacturers have tried to validate several sensing based structural health monitoring systems in order to apply in their aerial vehicles, which include acoustic emission sensors, fiber Bragg grating sensors embedded usually into the skin of a composite structure, eddy current foil sensors for the corrosion inspection in metallic structures, comparative vacuum monitoring sensors for the cracks detection and acousto-ultrasonic sensors for the monitoring and identification of any type of damage in any structure. Moreover, the Boeing Company has been exploring and discovering the affordability and limitless potential of SHM approaches to apply in the design optimization of each Boeing aircraft family, such as the significant reduction of costs, development time and structural weights. And until 2020, the Boeing Company will build the SHM confidence to expand the practical SHM applications in actual aircraft products, for instance, the multi-damage detections, corrosion detection, multi-scale physics based prognosis and so on [25]. Meanwhile, the Airbus Company has also been exploring the practical applications of SHM systems on their commercial airplanes, it is true, which is demonstrated in Figure 1.2.

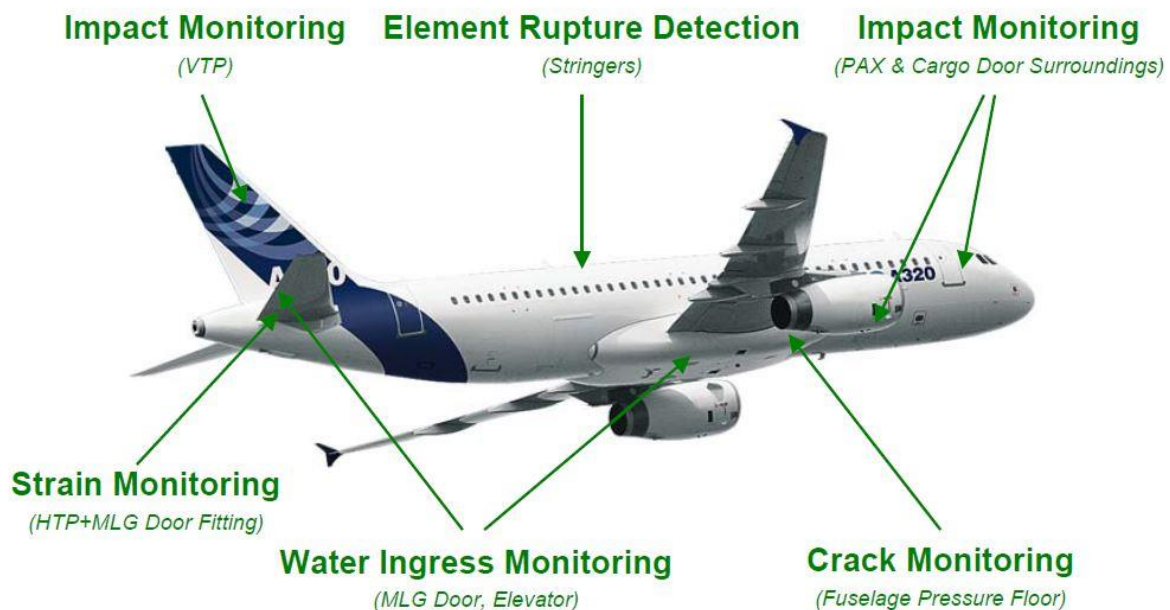


Figure 1.2 Structural Health Monitoring (SHM) scheme of Airbus A320 airplane [26]
(Source: Airbus)

1.2.1 Health Monitoring Techniques for Carbon Fiber Composite Structures

Throughout recent years, a significant amount of research has been conducted on the continuous monitoring and assessment techniques of the structural integrity and reliability. These techniques are supposed to be able to evaluate the effect of flaws on the structure's

strength and life, and to determine the extent of inner damage so as to predict further the remaining life of the structure. In addition, the reliable structural inspection techniques can also provide the capability of damage localization and characterization for the detected structures required. However, there are three typical SHM techniques of composite structures, which are widely applied in research work and technological developments.

The active structural health monitoring based on the characteristics of wave propagation and vibration in composites has indicated distinct advantages in damage inspection applications, as it is able to offer the authority to real-time interrogate the structural state by using surface-bonded or embedded wafer type actuators and sensors. Also, the active monitoring system can detect and identify various types and sizes of damage such as matrix cracks, delaminations and debonds in composite structures, as dynamic actuations with changing frequency and waveforms can be induced by the actuators. In recent years, on-going research is dedicated to developing a reliable online health monitoring system in order to realize the real-time tracking inspection of the composite structural state. This active SHM system is mostly based on the propagating characteristics of Lamb waves in composite structures, and applies the distributed sensor networks to perform real-time monitoring.

The optical fiber sensing based structural health monitoring has been developing for the integrity monitoring of composite structures. This SHM technique adopts embedded optical fiber sensors such as FBG sensors to monitor the structural strain variation at multiple locations due to external objects such as impacts and temperature diversification for the host composite structures. However, it is a difficulty and challenge for the embedding technique of FBG sensors to effectively overcome the effects of irrelevant thermo-mechanical loads, since the quality of the layout of FBG sensors directly affects the performance of sensors. For instance, the response of FBG sensors embedded in a composite laminate can be complicated due to non-unidirectional thermal and residual stress, thus under varying temperature conditions, the compensation for the embedding FBGs in composites needs to be investigated before they are applied in service; Also, it should be paid the attention that the strength/stiffness of a laminated structure is perhaps affected due to possible delaminations induced by the embedding FBGs [27].

The passive structural health monitoring is basically a prognosis-conceptual diagnosis method served for the damage inspection and evaluation, which is able to provide the first-hand knowledge of analysis and assessment for the structural responses resulting from basic loadings such as the impacts of hard landing or unforeseen or unknown events such as bird strikes, impacts from spattered runway stones during takeoff and tool drops during manufacture and maintenance. The events are all inevitable during the whole service time of composite structures. Accordingly, the passive SHM system is easy to supply the strong evidence and decision for possible further damage evaluation and the corresponding repair

solution if necessary. Over the last twenty years, the progression of passive SHM systems working for composite structures has been virtually dedicated only to the research of impact localization methodologies [28-32] such as the time differences method, the method of time of flight or arrival (TOF or TOA) of elastic waves, the probabilistic approach and propagating angles optimization methods. It is worth to mention that the impact localization method based on the time-reversal focusing algorithm firstly proposed by Fink, M. [33, 34] has been used to locate impacts on isotropic [35, 36] and anisotropic [37, 38] structures. Qiu *et al.* [39, 40] proposed an impact imaging method based on time reversal focusing to estimate impact location. But all of them were only able to estimate impact locations on composite structures and neglected the evaluation issue of impact forces, which led to a functional drawback for a passive SHM system. Actually, the evaluation of impact forces is much essential and crucial for a passive SHM system to commit to the further damage inspection and evaluation. Nevertheless, in order to achieve the actual applications of structural health monitoring techniques (or systems) on impact identification for in-service aircraft composite structures, many researchers [41-46] have proposed and developed their methods to detect and identify non-damaging impact events on composite structures by using distributed built-in or surface-mounted sensors. However, the identification procedure of impacts is known as a solving process of the inverse problem, as it means that the histories of forces are reconstructed using the data of structural responses resulting from unknown impact events. Tracy and Chang [47, 48] extended the use of the smoother/filter approach to a CFRP plate with a constant thickness, where a scalar function of the weighted least-squares was defined by Tracy to minimize the difference between the model output and the experimental output data, in which a Quasi-Newton gradient algorithm was then used to improve the estimation of the system parameters defined. However, Tracy didn't consider the presences of stiffeners and cutout holes for a complex aerospace structure, even didn't take into account existing adverse conditions in actual engineering environments, such as detrimental vibration environments.

1.3 Motivation and Objectives

In view of modern engineering demands, it is more imminent and favorable for aerial vehicles to develop an applicably robust and reliable structural health monitoring and identification (SHMI) technique including online impact identification approach and rapid multi-damage identification approach. The SHM based structural design criteria will significantly reduce the self-weight of the designed structures and decrease the design complexity and time, in contrast with the conservative damage tolerance approach based on damage uncertainty consideration, as the Boeing Company is creating the future pioneering new technologies for advanced structural design conception and the engineers and researchers have done the preliminary investigations [23, 49]. This SHM technique thereby enhances the optimization extent of structures, and then reduces redesign costs and improves the mechanical performance of structures. In addition, the SHMI technique also reduces the sustainment costs.

To sum up, the SHMI technique is a novel approach that increases the operational usage knowledge throughout the life cycle of a structure. In other words, the SHMI based structural monitoring criteria are able to improve the structural reliability effectively and further to increase the life cycle of structures and decrease products' life cycle costs.

In the real engineering applications of structural health monitoring and evaluation, many commercial structural health monitoring and measurement (SHM & M) systems have been developed for structural reliability and safety including impact issues worldwide. Although these structural health monitoring and measurement systems can report impact events in real-time, the reliability and robustness of their performances are still much difficult to satisfy the realistic demands from aerospace industries. Therefore, in order to overcome the limitations of the commercial SHM & M systems, the aim of this investigation was implemented to achieve as much as possible for engineering applicability. An ensemble structural health monitoring and identification (SHMI) technique is proposed and developed, and it has more significant dominances, in contrast to the commercial structural health monitoring and measurement systems. The primary advantages of the ensemble SHMI technique are that 1) the high accuracy of impact positioning, and the location error ratios are less than 18% of the sensor grid layout; 2) reporting the impact force history in real-time; 3) evaluating the structural state online; 4) estimating the impulse energies due to impacts in real-time; 5) the reliability and robustness of its performance for online monitoring unforeseen impact events. What is more, the developed SHMI technique is able to continuously execute the impact monitoring, identification and damage assessment for a structure in complex adverse environments, such as unfavorable vibration disturbances.

In the research progress of real-time impact identifications, most investigations [32, 37, 41-45, 47, 48, 50-58] previously mentioned have only taken into account their tested structure systems under "Perfectly Impracticable Environment Conditions" without any interfering factors,[2] such as, the changeable vibration disturbances from existing engineering environments. Hereupon, in order to realize the engineering applicability for in-service aerospace vehicles, a completely systematic technique needs to be developed to efficiently implement impact positioning, identification (force reconstructions), and structural state assessment under complex structure configurations, various impact conditions, and unpredictable environmental disturbances as random structural vibration. The realization of this technique would be very significant for solving practical aerospace engineering problems. Figure 1.3 demonstrates the future application of a highly-intelligent SHM system into the full-scale structure of a large commercial airplane.

In the research progress of damage identifications including localization and quantification and prediction, most researchers might not conduct a comprehensively rapid and effective damage inspection scheme. Whether some researchers could only develop the damage

localization methods to locate damage in a structure or proposed their damage quantification methods only to quantify damage in a composite structure, in particular, even if some investigators combined the damage localization and quantification into their damage identification approaches, but they still lost an essential and significant aspect of damage inspections, which develop the valid damage prediction function to evaluate possible damage growth. In that case, they are all not integrative and complete approaches or techniques to identify, predict and assess damage in a laminated composite structure. Nevertheless, a rapid multi-damage identification approach developed in the ensemble SHMI technique was proposed to carry out all of the above damage inspection issues, which are realized all by using the new developed damage indices – the multi-functional multi-metrics that are separately the energy density metric, the energy time-phase shift metric and phase divergence metric; also through their corresponding damage prediction trend functions (curves), it can be implemented to predict and evaluate possible increasing damage in a monitored laminated composite structure.

Accordingly, an integrally efficient and dependable technique, that is the ensemble structural health monitoring and identification (SHMI) technique, is proposed and developed to monitor automatically and real-time report visually the events' locations, force magnitudes, and the structural condition due to the impacts under unpredictably adverse vibration environments, what's more, to execute the further structural state assessment process by damage identifications since unforeseen external events such as impacts and lightning occurred. Accordingly, it would be very significant and helpful at safeguarding the safety and reliability of actual aerospace structures. To validate the engineering practicability of the SHMI technique, changeable environmental disturbances, different structural configurations and conditions were applied in this study. In the whole structural health monitoring and identification procedure, the functional module of signal data preprocessing can effectively eliminate complex disturbances from random vibrations using a new filter developed, and continuously provide stationary output response signals for the next sequential processing. Further to identify unknown impacts acting on structures, the functional module of the forward model generator can establish more accurate forward models based on the fast genetic algorithm parameters estimation. A forward model is constructed in terms of impulse response functions matrix that builds the relations between inputs and outputs.[2] Furthermore, the forward model can be employed in various structural configurations and for diverse types of impact objects once it is determined and built. Since the forward models provide simple model formulations, the inverse model operator can found rapid calculation models to reconstruct impact forces. Nevertheless, to achieve precise impact positioning, the functional module implements the two-steps localization approach. The entire impact positioning and identification (IPI) procedure becomes more pragmatic, functional and fast than the conventional model-based identification techniques [41, 42, 45, 59-63], because most of model-based identification techniques have only established the analytical models for flat and

constant property panels. Even if the analytical model or finite element model (FEM) can simulate the structural responses well, it is not feasible to found a simple inverse computational model to reappear the force history of an unknown impact from sensor measurement. Furthermore, the functional module of structural state awareness (SSA) is able to perform the localization and quantification of multiple damage such as matrix breakages, debonds and delaminations in laminated composites rapidly. In this thesis, the delamination damage type is focal to be investigated. Through the implementation of multiple damage identifications and damage growth predictions using a proposed novel Hilbert spectral analysis (HSA) based multi-damage indices approach, the structural state is thus easy to be assessed in real-time.

To interpret the SHMI technique developed, there are three major aspects included in this thesis, which are theoretical development, computer implementation, and experimental verification. In the theoretical development and computer implementation, a theoretical basis for constructing impulse response function matrix networks needs to be found from two different approaches to determine unknown impacts, which are that the one utilizes the training response data from the FEM simulations, and the other one adopts the training output data from the sensor measurements. In the subsequent chapter of experimental tests, a series of impact tests were performed under different conditions and unpredictable disturbances, also the validation tests of structural damage inspection were implemented using the CFRP panel structures with single or multiple damage. From all the evaluated results and discussion, the ensemble health monitoring and identification technique is verified sufficiently. There are reasons to believe that the developed SHMI technique is competent to online health monitoring and identification for composite structures in complex environments and conditions.

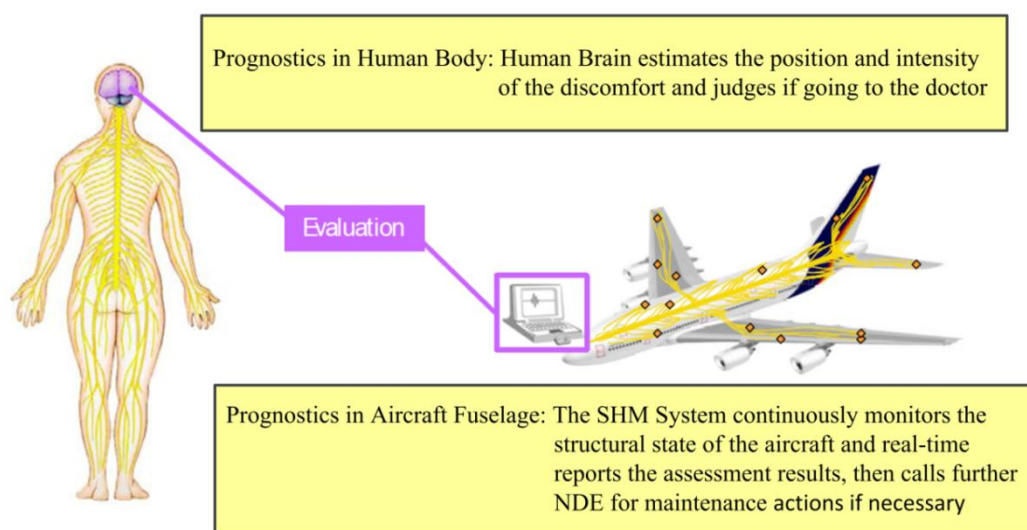


Figure 1.3 Demonstration on the future application of a smart SHM system into the full-scale structure of a commercial airplane (the human body and aircraft parts from [64], Source: Airbus).

2. Statement of Major Tasks

The objective of this research is to design and develop an automatic and robust structural health monitoring and identification technique (system) that can determine and report the impact location, reconstruct its force time history and its impulse energy in online mode, and can monitor the structural condition of an aerospace vehicle in real time through the visualized computations for the impulse energy distributions due to impact events, what's more, can rapidly assess the structural state by identifying and predicting possible damage induced by the external adverse objects. In addition, the ensemble structural health monitoring and identification (SHMI) technique is able to execute properly when some unexpectedly critical situations occur, such as an aerospace vehicle encounters an unforeseen impact event when it is in flight or operation. At that time, some conventional NDT techniques can't perform online to monitor and inspect the structural state of a vehicle in real time. Therefore, that is a significant problem for the reliability and safety of an operating aircraft vehicle.

Therefore, in view of the above detrimental background, several practical engineering problems were taken into account for our investigation of structural health monitoring and identification, for instance:

1. Different structure frames, e.g. different supporting structures which are the cantilever supporting structure and fixed supporting structure at all sides;
2. Randomly interfering noises from vibration;
3. Diverse structural components including a composite panel with a cutout hole and another panel with an I-crossbeam stiffener;
4. Various impact objects with different materials and masses.

The in-situ structural health monitoring and identification technique presented in Figure 2.1 was proposed, and this kind of SHMI system overcame all disturbances and unstable factors considered, and all mutative and detrimental conditions considered which are from structural complexity, the diversity of structure configurations, and the unfavorable effects of complex engineering environments. And also, this SHMI system overcame the significant shortcoming of the conventional NDT technique, which can't implement online monitoring and inspection for the safety of an operating aircraft vehicle.

Nevertheless, in case the developed structural health monitoring system could be validated successfully to implement efficiently impact positioning, identification and structural state assessment under the harsh conditions and unfavorable disturbance factors proposed above, it

would be a very significant step for the aerospace industry towards achieving a highly-intelligent aerospace vehicle [2].

On the basis of the objective of the in-situ structural health monitoring system, a novel layout means of distributed sensor arrays mounted on composite panel structures was proposed and applied to monitor and identify impacts on the structures, and to evaluate and learn the structural states in real time mode. In this case, the designed sensor networks using the layout approach could be used more easily and flexibly to record structural responses due to any impact event.

Here, the research addresses the monitoring and identification problem based on the following conditions:

- Impacts were conducted in the condition of low velocities. Low-velocity impacts may cause damage in CFRP panel structures as CFRP laminated composites are brittle and capable of withstanding a strain of less than 2% before breaking, and a small nick caused by such breakage can reduce the ultimate tensile strength by almost 50% [65]; even this damage in the struck region will be exacerbated owing to the non-visible or limited visual signature on the structural surface. Thus, an impact of the energy value of 20 J is enough to produce a small damage in a laminated composite. A reliable online monitoring and identification of low-velocity impacts is very significant for the demand of reliability and safety of composite structures, in particular, the large-scale composite structures of real aerial vehicles. Therefore, for the purpose of the impact force reconstructions, the impact energy might be considered specifically no more than 15–20 J. Without the impact force reconstruction issue, a high impact energy is not constrained and doesn't affect to estimate the impact location and assess the structural state.
- Impact durations are short enough (“millisecond”) so that damping doesn't need to be considered.
- Impacts are on the reverse side of panels from the side of sensors mounted and from stiffeners.
- The sizes of impactors are much less than the dimensions of the panels.
- The structure is not at rest before an impact event occurs on a structure, owing to adding complex vibration conditions to the structure. Random vibration environments were considered and introduced into a series of impact experimental tests in order to validate the robustness of the developed SHMI technique subject to complex adverse environments, thereby which improve the applicable possibility of this technique in practical engineering.

- The mounted sensors are small in order that the physical property of a monitored structure is not altered, and the sensor networks are variably spaced so that the stiffnesses of the panels are not affected.

To sum up, the proposed structural health monitoring and identification technique is generalized in Figure 2.2, and its implementation results in the basic structure of this thesis, which is dedicated to the following crucial processing chains:

Chapter 4 Signal Data Preprocessing

In this chapter, a mode decomposition based filtering method is proposed and used to eliminate the complex disturbance noises due to vibration from the original output signals of structural responses.

Chapter 5 Identification of Unknown Impacts

Firstly, structure system modeling is used to found a forward model that enables to describe the dynamic input-output relation between the external force and responses of a structure. Accordingly, an accurate forward model enables to simulate the precise structural response resulting from an unknown impact event. However, in modeling a structure system, the estimation and optimization processes of system parameters are crucial and essential for building an accurate forward model. Hence, a novel parameters estimation method – fast genetic algorithm parameters estimation (FGAPE), is proposed and developed in this thesis. And it is employed to reduce the prediction error in order to acquire the optimal model parameters a_i and b_j . Afterward an optimal forward model is founded, the corresponding inverse model needs to be built to reconstruct the force history of the unknown impact. In the inverse solution, the force history of the unknown impact can be predicted and reconstructed using the built inverse model.

Chapter 6 Structural State Assessment Including Damage Localization and Quantification

Impacts may cause any damage, especially, delaminations in laminated composites. Therefore, this proposed SHMI technique is a diagnosis technique that serves to real-time inspect unforeseen impacts and to assess the effects of the structural state due to the impacts. In case impacts result in structural damage such as delaminations, the technique will provide the relevant damage information for the monitored composite structure. However, how to launch automatically and implement the further comprehensive damage identification, a reliable safety threshold for the force magnitude or the magnitude of impact energy is set as the threshold of possible damage. A demonstration of an integrative structural health monitoring and identification technique is presented in Figure 11.1.

Chapter 7 Estimations of Multi-Impact Locations

In order to determine multi-locations of unknown impacts, there are two steps which need to be implemented. The first step is the initial location estimation based on a smooth energy distribution method; the second step is updating the impact location coordinates based on two solutions that are 1) the time-of-flight (TOF) based quadrilateral centroid principle and 2) the defined cost function.

Chapter 8 Sensor Modeling and Calibration

Since the inconsistency of the sensors used results from manufacturing technology, the inconsistency of adhesive layers, the complexity of monitored structures and so on, the piezoelectric sensors used are thus required to be calibrated so as to improve the accuracy of evaluation that the SHMI technique implements.

In short, the developed in-situ ensemble structural health monitoring and identification technique will be introduced comprehensively in the following chapters. In addition, through all the cases of impact tests considered, the ensemble SHMI technique will show its potential as an onboard rapid diagnostic tool for impact identification and damage assessment.

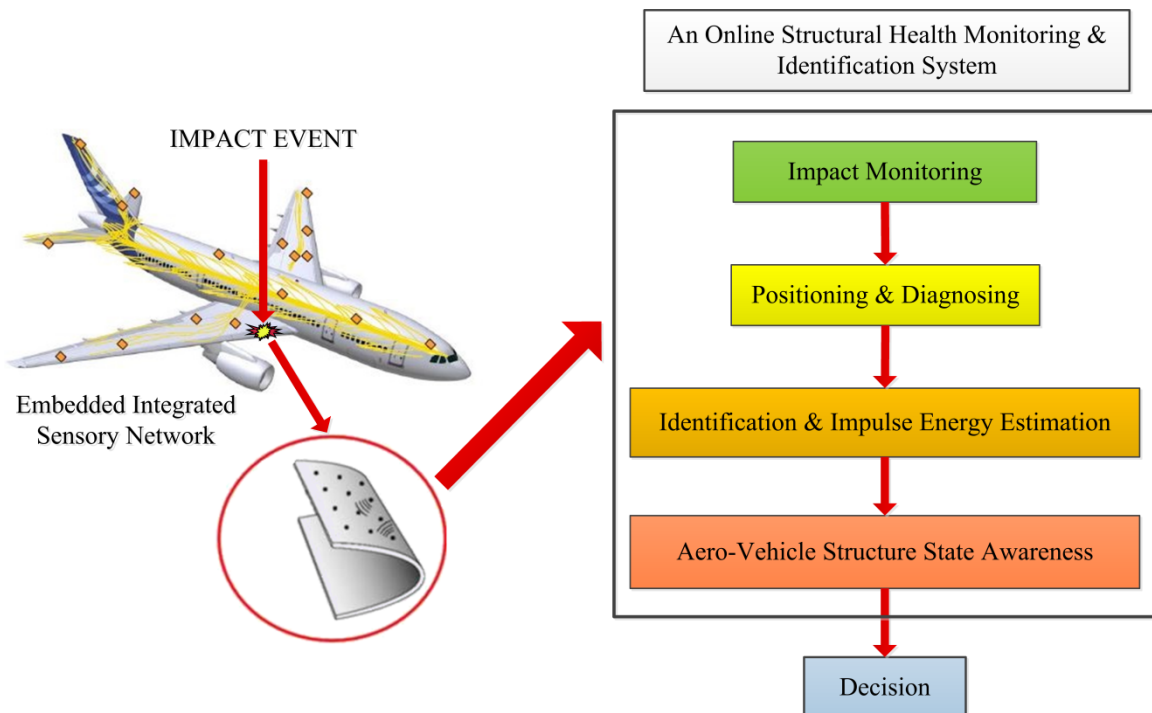


Figure 2.1 Overview of the architecture of the developed online structural health monitoring and identification system (the aircraft part from [26], Source: Airbus).

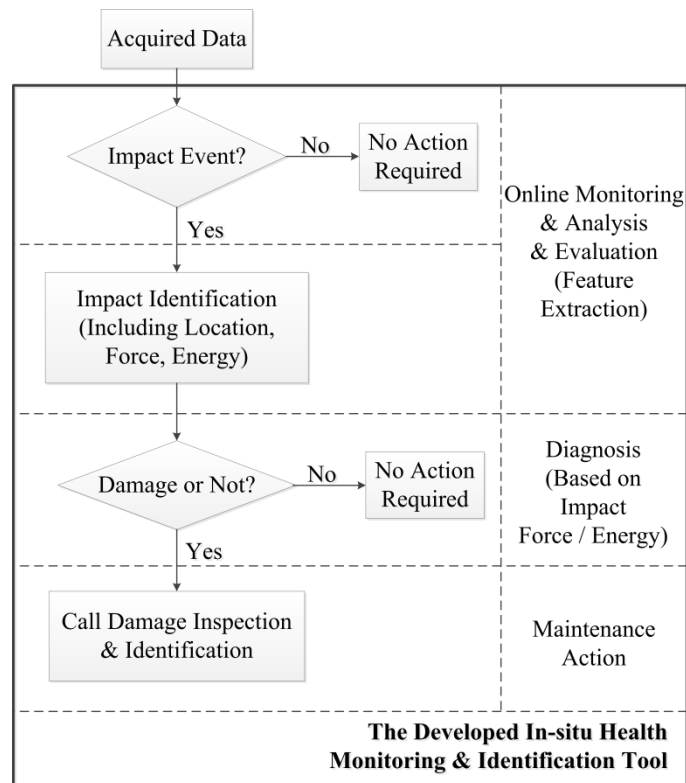
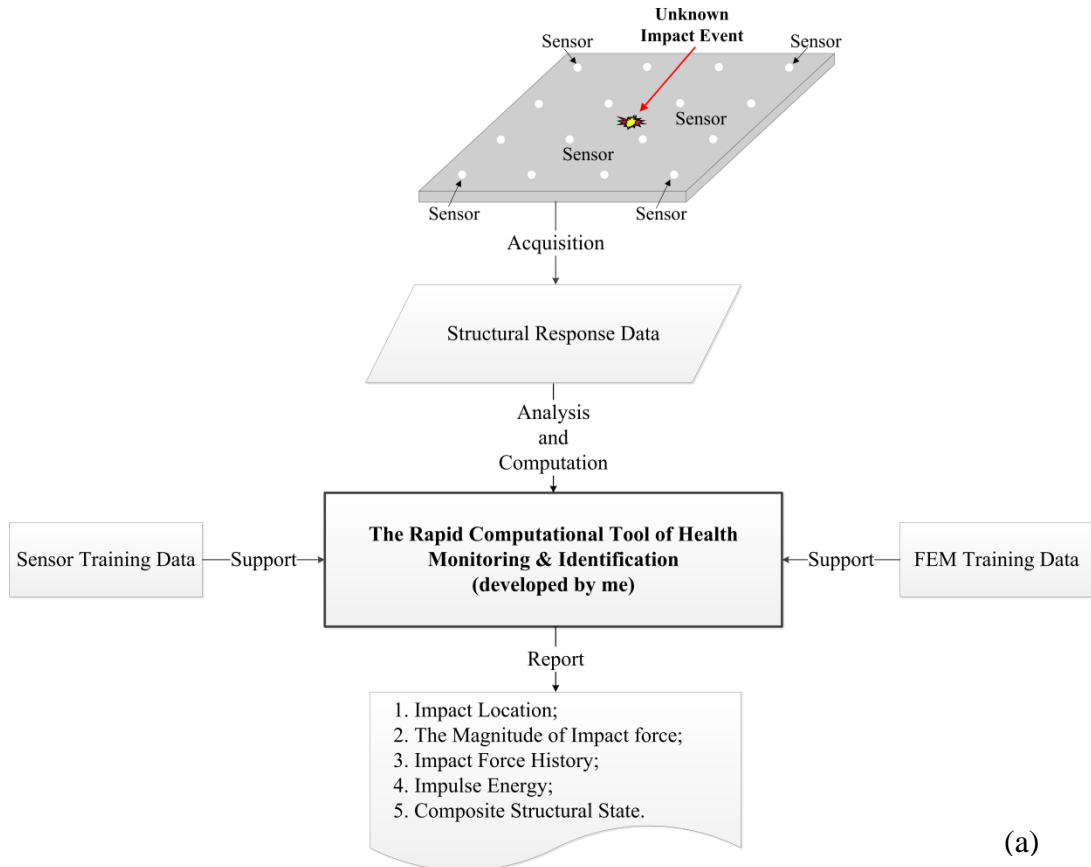


Figure 2.2 Flow charts of the proposed structural health monitoring and identification technique: (a) the implementation of the SHMI technique and (b) the general computation procedure in a health monitoring and identification.

3. Approach of Health Monitoring and Identification

This study included theoretical development, computer implementation, experimental verification and studies of practical engineering issues. The theoretical basis of the ensemble structural health monitoring and identification (SHMI) technique is established not only to identify and estimate unknown impacts from structural responses through the measurements of distributed sensor network. In forming impulse response function matrix, data sources are from two approaches, which are 1) sensor measurements from experimental tests and 2) simulated structural response data from FEM simulations. Further, the structural response outputs due to impacts are collected and utilized to reconstruct the force histories, to estimate the impact locations and to evaluate the structural conditions. But also, using the guided Lamb waves excited from the defined actuators of the configured sensing network, the structural state can be evaluated further through achieving structural damage identification, and the proposed multi-functional multi-metrics (MFMM) damage prediction trend curves can implement for possible structural damage expansions.

The entire identification procedure is all implemented in a developed software tool for real-time robust impact identification and rapid damage diagnosis. Additionally, in various experimental setups, diverse distributed piezoelectric sensor networks (or arrays) were designed and employed to measure the responses of the laminated composite structures due to external impacts or ultrasonic pulse actuations. Through the various experimental tests, the SHMI technique's performance of impact identification and damage assessment were validated and evaluated. Experimental results were also used to study practical implementation issues.

3.1 Theoretical Development

For impact monitoring and estimations, in order to obtain a general solution, a forward model is constructed using an SHMI technique developed by Si [2, 66]. The forward model is not designed from the mechanics and properties of a structure; instead, it is obtained by utilizing the responses of a structure due to impact loading from FEM simulations and experimental tests, which is referred as the dynamic mechanical model – the state-space formulations.

To reconstruct impact force histories using the measured structural responses, the forward model can be easy to construct generic model formula for the inverse model operator (IMO). Whereas, a conventional model (or so-called first principle model) based approach is difficult to apply to complicated structures, the IMO for reconstructing impact forces is quite intensive computationally, that is, it takes a long time, and can't implement in real-time mode. Meanwhile, a neural-network approach is also difficult to apply for various structure configurations and different impactors, since every large training set is required for varying structure configuration and every kind of impactor.

Figure 3.1 demonstrates an overview of the developed structural health monitoring and identification system. The sensor response outputs caused by an impact are collected and utilized to locate the impact, reconstruct the force history, and evaluate the structural state. For the whole positioning and identification procedure, a structure system model must be constructed for a given structure, and the model is obtained from 1) FEM simulations and 2) experimental measurements using the proposed SHMI technique.

The theory for each functional module of the developed structural health monitoring and identification technique will be discussed in this thesis, which includes:

1. Signal data preprocessing (SDP);
2. Forward model generator (FMG) including the robust fast genetic algorithm parameter estimation method proposed;
3. Inverse model operator (IMO);
4. Impact positioning calculator (IPC) and evaluation;
5. Structural state assessment (SSA) – damage identifications.

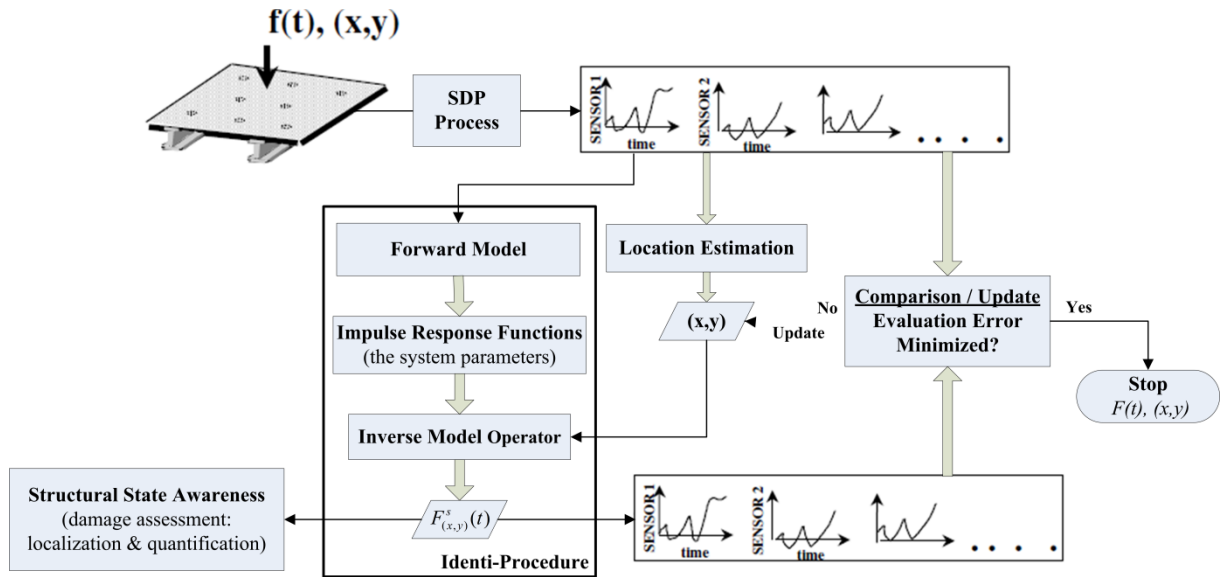


Figure 3.1 Overview of the systematic frame from the proposed ensemble SHMI system.

3.1.1 Signal Data Preprocessing

In order to de-noise from original sensor signals, a mode decomposition based filtering method — the fast empirical mode decomposition (EMD) based hybrid thresholding filter is adopted to eliminate interferences such as random interfering noises and transfer smoothly the nonlinear effects from non-stationary output signals due to random vibration to the linear dependence, that is, discovering and extracting the effective linear relation between the external input and response output of the structure subject to a sudden impact, which is hidden in the nonlinear condition [2]. The filter preprocessing scheme can be divided into two steps, which are 1) fast empirical mode decomposition to the acquired original sensor signals with random noises and 2) hybrid thresholding filtering based on intrinsic mode functions (IMFs) resulting from EMD. The details of anti-interference and denoising are discussed in Chapter 4.

3.1.2 Forward Model for Structural Responses

A forward model also referred as structure system model (SSM) is a mathematical expression realized through a digital signal processing (DSP) method. The constructed forward model describes the dynamic input-output relation between the external force and structural responses. Then, to obtain the structural response due to an impact, a forward model needs to be established. The forward model is constructed in the form of impulse response functions (IRFs) separately from the dynamic calculation model of finite element and the means of experimental measurements. The details of the structure system modeling are discussed in Section 5.1.

3.1.3 Impulse Response Functions

Impulse response functions (IRFs) are obtained using the proposed fast genetic algorithm parameter estimation based system identification method. The IRFs can provide a simplified simulation process to solve the inverse problem of impact force reconstruction. However, in the FEM simulation, the training data from simulated structural strain responses can be used to establish the grid network composed of impulse response functions. Whereas in the experimental measurements, the training data from sensor measurements can also be used to build the practical grid network formed of impulse response functions. The details of the constitution of the grid network of impulse response functions are discussed in Section 5.1.4.

3.1.4 Inverse Model Operator for Force Reconstructions

With the use of collected sensor data and an estimated impact location, the force reconstruction processing is able to estimate the force magnitude and to report the force history. In other words, by utilizing the impulse response functions constructed through the fast genetic algorithm parameter estimation based system identification method, the inverse solution for an unknown impact can be found. It means that the force history of an unforeseen impact can be reconstructed by using the data of sensor measurements resulting from structural responses. Nevertheless, the accuracy of force reconstructions is dependent upon the accuracy of the determined impulse response functions generated from the optimized values of model parameters (a_i, b_j) . The optimization procedure performed during structure system modeling is a key prerequisite to reconstruct the force history due to an impact, which is discussed in Section 5.2.

3.1.5 Structural State Assessment – Damage Identification

Once the force magnitudes or impulse energies produced by unknown impacts exceed the safe threshold set based on an empirical value of damage index parameter (DIP), or high-velocity impacts with high impulse energies occur, the functional module of structural state awareness will be launched automatically. In the structural state assessment, there are two major tasks need to be achieved, which are damage localization and quantification. Nevertheless, to implement the two goals successfully, three damage index parameters were defined and developed, which are the energy density metric, energy time-phase shift metric and Hilbert phase metric. In addition, the damage prediction trend curves (DPTCs) based on the multi-functional multi-metrics (MFMMs) are able to predict progressive delaminations in laminated composites. It will be detailed and discussed further in Chapter 6.

3.1.6 Estimation of Impact Locations

The impact positioning function is divided into two steps, which are 1) sensor region extraction and initial location estimation and 2) updating and locating the accurate impact coordinates. Because the SHMI technique is based on global sensor measurements, the impulse response functions are thus dependent upon the impact locations, and a location estimation element is required to generate an impact location prior to force reconstruction. The details of impact location estimations are discussed in Chapter 7.

3.1.7 Sensor Calibration

With the use of a structural health monitoring system with multi-sensor laid, an actual engineering structure often meets a problem of which each sensor mounted on (or embedded in) the structure has probably different response characteristics, even if they are all the same sensing material and dimension, in addition, they are laid at the symmetric locations in an isotropic region in the structure. The reasons are diversified and complicated, such as the inconsistency of the thicknesses of adhesive layers, etc.. Therefore, it is necessary to add a specific function component to the SHM system for calibrating the different responses. Even a slight irregularity of the bonding condition between sensors and a host structure may induce significant divergence in the sensing capability.

To achieve the above objective, it is required to have a sensor calibration procedure for different sensors of global measurements, because the impulse response functions are only good for one specific sensor. In the following, two calibration methods are proposed, which are the impedance based method and an alignment method of anti-symmetric impacts. The two methods of sensor calibration are discussed in Chapter 8.

3.2 Computer Implementation

Once the theoretical bases described above were defined and founded, they were implemented in the developed software tool. Using sensor measurements from the experimental tests, besides the locations, force histories, and the structural conditions could be determined and evaluated for unknown impacts, in the meantime, being visualized on the screen, multiple delaminations could also be located and quantified, which might be induced by impacts.

3.3 Experimental Verification and Accuracy Evaluation

The ensemble structural health monitoring and identification technique was tested under various structure configurations, various material configurations of panel structures, and diverse impact conditions along with experimental impacts of various types and locations.

Since the forward modeling is the key factor of the entire impact identification procedure, the impulse response function matrix was tested separately, as was the location estimation method. Finally, the developed ensemble structural health monitoring and identification technique was validated for accuracy through a series of relevant experimental tests. The experimental tests are described in Chapter 9, and the results and discussions are presented in Chapter 10.

3.4 Studies of Practical Engineering Issues

For a real aerospace vehicle, there exist a number of intricate and disturbing factors among the real engineering environment issues which affect the normal implementation and diagnosis of a structural health monitoring system. Thus, with regard to the development of a smart SHM system, vibration noise is a significant practical engineering problem existing in the aerospace industry. Then, in case random interfering noises resulting from structural vibration could also be taken into account to apply to our experimental tests, and the SHMI technique could be validated successfully for its effectiveness and robustness for anti-interference, it would be very significant to solve this kind of practical aerospace engineering problem. The details are discussed in Chapters 4 and 10, which include the novel filtering method to eliminate interferences and the comparison results from vibration-noise contamination and denoising effects.

4. Signal Data Preprocessing

In order to de-noise from original sensor signals, a mode decomposition based filtering method – the fast empirical mode decomposition (EMD [67]) based hybrid thresholding filter [68, 69] is developed to eliminate complex adverse disturbances such as random vibration noises resulting from a piezo-vibrator [2], and is adopted to transfer smoothly the nonlinear effects due to the vibration from non-stationary outputs to the linear dependence; that is, discovering and extracting the properly linear input-output relation between impacts and the structural responses, which is hidden in the nonlinear condition [2]. The filter preprocessing scheme is sequentially performed in two stages, which are the fast EMD decomposition division and filtering processing division. They will be described further in Section 4.2 and 4.3.

4.1 Background

To verify the robustness of the ensemble SHMI technique with respect to the impact monitoring and identification, variable random vibrations were proposed and introduced on purpose into our impact tests, which is deemed to be adverse disturbances. Under the complex disturbance environment, the accuracy of impact identifications using the ensemble SHMI technique was validated. Nevertheless, to perform the implementation of random structural vibration, an experimental approach that a piezo-composite stack mounted on a tested composite structure was used to act as a vibrator was applied in the validation tests of impact identification robustness. As structural vibration disturbances are produced in a monitored structure, a fast empirical mode decomposition based hybrid thresholding (FEMD-HT) filtering module is developed, and also it is essential and a crucial processing module for the ensemble SHMI technique to reliably serve for the in-situ impact monitoring and identification under adverse environmental contaminations.

In a word, for considering the engineering applicability of the ensemble SHMI technique, the FEMD-HT filtering method was proposed and integrated into the ensemble SHMI technique so as to improve the reliability and robustness of this SHMI technique applied in diverse real-adverse environments.

4.2 Fast Empirical Mode Decomposition Module

To indicate the superior anti-interfering performance due to random vibration, the novel mode decomposition based hybrid thresholding filtering method was proposed, which differs from other conventional filtering methods such as the Fourier and Wavelet filtering method. For the Wavelet filtering method, it can perform data processing using the basis functions that are formed of a series of scaled and shifted functions from a particular function, but intrawave frequency modulations can't be resolved, and the observation in high-frequency range can only reveal local events, as the limited length of the fundamental wavelet function leads to the leakage. Also, it doesn't have the adaptive nature. Whereas, for the FEMD based filtering method, it is able to define explicitly both intra- and interwave frequency modulation, and further it can generalize Fourier analysis with varying frequencies and amplitudes. Meanwhile, it is robust for nonlinear and non-stationary data processing through the first local and adaptive method. There are reasons to believe the mode decomposition based filtering method to signal data processing is sometimes better than that of the Wavelet filtering method, depending on individual cases and demands.

Once the sensor response data are collected from experimental tests, the signal data will firstly be decomposed into an aggregate of intrinsic mode functions (IMFs). Since the intrinsic mode functions have well-behaved compatibility and transformative, the IMFs are thus decomposed from the originally puzzled noise signals recorded by sensors using the fast empirical mode

decomposition. Meanwhile, the composed IMF components can be employed further to serve for some particular applications such as the filter design, which will be detailed in Section 4.3 concerning the developed signal filtering unit.

To facilitate the goal of online signal data preprocess to meet the demand of actual engineering, there are two sub-processing blocks conducted in the whole fast empirical mode decomposition procedure. Figure 4.1 indicates the systematic execution flow of the FEMD completely.

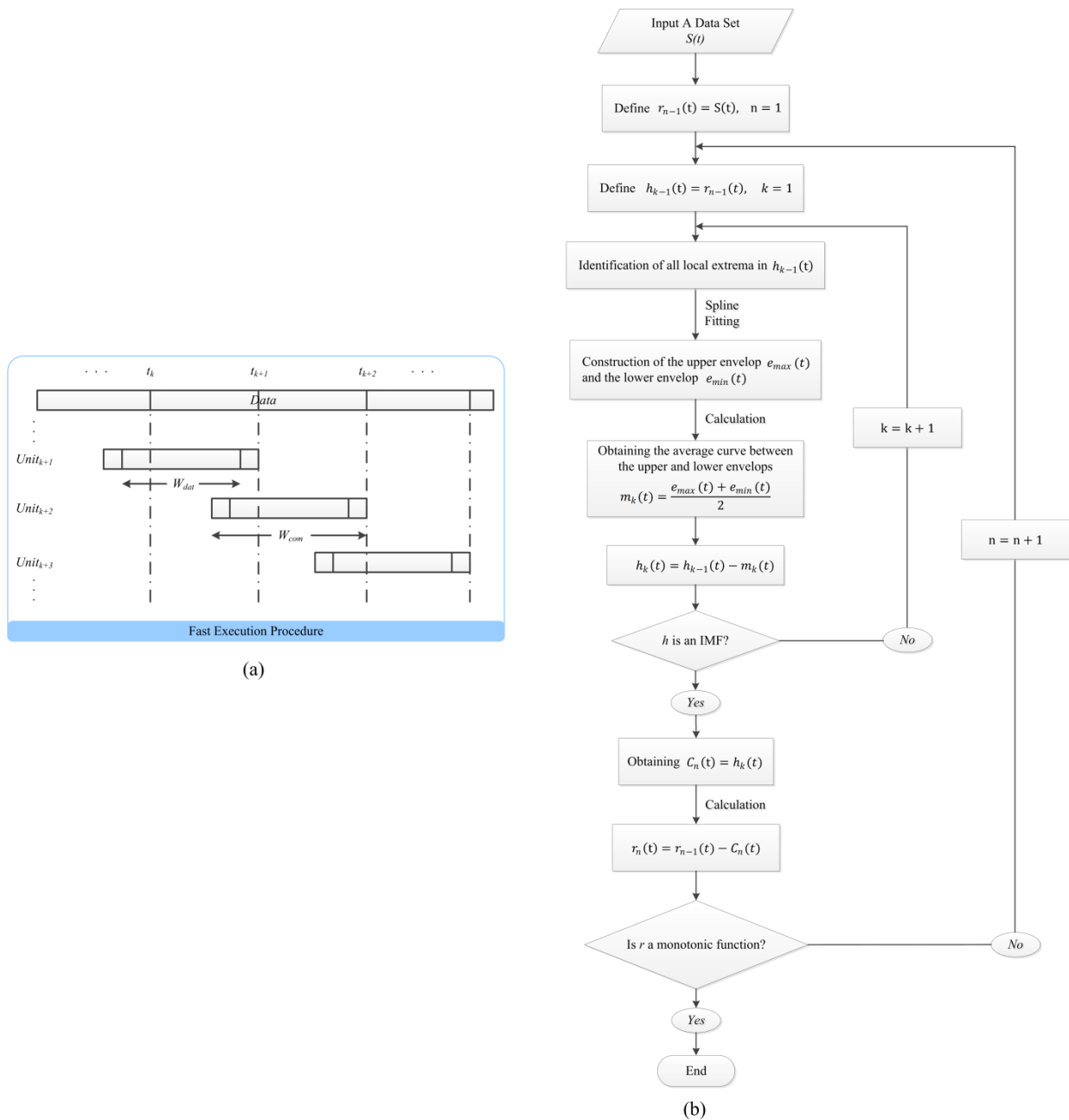


Figure 4.1 Flowchart of the FEMD decomposition procedure: (a) the fast execution module, (b) the EMD [67] module.

From the FEMD process, it can be seen that at the left side, the fast execution module, it can be easy to achieve the online data process by which multiplex data series are divided into multiple computation windows; and at the right side, each divided data set would be processed further through the EMD decomposition.

Hence, the empirical mode decomposition was introduced into the FEMD sub-processing division of the signal data preprocessing (SDP) module. This adaptive mode decomposition method is performed through the sifting process based on the spline fitting. Through the sifting process, a chaotic data can be decomposed into several intrinsic mode function (IMF) components with significant instantaneous frequencies. A flow demonstration of the complete EMD decomposition is presented in Figure 4.2, where an original signal is decomposed using the EMD.

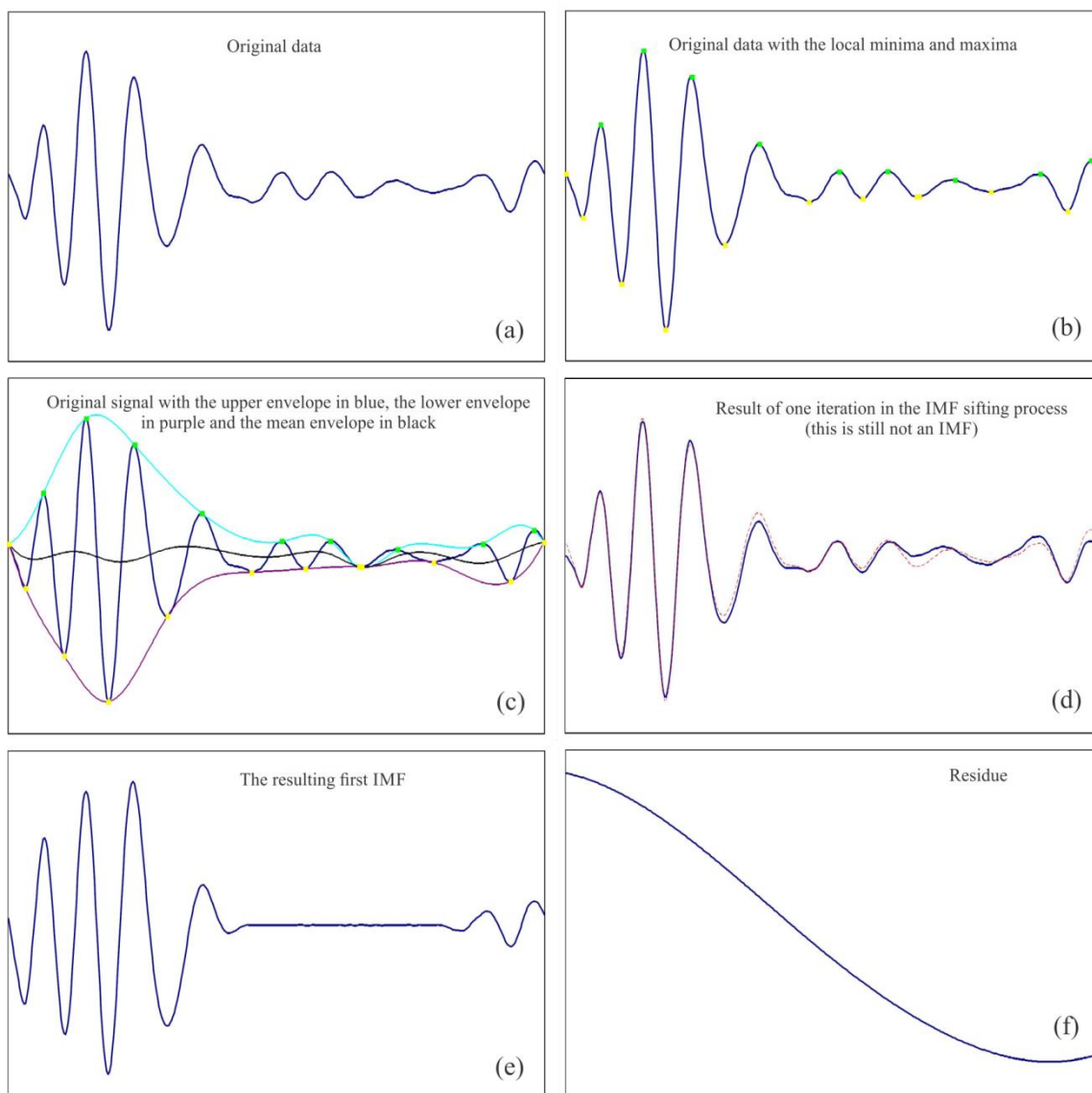


Figure 4.2 Sifting process used to illustrate an EMD [67] decomposition steps: (a)→(b)→(c)→(d)→(e)→(f)

A comprehensive knowledge of the empirical mode decomposition is introduced in Huang's book [67]. Here, it would not be popularized too much. But it needs to emphasize that the intrinsic mode functions will turn into a crucial basis for the sequential filter bank. Therefore, the IMF should be instructed to make more explicit for its unique feature. Each intrinsic mode function is a monotonic function that reveals the oscillatory mode embedded within data. Each oscillatory mode from an IMF component doesn't take multiplex riding waves.

In real engineering environments, there exist lots of complex disturbance factors that affect the dependability and accuracy of structural state diagnosis and assessment directly. In particular, the mechanical vibration results in random noise environments for a structure, which interfere the evaluation for the structural condition due to unknown external impact events. What's more, most of the data collected from engineering structures are not naturally intrinsic mode function data. Meanwhile, the common filtering methods employed, such as the frequency extraction based and Chebyshev based filtering methods, all cannot provide perfectly the full description of the frequency contents once the data involve more than one oscillatory mode in a given time window. Hence, a way to decompose the non-stationary nonlinear data of multiple oscillatory modes into a set of independent mono-IMF components should be founded.

Consequently, a fast EMD based filtering approach was proposed and developed to satisfy the practical demands from complicated engineering environments. In our validation experiments on random vibrations, all of the sensor data collected within the vibration noises contamination were decomposed successfully so as to serve for the sequential filter bank. An example of the FEMD decomposition for an original sensor data is presented in Figure 4.3, where the sensor data is decomposed effectively. The original sensor data was outputted from structural response within comparatively high random noises of signal-to-noise ratio (SNR) of 10.

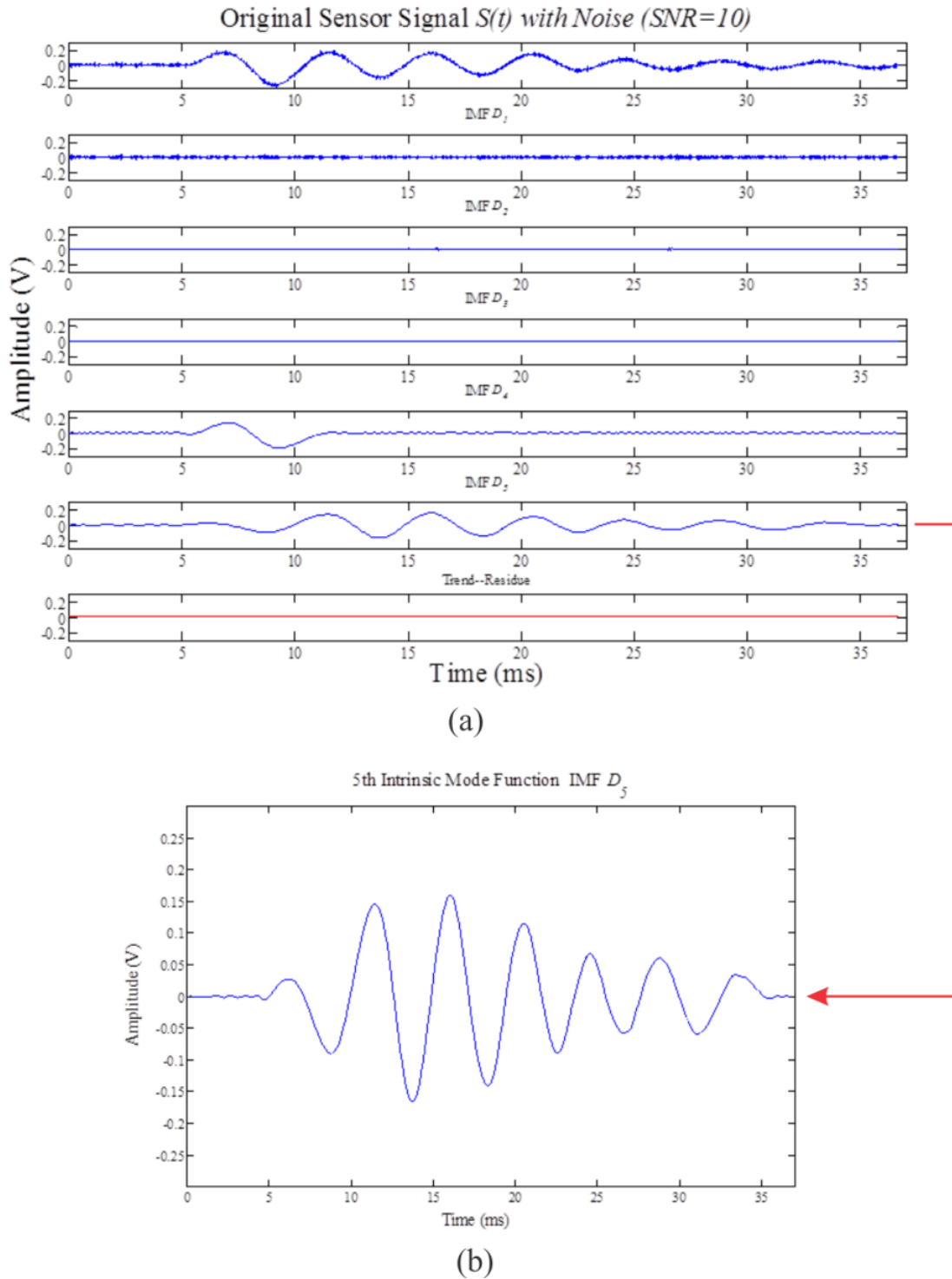


Figure 4.3 FEMD for an original sensor data: (a) the sensor data with noise decomposed by FEMD, (b) an example of the 5th IMF.

From the detailed decomposition process in Figures 4.2 and 4.3, the sifting process of the EMD is to remove redundant interfering waves and to make the wave profiles more symmetric within smoothing uneven amplitudes. As the intrinsic mode functions derived from the sifting process have unique local frequencies, the fast empirical mode decomposition

enables to decompose any fuzzy nonlinear data of multi-modes into n pieces of monotonic empirical modes and a mono-residue.

4.2.1 The Stoppage Criteria

An appropriate stoppage criterion should be determined to work for the sifting process, since the intrinsic mode functions need to preserve enough physical nature of both frequency and amplitude modulations. On one hand, a too stringent stoppage criterion can lead to over-decompose the data, where the intrinsic mode functions of non-physical meaning might be generated. On the other hand, a too lax stoppage criterion could not be competent to extract the true intrinsic mode functions obscured from the blurred data.

Huang, N. E. [70] firstly proposed to use the standard deviation acted as a stoppage criterion. It similar to the Cauchy convergence test, while the standard deviation, SD , is computed from a squared sum of the absolute difference of two consecutive sifting results as

$$SD_i = \frac{\sum_{t=0}^T |H_{i-1}(t) - H_i(t)|^2}{\sum_{t=0}^T H_{i-1}^2(t)} \quad (4.1)$$

Then the sifting process stops when SD is smaller than a pre-given value. But such stop criterion is difficult to realize rapid computations, as it requires many siftings and therefore increases the computer time in extracting each intrinsic mode function.

In addition, a novel stoppage criterion have been considered by Rilling, et al. [71], which takes into account the locally large excursions while ensuring globally small fluctuations in the mean. This stoppage criterion is based on two thresholds θ_1 and θ_2 and an evaluation function

$$\rho_k(t) = \frac{m_k(t)}{a_k(t)} \quad (4.2)$$

where

$$a_k(t) = \frac{e_{\max}(t) - e_{\min}(t)}{2} \quad (4.3a)$$

$$m_k(t) = \frac{e_{\max}(t) + e_{\min}(t)}{2} \quad (4.3b)$$

where $m_k(t)$ is referred as a local trend per iteration, or called an envelop mean per iteration; $a_k(t)$ is known as a mode amplitude per iteration; $e_{\max}(t)$ is an upper envelop function obtained by interpolating the cubic spline for the local maxima; whereas $e_{\min}(t)$ is an lower

envelop function obtained by interpolating the cubic spline for the local minima. The sifting process is duplicated until $\rho_k(t) < \theta_1$ for 95% of the total duration, while $\rho_k(t) < \theta_2$ for the leftover part.

These two different stoppage criteria have been tested, and the most efficient one turns out to be the last one in terms of the number of iterations and computer time.

4.3 Filtering Processing Module

In this part, most of the knowledge has been described and published in Si's paper [2]. Here, some crucial knowledge points are also stated as follows,

The signal data preprocessing (SDP) procedure based on the fast EMD-hybrid thresholding (HT) filter as shown in Figure 4.4 is as follows:

- 1) Sensor temporal signals $S(t)$ with random noises are decomposed by fast EMD, as illustrated in Figure 4.3;
- 2) From the scales with the valuable information, the first five scales (such as 1st, 2nd, 3rd, 4th, 5th scales) with the highest energies are normally extracted, and then an appropriate threshold is chosen at every scale to remove the interfering noise components. Hence, the hybrid threshold function is defined as:

$$\begin{aligned}
 & IMF'(D_i) \\
 &= \begin{cases} 0, & \text{if } |IMF(D_i)| < C_1 \\ \text{sign}(IMF(D_i)) \cdot \left[\lambda_1 - \sqrt{(\lambda_1^2 - C_1^2) + (2C_1 + |IMF(D_i)|)|IMF(D_i)|} \right], & \text{if } C_1 \leq |IMF(D_i)| < C_2 \\ \text{sign}(IMF(D_i)) \cdot \left[\lambda_1 + \sqrt{-C_2(2\lambda_2 + C_2) + 2(\lambda_2 + C_2)|IMF(D_i)| - |IMF(D_i)|^2} \right], & \text{if } C_2 \leq |IMF(D_i)| < C_3 \\ IMF(D_i), & \text{if } |IMF(D_i)| \geq C_3 \end{cases} \\
 & \dots\dots(4.4)
 \end{aligned}$$

where $IMF'(D_i)$ are the effective components of response signals obtained from the filtering process $i = 1, 2, \dots$. C_2 is the threshold which will be determined by a kurtosis-based approach individually for every scale and is given by

$$C_2 = \frac{\max(|Z|)}{Kurt(Z)/3} \tag{4.5}$$

where Z is the intrinsic mode function coefficient of a scale, $Kurt(Z)$ is kurtosis of the decomposed components. Nevertheless, C_1 , C_3 , λ_1 and λ_2 will be specified according to the C_2 value in each scale. They are expressed by

$$C_1 = \frac{C_2}{p_s} \quad (4.6a)$$

$$C_3 = \left(1 + \frac{1}{\sqrt{2}p_s}\right) \cdot C_2 \quad (4.6b)$$

$$\lambda_1 = \left(1 - \frac{1}{p_s}\right) \cdot C_2 \quad (4.6c)$$

$$\lambda_2 = \frac{1 + \sqrt{2}}{p_s} C_2 \quad (4.6d)$$

where a specific parameter p_s is defined as $p_s = 1 + \max(Kurt(Z) - 3, 0)$, since a higher kurtosis indicates more significant components existed. In order to make the connection curves tangential at the threshold value, there are two arcs need to be obtained through calculating the two radii λ_1 and λ_2 . This ensures a continuous smooth transition.

The proceeded intrinsic mode function coefficients mainly from the first 5 scales are combined and reconstructed. Finally, the filtered signal can be obtained from the reconstruction process, which is illustrated in Figures 4.5 and 4.6. Figure 4.5 presents that an original sensor data is denoised successfully using the developed FEMD-HT filter, and the sensor data within moderate-intensity random vibration noises of SNR=15 was recorded from the structural responses. Figure 4.6 presents that the developed FEMD-HT filter was employed to denoise effectively another original sensor data, which was collected from the structural responses within high-intensity random vibration noises of SNR=10.

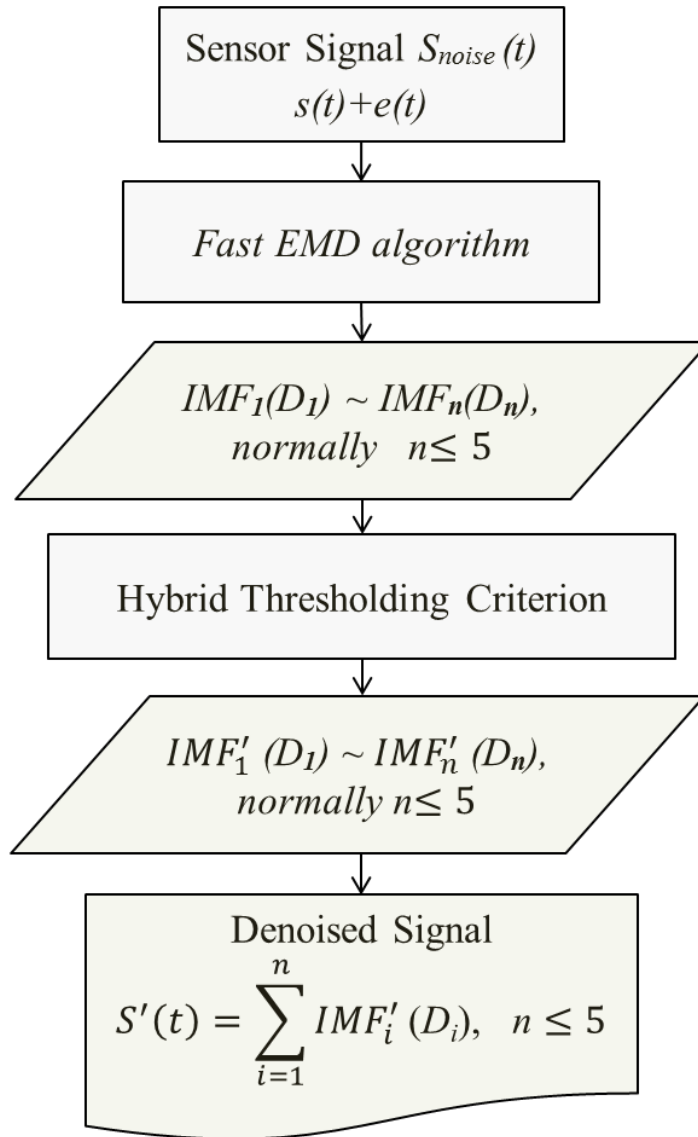


Figure 4.4 Flowchart of the FEMD based hybrid thresholding filtering process.

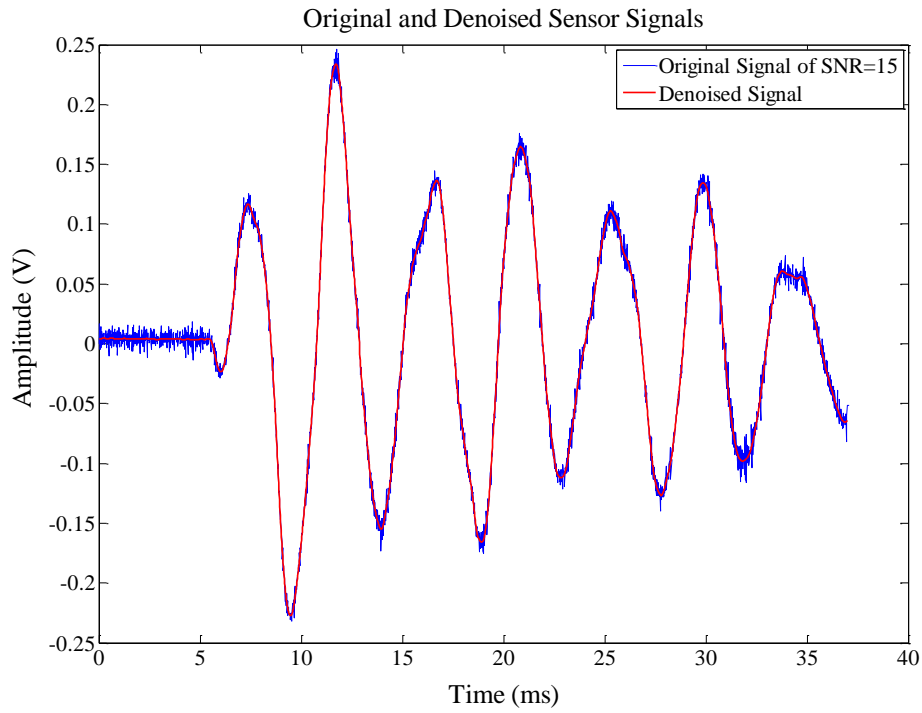


Figure 4.5 An original sensor data from structural response within random noises of SNR=15.

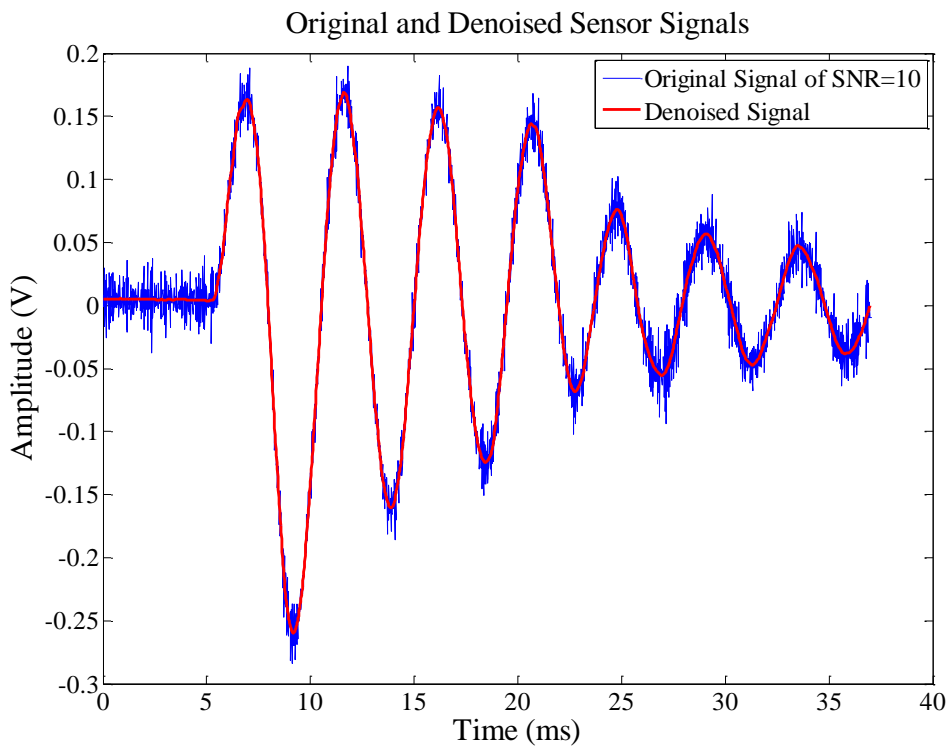


Figure 4.6 An original sensor data from structural response within random noises of SNR=10.

5. Impact Monitoring and Identification

In the research field of the impact monitoring, some researchers have dedicated their efforts to develop an applicable impact identification method to estimate external impacts and the effects on the reliability of a structure due to impacts, such as Markmiller and Chang [72], Jacquelin [73], Qiu and Yuan [74], Chen and Yuan [36, 75], and Wu [76]. A dependable and robust impact monitoring and identification approach has been proposed and developed by L. Si [2, 77] to estimate impact locations, reconstruct force histories and evaluate the structural condition due to unexpectedly unknown impacts. The conception and architecture of the IMI approach have also been described in Si's impact monitoring papers.

In this chapter, it will primarily be described how does the proposed fast genetic algorithm parameters estimation (FGAPE) based impact monitoring and identification (IMI) approach execute to identify rapidly and effectively them once unknown impacts occurred on a composite structure. Meanwhile, the dependability and robustness of impact identifications using the FGAPE based IMI approach will also be discussed. This developed impact monitoring and identification procedure is substantially divided into three processing parts, which are the construction of forward model (including model parameters estimation and optimization, etc.), inverse model solver (IMS) and formation of networks of IRF grids. To build the accurate, realistic and robust forward models for impact identifications, a forward model is simplified and constructed in terms of the impulse response functions (IRFs) obtained from two approaches that are FEM simulations and experimental training. Finally, an unknown impact can be identified reliably as the form of the force history reconstruction by using the inverse model operator.

5.1 Forward Modeling

Whether an unknown impact on a composite structure can effectively be identified, a valid, accurate and stable forward model needs to be constructed. In this section, it will be introduced in detail that a forward model is constructed successfully using the system modeling approach based on the fast genetic algorithm parameters estimation.

5.1.1 Basic Approach

The construction of the forward model for any given composite structure with or without multi-stiffeners is illustrated in Figure 5.1, which is realized based on an adaptive computation network of the impulse response functions overlaying the whole structure.

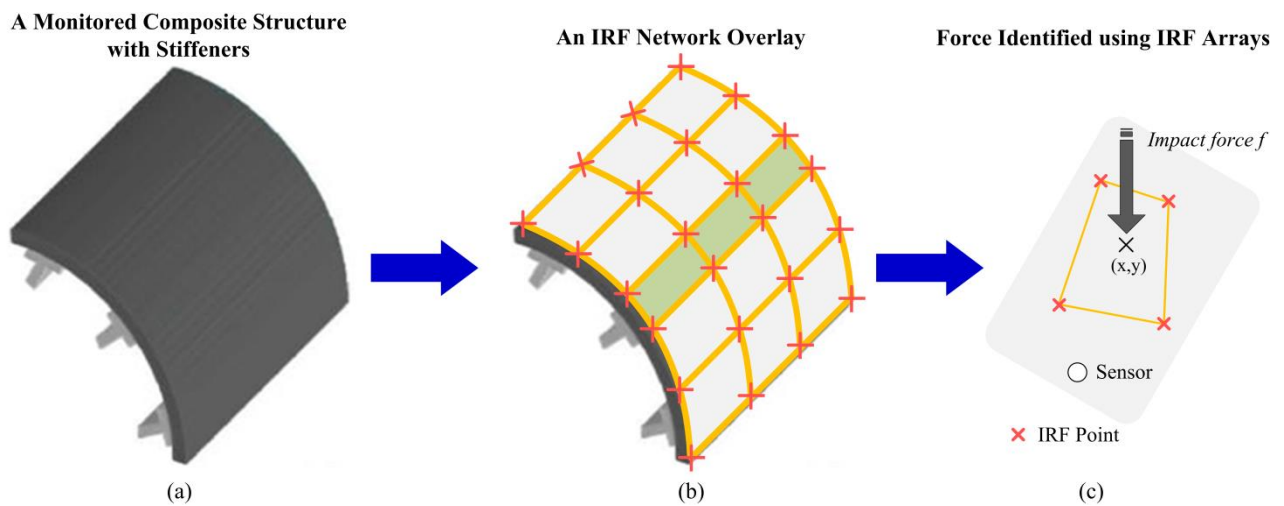


Figure 5.1 A complex composite structure with multi-stiffeners overlaid with a grid network of impulse response functions: (a) the monitored stiffened composite structure, (b) an adaptive-laid computation network of impulse response functions overlaying the whole structure, (c) the identification of an unknown impact through the recognized impulse response function grid.

For any given complex composite structure with multiple stiffeners as shown in Fig. 5.1, the dynamics of the entire structure due to impacts can be calculated and learned using an adaptive-laid computation network of multiple impulse response functions grids in two-dimension. At each grid node, an impulse response function is established with regard to a specified sensor through small amounts of training. Consequently, as the full-scale dynamic responses of a composite structure need to be acquired, a dependable network of the grids connected with a finite number of impulse response functions should be considered to construct. Once this computation network of IRFs is constructed for the dynamic calculation of a structure, the forward model of the structure can be derived from the state-space

representations using the developed system modeling approach. And the stable forward model is a good basis for the inverse model to rapidly compute and identify any impact at any location on the structure.

Once a stable computation network of IRFs is constructed, an unknown impact at any position on the composite structure can be reconstructed through a bilinear interpolation method. In other words, with the use of the bilinear interpolation method, the impact force can be reconstructed by using the determined grid of four neighboring impulse response functions, which includes the estimated impact location. The computational principle of the impact force reconstruction is demonstrated in Fig. 5.1c.

To achieve successfully the goal that is to establish the accurate and reliable forward model, three main functions should be performed so as to obtain a general solution that can solve the inverse problem of impact forces reconstructions using the simplified model (formulations).

5.1.1.1 Function 1: Determination of the Forward Prediction Model Structure

First, the structure of forward prediction model should be determined. The forward prediction model is constructed in terms of a linear finite difference representation. As the linear difference model is able to provide the meaningful model parameters so as to found the valid and stable forward model of structural responses due to external impacts, the derivation of the inverse model would become much simpler (faster) and more stable (robust) than that of the conventional analytical model or FEM based approach. Meanwhile, the direct benefits taken are to simplify and accelerate the computation procedure of impact identifications, and are entitled to qualify various structure configurations such as cutout and stiffened composite structures.

5.1.1.2 Function 2: Construction of Forward Model based on the Fast Genetic

Algorithm Parameters Estimation

The forward model can be derived from the state-space representations by transferring into a controllable canonical form. However, the controllable canonical realization can be represented in the form of the model parameters (a_i, b_j) . Thereupon, for the model parameters, they can be obtained through the fast genetic algorithm parameters estimation (FGAPE) procedure. The core idea of the parameters estimation method is to minimize the prediction errors between the real outputs and the modeled outputs on the basis of a specific model order [2]. Accordingly, it is the task of the FGA parameters estimation procedure to produce the optimally-estimated values of the model parameters a_i and b_j .

5.1.1.3 Function 3: Selection of the Optimized Model Order

As a part of modeling the structure system, one always validates the modeled forward system model through comparing it with the real responses from the structure system. Actually, it is impossible to build a system model that describes the true structure system comprehensively, that is, the modeled system model cannot describe completely every feature existed in the true structure system. This is why the optimized model order selection is a critical part of the entire impact identification procedure. Therefore, the optimized model order selection addresses the crucial problem of searching out whether the modeled system model is satisfied to its intended purpose through the prediction error minimization (PEM) method.

5.1.2 Determination of Model Structure

Considering the dynamic response model of a structure can be applicable to any complex structure, the structure system of multi-degree of freedom (MOF) is thus represented by the discrete-time state-space expressions.

$$\dot{x}(k) = Ax(k) + Bu(k) \quad (5.1a)$$

$$s(k) = Cx(k) + Du(k) \quad (5.1b)$$

where A is called a structural state matrix, B is called an input matrix, C is called an output matrix, D is called a feedforward matrix. For the state-space equations (5.1), it can be made in terms of Laplace transformation and yields

$$pX(p) = AX(p) + BU(p) \quad (5.2a)$$

$$S(p) = CX(p) + DU(p) \quad (5.2b)$$

Next, the state equation (5.2a) can be simplified as follows,

$$(pI - A)X(p) = BU(p) \quad (5.3)$$

Now, substituting for the state vector $X(p)$ in the output equation (5.2b), thus Eq. (5.4) can be obtained as

$$S(p) = C((pI - A)^{-1} BU(p)) + DU(p) \quad (5.4)$$

Here, as the impulse response function $G(p)$ of a structure can be derived out in terms of the ratio of the output to the input of the structure, thus having the following equation

$$G(p) = \frac{S(p)}{U(p)} \quad (5.5)$$

and substituting for $S(p)$ in the impulse response equation (5.5) with respect to $U(p)$, the following expression can be obtained,

$$G(p) = C(pI - A)^{-1} B + D \quad (5.6)$$

where $G(p)$ is a q by p dimensional matrix, because of the structure system with p inputs and q outputs. As the dynamic response model of a structure is a multiple-input and multiple-output model, every component element from the impulse response function matrix is a set of the specific functions between an input and multiple outputs, that is, there are q impulse response functions with regard to multi-outputs at one position, due to every input.

Therefore, now it is much important to find out the input-output relation between the force signals $u(k)$ and the sensor signals $s(k)$. In other words, the objective of forward system modeling is to describe $s(k)$ as a function of previous outputs and inputs, and together with noises $e(k)$. The relative details will be discussed in the following subsections.

5.1.2.1 Model Structures

As the structural deformation due to an external impact turns into nonlinear owing to external environment disturbances such as random mechanical vibrations, the dynamic response model of the structure can still be determined to depend linearly upon the input force since the process of the previous signal data preprocessing module is able to eliminate effectively redundant disturbances from original structural response data. Accordingly, the structural response signal s from a particular sensing position can be obtained through the linear expression between the impulse response function and an impact event f acting at the location (x, y) of a structure, as shown in Figure 5.2.

The most basic use of a prediction model is to simulate the dynamic response of a structure to various input scenarios. To achieve our goal, the relationship between the input signals $u(t)$ and the output signals $s(t)$ in most model sets is interested in. In other words, our goal is to describe $s(t)$ as a function of previous outputs and inputs, and together with disturbances that can be represented as a realization of a uncorrelated white-noise stochastic process with variance λ . Therefore, a set of models are postulated, within which the best description of the true structure system will be searched for.

$$s(t) = G(q, \theta)u(t) + H(q, \theta)e(t) \quad (5.7)$$

where $e(t)$ is an sequence of uncorrelated random white noises with the probability density function (PDF) $f_e(x, \theta)$.

$$G(q, \theta) = \sum_{k=1}^{\infty} g(k) q^{-k} \quad (5.8a)$$

$$H(q, \theta) = 1 + \sum_{k=1}^{\infty} h(k) q^{-k} \quad (5.8b)$$

where the symbol θ is a vector of model parameters containing all the coefficients of the transfer operators $G(q, \theta)$ and $H(q, \theta)$. And the parameter vector θ ranges over a subset of R^d , where d is the dimension of θ , then

$$\theta \in V_m \subset R^d \quad (5.9)$$

where V_m is set of values over which θ ranges in a model structure. For a model structure, it is a differentiable mapping from a connected, open subset V_m of R^d to a model set M^* , such that the gradients of the predictor function is stable.

From Eq. (5.7), $G(q, \theta)u(t)$ is referred to the dynamic response model of the structure, whereas $H(q, \theta)e(t)$ is referred to the disturbance model of the structure system. While, $G(q, \theta)$ is an impulse response (IR) function to its model structure from the input force $u(t)$ to the output $s(t)$, and corresponding to its parameter vector θ . And $H(q, \theta)$ is a transfer function to its model structure from the disturbance $e(t)$ to the output $s(t)$, and corresponding to its parameter vector θ .

Notice that from Eq. (5.7) to Eq. (5.9), it is a set of models, no longer is a model, and it is used for the estimation procedure to select the members in the set, which appear to be most suitable for the true structure system. There are several different model structures tied in with the above Eq. (5.7) postulated. However, a general representation of model structures can be applied,

$$A(q)s(t) = \frac{B(q)}{F(q)}u(t) + \frac{C(q)}{D(q)}e(t) \quad (5.10)$$

From Eq. (5.7), the IR function $G(q)$ for the structural dynamics and the transfer function $H(q)$ for the disturbances are both expressed in the polynomials of q^{-k} . As for doing so, the reason is to be consistent with the conventional definition of the z -transform which is described in Subsection 5.1.3. According to equation (5.10), it can help to found effectively and easily the impulse response function $G(z)$ of a structure system. Finally, the different model structures to various purposes can be formed, depending on which of the polynomials are used in Eq. (5.10).

5.1.3 Predictor Formation

Based on the description of a system model Eq. (5.7) subject to additional random disturbances $e(t)$, and assume that $y(k)$ and $x(k)$ are both known for $k \leq t-1$, the conditional expectation of $s(t)$ is presented finally by Eq. (5.11) through a series of relevant derivation procedure.

$$\hat{s}(t|t-1) = [1 - H^{-1}(q)]s(t) + H^{-1}(q)G(q)u(t) \quad (5.11)$$

It is a more general and convenient expression for the prediction. To establish the appropriate predictor for a structure system, Eq. (5.11) is necessary to be denoted by in terms of $\hat{s}(t|\theta)$ so as to reveal its dependence on the system parameter vector θ . Thence, the predictor has the following form,

$$\hat{s}(t|\theta) = [1 - H^{-1}(q, \theta)]s(t) + H^{-1}(q, \theta)G(q, \theta)u(t) \quad (5.12)$$

Eq. (5.12) is a general expression for a predictor of the future output from a structure system. From Eq. (5.12), this predictor does not depend on the random disturbances $e(t)$. Furthermore, in order to give a complete characterization of the probabilistic properties of the system, the system models need to be replaced by the form of *predictor models* that will signify the system model Eq. (5.7) based on probabilistic models.

In such case, a set of models [78] needs to be postulated, within which the best description of the true structure system will be searched for. Then, the forward system model for a structure can be expressed as a nonlinear difference equation with constant coefficients, and has the general form.

$$s(k) = [1 - A(q)]s(k) + B(q)u(k) + e(k) \quad (5.13)$$

where $e(k)$ is a sequence of the disturbance of white-noise stochastic process, or called uncorrelated random noises. Because that $e(k)$ has been denoised through the procedure of signal data preprocessing as described in Chapter 4, thus for the impulse response representation related between input and output, it can be modeled linearly through the following recurrence relation (5.14) that is called a predictor of the output $s(k)$ from the structural response, that is, known as the forward system model.

$$\hat{s}(k|\theta) = \sum_{i=1}^n a_i s(k-i) + \sum_{j=1}^m b_j u(k-j) \quad (5.14)$$

where $s(k)$ is a sequence of response outputs, and $u(k)$ is a sequence of external inputs. Since the inputs and response outputs are employed in the discrete-time domain, the values of

the time t for the input or the output signals sampled are thus used as $t = kT$; here k is a sequence number, and T is the sampling period, which is the reciprocal of the sampling frequency. And in Eq. (5.14), a_i and b_j represent the autocorrelation variables, also be called the instrumental variables.

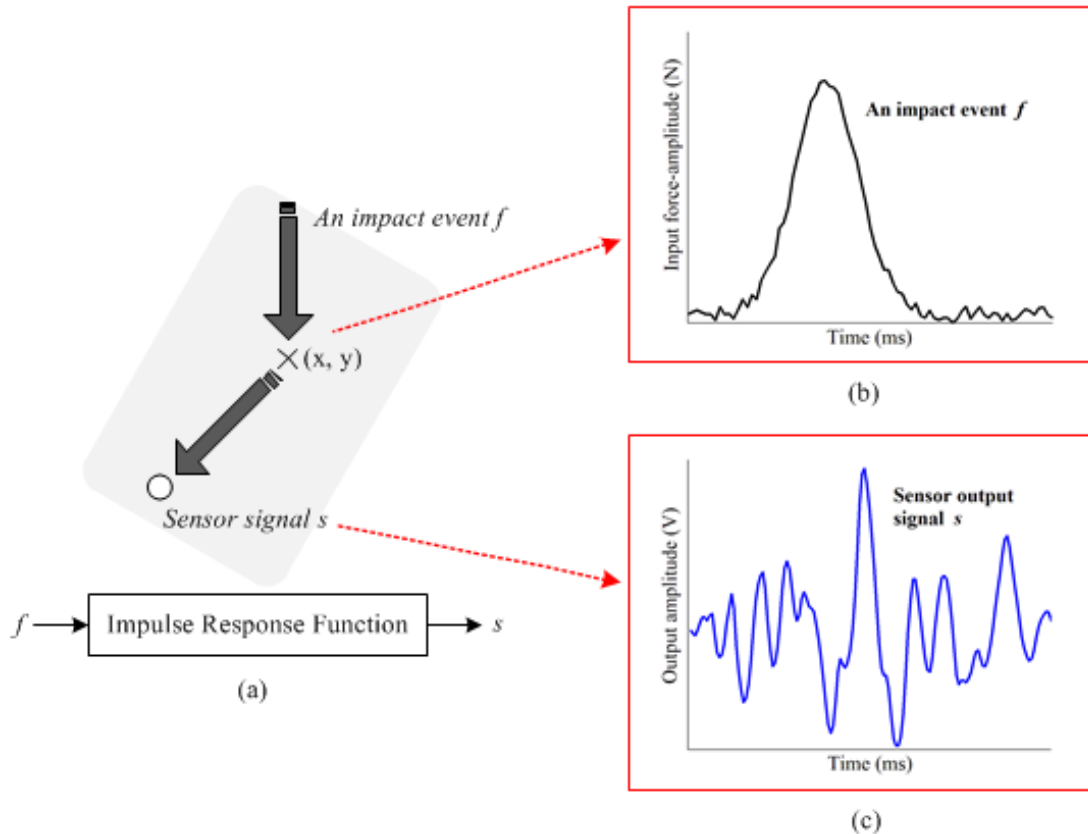


Figure 5.2 The linear relationship between an impact force and a structural response from a sensor: (a) the linear input-output relation based on the impulse response function, (b) a force signal resulting from an impact acting on the structure, (c) the corresponding structural response output from a specified sensor.

Overall, the purpose of constructing the forward prediction model is to determine the future output values using the previous observations known.

5.1.3.1 Discrete Laplace Transform of Impulse Response Function

As known, Z-transform is the simplified Laplace transform of an ideally sampled (discrete) signal with the substitution of

$$z \stackrel{\text{def}}{=} e^{sT} \quad (5.15)$$

where $T = 1/f_s$, f_s is the sampling rate, of which the unit is Hertz.

The impulse response function of a structure can be defined as the ratio of the Z-transform of the structure response $s(k)$ to the Z-transform of the excitation $u(k)$. Therefore, the impulse response function $g(k)$ can be defined as the Z-transform of a discrete time function

$$G(z) = \sum_{k=1}^{\infty} g(k) z^{-k} \quad (5.16)$$

Then, the key property of the linear difference equation (5.14) can be to help easily establish the Z-transform form of the IRF, $G(z)$, of a structure. Using the Eq. (5.14), the Z-transform of impulse response function $G(z)$ can be easily obtained, as follows,

$$G(z) = \frac{S(z)}{U(z)} = \frac{b_1 z^{-1} + b_2 z^{-2} + \dots + b_m z^{-m}}{1 + a_1 z^{-1} + a_2 z^{-2} + \dots + a_n z^{-n}} \quad (5.17)$$

where $S(z)$ is the Z-transform of $s(k)$ and $U(z)$ is the Z-transform of $u(k)$.

However, Eq. (5.17) can be rewritten as the form

$$G(z) = \frac{S(z)}{U(z)} = \frac{b_1 \prod_{j=1}^m (z - z_j)}{\prod_{i=1}^n (z - p_i)} \quad (5.18)$$

where z_1, z_2, \dots, z_m are referred to as the zeros of the Z-plane of a system model, and p_1, p_2, \dots, p_n are referred to as the poles of the Z-plane.

The zeros-poles diagram of an input-output prediction model is plotted in a complex plane, which is referred to the Z-plane. And this plane is a physical meaning representation of a Z-transformation. The Z-plane plot is very significant to analyze the robustness of a constructed input-output prediction model and to identify the dependable condition of the model, which will be discussed in the following subsection.

5.1.3.2 Robustness of Prediction Model Structure

In order to ensure the robustness and stability of an estimated system model, there are various ways to inspect the states of the system model, such as, a method of Zeros and Poles, a means of Frequency Response, a way of Model Residuals. In this thesis, the method of Zeros and Poles is chosen to examine the system model robust and stable.

Once an estimated system model is obtained, its properties can be investigated so that its poles and zeros can be analyzed as the plane of zeros and poles is an effective way to describe the coefficients of the predictor as expressed in the linear difference equation (5.14), and to evaluate the dependability and robustness of its prediction.

However, for the impulse response function $G(z)$ Eq. (5.18), its poles have a direct effect in the dynamic properties of the prediction model. It can be indicated that its model structure or inverse model or both is non-robust and unstable if any pole point is outside of the unit circle in the pole-zero plot of an input-output prediction model. An example of a plot of poles and zeros is demonstrated in Figure 5.3, where all poles are inside the unit circle of the pole-zero plane. Thus, it indicates the prediction model is robust and stable.

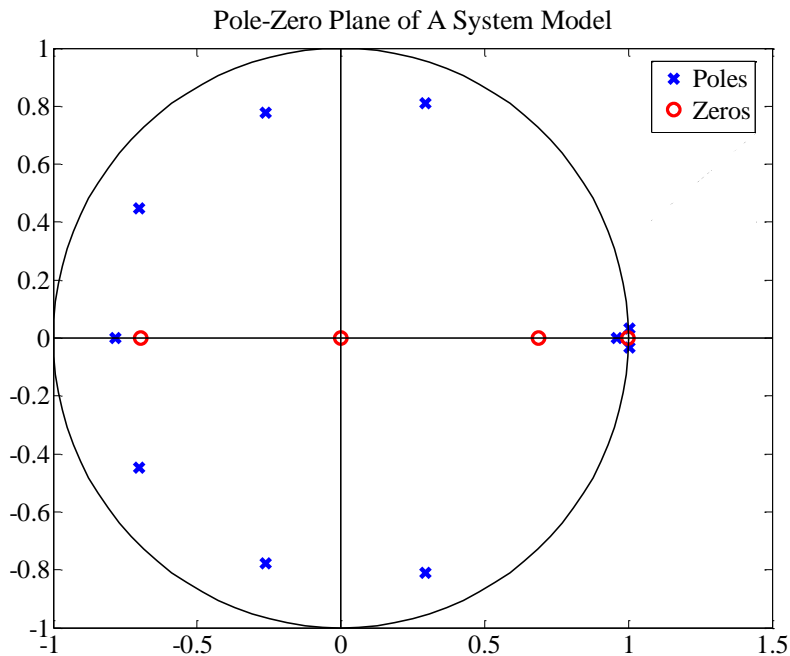


Figure 5.3 Demonstration for a pole-zero plot of a system model order ($n = 10, m = 4$)

In short, the pole-zero plane of a constructed prediction model gives a sense of the properties of the model, as it displays the model properties in terms of the physical meaning quantities.

Pole-Zero Inversion Matching for Inverse Model

The robustness of an inverse model is very critical, as it enables us to reconstruct reliably the impulse force using sensor output signals. Nevertheless, to construct a robust structural response model (5.19) and its corresponding inverse model, it is crucial to obtain a stable impulse response function $G(k)$.

$$S(k) = G(k)U(k) \quad (5.19)$$

Using Eq. (5.18), the inverse function of an impulse response $\hat{G}(z)$ is expressed by

$$\hat{G}(z) = \frac{1}{G(z)} = \frac{\prod_{i=1}^n (z - p_i)}{b_1 \prod_{j=1}^m (z - z_j)} \quad (5.20)$$

In Eq. (5.20), the zeros of the inverse function of the IR are the poles of the forward IRF, and the poles of the inverse function of the IR are the zeros of the forward IRF. From the robustness criteria described previously, the zeros of the forward IRF should be in the unit circle for the inverse system to be robust and stable. Then, in order that a structure system is robust and its inverse system is also robust, all of zeros and poles must be thence inside the unit circle.

If every bounded input sequence produces a bounded output sequence, the input-output model is robust in the bounded input-output sense and also the inverse input-output model is robust when the bounded input-output condition is satisfied. Therefore, the structure response due to an impact is stable, because any input force is bounded signal and thus produces naturally a bounded output sensor signal. Whereas, when the forward impulse response function is overestimated or over-parameterized, the inverse impulse response function will become unstable. In that case, the forward IRF may be singular, and the corresponding inverse IRF will also become unstable. The details will be discussed in Section 5.1.4.

5.1.3.3 Controllable Canonical Realization

Since the impulse response function is a strictly proper function as its z-transform form presented in Eq. (5.17), the forward model can thus be constructed from the state space representations (5.1), and also the coefficients (a_i, b_j) are substituted into the state-space model as follows:

$$x(k+1) = \begin{bmatrix} a_1 & a_2 & \cdots & a_{n-1} & a_n \\ 1 & 0 & \cdots & 0 & 0 \\ 0 & 1 & 0 & \cdots & 0 \\ M & 0 & \ddots & M & M \\ 0 & 0 & \cdots & 1 & 0 \end{bmatrix} x(k) + \begin{bmatrix} 1 \\ 0 \\ 0 \\ M \\ 0 \end{bmatrix} u(k) \quad (5.21a)$$

$$s(k) = [b_1 \quad b_2 \quad \cdots \quad b_{m-1} \quad b_m] x(k) \quad (5.21b)$$

where the structural state matrix A , the input matrix B and the output matrix C are expressed in equation (5.22). For a strictly proper structure system, the dynamic response model does not have a direct feedthrough, and the feedforward matrix D is thus a zero matrix.

$$A = \begin{bmatrix} a_1 & a_2 & \cdots & a_{n-1} & a_n \\ 1 & 0 & \cdots & 0 & 0 \\ 0 & 1 & 0 & \cdots & 0 \\ M & 0 & \ddots & M & M \\ 0 & 0 & \cdots & 1 & 0 \end{bmatrix}; \quad B = \begin{bmatrix} 1 \\ 0 \\ 0 \\ M \\ 0 \end{bmatrix}; \quad C = \begin{bmatrix} b_1 \\ b_2 \\ M \\ b_{m-1} \\ b_m \end{bmatrix}^T \quad (5.22)$$

A dynamic response model derived from the controllable canonical realization (5.21) is controllable so as to move every state, as the control enters a chain of integrators. Meanwhile, the controllable canonical realization can be obtained through the calculation of system parameters a_i and b_j from the forward system model defined in Eq. (5.14). Thus, the state space realization is a canonical realization for the determined dynamic response model of a structure.

5.1.4 Construction of Forward Model Based on Fast Genetic Algorithm Parameters Estimation

As the topic of this section, a novel fast genetic algorithm parameters estimation (FGAPE) method developed will be introduced and discussed in detail, where will describe how to obtain the optimal system parameters a_i and b_j using the FGAPE method. The fast genetic algorithm parameters estimation method can found an optimal dynamic structure system model effectively using the observations from the modeled system structure. In this section, a discussion on different model sets based on a generalized model structure will be interpreted. For the constructed forward model used in this thesis, the model parameters estimation procedure (reduction of the prediction error using the fast genetic algorithm parameters estimation) will be presented in subsection 5.1.4.3.

Then, based on zero initial conditions, the forward model can be modeled using the impulse response representation (5.23) derived from the state-space model mentioned previously.

$$\hat{s}(k) = \sum_{i=0}^k g(i)u(k-i) \quad k = 1, 2, \dots \quad (5.23)$$

where $\hat{s}(k)$ is defined as the impulse response simulator of a structure due to external inputs u . $g(i)$ is referred to the impulse response function of the structure. On the basis of the resulting equation (5.6), the impulse response function $g(i)$ has the form as presented in Eq. (5.24).

$$g(0) = D \quad g(i) = CA^{i-1}B \quad i = 1, 2, \dots \quad (5.24)$$

From the forward model (5.23), the impulse response function $g(i)$ presents the dynamic responses of a structure. Thus, it describes the dynamic relation between the structural response and input pulse.

In that way, the structural impulse response $s(k)$ due to an impact can be denoted in a matrix convolution formulation as

$$S_{(x_i, y_i)} = G_f^s U_{(x, y)} \quad (5.25)$$

where

$$G_f^s = \begin{bmatrix} g(0) & 0 & 0 & \Lambda & 0 \\ g(1) & g(0) & 0 & \Lambda & 0 \\ M & M & O & 0 & M \\ g(n-2) & g(n-3) & O & O & 0 \\ g(n-1) & g(n-2) & \Lambda & g(1) & g(0) \end{bmatrix} \quad (5.26)$$

Here, G_f^s is the IRF polynomial matrix of a structure and it relates an input force f impacting at the location (x, y) and a response output $S_{(x_i, y_i)}$ at a specified position in the structure [77]. Then, the response output $S_{(x_i, y_i)}$ is simulated through the convolution process of the recorded input force $U_{(x, y)}$ and the impulse response matrix G_f^s , which is built using the optimal model parameters a_i and b_j calculated from the input-output prediction model as presented in Eq. (5.14). And the impulse response matrix G_f^s is constructed in terms of the model parameters.

In this research, the optimal model parameters a_i and b_j were obtained using the developed fast genetic algorithm parameters estimation method. This parameters estimation method will be described in the following subsections. What's more, two collection approaches of impact response data were proposed to provide the required training input-output data, in order to make the constructed forward model more dependable and robust, thereby the corresponding inverse model can be stable to reconstruct the time history of any unknown impact force. In this case, the ensemble impact monitoring and identification approach is able to guarantee the trustworthy and applicable impact localization and quantification once a composite structure encounters an unforeseen impact. They are presented as follows for the two data collection approaches.

1) The FEM simulation approach is to obtain several sets of the simulated structure response data due to impact at every layout point on a structure. And the FE model based simulation approach is illustrated in Figures 5.4 and 5.5.

2) Experimental impact tests to obtain several sets of the experimental structure response data due to impact at every layout point on a structure.

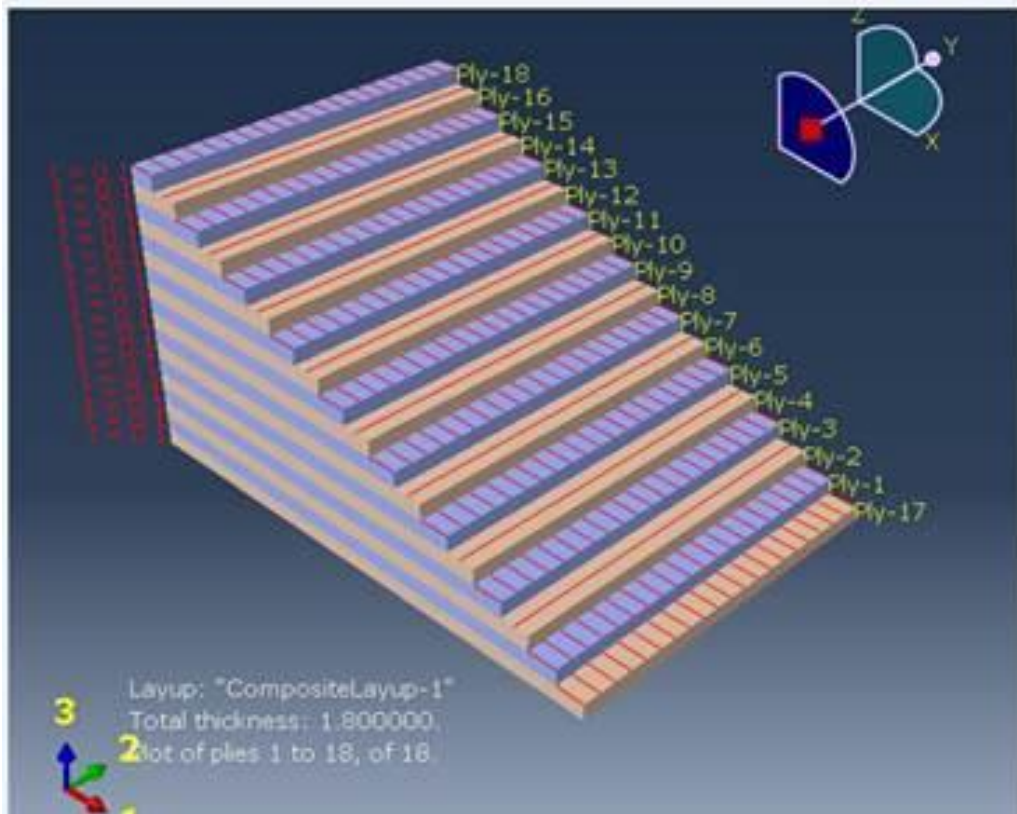


Figure 5.4 The layup structure of a monitored laminated composite panel

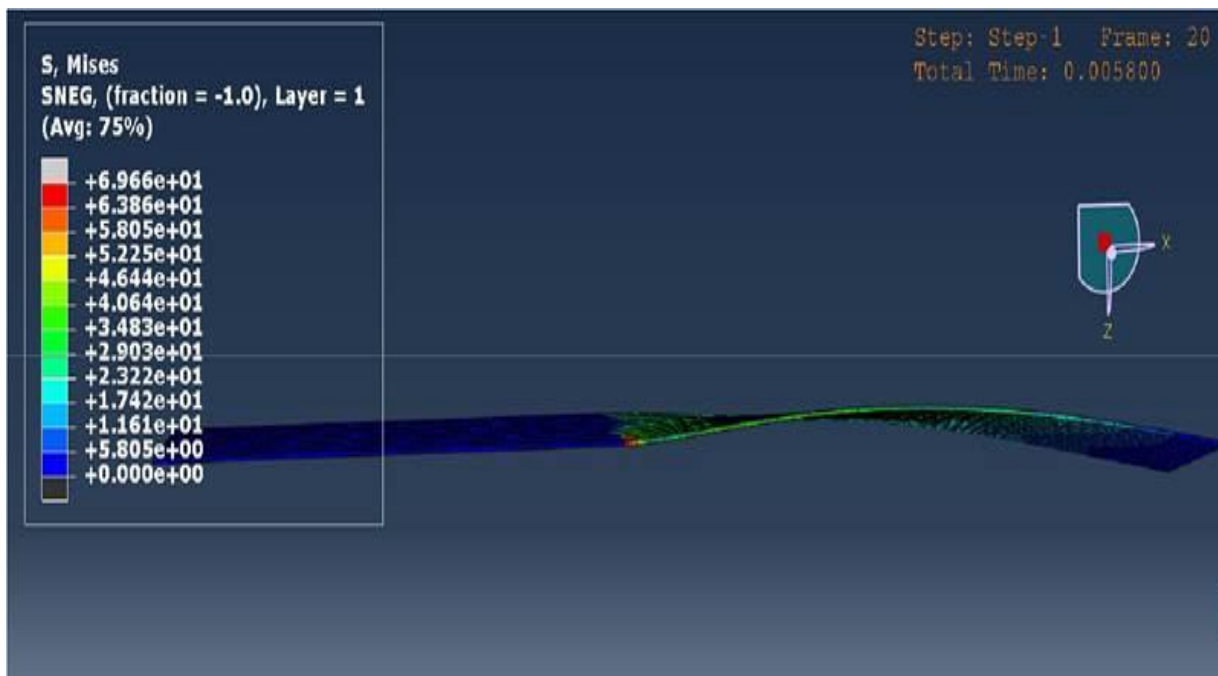


Figure 5.5 The modeled impulse response of the composite structure due to an impact

5.1.4.1 Background of the FGA Parameters Estimation

The determination of an appropriate system model set is most crucial to a successful identification and estimation procedure for system parameters a_i and b_j . Therefore, in this chapter the identification and estimation procedure of system parameters shall be implemented systematically. Figure 5.6 shows the overall system parameters estimation procedure based on the fast genetic algorithm estimation loop. In fact, the objective of the FGAPE identification function block is to gain an effective mathematical polynomial that reliably simulates the dynamic behavior of structural responses induced by input impulse, using the training input-output data collected both from 1) the simulated results of FE model built and 2) the in-situ measured results of experimental tests. The FGAPE method reveals completely the dynamic characteristics of a structure system from the perspective of the digital signal processing (DSP) algorithm, without the need of material and structural properties, and avoids numerous and tangled mathematic or physical models. Also, there are several different methodologies to solve the identification and estimation problem, which can be divided into two primary approaches: nonparametric and parametric estimation methods. The main purpose of the nonparametric estimation method is to focus on estimating the entire spectra or the step responses, etc.. Whereas, the main purpose of the parametric estimation method is to focus on estimating a system through a specified number of its component parameters. In this thesis, a new parametric estimation method – the fast genetic algorithm error estimation, was developed and employed to deal with the met model parameters estimation problem.

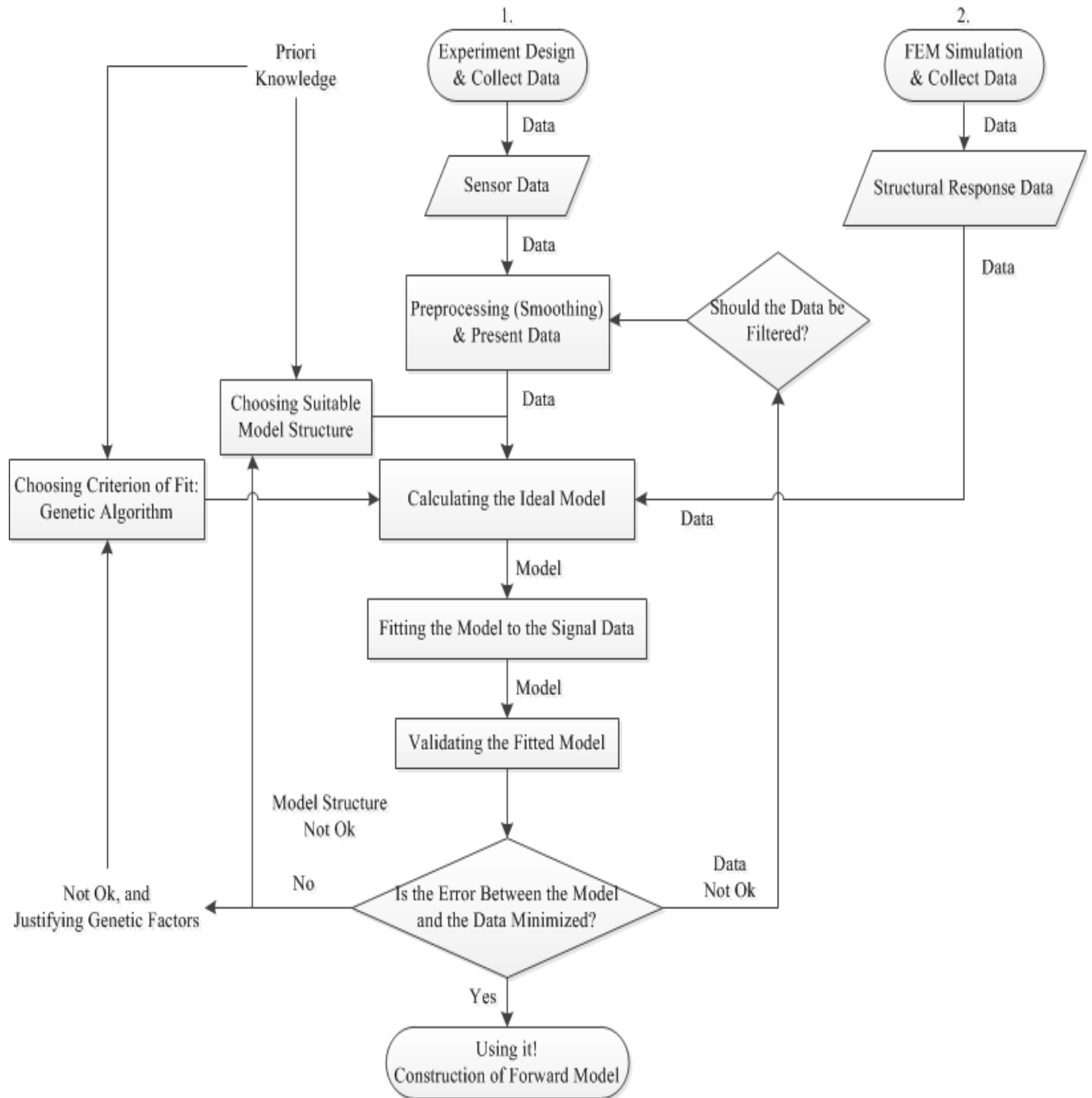


Figure 5.6 Model parameters estimation with the FGAPE loop.

5.1.4.2 Predictor Construction for Impact Condition

With regard to the met impact condition, there exists a common model structure to simplify the procedure of prediction and estimation for the structural response $s(t)$. And the chosen prediction model structure is expressed in Eq. (5.27), which is also illustrated in Figure 5.7.

$$s(t) = \frac{B(q)}{A(q)}u(t) + \frac{1}{A(q)}e(t) \quad (5.27)$$

where

$$G(q, \theta) = \frac{B(q)}{A(q)}, \quad H(q, \theta) = \frac{1}{A(q)} \quad (5.28)$$

Also, Eq. (5.27) can be expressed in a sequence formulation

$$s(t) = \sum_{i=1}^n a_i s(t-i) + \sum_{j=1}^m b_j u(t-j) + e(t) \quad (5.29)$$

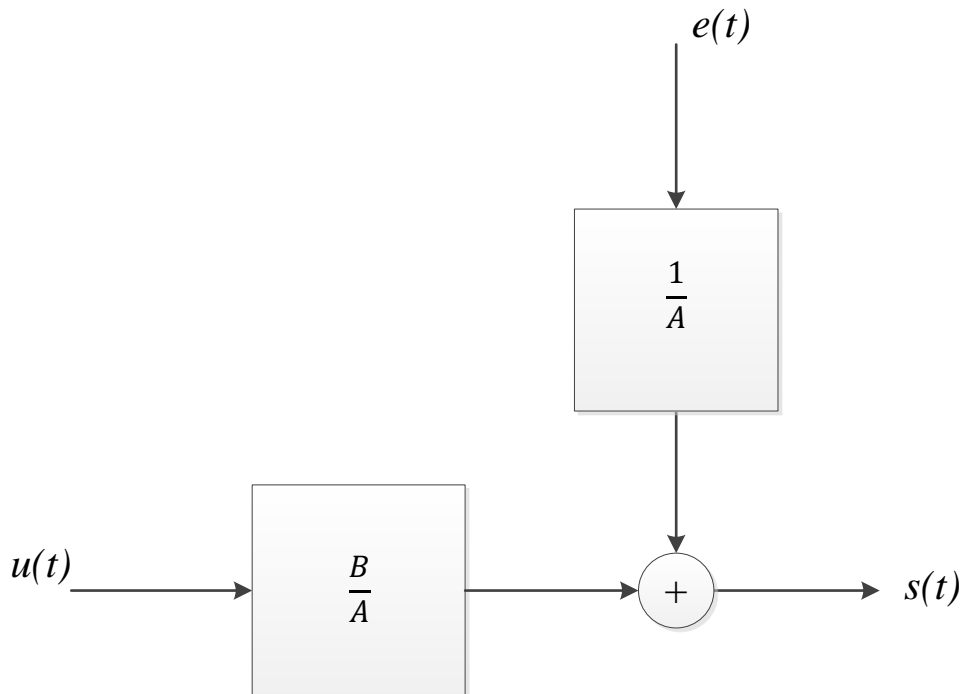


Figure 5.7 The chosen structure of the input-output prediction model [78]

From the signal flowchart Fig. 5.7, the prediction model Eq. (5.29) is referred to the output error model (OEM), as the denominator dynamics of the model was being affected by the disturbance $e(t)$ before it is added to the model output. Thus, the prediction model can be constructed as a linear regression machine once eliminating the disturbance.

Therefore, it is possible to predict the response output $s(t)$ from the prediction model Eq. (5.27), based on the input and output training data both from FEM simulations and experimental measurements. Then, the predictor $\hat{s}(t|\theta)$ for the prediction model Eq. (5.27) now needs to be derived, and is obtained by inserting Eq. (5.28) into Eq. (5.12), as

$$\hat{s}(t|\theta) = [1 + A(q)]s(t) + B(q)u(t) \quad (5.30)$$

Here, $\hat{s}(t|\theta)$ is the prediction output of the response $s(t)$ based on the model parameter vector θ . Clearly, because the disturbances $e(t)$ can be denoised to become “insignificant” through the procedure of signal data preprocessing as described in Chapter 4, the predictor Eq. (5.30) is a natural choice and is also a perfect natural to work for the “deterministic” system model.

However, the regression vector $\varphi(t)$ shall be substituted into the predictor Eq. (5.30). Now, the predictor Eq. (5.30) can be rewritten as

$$\hat{s}(t|\theta) = \theta^T \varphi(t) = \varphi^T(t) \theta \quad (5.31)$$

Further the predictor $\hat{s}(t|\theta)$ for the system model can become

$$\hat{s}(t|\theta) = \sum_{i=1}^n a_i s(t-i) + \sum_{j=1}^m b_j u(t-j) \quad (5.32)$$

It is clear that the prediction Eq. (5.32) for the prediction model is not only based on the input force $u(t)$, but also on the previous output signal data $s(t)$. This is the important property of the prediction model Eq. (5.29). And the predictor is a scalar product between the regression vector $\varphi(t)$ of a known prior data and the model parameter vector θ . Such a model is called as a linear regression in statistics. Its role is very significant, since some powerful and simple estimation methods can be utilized to evaluate and optimize the model parameters a_i and b_j from the parameter vector θ .

5.1.4.3 Prediction Error Estimation and Reduction

The model parameters a_i and b_j can be obtained through the prediction error estimation and reduction procedure. One of the core ideas of the fast genetic algorithm parameters estimation method used in this thesis is to minimize the prediction errors. In other words, it is the principal task of the FGAPE technique to calculate the optimal values of the model parameters a_i and b_j , further to forming the parameter vector θ .

In order to express intuitively and compute rapidly, we introduce the model parameter vector θ Eq. (5.33) and the regression vector $\varphi(t)$ Eq. (5.34) from the input-output data $[s(t), u(t)]$ as follows,

$$\theta = [a_1 \cdots a_n \ b_1 \cdots b_m]^T \quad (5.33)$$

$$\varphi(t) = [-s(t-1), \dots, -s(t-n) \ u(t-1), \dots, u(t-m)]^T \quad (5.34)$$

Fast Genetic Algorithm Error Estimation [77]

With these vectors, the prior input-output based prediction model for the response at time t can be realized from Eq. (5.35),

$$\hat{s}(t|\theta) = \varphi^T(t)\theta \quad (5.35)$$

So that the predicted output signals $\hat{s}(t|\theta)$ from the constructed forward model match well with the recorded and simulated output signals $s(t)$ both from the experimental measurements and FEM simulations respectively, the prediction error function (sequence) $I(\theta)$ needs to be defined as Eq. (5.36), and the prediction error sequence $I(\theta)$ still needs to be minimized to obtain the fittest values of the system parameter vector θ . Hence, the purpose needs to be implemented through an advanced genetic algorithm optimization method.

$$I(\theta) = I(s, \hat{s}) = s(t) - \hat{s}(t|\theta) \quad (5.36)$$

And the PE sequence $I(\theta)$ can be defined as a vector in R^N , of which the size can be measured using any norm in R^N , quadratic and non-quadratic. This leaves a substantial number of choices. Accordingly, this freedom shall be restricted somewhat by using the fast genetic algorithm training method of evaluating “how large” the prediction error sequence is.

$$\tilde{\theta}[a_n, b_m]_{opt} = H(a_n, b_m) \quad (5.37)$$

The entropy $H(a_n, b_m)$ in the above equation is given by

$$H(a_n) = -\sum_{i=1}^n P(a_n) \log P(a_n) \quad (5.38)$$

$$H(b_m) = -\sum_{i=1}^m P(b_m) \log P(b_m) \quad (5.39)$$

The prediction estimation procedure is implemented based on minimization of error (MOE) using the fast genetic algorithm estimation, and the evaluation loop procedure is flowcharted in Figure 5.8 in a nutshell.

In the execution of the genetic operations [79], four FGA parameters have the effects on the accuracy of the simulated output model, respectively. And the four FGA parameters are separately 1) population size, 2) mutation rate, 3) number of iterations and 4) error tolerance. In every estimation, the prediction model is compared with the real response output, and an average absolute error of the simulated in contrast to the real is calculated out so as to learn how perfect the built prediction model is. To achieve a goal of dependability and accuracy of impact force identification, the output model can be adjusted flexibly on demand by altering the FGA parameters appropriately in order to found the robust prediction model for force reconstructions.

Then, from a set of given input-output data, a response model is constructed. Consequently, the response model is compared with the responses from the FEM simulations and experimental measurements. Finally, a forward model with the optimal system parameters a_i and b_j could be determined from the optimization procedure using the fast genetic algorithm estimation method, which is demonstrated in the developed FGA Identification Interface (FGAII) as shown in Figure 5.9, that is, a Graphical User Interface (GUI) for manipulating genetic operations.

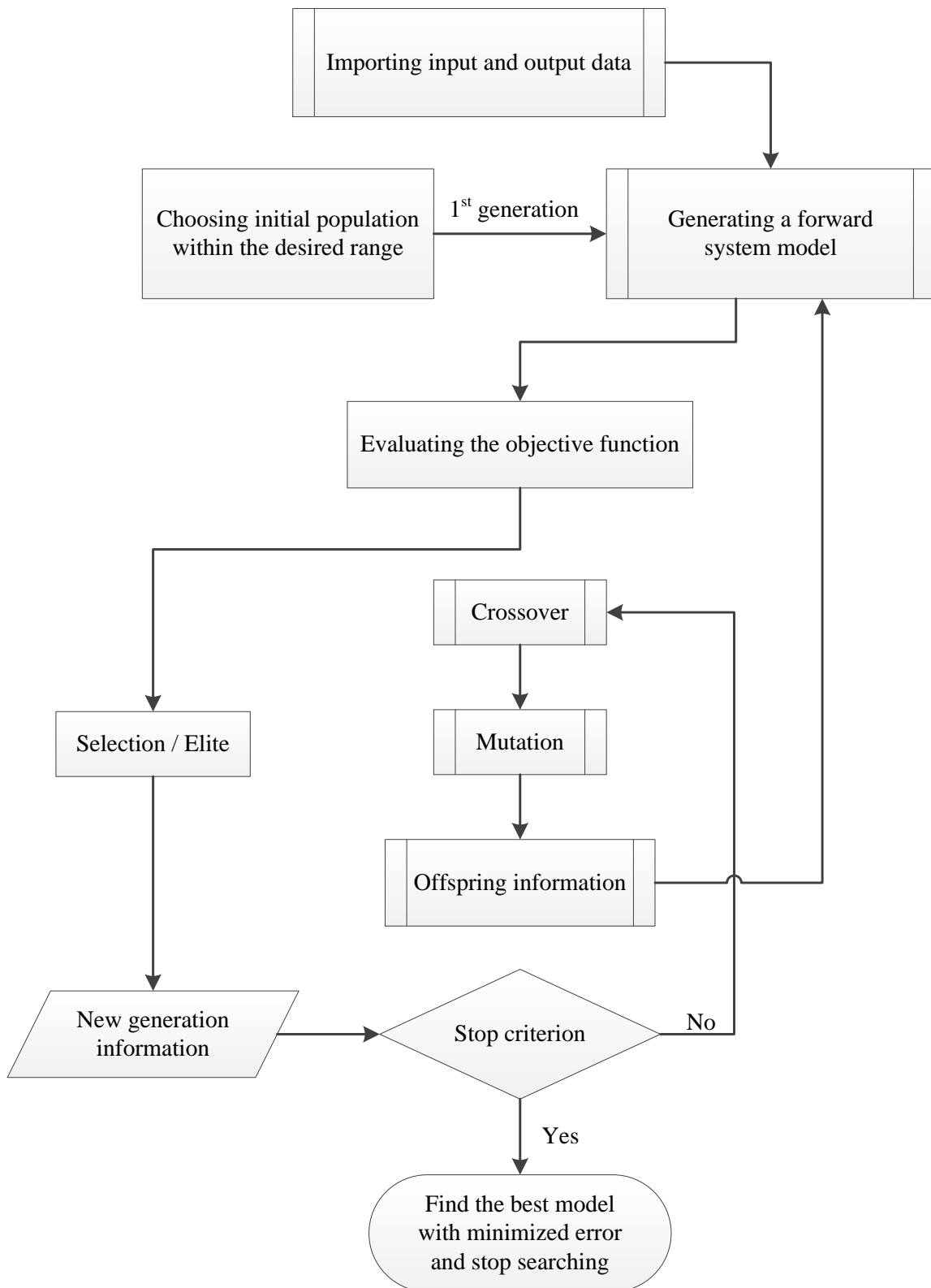


Figure 5.8 Flowchart of the prediction estimation based on minimization of error (MoE) through the fast genetic algorithm estimation method

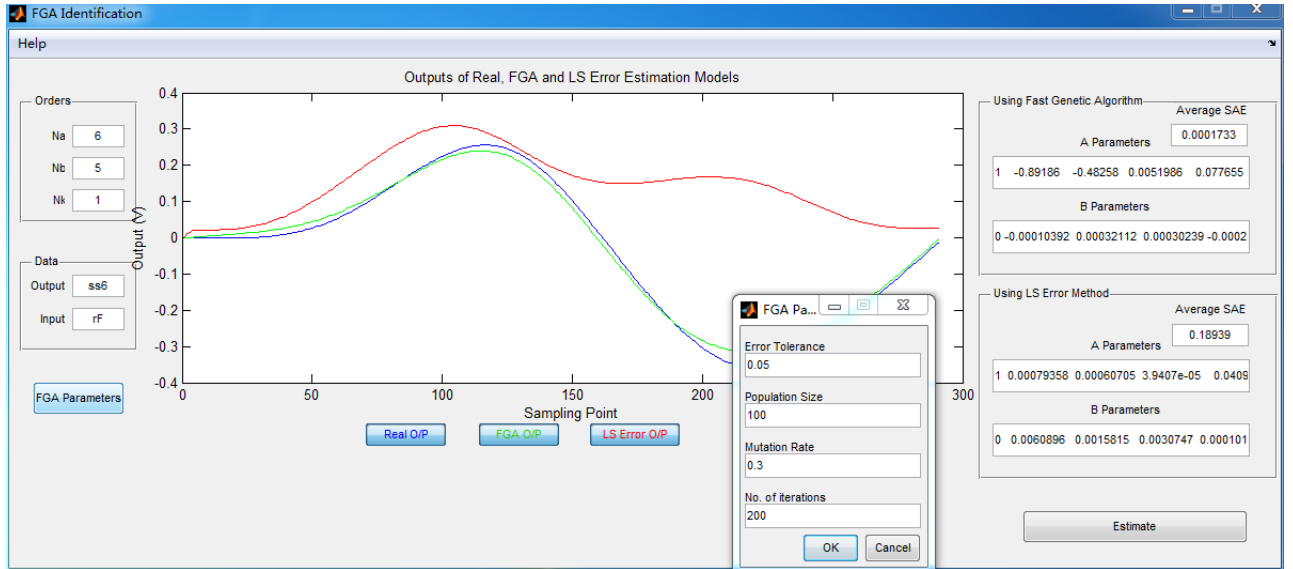


Figure 5.9 The results of system parameters (a_i, b_j) estimation and prediction error estimation in the developed FGA Identification Interface

Comparison with Least Squares Error Estimate (LSEE)

The predictor for a system can be employed as a linear regression model expressed in Eq. (5.35).

$$\hat{s}(t|\theta) = \varphi^T(t)\theta \quad (5.35)$$

Next, a classical parameter estimation method — the least squares error estimate (LSEE) will be interpreted as follows,

Least Squares Error Criterion

With Eq. (5.35), the prediction error (PE) sequence becomes

$$\varepsilon = s(t) - \hat{s}(t|\theta) \quad (5.40)$$

The PE sequence ε needs to be filtered by a stable linear filter, the filtered PE is then normalized. Now the criterion function Eq. (5.41) needs to be derived with the filter $L(q) = 1$ and a scalar function $\rho(\varepsilon) = \varepsilon_f^2$,

$$V_N(\theta|\Phi_i^N) = \frac{1}{N} \sum_{t=1}^N [s(t) - \varphi^T(t)\theta]^2 \quad (5.41)$$

This is the LS criterion for the linear regression predictor Eq. (5.35).

Nevertheless, for a given structure system, typically the exact priori information are not supplied with the relationship between the response outputs $s(t)$ and the regression vector $\varphi(t)$. Thus, what substituted for are “historic data”, a collection of previous observations of the related values of input data $u(t)$ and output data $s(t)$. In order to minimize the prediction error argument from Eq. (5.41), it is necessary to select a suitable θ by the least squares method so that the simulated response outputs $\hat{s}(t|\theta)$ from the determined prediction model fit the real response outputs $s(t)$ both from the FEM simulations and experimental measurements.

$$\hat{\theta}_N = \arg \min_{\theta} V_N(\theta | \Phi_t^N) \quad (5.42)$$

The estimated parameter vector $\hat{\theta}_N$ is simply the value that gives the best performing predictor function (5.43), when applied to the historic data.

$$\hat{s}(\theta) = \varphi^T \hat{\theta}_N \quad (5.43)$$

Because of the unique feature of the least squares criterion, the prediction function is founded using the quadratic criterion and the linear parameterization. $V_N(\theta | \Phi_t^N)$ is thus a quadratic function with respect to the model parameter (autocorrelation) vector θ , and it can be minimized analytically.

Therefore, all of $\hat{\theta}_N$ can be constructed easily by setting the derivative to zero,

$$\frac{dV_N(\theta | \Phi_t^N)}{d\theta} = \frac{2}{N} \sum_{t=1}^N \varphi(t) [s(t) - \varphi^T(t) \hat{\theta}_N] = 0 \quad (5.44)$$

which satisfy

$$\frac{1}{N} \sum_{t=1}^N \varphi(t) s(t) = \frac{1}{N} \sum_{t=1}^N \varphi(t) \varphi^T(t) \hat{\theta}_N \quad (5.45)$$

yield the global minimum of $V_N(\theta | \Phi_t^N)$. If the matrix on the left from Eq. (5.45) is reversible, then the least squares estimate for the adjustable parameters vector θ is constructed as Eq. (5.46).

$$\hat{\theta}_N = \left[\sum_{t=1}^N \varphi(t) \varphi^T(t) \right]^{-1} \sum_{t=1}^N \varphi(t) s(t) \quad (5.46)$$

Finally, using the sensor data collected from experimental tests, the response output models with different accuracies were simulated respectively through the proposed fast genetic algorithm error estimation and least squares error estimate procedures. Meanwhile, these simulated output models were compared with the actual response output, and a best suitable model could be constructed as the prediction model sequence $\hat{s}(t|\theta)$ matched well with the real response sequence $s(t)$ recorded, of which the demonstration is presented in Figure 5.10.

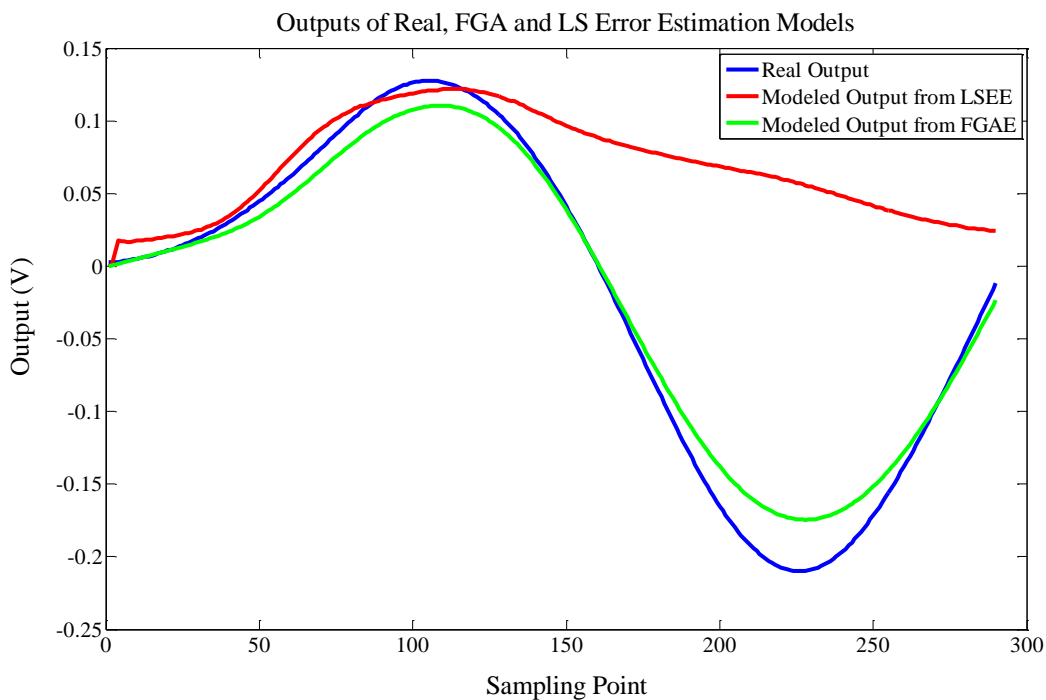


Figure 5.10 Comparison for the prediction estimation of a structural response using the fast genetic algorithm error estimation and least squares error estimate methods

5.1.4.4 Model Verification for Its Robustness and Stability

As the model parameters estimation procedure picks out the “best” prediction model within the selected model structure, the robustness and stability of the prediction model are necessary to be examined by checking the pole-zero plane of the prediction model, which has been interpreted in Subsection 5.1.3.2. On the basis of the conclusion, the prediction model and its inversion should be robust and stable in order that this “best” system model is “good enough”. In other words, all poles and zeros of the model should be inside the unit circle of its Z-plane.

Consequently, the following pole-zero plot of an examined prediction model is illustrated in Figure 5.11. From Fig. 5.11, all poles and zeros of the prediction model are seen to be inside of its unit circle. Accordingly, the prediction model can be considered to be robust and stable, and so is its inversion.

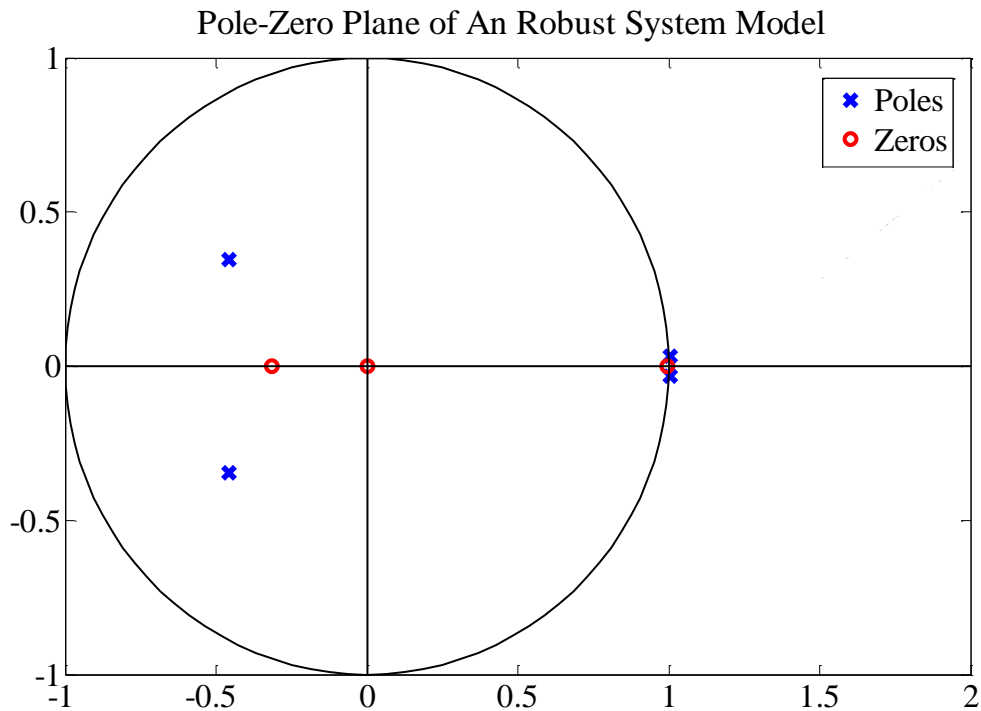


Figure 5.11 Pole-zero plot of an examined system model with the model order of ($n = 4, m = 3$)

Under the stable and robust prediction model and its inversion, an impact force acting on a structure can be reconstructed through the convolution of the inverse IRF matrix \hat{G}_s^f of the inverse model and a specific sensor signal $S_{(x_i, y_i)}$ recorded. Figure 5.12 illustrates an example of force reconstruction under the robust prediction model and its inversion. The relational contents of force reconstruction will be discussed comprehensively in Section 5.2.

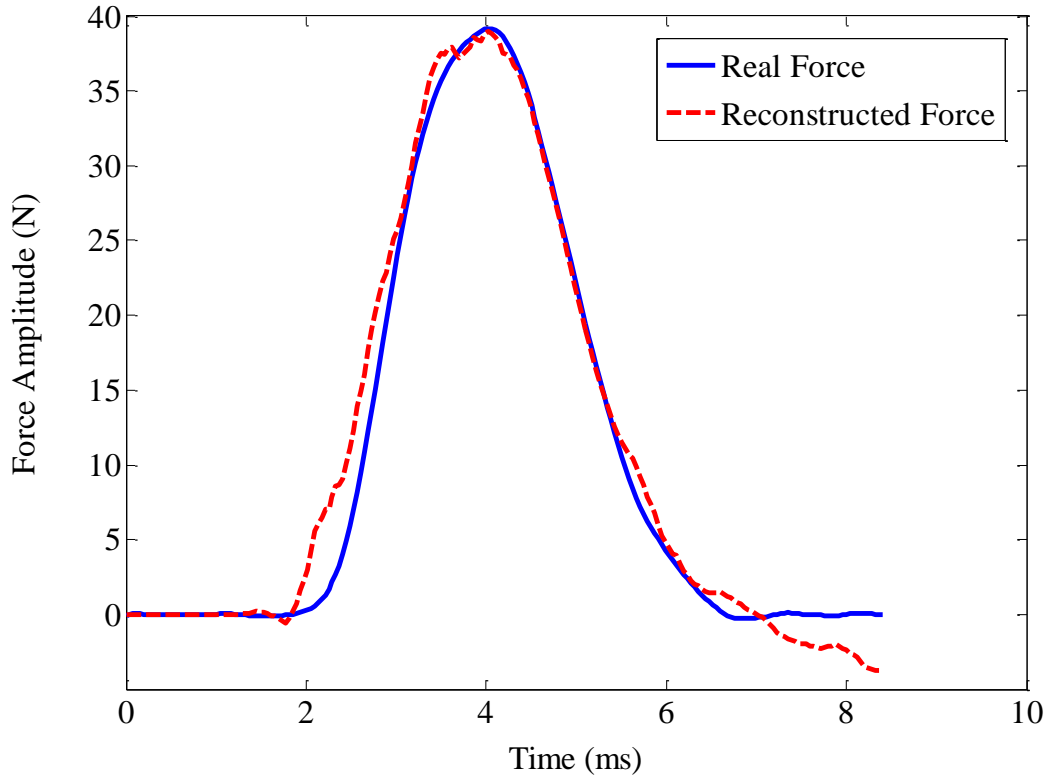


Figure 5.12 An example of force reconstruction under a robust prediction model and its inversion

Nevertheless, if there exists any zero of a prediction model outside of its unit circle, it means that its inverse model thus become non-robust and unstable. A demonstration of the pole-zero plot is shown in Figure 5.13 to illustrate the nonrobust prediction model with the unstable zeros. Thereupon, the force reconstruction will be performed under a relative significant bias condition.

Using the same input-output data, the impulse response function matrix G_f^S is obtained with the different model order $n = 10$. From Fig. 5.13, the inverse model is nonrobust and unstable, because there are four unstable *Zero* points in the pole-zero plane of the prediction model. Therefore, the force reconstruction using the nonrobust inverse model is not stable and is with a bigger distortion, of which the result is as shown in Figure 5.14. A possible reason to produce the large error of force reconstruction is that the singularity of the impulse response function G_f^S .

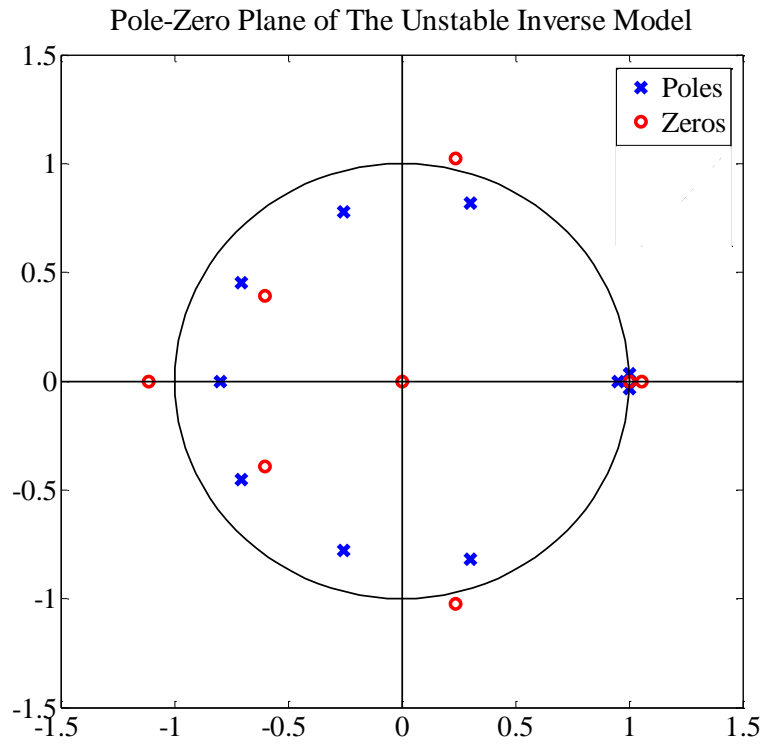


Figure 5.13 A nonrobust demonstration of the inverse model with unstable zeros ($n = 10, m = 8$)

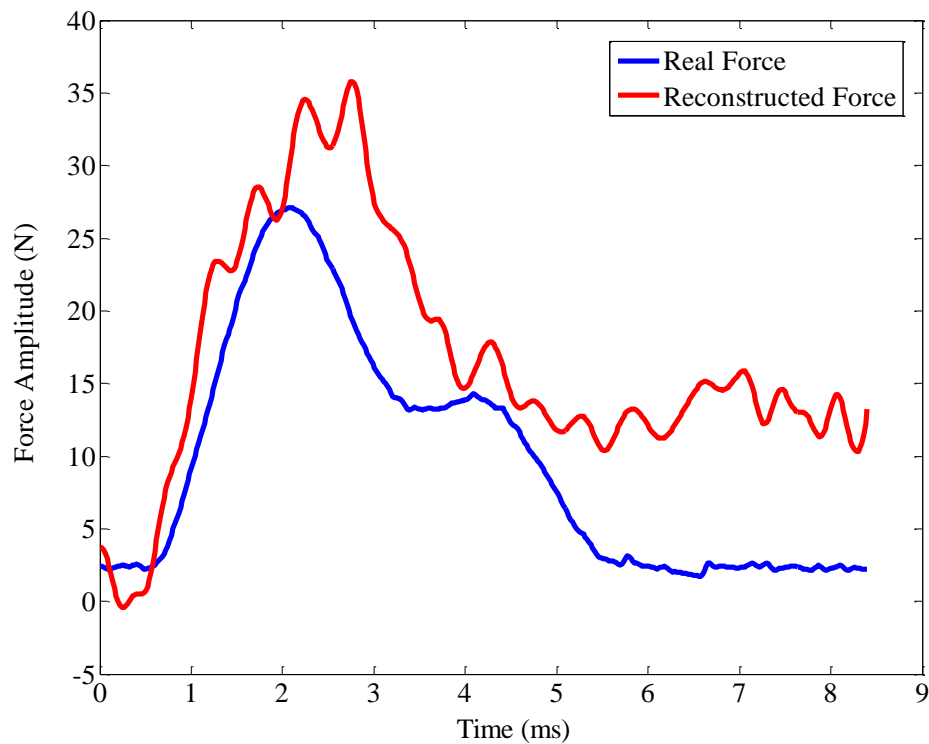


Figure 5.14 An example of force reconstruction under the nonrobust inverse model

5.1.5 Model Order Optimization

To search for the “best” forward prediction model, the model order is necessary to be optimized and determined whether the “best” prediction model is “good enough”. Hence, as a critical part of the construction of a correct and dependable prediction model, one always validates and determines the chosen prediction model through comparing it with the real structure response, of which the reason is that it is impossible to seek a perfect model that completely describes the true responses of a structure. As a result, the model validation addresses an important issue of finding out whether the simulated prediction model is suitable for its intended purpose.

However, the construction of the regression vector $\varphi(t)$ is a crucial basis for the parametric identification of prediction models, which is known as

$$\varphi(t) = [-s(t-1), \dots, -s(t-n) \quad u(t-1), \dots, u(t-m)]^T \quad (5.34)$$

thereby the degree n of the denominator from the Z-transform of impulse response function as Eq. (5.17) needs to be determined. Actually, an incorrect choice for the degree n will generate relatively big errors and lead to more difficult. Thereupon, two conditions are caused mainly as follows:

On the one hand, selecting a value for the degree n too large is referred to over-parameterization, and it leads directly to the relative impulse response function matrix being close to singular, which is not sufficient to determine the values of the model parameters a_i and b_j .

On the other hand, selecting a value for the degree n too small will lead to mismatch between the simulated prediction model and the actual output from the structure, and then the related errors or residuals will be large.

Next, sets of input-output data were used to build an adaptive system model that is capable of reproducing the response of the real structure system for any kind of input produced by impact events. One approach to validation is to make any new input sequence and utilize it into both the real structure system S_r and the system model S_m built. The outputs from both the S_r and S_m are compared, of which the result gives an indication of how good the system model S_m is.

To optimize the parameterized prediction models based on input-output data, a sifting criterion should be formulated and conducted. Thus, it is selected as the basis of the sifting criterion to minimize the prediction error from the different outputs between the simulated

system model and the real structure system. Accordingly, it is necessary to compute the prediction error for evaluating the system models as Eq. (5.14) at time t using Eq. (5.47).

$$\varepsilon(t) = \hat{s}(t|\theta) - s(t) = \varphi(t)^T \theta - s(t) \quad (5.47)$$

where θ is referred to the model parameters vector, also called instrumental variables vector.

$$\theta = [a_1 \cdots a_n \ b_1 \cdots b_m]^T \quad (5.33)$$

From Eq. (5.47), the prediction error $\varepsilon(t)$ is correlative with the adjustable vector θ , and thus it is referred as the predicted deviation variables with respect to θ . Then the prediction residual $\tilde{\varepsilon}(t)$ related to the optimal model parameters vector $\tilde{\theta}$ is defined, which is expressed in Eq. (5.48).

$$\tilde{\varepsilon} = \varepsilon(t, \tilde{\theta}) \quad (5.48)$$

Essentially, it is required to assess continuously how well the output of predicted models $\hat{s}(t|\theta)$ simulates the real output of a structure. According to the reference [80], the Ratio Ω^2 is defined as

$$\Omega^2 = 1 - \frac{\sum_{t=0}^n \tilde{\varepsilon}^2(t)}{\sum_{t=0}^n s^2(t)} \quad (5.49)$$

and monitors the state of the total variation of the simulated system model S_m . And the ratio is referred to the *recursive coefficient*. This coefficient measures how much of the information on the actual structure system response $s(t)$ is contained in that of the simulated system model $\hat{s}(t|\theta)$.

Therefore, to obtain the optimal model order, the following sifting criterion is formulated and executed:

- a) Start with an appropriate small model order (normally the selection range of model orders $2 \leq n \leq 8$);
- b) Increase model order until the recursive coefficient Ω^2 is high enough and close to 1, so that the system model matches well with the actual structure response;
- c) If Ω^2 is high enough and increasing model order doesn't help increasing the value of Ω^2 , then selecting the system model with the smallest order;

d) If the modeled system has any unstable pole or zero, then decreasing the prediction model order until it doesn't have any unstable pole or zero.

5.2 Inverse Model Solver

To identify unknown impacts on a composite structure, the force history of impacts can be predicted through the force reconstruction process using selected sensor response data. Then, the inverse model (IM) for force reconstruction is required to construct, and the force history corresponding to any unknown impact can be estimated from this inverse procedure, where the constructed forward model, structural system matrix A , input matrix B , output matrix C and feedforward matrix D are all used to establish the corresponding inverse model, which are obtained from the optimal model parameters a_i and b_j as described in Section 5.1.

5.2.1 Inverse Reconstruction Functions

The inverse reconstruction function block includes two sub-function blocks, which are the inverse model operator and generalization of force reconstruction. The goal of this inverse reconstruction function block is to reappear effectively any unknown impact force in real-time mode through the inverse model found using the output data from structural responses. When a random impact event occurs and is applied at any location (x, y) on a structure, four component forces corresponding to the actual impact force can be reconstructed by Eq. (5.58) that is a matrix convolution expression of Eq. (5.55), and then the four component forces are generalized through the interpolation method as shown in Eq. (5.60), finally the estimated impact force can be calculated by the Gauss-Newton Optimization method for the four component forces.

5.2.1.1 Function 1: Inverse Model Operator (IMO) [2]

In order to reconstruct impact forces, the force signals resulting from impacts can be predicted based on the inverse model operator only using the output data of the structure responses. Then, through combining the state-space model (Eq. (5.1a) and Eq. (5.1b)) with the forward model (Eq. (5.23)) described in Section 5.1, the inverse model for force reconstruction can be constructed and the corresponding input forces resulting from impacts can also be estimated by this inverse procedure. The details of this function will be discussed in Section 5.2.2.

5.2.1.2 Function 2: Generalization of Force Reconstruction

An unforeseen impact occurred at a general location of a structure can be reconstructed in terms of the reconstructed component forces obtained at the identified grid points of impulse response functions. Then, an attacked region due to an impact is surrounded by the four

positions of impulse response functions in the neighborhood to the impact location, which is illustrated in Figure 5.15. As the impact event happens at any location of the region, the impact force can be reconstructed using the set of impulse response functions through the proposed Gauss-Newton optimization and interpolation method. The details of this function will be discussed in Section 5.2.3.

5.2.2 Inverse System Model Operator for Force Reconstructions

This description on how to reconstruct unknown impact forces was presented in Si's article [2, 77]. As the dynamic responses of a MOF structure can be represented by the discrete time state-space model (Eq. (5.1a) and Eq. (5.1b)), the state-space model is controllable due to its property of full rank, thereby an external input and corresponding response output can be exchanged [81]. An inverse dynamic response model can be deduced as

$$\dot{x}(k) = \hat{A}x(k) + \hat{B}s(k) \quad (5.50a)$$

$$u(k) = \hat{C}x(k) + \hat{D}s(k) \quad (5.50b)$$

where \hat{A} is the inverse structure system matrix, \hat{B} is the inverse input matrix, \hat{C} is the inverse output matrix and \hat{D} is the inverse feedforward matrix, and they are defined respectively as

$$\begin{aligned} \hat{A} &= A - B\hat{D}C & \hat{B} &= B\hat{D} \\ \hat{C} &= -\hat{D}C & \hat{D} &= D^T \end{aligned} \quad (5.51)$$

Nevertheless, the inverse model of a robust dynamic response model due to external inputs can be expressed as

$$u(k) = \sum_{i=0}^k \hat{g}(i)s(k-i) \quad (5.52)$$

where the inverse function of impulse responses $\hat{g}(i)$ of the inverse model is given by

$$\hat{g}(0) = \hat{D}, \quad \hat{g}(i) = \hat{C}\hat{A}^{i-1}\hat{B} \quad \text{where } i = 1, 2, \dots \quad (5.53)$$

However, the controllable canonical form of the state-space realization for the dynamic response model as represented in Eq. (5.21) is a strictly proper, thus the model does not have a direct feedthrough and D is equal to zero.

Now, in order to obtain the rational and correct inverse model with regard to the zero initial conditions, the canonical state-space realization Eq. (5.21) must be re-established to generate a new forward dynamic response model fitting for the inverse reconstruction problem. Thereupon, the new dynamic response model can be constructed as

$$\dot{x}(k) = Ax(k) + Bu(k) \quad (5.54a)$$

$$\dot{s}(k) = C\dot{x}(k) + CBu(k) \quad (5.54b)$$

Under the above condition, the reconstructed impact force f_r at time kT is now a function of the impulse response of a structure at future times, $kT + 1$ through $kT + 1 + r$. Nevertheless, supposing $T = 0$, the new and rational inverse model is thus established simply as

$$u(k) = \sum_{i=0}^k \hat{g}(i) s(k+r-i) \quad k = 1, 2, \dots \quad (5.55)$$

where the inverse IRF matrix for the new inverse model can be defined by

$$\hat{g}(0) = (CA^{r-1}B)^T \quad \hat{g}(i) = \hat{C}\hat{A}^{i-1}\hat{B} \quad i = 1, 2, \dots \quad (5.56)$$

where

$$\begin{aligned} \hat{A} &= A - B(CA^{r-1}B)^T CA^r \\ \hat{B} &= B(CA^{r-1}B)^T \quad \hat{C} = -(CA^{r-1}B)^T CA^r \end{aligned} \quad (5.57)$$

Finally, the inverse model (IM) can also be represented in the matrix convolution formulation as

$$U_{(x,y)} = \hat{G}_s^f S_{(x_i,y_i)} \quad (5.58)$$

where

$$U_{(x,y)} = [u(0) \ u(1) \ \dots \ u(n-r-1)]^T \quad (5.59a)$$

$$S_{(x_i,y_i)} = [s(r) \ s(r+1) \ \dots \ s(n-1)]^T \quad (5.59b)$$

$$\hat{G}_s^f = \begin{bmatrix} \hat{g}(0) & 0 & 0 & \Lambda & 0 \\ \hat{g}(1) & \hat{g}(0) & 0 & \Lambda & 0 \\ M & M & O & 0 & M \\ \hat{g}(n-r-2) & \hat{g}(n-r-3) & O & O & 0 \\ \hat{g}(n-r-1) & \hat{g}(n-r-2) & \Lambda & \hat{g}(1) & \hat{g}(0) \end{bmatrix} \quad (5.59c)$$

\hat{G}_s^f is the inverse IRF polynomial matrix of a structure system and it relates an recorded specific sensor signal $S_{(x_i,y_i)}$ and an unknown input force f impacting at the location (x, y) . Meanwhile, all components from the IIRF \hat{G}_s^f can be calculated through in terms of the instrumental variables (the system parameters) a_i and b_j from Eq. (5.56) and combining with Eq. (5.22). Consequently, the unknown impact force can be obtained through the simple convolution Eq. (5.58) using the inverse IRF matrix \hat{G}_s^f and the specified sensor output signal $S_{(x_i,y_i)}$ recorded.

Here, a demonstration of the force reconstruction of an unknown impact is illustrated in Figure 5.15.

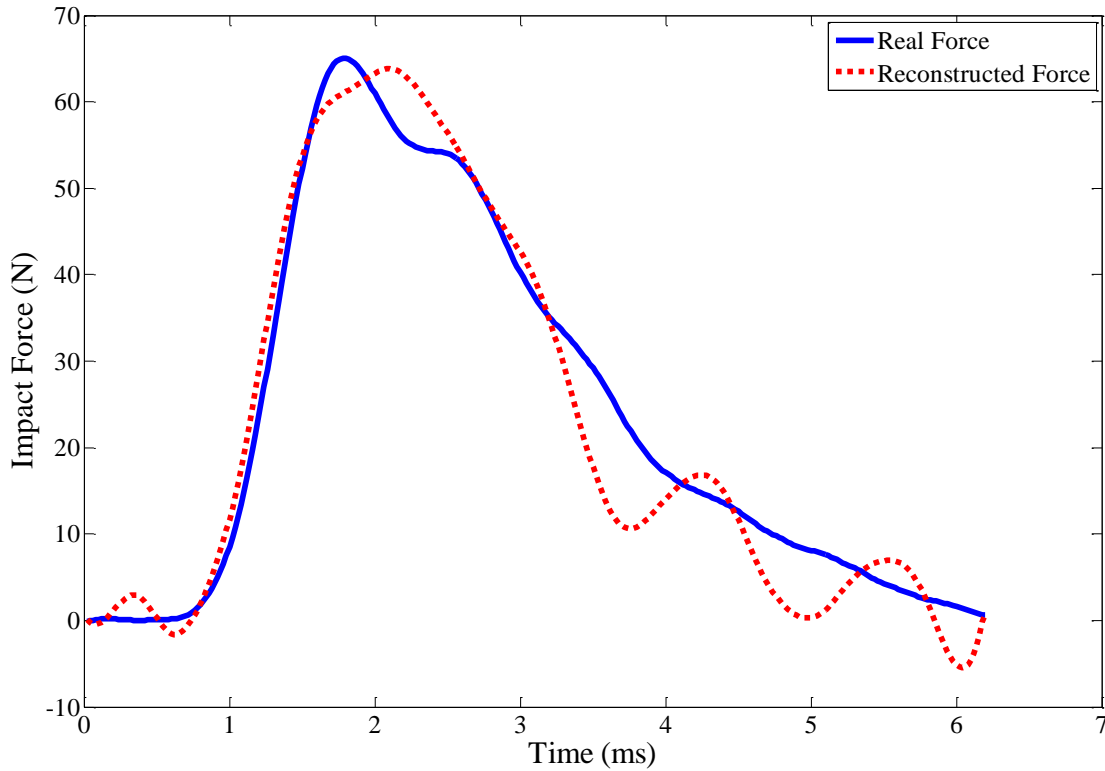


Figure 5.15 A demonstration of force reconstruction of an unknown impact.

5.2.3 Generalization of Impact Force Reconstruction

As an unknown impact acts at any general location on a structure, the force can be reconstructed in terms of the component forces estimated at the discrete inverse IRF \hat{G}_s^f positions of an identified grid. To achieve this propose, a certain number of quadrilateral grids with four inverse IRF points need to be formed of an identifying grid network overlaying the whole structure. Then, this execution is implemented using a smoothing formula approach which is typically applied in the imaging process method. A set of four inverse IR functions \hat{G}_s^f are considered as an element and are obtained at four arbitrary positions as shown in Figure 5.16, with the four nodes numbered one to four. And also the i th node owns its physical coordinates (x, y) . With regard to the element composed of the four IR functions \hat{G}_s^f , the original physical element is substituted with a normalized element of same topology, of which the edges have a non-dimensional length.

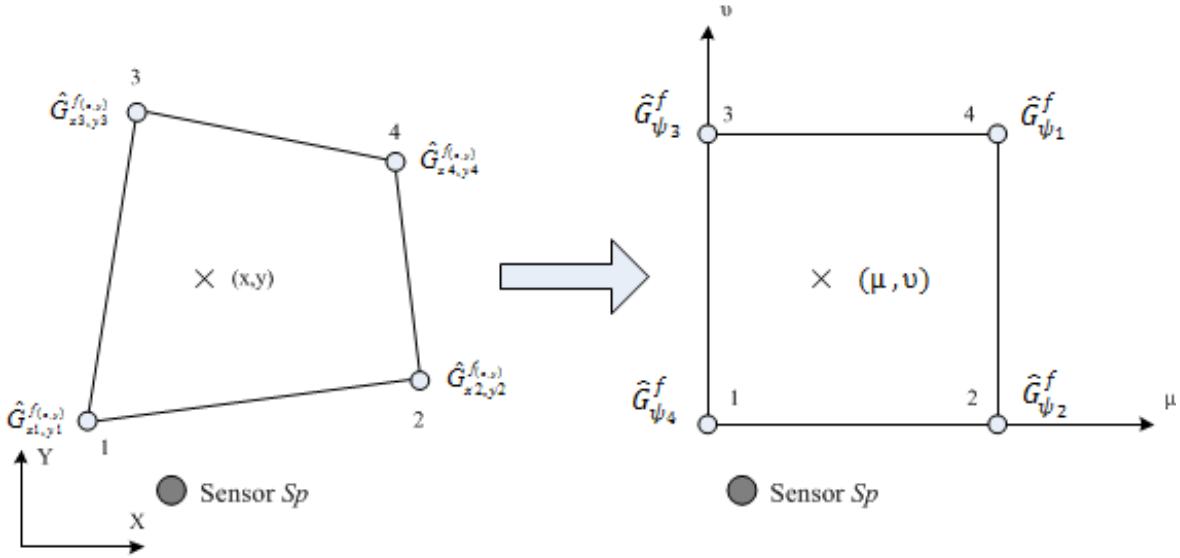


Figure 5.16 Generalization for an impact force acting at arbitrary location

From Fig. 5.16, the parametric and physical coordinates are associated each other by the interpolation functions, and the corresponding nodes in the parametric coordinate system have all the individual coordinates (μ, ν) . In this case, the positional functions in a two-dimensional space need to be defined by the biharmonic interpolation method and be employed through the following form.

$$\psi_1(\mu, \nu) = (1 - \mu)(1 - \nu) \quad (5.60a)$$

$$\psi_2(\mu, \nu) = \mu(1 - \nu) \quad (5.60b)$$

$$\psi_3(\mu, \nu) = (1 - \mu)\nu \quad (5.60c)$$

$$\psi_4(\mu, \nu) = \mu\nu \quad (5.60d)$$

It should meet the following conditions to interpolate successfully impact forces if this kind of positional interpolation method applied into the transformation between the physical and parametric coordinates can be executed,

a) With the application of the mesh grids approach for a structure, as the structure is impacted at a position and the structural deformation is assumed to be small, each element from the structure can be considered to omit the geometric nonlinearity effect;

b) There is no discontinuous change of structure property in the element, in the other words, there owns isotropic structure feature in the structural element, however comparing to the entire anisotropic structure properties.

From structure properties, input force reconstructed can't be interpolated linearly if there is any discontinuity in a structural element, such as cutouts, stiffeners and so on. In this case, several sets of additional elements in the particular parts of the structure should be considered to construct so that the structural response on anywhere of the structure can be deemed to have a linear dependency on the location.

With the use of the above assumption, the interpolation method is competent to reconstruct the input impact force. As shown in Figure 5.16, the response signal from a specified sensor s_p is generated due to an impact at a position point, of which the physical coordinates are (x, y) and the corresponding parametric coordinates are (μ, ν) , then the component force f_{ψ_i} at the ψ_i node can be reconstructed using the inverse model Eq. (5.58),

$$f_{\psi_1} = \hat{G}_{\psi_1}^f S_p \quad f_{\psi_2} = \hat{G}_{\psi_2}^f S_p \quad (5.61a)$$

$$f_{\psi_3} = \hat{G}_{\psi_3}^f S_p \quad f_{\psi_4} = \hat{G}_{\psi_4}^f S_p \quad (5.61b)$$

Finally, the reconstructed F at the point (μ, ν) due to a random impact event is found from

$$F_{(\mu,\nu)} = \sum_{i=1}^4 \psi_i f_{\psi_i} \quad (5.62)$$

In brief, once a structure is overlaid by an integral network of (inverse) impulse response functions grids, any impact occurring at any location on the structure can be reconstructed using Eq. (5.62). By applying this conception, a full-scale panel structure can be modeled with comparative few number of IRFs grids, which enables to avoid numerous impact training procedures both from the FEM simulation training and experimental training, and also save the price of time for modeling the integral inverse impulse response function matrix to an entire complex structure.

5.3 Formation of Networks of Impulse Response Functions grids

For improving the inverse accuracy of reconstructing force histories, it depends on the interval of the impulse response function points, also called the grid nodes. Generally, the accuracy of force reconstructions is inversely proportional to the interval of the IRF points increases. However, the interval of IRF points can be determined through the reconstruction error ratio (RER) method defined. The details of this function of networking and gridding (NAG) of impulse response function points are described in this section.

For impact forces reconstructions using the FGAPE based impact monitoring and identification approach, their accuracy and dependability are primarily dependent on two main factors that are 1) the interval of the impulse response function points, and 2) the sensor interval. Then, for the interval of the impulse response function points, it is described in this section, and for the sensor interval, it will be interpreted in Appendix A.2. Generally, the accuracy increases as the interval decreases, regardless of the interval of IRF points or the sensor interval, and the relationship between the accuracy and the interval is inversely proportional. The interval of IRF points can be determined for the demanded accuracy through a calibrated test.

To determine the interval of IRF points required, the differences between the forces recorded and reconstructed are checked with different intervals, and the relevant errors are used to adjust the interval of the IRF points, finally obtaining the optimal interval of the impulse response function points to the desired precision. The error between the recorded and reconstructed forces is defined in Eq. (5.63), which is the ratio of the difference between the reconstructed and recorded amplitudes chosen in a certain time interval as shown in Figure 5.17.

$$Error(\%) = \frac{|A_{record} - A_{recons}|}{A_{recons}} \times 100 \quad (5.63)$$

where A_{record} is the recorded amplitude of real impact force, and A_{recons} is the estimated amplitude of the corresponding reconstructed force.

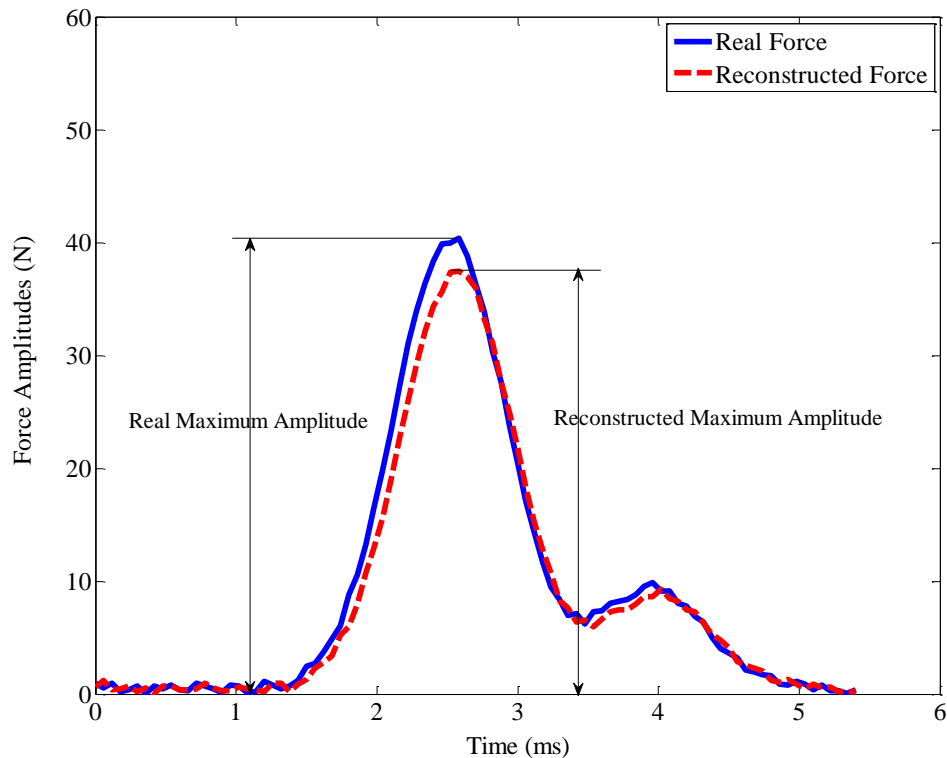


Figure 5.17 Amplitude difference between real and reconstructed impact forces

Nevertheless, in order to select the appropriate interval for impulse response function points, the following evaluation process thus needs to be conducted:

- 1) First, a set of impulse response functions are obtained with a specific interval, which is generally a square region composed of four impulse response function points;
- 2) Additional evaluation positions are set inside of the grid made up of the previous four impulse response function points, and impact tests need to be executed at the corresponding positions;
- 3) The input impact forces at the evaluation points are constructed using the set of impulse response functions through the force reconstruction formula Eq. (5.62);
- 4) From the several evaluation points, maximum error is investigated;
- 5) If the maximum error does not meet the required precision, then to decrease the previously specified interval. Meanwhile, returning to Step (1) and performing again with the new interval.

5.4 Conclusion

In this chapter, a robust and integral impact monitoring and identification (IMI) approach was proposed and developed. This impact identification approach is able to locate properly and quantify any unforeseen impact event for laminated composite structures under multiplex disturbances such as mechanical vibration environments and complex varying structure configurations in real time. Furthermore, the IMI approach can also evaluate systematically the structural condition as a structure encountered an unexpected impact event. It is worth mentioning that the forward model that can represent the structural responses can be constructed with a constant number of impulse response functions; whereas, the corresponding inverse model can effectively reconstruct unknown impact forces. Nevertheless, the accuracy and dependability of the force awareness for an unknown impact depend on the density and number of the designed impulse response function grids. Through a series of the validation of impact tests, the estimation results using the developed impact identification approach were satisfactory.

6. Structural State Awareness - Damage Identification

In the research field of the damage inspection, some researchers have proposed and developed their damage inspection methods [82-88] to locate and quantify structural damage such as delaminations, debonds and matrix breakages, which are probably induced by external impacts. These damage hidden in a structure affect significantly the integrity of the structure. A reliable in-situ rapid multi-damage identification (RMDI) approach has been developed by L. Si to determine any damage presence, to locate and quantify single and multiple damage in a laminated composite structure, thereby to give an assessment of the structure state. The conception and architecture of the RMDI approach will be introduced briefly in this chapter. Nevertheless, the more detailed introduction and description on multiple damage identification for laminated composites have been presented in Si's damage identification paper [66]. In addition, the third type of damage index parameter – the phase divergence metric (PDM) will be supplemented and described in detail in this chapter.

The developed rapid multi-damage identification approach is composed of two functional modules, which are the wave velocity computation (WVC) and the damage index parameters (DIPs) [66]. It is worthy to mention that the DIPs function module makes up of three multi-functional multi-metrics (referred as MFMMs), which are separately the energy density metric (EDM), the energy time-phase shift metric (ETPSM) and the phase divergence metric (PDM). The MFMMs is a set of newly developed damage indices to identify structural flaws in laminated composites effectively during the manufacturing process, and also is enabled to dependably trace the extents of the progressive damage using the individual damage prediction trend functions (DPTF) for laminated composites due to a variety of multiplex environmental factors such as external impacts.

6.1 Determination of the Group Velocity of Propagating Waves

To predict the A_0 group velocity of the propagating waves in a composite structure, wave velocity computation method was proposed in detail in Si's paper [66]. The wavenumber-frequency relationships should be constructed, once the bending stiffness coefficients and the mass of the composite structure are obtained. And then, the wave group velocity can be easily deduced from the evaluated wave dispersion relations. For the low-frequency wave propagation, the CLPT theory is retained to compute the wave group velocity of the A_0 Lamb mode from the evaluated wavenumber-frequency relationships. The theoretical supports of the solving process of the wave velocity have been presented in Appendix B. For the high-frequency wave propagation, a finite element model constructed by Cortes [89] with the consideration of the shear deformation was used to predict the Lamb wave propagations in laminated composites. In our validation experiments of damage identification, the low frequency A_0 mode is more suitable to inspect and identify the inter-laminar delaminations in the examined laminated composites.

In an examined laminated composite, the dispersion properties of wave propagation on the group velocity are presented in the propagation directions of 0° and 90° as illustrated in Figure 6.1. Once the group velocity is determined, the location of any damage can be inferred using the multi-damage index parameters – multi-functional multi-metrics. Accordingly, they are suitable for the rapid damage identification online.

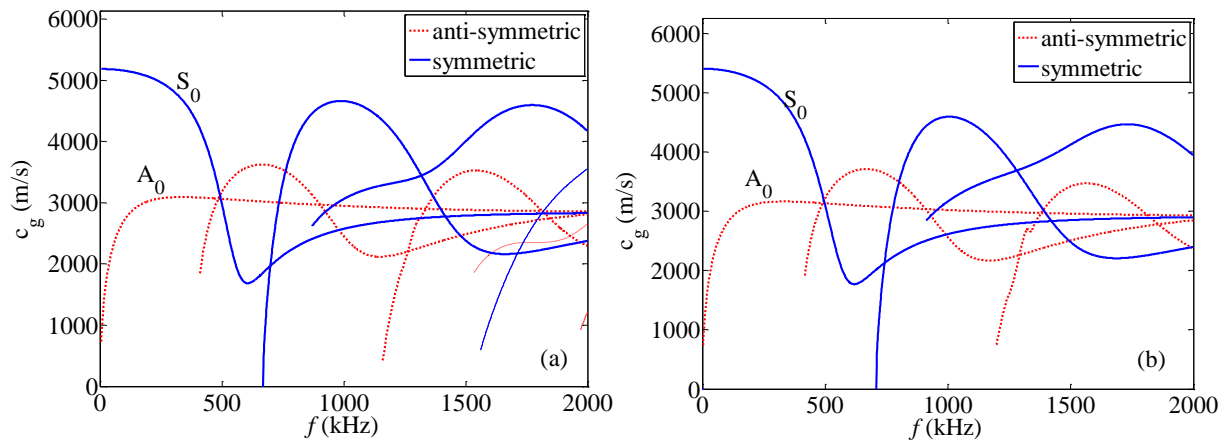


Figure 6.1 Dispersion characteristics of wave group velocities c_g in a tested laminated composite: (a) in wave propagation of the 0° direction, (b) in wave propagation of the 90° direction.

6.2 Rapid Multi-Damage Indices Algorithm Based on Multi-Functional Multi-Metrics

The proposed rapid multi-damage index algorithm (MDIA) is composed of two metrics that are the energy density metric and the energy time-phase shift metric. The rapid MDIA is then used to process the signal data from the sensors' dynamic responses, infer the presence of any damage, determine the locations of damage, and diagnose the extents of damage. Meanwhile, the rapid MDIA is also shown to trace increasing amount of damage based on the multi-functional multi-metrics. Therefore, it has the potential to promote the development of damage visualization techniques.

6.2.1 Fast Ensemble Empirical Mode Decomposition (FEEMD) and Hilbert Spectral Analysis

To clarify the computation and decomposition process, the flow chart in Figure 6.2 [66] summarizes the primary procedure of the FEEMD decomposition for a recorded non-stationary sensor signal data.

In the decomposition procedure of FEEMD, the original sensor response data are decomposed into a collection of intrinsic mode functions (IMFs). For instance, an original sensor signal $s(t)$ is decomposed into n IMFs $D_j(t)$ and can be expressed as:

$$s(t) = \sum_{j=1}^n D_j(t) + R_n(t) \quad (6.1)$$

where the residue $R_n(t)$ is a mean trend, from which no more IMF need to be extracted. It has been left out on purpose from the decomposition. To obtain the IMF components $D_j(t)$, an iterative sifting procedure needs to be conducted. With the property of time-dependent amplitudes and frequencies, therefore, each intrinsic mode function can be treated as an individual signal, into which the Hilbert transform can be applied by:

$$D_j(t) = \lambda_j(t) * \exp\left(i \int \omega_j(t) dt\right) \quad (6.2)$$

where $D_j(t)$ is a monotonic component signal, which has a positive instantaneous frequency and a monotonically increasing phase. Each IMF is a frequency- and amplitude-modulated signal so that the IMFs have well-behaved Hilbert transformations.

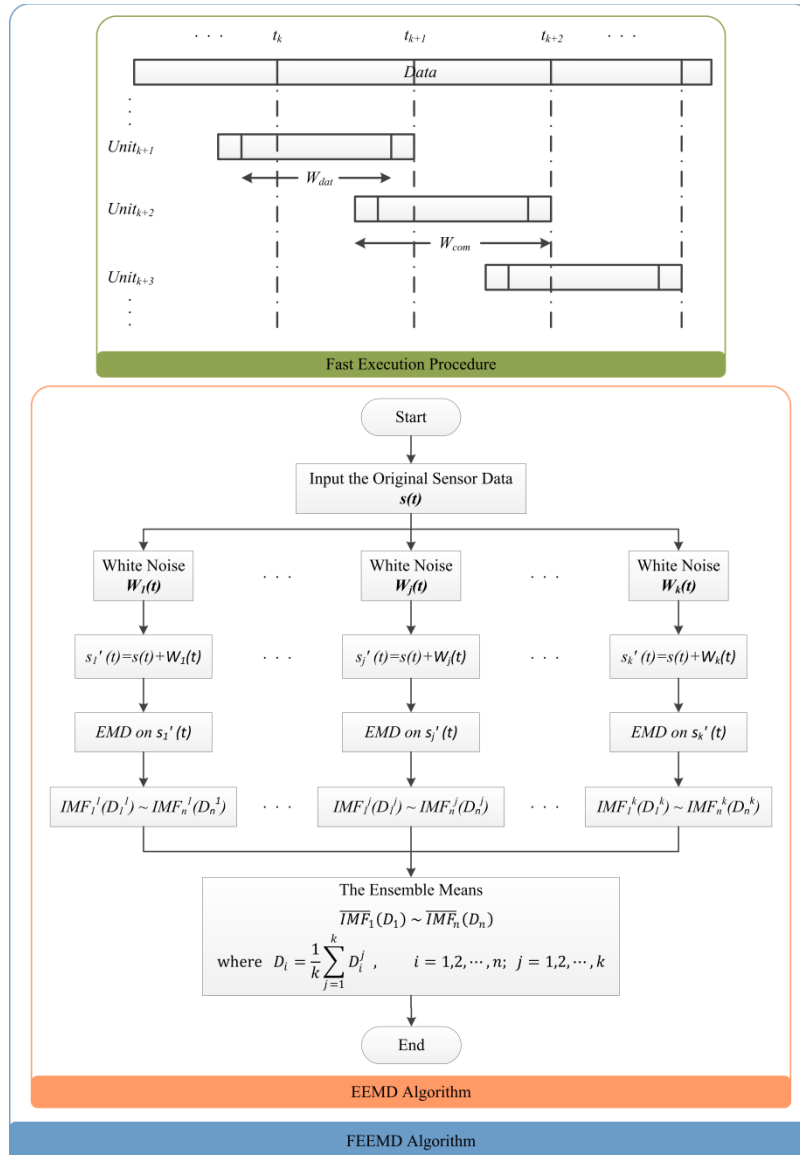


Figure 6.2 The fast ensemble empirical mode decomposition procedure.

To reveal the merits of the FEEMD, an undamaged and damaged case are demonstrated in Figure 6.3. And the waveform from the excited diagnostic signal is made up of a 5 peaks narrow-band sine tone burst at 160 kHz modulated by a cosine Gaussian envelope. The decomposed IMFs resulting from the FEEMD processing for the selected sensor response signals are shown in Fig. 6.3.

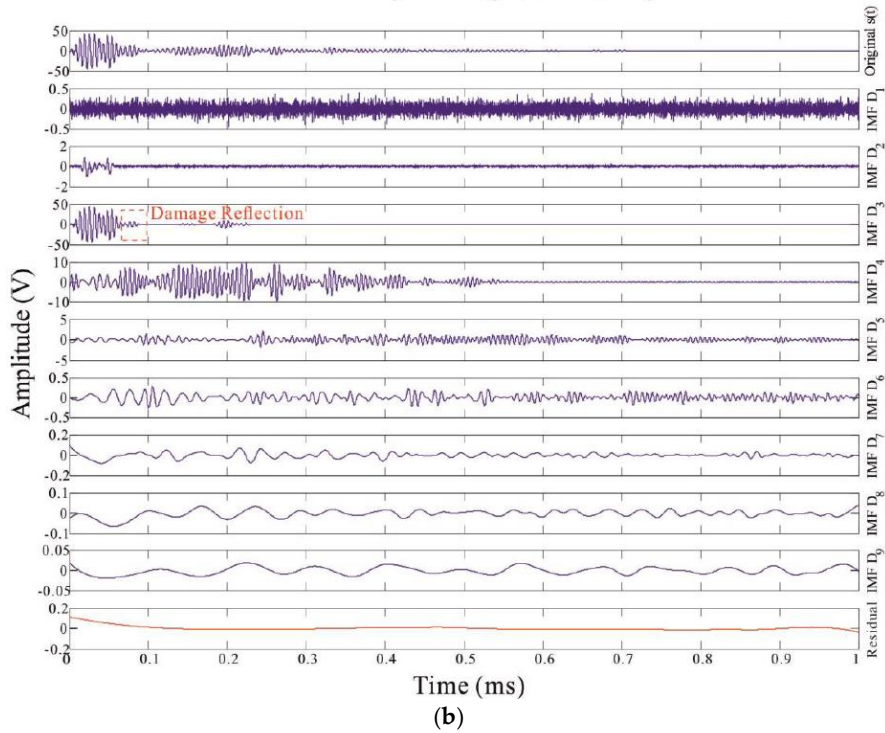
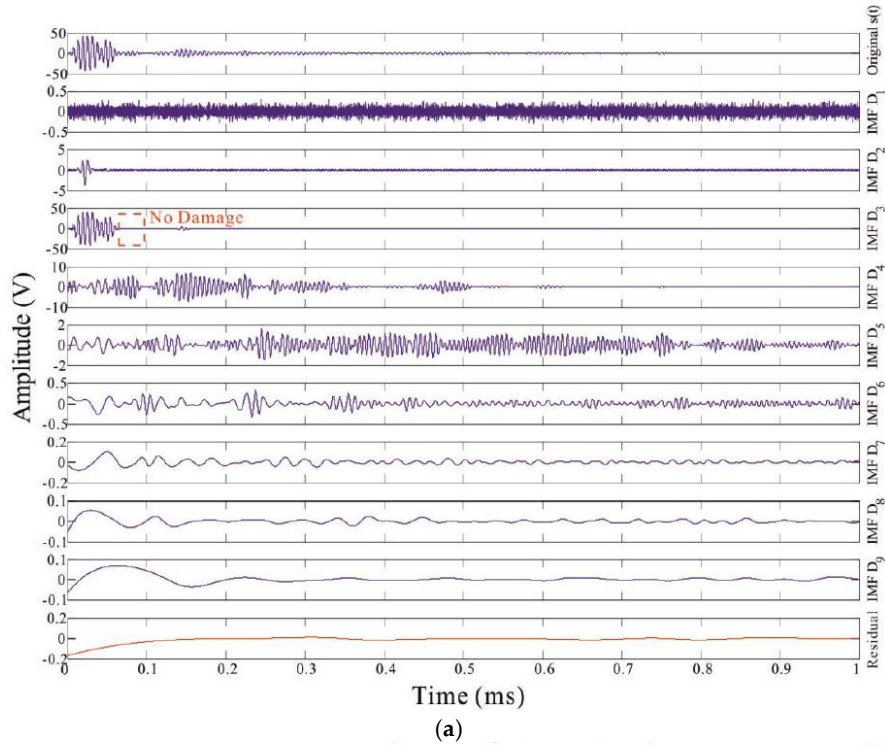


Figure 6.3 FEEMD processing for the sensor signals without (a), and with damage (b).

Actually in the Hilbert space, a given original sensor data $s(t)$ can be expressed as the combination of each analytic signal corresponding to each IMF $D_j(t)$:

$$s(t) = \sum_{j=1}^n z_j(t) = \text{RE} \left[\sum_{j=1}^n \lambda_j(t) e^{i\omega_j(t)t} \right] \quad (6.3)$$

From Eq. (6.3), a time-frequency spectrum can be obtained by the integration of $H(t, \omega)$ covering the total data period, and indicates the total energy contribution of sensor data. In a word, the HSA-FEEMD method is suitable for complex data processing, especially in structural damage inspection applications, discovering tiny variation in oscillation during wave propagation.

Through the corresponding Hilbert transform for the IMFs, any variation due to possible damage could be localized on the time as well as the frequency axis in the evaluated time-frequency spectrum.

6.2.2 Multi-Damage Index Parameters—Multi-functional Multi-Metrics (MFMMs) Based on HSA-FEEMD

The aim of the proposed RMDI approach is to discover new damage index parameters, which can extract effectively and identify accurately complete multiple damage information for a structure. A functional metric will become the key tool to give the necessary information about possible or diverse damage situations. There are three defined multi-damage index parameters (MDIPs) used into the rapid multi-damage identification approach, which are the energy density metric, the energy time-phase shift metric and phase divergence metric.

6.2.2.1 Energy Density Metric (EDM) [66]

Collected sensor signals are used to produce the corresponding energy time-frequency spectra. An energy time-frequency spectrum is defined as the energy density metric that is obtained from the squared values of the instantaneous amplitudes. The amplitudes are deduced by the Hilbert transform of the high-energy IMFs. This metric is designated as a damage index parameter that can provide a high definition energy time-frequency representation. And also it can describe precisely the frequency content of any non-stationary or nonlinear signal based on the FEEMD process. Hence, the different features concealed in sensor signals can be revealed and better understood. In view of these reasons, the energy density spectrum needs to be found and used to identify and assess structural damage from the reflected wave energy.

The energy density metric could not only quantify the extents of damage, but also map out the relationship between the released energies upon reflections and the defect growth through the corresponding energy time-frequency spectra of the sensor response data. The energy density is expressed as Equation (6.4):

$$E = \int_f \int_t |H_e(t, f)| = \int_f \int_t |\lambda(t)|^2 \quad (6.4)$$

where $H_e(t, f)$ is called the Hilbert energy spectrum, and $\lambda(t)$ is the instantaneous amplitude resulting from the Hilbert transform. To reveal the damage quantification, the evaluation results obtained by the energy density metric is illustrated in Figure 6.4. The analysis of any damaged structure becomes facilitated by using the high-definition energy density spectrum.

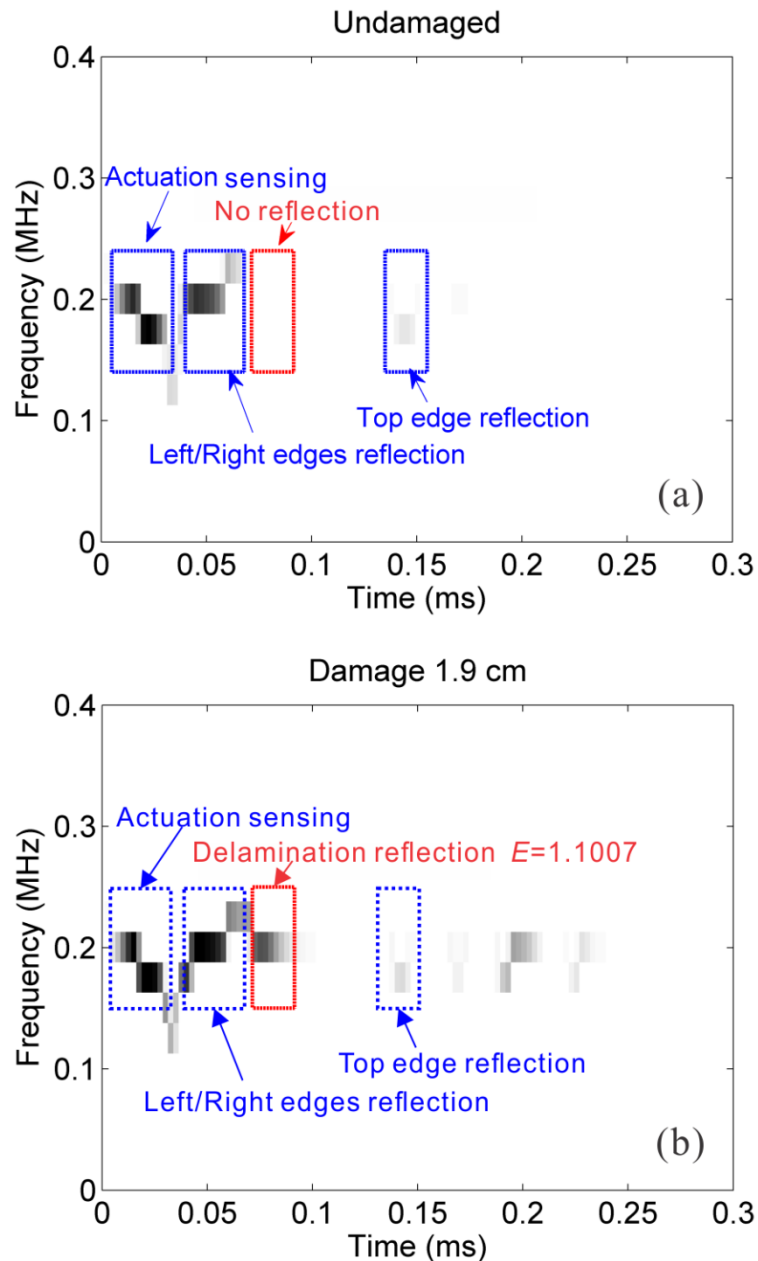


Figure 6.4 Energy density metrics: (a) an undamaged case, (b) a delamination case of 1.9 cm diameter with its reflected energy of 1.1007.

6.2.2.2 Energy Time-Phase Shift Metric (ETPSM) [66]

In most damage inspection schemes, the time of flight (TOF) is a crucial damage index parameter used often. Here, the TOF is defined as the time duration taken from the energy peak of an actuation sensing wave to the energy peak of a reflected wave due to damage, which can be measured by sensors. A demonstration of the TOF definition is illustrated in Figure 6.5. However, in order to easily obtain accurate time information to serve for the TOF, a high-definition energy time spectrum was proposed and developed based on the Hilbert spectral analysis. In the energy time spectrum, the time resolution becomes more demarcative so as to calculate conveniently a precise TOF demanded. Then using the evaluated result of the TOF, the location of a structural discontinuity can be estimated with the information of the wave propagation velocity.

In the energy time spectrum obtained from the selected IMF components containing the highest energies, the peaks give the arrival times of interest for the waves. Nevertheless, the location of any damage can be determined by the basic formula (6.5), which is referred as the damage positioning function (DPF):

$$L_{\text{dam}} = \frac{C_g(\theta) \times t_f}{2} \quad (6.5)$$

where L_{dam} is the distance of any damage away from a specific sensor. $C_g(\theta)$ is the group velocity of a propagating path. t_f is the corresponding time of flight.

If the time resolution of an obtained energy time spectrum is distinct enough to recognize the small fluctuations from the different TOF corresponding to the diverse damage dimensions, the estimation for the severities of progressive damage would be feasible. In other words, it would be possible to trace damage increasing even if the dimension of an initial damage is unknown.

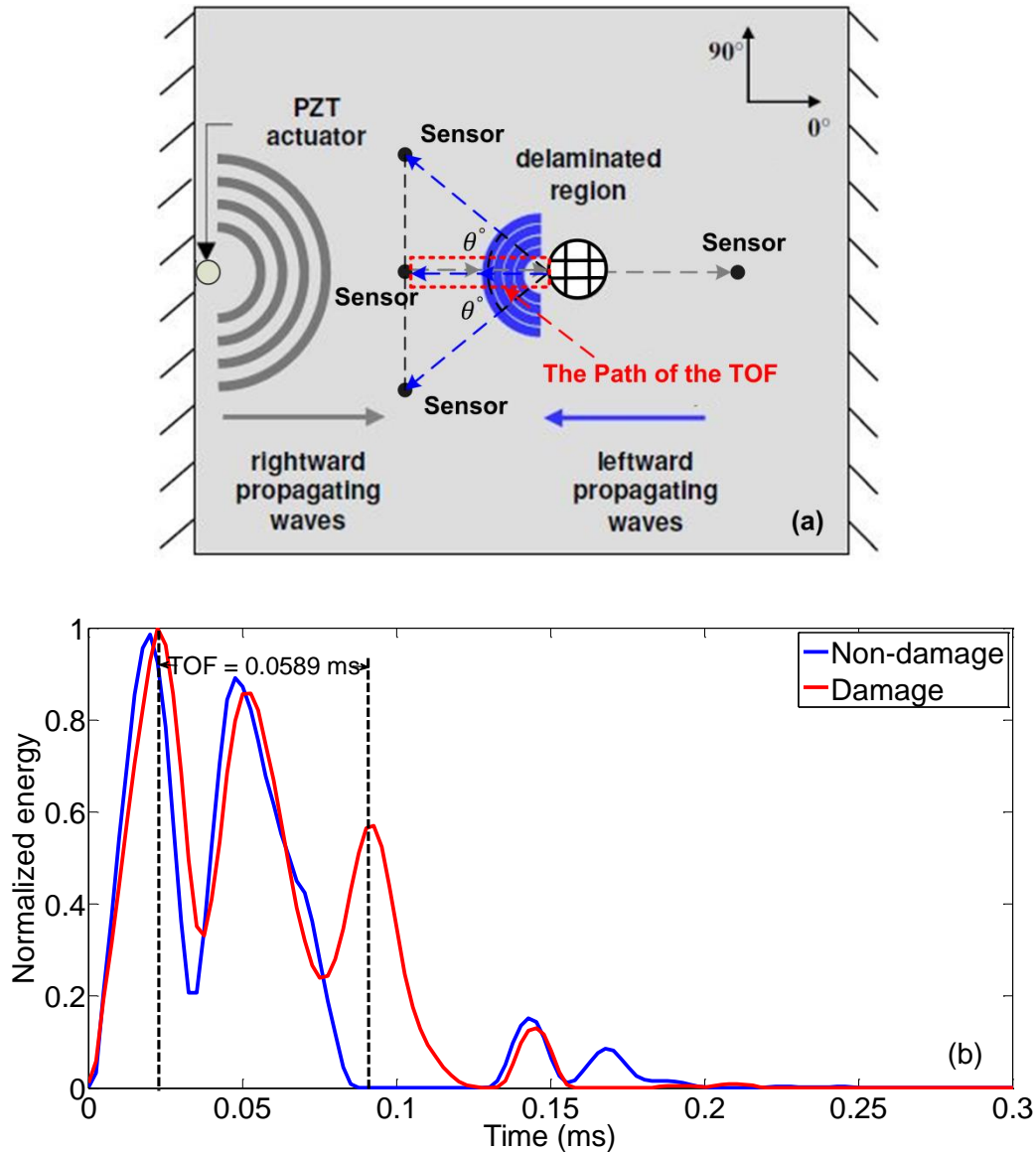


Figure 6.5 A demonstration of the TOF definition: (a) the wave propagating path encountering a delamination in a CFRP specimen, (b) Extraction of the TOF of the delamination.

6.2.2.3 Phase Divergence Metric

The Hilbert phase can give consistent results in comparison to the other damage inspection methods and is competent to locate and quantify the extents of damage through the corresponding time divergence to phase variations. To realize the damage localization and quantification, the phase divergence metric (PDM) was proposed and developed to execute the rapid multi-damage identification for laminated composite structures. What's more, using a new developed root-mean-square phase deviation (PDRms), the progressive damage can be rapidly evaluated and predicted by the calculated damage prediction trend curve (DPTC).

Any physical (mechanical) characteristics variations in a laminated composite normally lead to the alterations of energy propagation behaviors such as the instantaneous phase of propagating waves. The alterations are characterized by the deviations of instantaneous Hilbert phase at structural discontinuities such as delaminations, debonds and matrix cracks. The instantaneous phase is local characteristic and is a function of monotonous increment with respect to time, as the decomposed IMF components are symmetrically local with regard to the mean zero line.

The total phase function $\theta(t)$ corresponding to all IMF components can be defined as

$$\theta(t) = \sum_{i=1}^n \theta_i(t) = \sum_{i=1}^n \arctan\left(\frac{H[d_i(t)]}{d_i(t)}\right) \quad (6.6)$$

where $\theta_i(t)$ represents the phase function of the i th IMF function. Each phase function increase monotonically in a 2π interval.

To obtain the well-visible phase divergence metric to reveal the phase transmutation due to damage presence in a laminated composite, the total instantaneous phase function $\theta(t)$ to an examined sensor response signal is unwrapped by adding a series of 2π when the absolute jumps of consecutive phase elements are equal to or greater than π . Similar with the function of the reflection energy density metric, the instantaneous phase enables the structural damage to be located by searching out the corresponding time-of-arrival (TOA) with respect to the varying position of the instantaneous phases between the intact and damaged cases; meanwhile, the instantaneous phase is also able to quantify any structural damage and progressive multiple damage by the root-mean-square phase deviation curve function, which is represented as

$$PD_{rms} = \sqrt{\frac{\sum_{t=1}^n [\theta_{dam}(t) - \theta_{und}(t)]^2}{\sum_{t=1}^n \theta_{und}^2(t)}} \quad (6.7)$$

where $\theta_{und}(t)$ and $\theta_{dam}(t)$ represent the phase functions of the baseline (undamaged) and the damaged cases. The summation covers all the time sampling point (n time point in total).

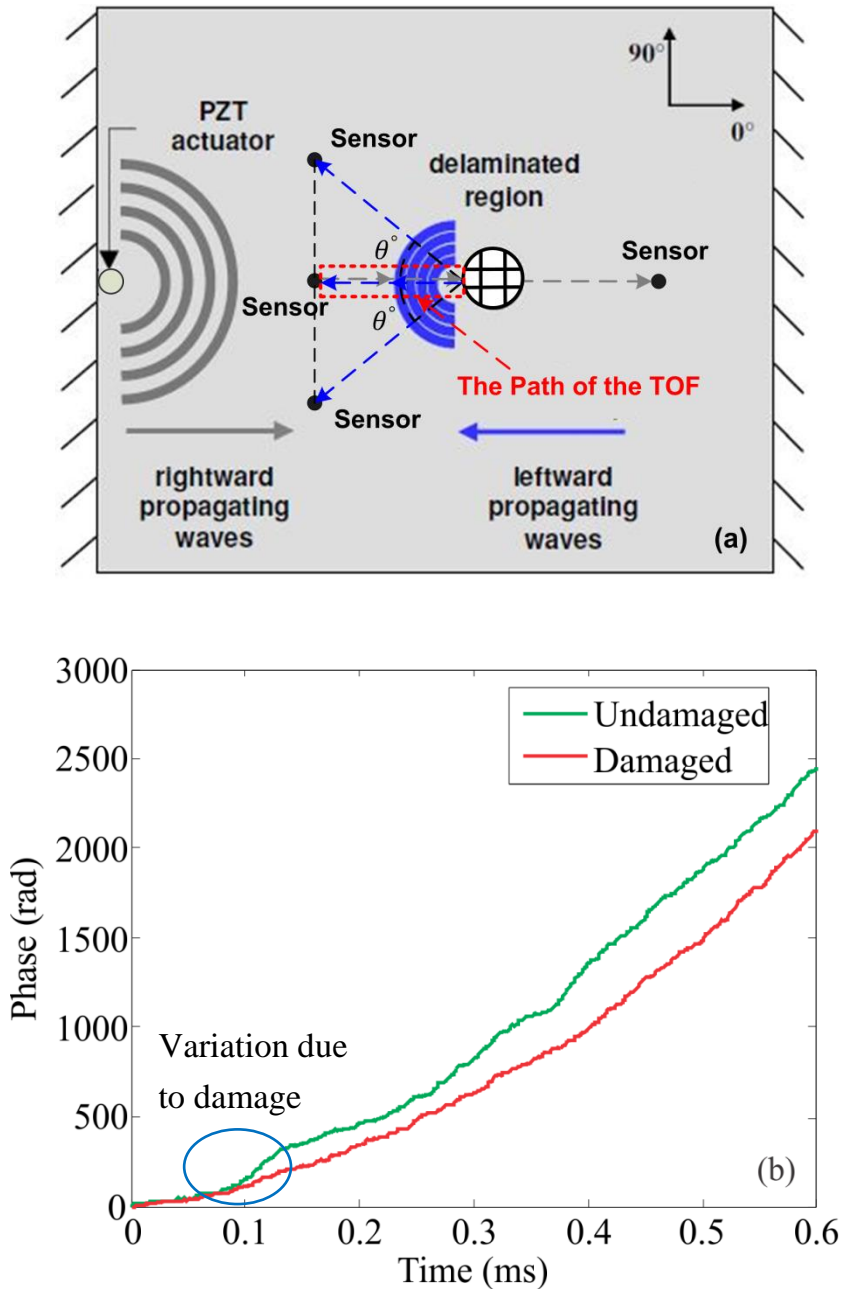


Figure 6.6 Phase divergence metric used to discriminate damage existing in a laminated composite: (a) the wave propagating path encountering a delamination in a CFRP specimen, (b) the instantaneous phase variation between the undamaged and damaged cases.

From Fig. 6.6, it can be seen that the wave reflection due to damage in a laminated composite can be indicated by the phase slope variation in the phase divergence metric, as the propagation speed of the wave energy would be diversified when a wave propagating in a composite structure encounters damage. Afterwards, the wave traverses over the damage, the

propagation property of the wave energy will not be interfered, and its phase will also return to the previous behaviors as that of the intact case.

7. Estimations of Multi-Impact Locations

As for precise impact localizations, some classical impact localization methods have been proposed by researchers [61, 90, 91] to effectively estimate impact locations in a structure. In this thesis, the detailed introductions on the proposed impact positioning methods have also been interpreted in Si's impact monitoring papers. In this chapter, the primary contents are presented from Si's papers [2, 77].

In order to determine multi-locations of impacts and decrease the estimation times both for impact locations and reconstructions, an initial estimation method needs to be developed and applied. Therefore, a smooth energy distribution method with rapid and reliable computation properties is proposed to search for and identify the sensors closest to the impact positions, in order to locate the impacted regions without susceptibility from any measurement noise. This method allows one or multiple regions of sensor arrays to be formed and isolated and afterwards distributed to update the accuracy locations of impact forces. Furthermore, an estimated impact location can be updated using two solutions which are 1) Time of Flight (TOF) based quadrilateral centroid principle; and 2) minimization of the differences in the forces reconstructed from a selected triangular sensor network. The details of the impact locations estimations will be presented in this chapter.

7.1 Impact Region Extraction

An initial localization method was proposed in Si's article [2]. By comparing the energies in the chosen time windows of sensor output data, the close sensor array is determined, and the corresponding energies from the sensor signals can be calculated as,

$$E_i = \sum_{k=t_0}^{t_1} s_{\text{exp}}^2(k) \quad (7.1)$$

where E_i is the energy of the each sensor interested; s_{exp} is the experimental signal data recorded from the selected sensor; t_0 is the initial time point, and t_1 is the final time point chosen. As for the selection of the interested time window, it should be determined from a chosen sensor signal so that a sensor array close to each impact detects a great deal of energy but other sensor arrays far away detect a descending amount of energy until the amount of energy detected falls close to zero.

Once impacts occur, the energy of each sensor signal can be calculated in a chosen time window using Eq. (7.1). As a composite structure encounters an impact event and the value of the corresponding impact energy is calculated at each sensor position, a smooth energy distribution with minimum curvature can be found using the Robust Loess Smoothing method, and then the smoothed energy distribution can be expressed in terms of x and y coordinates, as follows:

$$E_i = E_i(x_i, y_i) \quad i = 1, 2, \dots \quad (7.2)$$

Using the smoothed energy distribution found in Equation (7.2), an impact location can be estimated in connection with the centroid of the corresponding impact energy. In the two-dimensional x - y coordinates system of a structure, the centroid can be given by:

$$x_c = \frac{\sum E_i \cdot x_i}{\sum E_i} \quad y_c = \frac{\sum E_i \cdot y_i}{\sum E_i} \quad (7.3)$$

where x_c is centre of the x axis, and y_c is centre of the y axis.

In experimental tests implemented, a CFRP cantilever structure was used to verify that this method provides a reliable and effective way to isolate an impacted region made up of sensor array, regardless of the conditions of vibration noise contamination. The following Figure 7.1 demonstrates the extraction of the impact region by the smooth energy distribution method proposed.

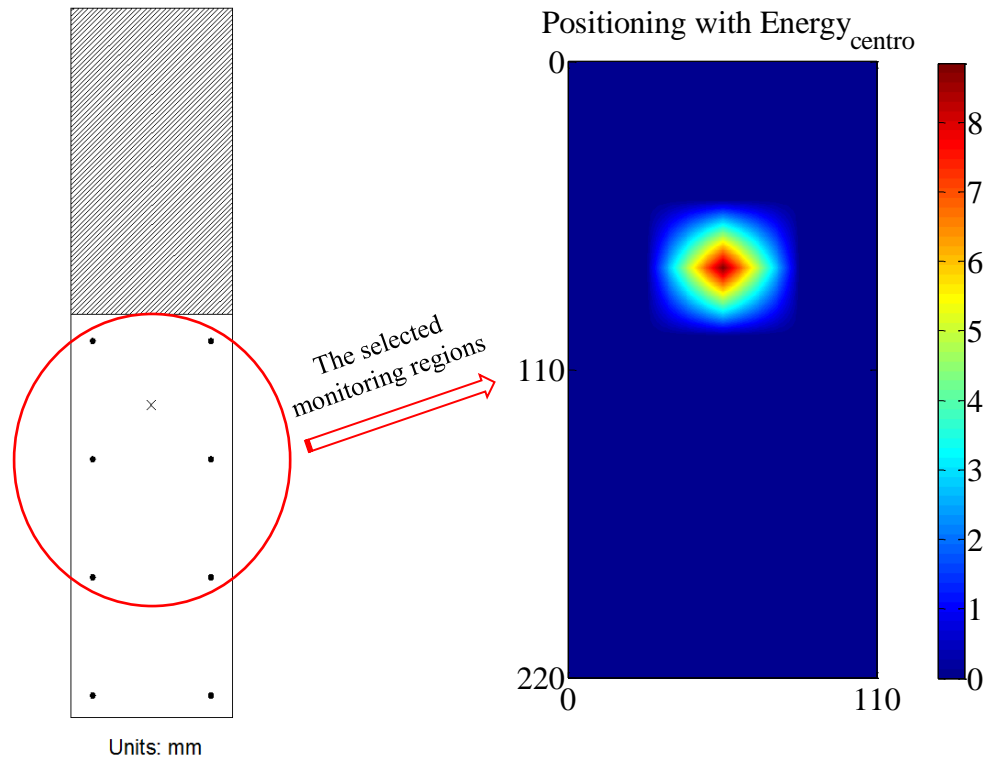


Figure 7.1 Estimation of the initial location for an impact event

7.2 Locating Impact Coordinates

The two solutions of multi-impact localizations are developed to update the precise locations of impacts acting on a laminated composite structure. The one is the quadrilateral centroid of impact localization method based on the time-of-flight; the other one is the mean cost function of impact localization method. They will be introduced in the following subsections.

7.2.1 Updating Impact Location Using the TOF Based Quadrilateral Centroid

Principle

The precise localization method was developed by Si [2]. An effective search parameter index – the Time-Of-Flight (TOF) is a significant characteristic parameter that represents the propagation of stress waves in a structure. Thus, it is often used in impact monitoring and identification schemes. The TOF between an impact location and the locations of multiple sensors is primarily dependent upon the behaviors of wave propagation in the structure, which are described in details in Appendix B.

To obtain a comparatively exact TOF, it is indispensable to get an excellent time resolution as the extraction of a correct TOF can be conducted only under a good time resolution. A stress wave resulting from an impact event generally propagates at a steady velocity in a structure, which is also dependent upon the impact conditions, e.g. the impact velocity, the impact duration, and so on. The time differences between the time histories of the impact input signal and the output sensor signals from the identified sensor region can give the time needed for the wave to propagate.

Within an identified impact zone composed of four neighboring sensors, using the initially assumed wave propagation angles θ_i , the initial distance L_i between an unknown impact position and every sensor S_i can be calculated firstly in Eq. (7.4), and four initially estimated impact positions resulting from L_i are also obtained simultaneously. Then a quadrilateral is composed of those positions. Finally, to obtain the accurate impact coordinates, a procedure to minimize the area of the dashed quadrilateral needs to be executed, as shown in Figure 7.3. A final estimation of the unknown impact coordinates can be calculated with the principle of the quadrilateral centroid, which is expressed in Eq. (7.6) and Eq. (7.7).

Then the basic formula in Eq. (7.4) is used to locate the impact force using an output signal from a single sensor.

$$L_i = C_p(\theta_i) \times \Delta T_i \quad i = 1, 2, 3, 4 \quad (7.4)$$

where L_i is referred to as the linear distance between an impact location and a specified sensor; $C_p(\theta_i)$ is the phase velocity of stress waves [92-95] that is shown in Figure 7.2 with the deflection angle of the propagation path from the impact location to the sensor S_i in a panel structure, of which the theory is described in detail in Appendix B. Solving the phase velocity of stress waves is implemented by the compiled MATLAB codes; ΔT_i is defined as the time of flight in Eq. (7.5), that is, the time difference between the acting time of an impact force and the time of arrival (TOA) recorded by a specific sensor.

$$\Delta T_i = |t_a - t_f| \quad (7.5)$$

where t_a is the time of arrival recorded by the specific sensor, and t_f is the acting time of the impact force from the reconstructed force time history.

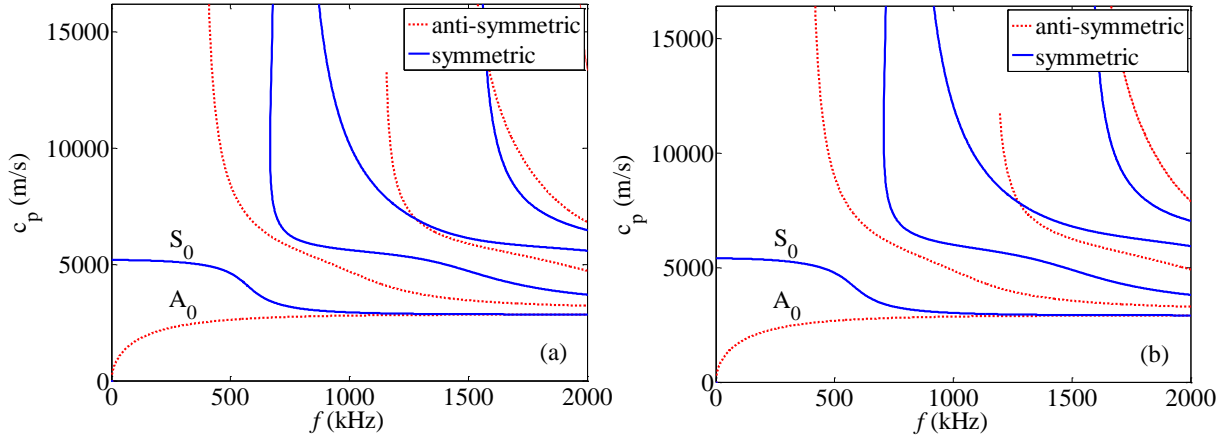


Figure 7.2 Dispersion characteristics of wave phase velocities c_p in a tested laminated composite: (a) in wave propagation of the 0° direction, (b) in wave propagation of the 90° direction.

Meanwhile, four different angles (namely $\theta_1, \theta_2, \theta_3, \theta_4$) for wave propagation directions are assumed. Additionally, ΔT_i is the time of flight for sensor S_i .

$$X_{imp} = \frac{1}{6M} \sum_{i=1}^4 (x_i + x_{i+1})(x_i y_{i+1} - x_{i+1} y_i) \quad (7.6)$$

$$Y_{imp} = \frac{1}{6M} \sum_{i=1}^4 (y_i + y_{i+1})(x_i y_{i+1} - x_{i+1} y_i) \quad (7.7)$$

where M is the area of the quadrilateral, $M = \frac{1}{2} \sum_{i=1}^4 (x_i y_{i+1} - x_{i+1} y_i)$. x_i and y_i are the x and y coordinates for the vertices V_i ($i=1, 2, 3, 4$), respectively. The entire procedure is presented graphically in Figure 7.3, and can be implemented for any configuration of a quadrilateral sensor network.

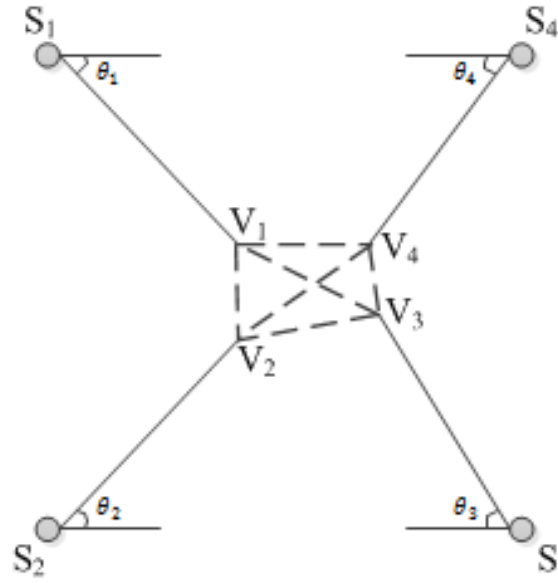


Figure 7.3 Demonstration of impact positioning procedure through updating quadrilateral

Here, it needs to be pointed out that when locating an impact force precisely, the sensor triangulation method may also be considered to utilize for the sake of simplified implementation, which will be described in the following subsection 7.2.2.

7.2.2 Updating Impact Location Using the Mean Cost Function

The other precise mean cost function (MCF) based localization method was proposed by Si [77]. The sensors with the greatest energies and the corresponding impact regions in the structure are then used to update the accurate coordinates of the impact force. Accordingly, the impact location estimated is updated by minimizing the defined mean cost function ϕ . Determining the coordinates of an impact location using the triangular sensor network selected is shown in Figure 7.4, in which the impact force is included, and each sensor has 4 effective impulse response function matrices that are from the solid discovered impact zone, that is, the small impulse response zone is composed of four IRF points shown in Figure 7.4. From an estimated impact location (x, y) , the corresponding forces F_{s_2} , F_{s_3} and F_{s_4} can be reconstructed from Sensor 2, Sensor 3 and Sensor 4 by using Equations (5.61) and (5.62). As the estimated location is closer to the real impact location, the error between each reconstructed force resulting from each sensor such as Sensor 2, Sensor 3 and Sensor 4 would decrease.

Accordingly, the precise impact location is updated using the mean cost function ϕ given by

$$\phi = \frac{1}{N_s} \left[(F_{s_2} - F_{s_3})^2 + (F_{s_4} - F_{s_2})^2 + (F_{s_3} - F_{s_4})^2 \right] \quad (7.8)$$

Once the minimized mean cost function ϕ is obtained, the estimation process of impact location coordinates is terminated, thereby the precise impact location is searched out.

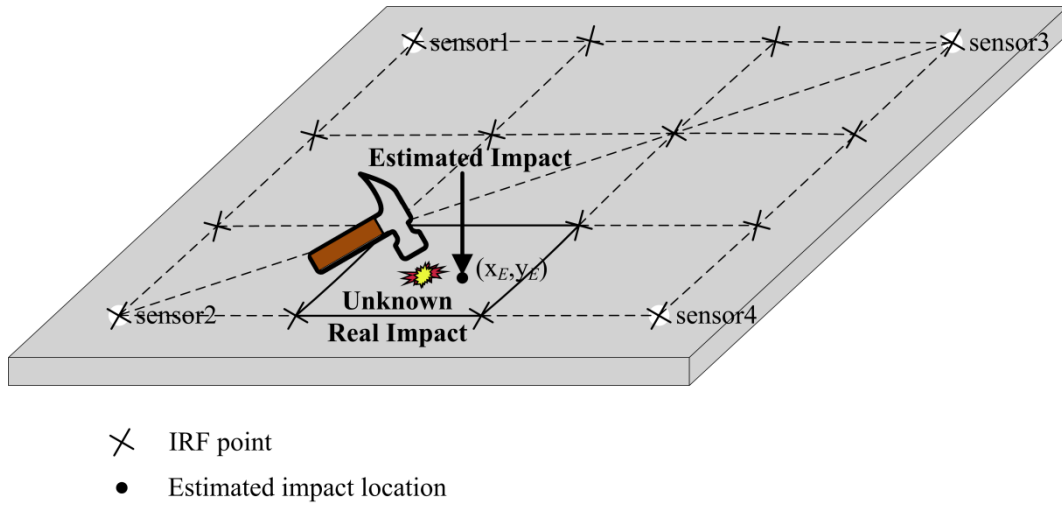


Figure 7.4 Demonstration of locating the coordinates of an impact by the mean cost function using the determined triangular sensor network

8. Piezoelectric Sensor Modeling and Calibration

With regard to the consideration of practical engineering environments, generally the consistency of the sensors attached to a structure are not comparative better, since various possible unfavorable factors come from actual environment interferences, for instance, the inconsistency of the used sensors resulting from manufacturing technology, the inconsistency of adhesive layers, the complexity of monitored structures and so on. In addition, the detrimental factors affect the evaluation precision of the ensemble impact monitoring and identification technique directly. Hence, the piezoelectric sensors used are necessary to be calibrated in order to improve the accuracies of a series of evaluations that the EIMI technique implements.

8.1 Sensor Selection and Design

It is firstly more substantial basis for impact monitoring and identification to select the appropriate sensor material, design the rational shape, and to determine the applied sizes. The model design for the sensor used is shown in Figure 8.1. However, to measure the voltage value from a sensor, an equation is given by

$$V_{S_i} = \frac{t_s}{d_{31}} \frac{1}{(1-\nu)} (\varepsilon_{xx} + \varepsilon_{yy}) \quad (8.1)$$

where,

V —sensor voltage

t_s —the sensor thickness

d_{31} — Piezoelectric charge constant

ν — Poisson's ratio

ε_{xx} —strain in X direction

ε_{yy} —strain in Y direction

Then, the prototype of one type of used sensors is illustrated in Figure 8.2. The small circular piezoelectric wafer sensors (PEWS, which were customized specially from PI Ceramic GmbH) were designed by me and employed to measure the non-directional strain variation, and the sensors were poled in the Z -direction. The combination of strains, $\varepsilon_{xx} + \varepsilon_{yy}$, is a two-dimensional strain invariant. Thereby, the strain measurement is independent, because it is not altered as the orientation of the coordinate system is varying. This can be certified using the two-dimensional strain transformation tensor.

$$\begin{bmatrix} \varepsilon'_{xx} \\ \varepsilon'_{yy} \\ \varepsilon'_{xy} \end{bmatrix} = \begin{bmatrix} \cos^2 \theta & \sin^2 \theta & \cos \theta \sin \theta \\ \sin^2 \theta & \cos^2 \theta & -\cos \theta \sin \theta \\ -2 \cos \theta \sin \theta & 2 \cos \theta \sin \theta & \cos^2 \theta - \sin^2 \theta \end{bmatrix} \begin{bmatrix} \varepsilon_{xx} \\ \varepsilon_{yy} \\ \varepsilon_{xy} \end{bmatrix} \quad (8.2)$$

where θ is the angle of coordinate rotation.

The strain combination is then

$$\varepsilon_{xx} + \varepsilon_{yy} = \varepsilon'_{xx} + \varepsilon'_{yy} \quad (8.3)$$

The quantity of the two-dimensional strain is not changed as the coordinate system rotates. By using the non-directional constraint of the strain measurement of structural responses provided by the PEWS, the circular piezoelectric wafer sensor simplifies the solution process for the inverse problem of impact identifications.

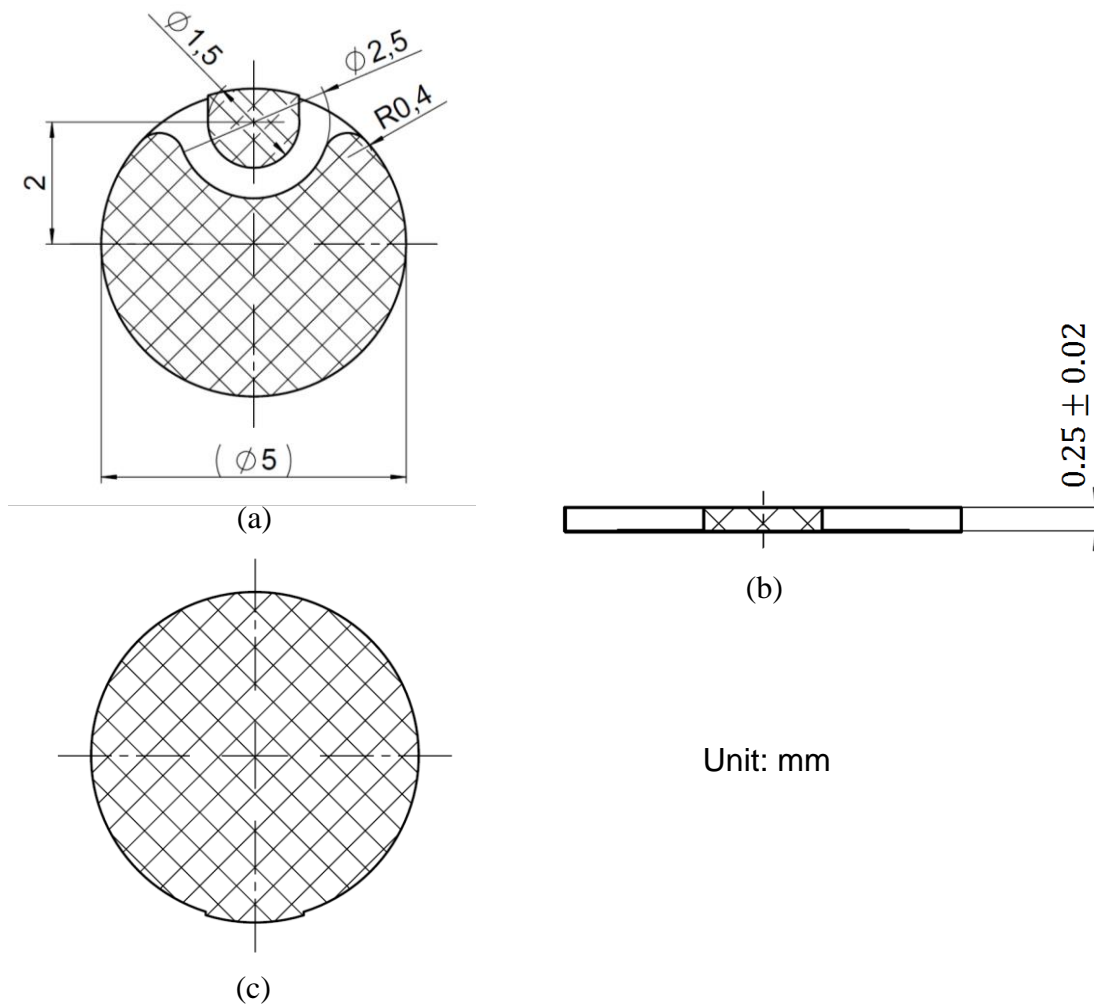


Figure 8.1 Model diagram of sensor design: (a) the anode surface of the circular piezoelectric sensor, (b) the thickness of sensor, and (c) the cathode surface of the circular piezoelectric sensor.

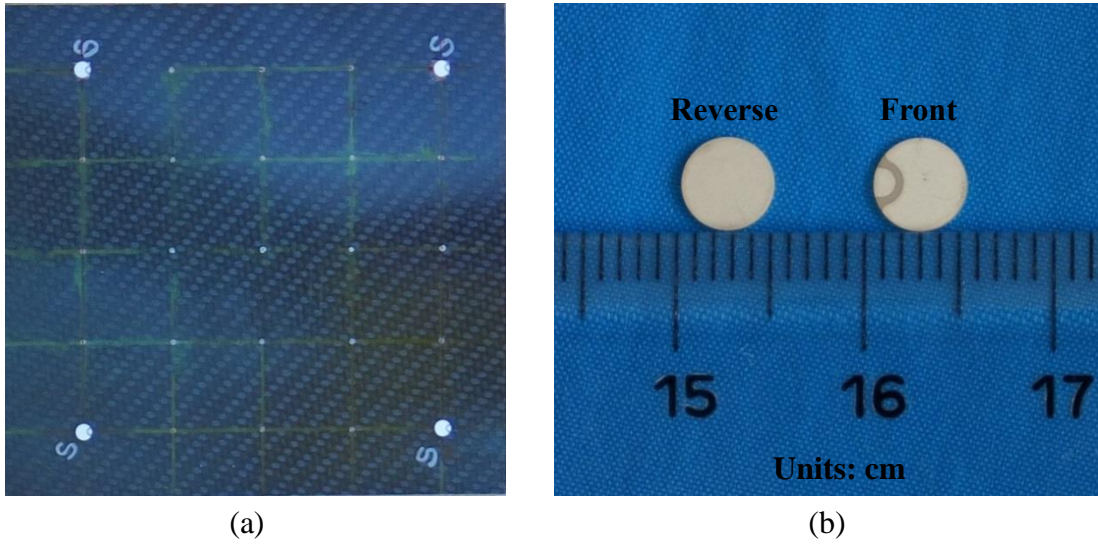


Figure 8.2 Piezoelectric disc sensors used to measure strain data: (a) sensors mounted on a CFRP structure, (b) sensor prototype.

8.2 Sensor Modeling

In view of Eq. (8.1), by combining the contributions of all the constants into a gain constant g , a simplified expression is obtained as follows,

$$V_{s_i} = g (\varepsilon_{xx} + \varepsilon_{yy}) \quad (8.4)$$

Using the kinematics of classical plate theory

$$V_{s_i} = g \frac{h}{2} \left(\frac{\partial^2 \mu}{\partial x^2} + \frac{\partial^2 \mu}{\partial y^2} \right) \quad (8.5)$$

and rewriting in terms of the generalized displacement leads to

$$V_{s_i} = g \frac{h}{2} \left(\frac{\partial^2 \phi}{\partial x^2} + \frac{\partial^2 \phi}{\partial y^2} \right) \varpi \quad (8.6)$$

Finally, writing in terms of the modal displacements, and defining \mathbf{C} as the matrix that transfers the displacement vector to the sensor measurements vector [96]:

$$V_{s_i} = g \frac{h}{2} \left(\frac{\partial^2 \phi}{\partial x^2} + \frac{\partial^2 \phi}{\partial y^2} \right) V \bar{\mu} \quad (8.7)$$

$$V_{s_i} = C_i \bar{\mu} \quad (8.8)$$

$$C = \begin{bmatrix} C_1 \\ C_2 \\ \vdots \\ C_{Nsensors} \end{bmatrix} \quad (8.9)$$

This expression is unchanged once the calculations are executed in the discrete time.

Figure 8.3 indicates the procedure of sensor modeling and reveals the hidden relation between mechanics and electronics from the piezoelectric principle of piezoceramic sensors, which is a variation of electric charge density in response to applied mechanical stress.

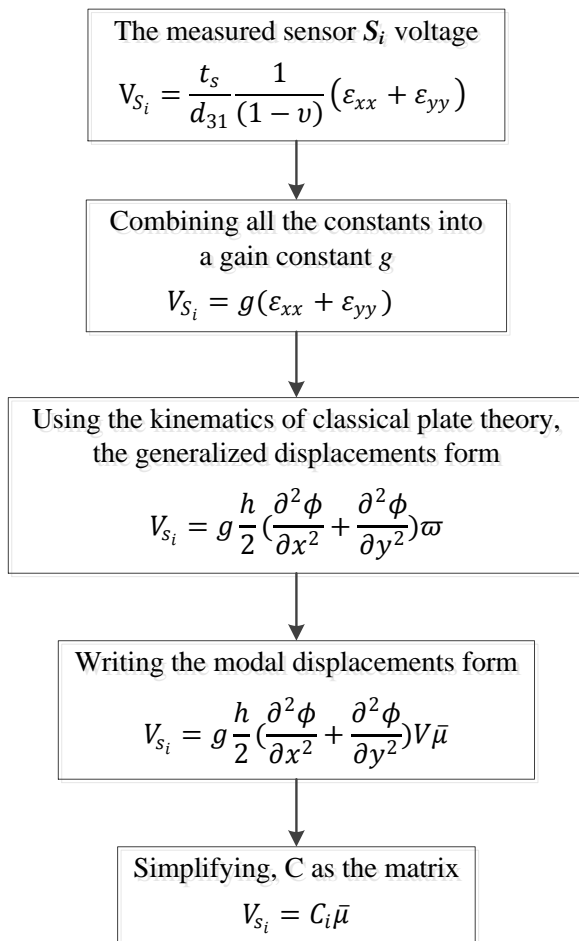


Figure 8.3 Flowchart of Sensor Modeling

8.3 Sensor Calibration

8.3.1 Calibration from Theoretical Calculation

The impedance modeling method is proposed and applied in the calibration procedure of different sensors. A mutation in a sensing response results from any variation in the electrical impedance signature.

Since every sensor is usually mounted onto a host structure, a high-strength adhesive material needs to be employed to ensure a better mechanical interaction between sensors and the structure, which is illustrated in Figure 8.4. Thus, we should consider the effect of bonding layers, and also build an electro-mechanical impedance model.

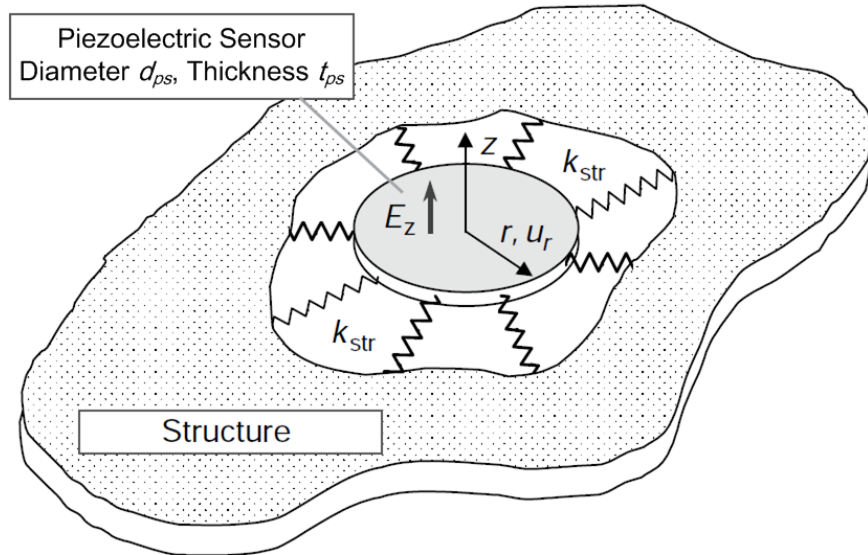


Figure 8.4 A circular PZT sensor constrained by structural stiffness k_{str} [97]

To solve this problem, the equation of the frequency-dependent electrical admittance [98, 99] is derived by

$$Y(\omega) = Z^{-1}(\omega) = \frac{1}{R} + j\omega p \left(\varepsilon_{31}^{\sigma} - d_{31}^2 \lambda_{11}^E + \frac{d_{31}^2 \lambda_{11}^E Z_a}{Z_p + \gamma Z_s} \frac{tg(kl)}{kl} \right) \quad (8.10)$$

where,

Y : the electrical admittance (the inverse of impedance);

Z_p : PZT's mechanical impedance;

Z_s : the structure's mechanical impedance;

d_{31} : Piezoelectric coupling constant at zero stress;

ε_{31}^σ : Dielectric constant at zero stress;

p : geometric constant of the PZT;

$$\text{Coefficient } \gamma = \frac{1}{1 + K_s / K_b};$$

$$K_s = -m_s \omega^2 + j\omega C_s + k_s;$$

$$K_b = -m_b \omega^2 + j\omega C_b + k_b;$$

$$k^2 = \frac{\rho \omega^2}{\lambda_{11}^E}; \rho \text{ is the density, } \lambda_{11}^E \text{ is the elastic modulus under a constant electric field.}$$

As regarding the coefficient γ , it can be also represented as follows,

$$\gamma = \frac{1}{1 + K_s / K_b} = \frac{1}{1 + C_1 / \overline{PZT}} \quad (8.11)$$

where $\overline{PZT} = \frac{w_{PZT} G_b}{Z_s h_b j\omega}$, C_1 is constant number.

Obviously, the thickness and shear modulus of bonding layer affect the value of K_b significantly. From the equation (8.10), it represents that as γ decreases, the electrical impedance of the sensor decreases and is directly associated with the mechanical impedance of a host structure. On the contrary, from the equation (8.11), as γ increases, the thickness of bonding layer h_b decrease. However, the impedance of the host structure is always multiplied by a coefficient γ which includes the bonding layer's dynamic stiffness. While, if $\gamma = 1$, the bonding layer has no effect on the impedance and it happens only in the case of perfect bonding when $K_s/K_b = 0$, i.e. $K_b \gg K_s$.

The shear lag effect on sensor response, the function of the shear lag parameter is described as follows,

$$\Gamma^2 = \frac{G_b}{E_{PZT} h_b h_{PZT}} + \frac{3G_b w_{PZT}}{E_s w_s h_s h_{PZT}} \quad (8.12)$$

where,

G_b : shear modulus of bonding layer;

E_s : Young's modulus of plate;

E_{PZT} : Young's modulus of PZT sensor.

As the shear lag effect results in the different strains from between the PZT sensors and the host structure, a PZT sensor would produce less and untrue voltage across its terminals under the imperfect bonding condition. To quantify the effect of shear lag, the valid length l_{eff} of a sensor is defined as follows,

$$\frac{l_{eff}}{l_1} = 1 - \frac{\tanh\left(\Gamma l_1 \frac{1}{2}\right)}{\Gamma l_1 \frac{1}{2}}, \quad \text{where } l_1 = \frac{l}{2} \quad (8.13)$$

It shows that as h_b increases, the shear lag effect increases and the valid length decreases.

With respect to the sensing calibration of sensor response for the impact identification, the difference in impedances could be related to the difference in sensor responses. Therefore, we should define the difference in impedances between two sensors as impedance gain factor (IGF) to calibrate sensors; the equation is represented as follows,

$$IGF = \frac{1}{N} \sum_{i=1}^N \frac{Z_c(i) - Z_0(i)}{Z_0(i)} \quad (8.14)$$

where, N is the number of frequency recorded, Z_0 is the impedance of the reference sensor, Z_c is the impedance of a sensor to be calibrated.

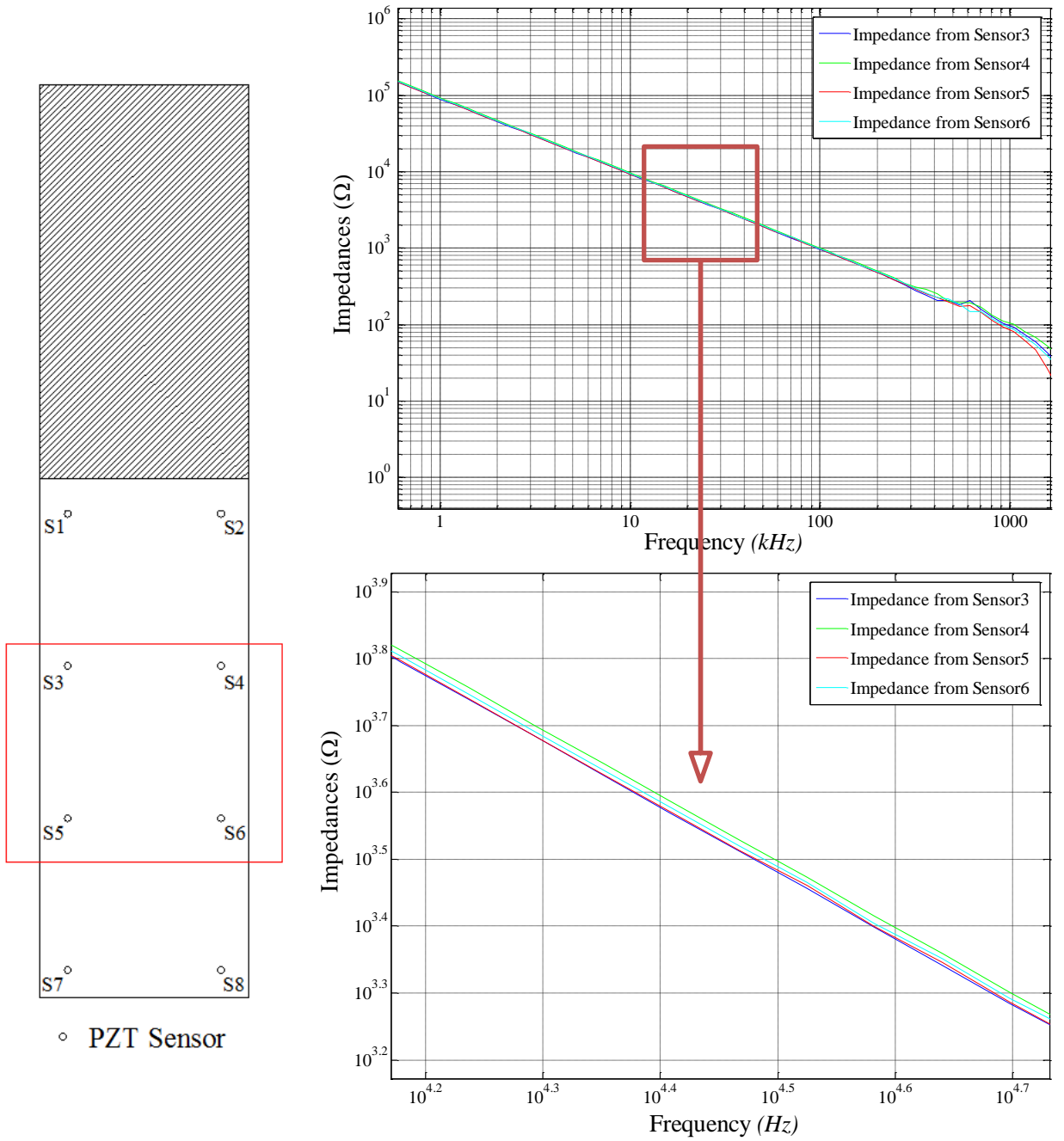


Figure 8.5 Impedances from different sensors

Furthermore, the difference in sensor responses (DSR) can be expressed in terms of the ratio of the valid length between two sensors,

$$DSR = \frac{\left(\frac{l_{eff}}{l_1} \right)_C - \left(\frac{l_{eff}}{l_1} \right)_0}{\left(\frac{l_{eff}}{l_1} \right)_0} \quad (8.15)$$

Normally, a given sensor S_c can be calibrated as follows,

$$S_c = (1 + DSR) \times S_o \quad (8.16)$$

where S_c is the response of the calibrated sensor, S_o is the response of the reference sensor.

8.3.2 Calibration under In-Situ Conditions

In order to overcome three practical engineering problems met, an alignment method of anti-symmetric impacts which calibrates the sensors mounted on a complex structure such as a stiffened structure is proposed to further improve the accuracy and reliability of impact location and identification. The three thorny engineering problems are as follows:

- 1) The inconsistency of adhesive layers due to sensor installation technology limitation, as shown in Figure 8.6;
- 2) Complex structure components from a real aircraft structure, as demonstrated in Figure 8.7a;
- 3) Asymmetrical sensors layouts on a structure component, as also shown in Figure 8.7b.

Then, a sensor S_1 with better waveform is set as the standard sensor; the other sensor S_2 is referred as the original sensor that will be calibrated, which are presented in Figure 8.7. Through utilizing the alignment method defined in equations (8.17), (8.18) and (8.19), the calibrated result fall well within the satisfactory range, and the calibrated signal from sensor S_2 is so closed to the standard signal from sensor S_1 , which is illustrated in Figure 8.8. Furthermore, the alignment method has been used successfully, the consistencies of sensors' performances are improved, and the accuracy of impact location and identification is also enhanced effectively.

$$C = \int_{t_0}^{t_n} |s(t)| dt \quad (8.17)$$

According to the linear relationship between input force and output response, it assumes that the impact forces F_i and F_j are imposed at a same position, and the waveforms from both forces are similar but just the amplitudes are different, the ratio of force signals from the impacts F_i and F_j is thus equal to the ratio of the response signals from the sensor outputs S_i and S_j . The correction expressions are given by,

$$\frac{C_{f_i}}{C_{f_j}} = \frac{C_{ii}}{\sigma \cdot C_{jj}} = \frac{\sigma \cdot C_{ij}}{C_{ji}} \quad (8.18)$$

$$\sigma = \sqrt{\frac{C_{ii} \cdot C_{jj}}{C_{ij} \cdot C_{ji}}} \quad (8.19)$$

where C is the integral of the absolute value of a sensor signal in the limited time range $[t_0, t_n]$. Then on the basis of the above example, the impact forces F_1 and F_2 were imposed at the two anti-symmetric positions, thus C_{ij} means that the integral of the response signal from sensor j due to the impact F_i . $s(t)$ is a time domain signal from a sensor. t_0 is the start time determined, t_n is the end time determined. σ is a correction coefficient used to be multiplied by the original signal s_o , finally to obtain the calibrated signal s_c .

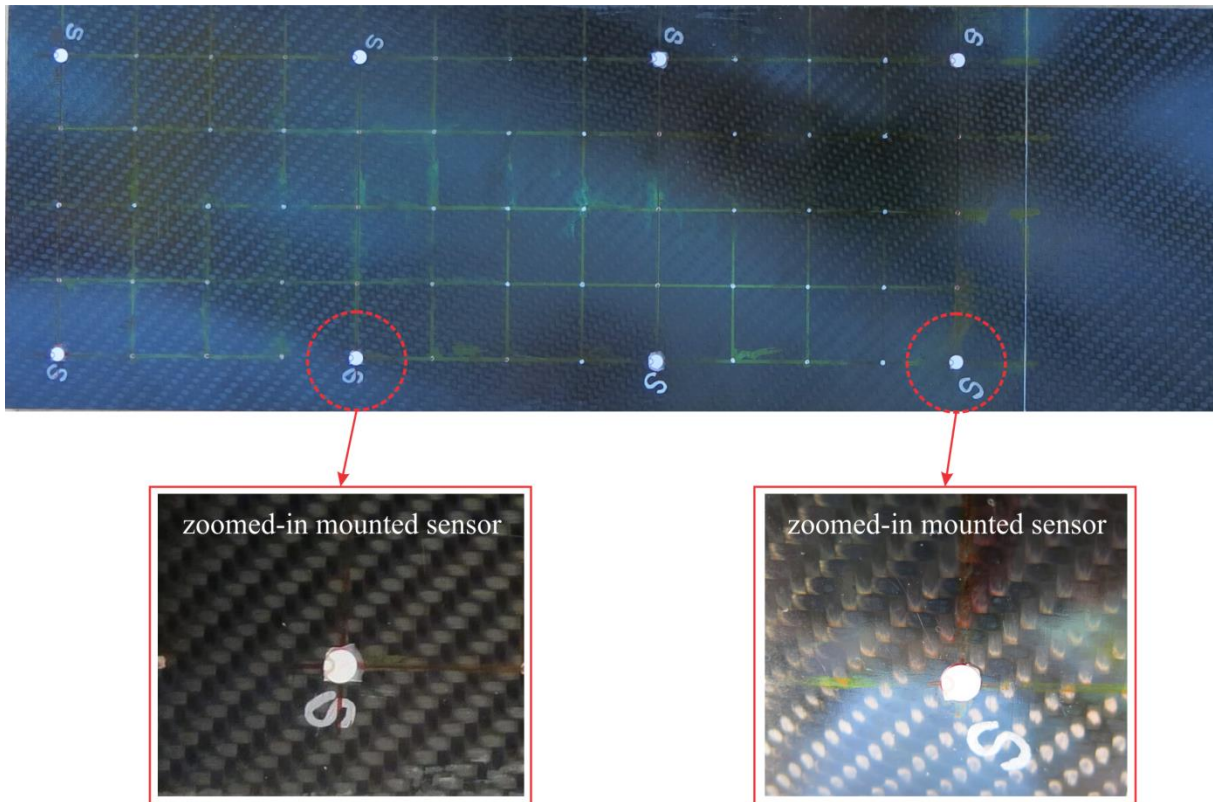


Figure 8.6 Piezoelectric sensors mounted on the bottom surface of a CFRP Panel: (left) undesirable adhesive layer, (right) perfect adhesive layer.

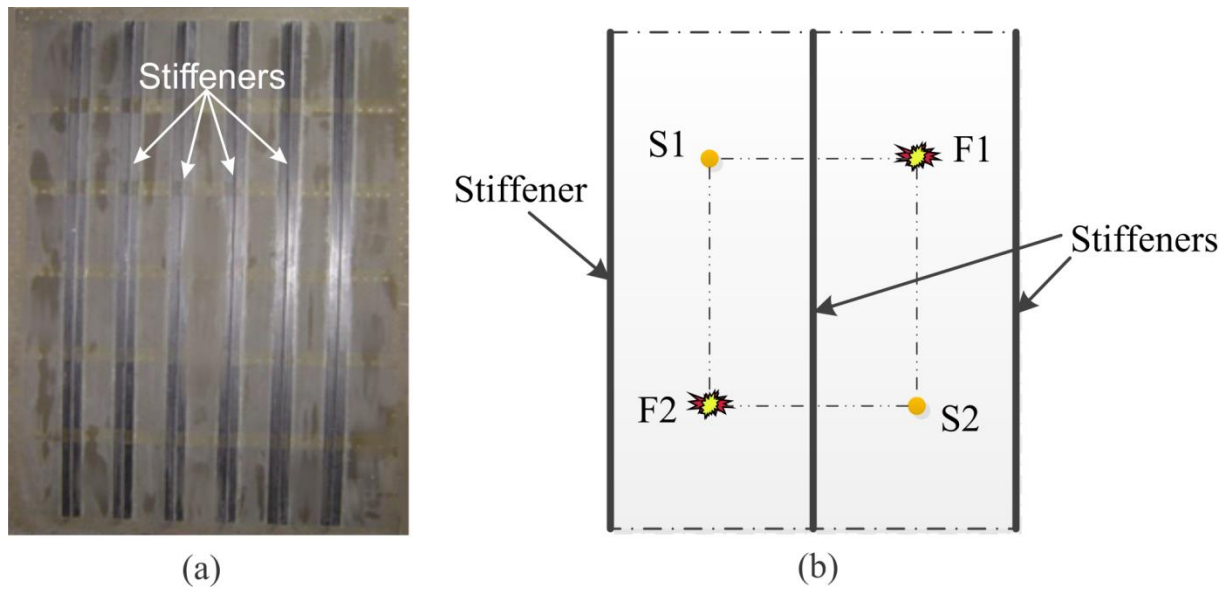


Figure 8.7 Asymmetrical sensor layouts on a real aircraft panel component with multi-stiffeners: (a) a complex structure component with multi-stiffeners, (b) asymmetrical sensor layouts on the panel structure.

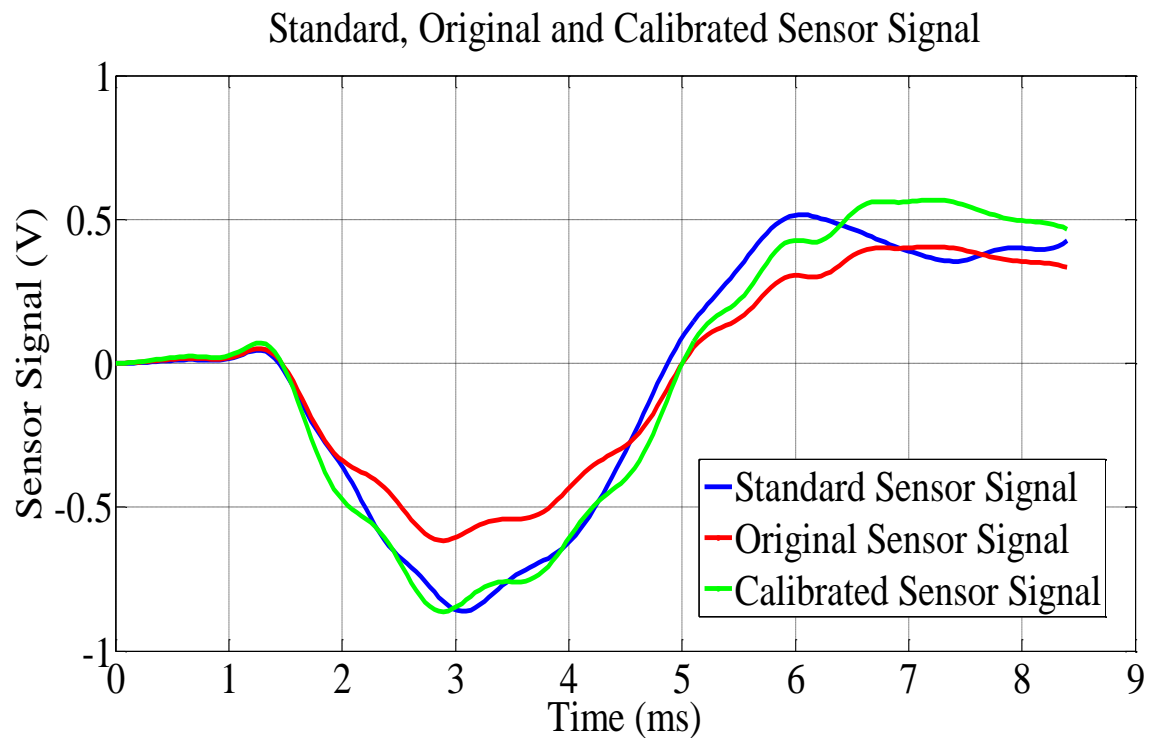


Figure 8.8 Comparison of original and calibrated sensor signals

8.4 Discussion

The importance and indispensability of sensing calibrations should be paid more attention, as sensing calibrations are very significant to guarantee the reliability and robustness of health monitoring of a structure. In other words, the sensing calibration (or compensations of condition (COC)) is an essential functional component for an integral structural health monitoring technique (or system). In particular, compensations of conditions must be done for aging aerial structures and under adverse environments. For instance, for an aging aerial structure, strain compensations to the used sensors should be conducted as plastic deformations have already occurred in the aging structure; and under varying temperatures, compensations of temperatures should be executed obviously. With regard to temperature compensations, it will be set as a future research direction, which is carried out by us.

9. Experimental Tests

With the use of the theoretical development and computer implementation of the ensemble impact monitoring and identification technique, the next step is setting up the experimental tests for several particular practical applications. The experimental tests were conducted on the three different CFRP panel structures. Among them, specimen 1 is a narrow CFRP plate without any stiffener; specimen 2 is a square CFRP panel fabricated with an I-crossbeam stiffener trans-laying the length of the panel; and specimen 3 is a CFRP plate with a cutout hole.

Nevertheless, there were three laminated composite panels prepared to use in the validation tests of the rapid multi-damage identification approach. One is a perfect laminated composite fabricated without any damage; another one is the same dimensions of laminated composite fabricated with a single delamination; the other one is also the same dimensions of laminated composite plate fabricated with multiple delaminations.

9.1 Experimental Specimens

Specimen 1 as shown in Figure 9.1 is a CFRP plate with 660 by 150 by 5 mm³ sizes, and its layups are given in Table 9.1.

Specimen 2 as illustrated in Figure 9.2 is also a CFRP panel fabricated with an I-crossbeam stiffener trans-laying the length of the specimen, and its sizes are 390 by 390 by 3 mm³. The sensor interval is shown in Figure 9.2 too. The location of the ply groups is shown in Figure 9.4, and the layups for each ply group are given in Table 9.2.

Specimen 3 as shown in Figure 9.3 is similar to specimen 1, and it owns the same sizes and layups with specimen 1. But the structure of the plate is a little more complicated than that of specimen 1, because that it is an inhomogeneous structure with the surfaces of orange peel, where it owns a circular cutout hole in the plate as shown in Figure 9.3.

Two kinds of distributed piezoelectric sensory networks and associated wiring were installed individually on the backward surfaces of the three CFRP panel structures, which are considered from the perspective of practical engineering demands and are also convenient to impacts on the forward surfaces of three CFRP panels with an instrumented hammer and several small balls. In order to guarantee the good surface conduction at sensor positions, the structural surface areas at the sensor positions were polished smooth, and a small amount of conductive epoxy adhesive was utilized to bond sensors on the structural surfaces.

In addition, as for specimen 2, since the stiffener's property is defined approximately in the FE model, the FE model could not simulate precise response outputs from the stiffener area or nearby it. The stiffener area is more rigid than the bay areas, as the rib and flange sections can absorb more mechanical affords. Therefore, the sensors placed in the bays on specimen 2 may be more sensitive to the stress waves resulting from impacts. Accordingly, in regard to impact monitoring and identification experiments on complex structures, it is better that all sensors are placed in the bays on the stiffened panel structures, which is illustrated in Figure 9.2. However, as for specimen 1, the sensor interval is determined easily as 110 by 110 mm², as shown in Figure 9.1.

In the validation tests of multi-damage identifications, three fabricated laminated composite plates with same dimensions and same carbon fiber layups and epoxy matrix were used to conduct the experimental tests of damage identifications. However, there exist the differences of the mechanical performance among the three laminated composite specimens, which are separately intact (non-damage), single delamination, and three different diameters of delaminations. The tested composite specimens were fabricated using the carbon-fiber prepreg laminates T700S/E022, and with the stacking sequence of

$(0^\circ/90^\circ)/[0^\circ/90^\circ]_s/(0^\circ/90^\circ)$. And the dimensions of the laminated composite specimens are all 750 mm length, 400 mm width and 4 mm thickness. In the two delaminated composite plates, a different type of material patch – the circular Teflon patch was employed to seed as the delamination, and the implanted Teflon patches were seeded in the middle layer of the tested composite plates, which are located in between a 90° and a 0° plies. For the laminated composite specimen with a single delamination, the diameter of the delamination is 1.9 cm. Nevertheless, the diameters of the three delaminations seeded in the other laminated composite specimen are sequentially 1.0 cm, 1.9 cm and 3.0 cm. To demonstrate the profile of the laminated composite plates, the dimensions of one of the composite plates is presented in Figure 9.5.

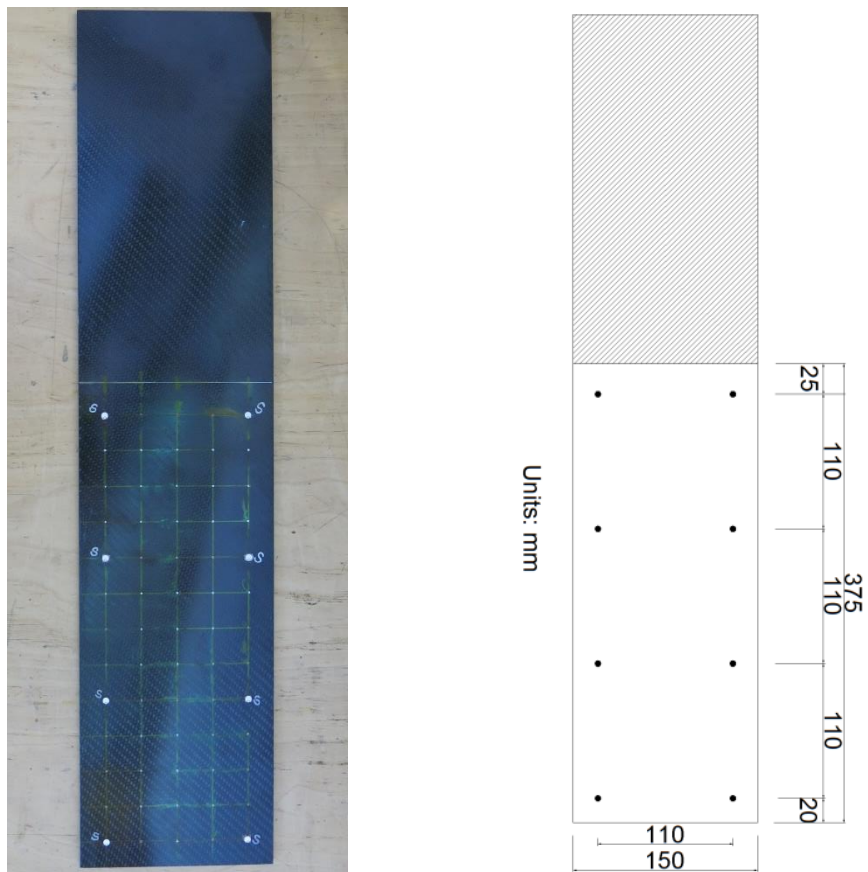


Figure 9.1 Geometry of the CFRP plate (Specimen 1) and its sensor layouts

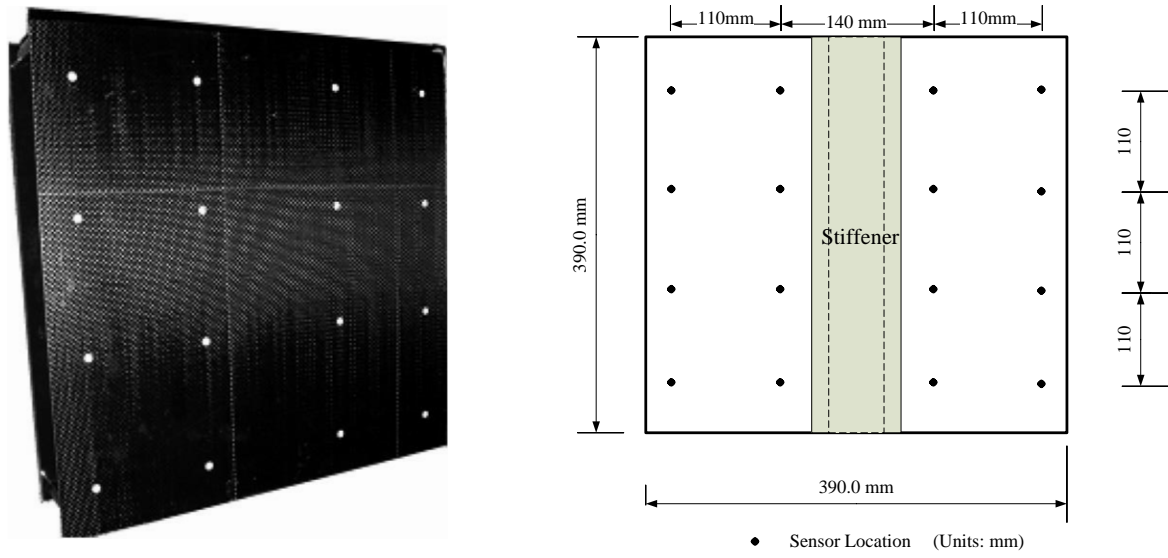


Figure 9.2 Geometry of the stiffened CFRP panel (Specimen 2) and its sensor layouts

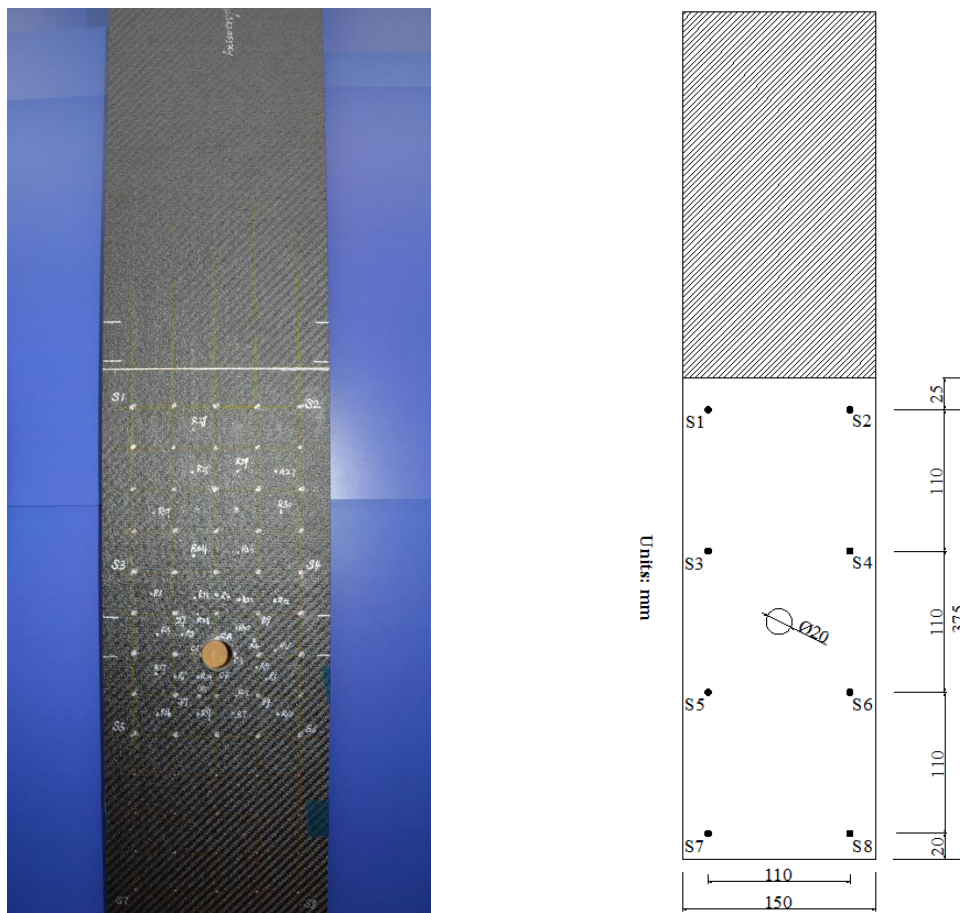


Figure 9.3 Geometry of the CFRP plate (Specimen 3) and its sensor layouts

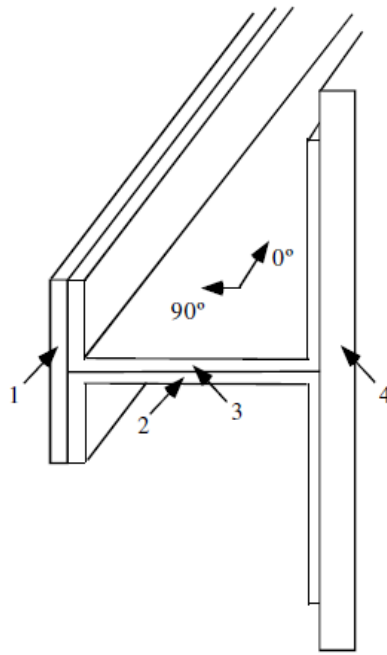


Figure 9.4 Location of layup groups for specimen 2 and the indicated axes on the rib

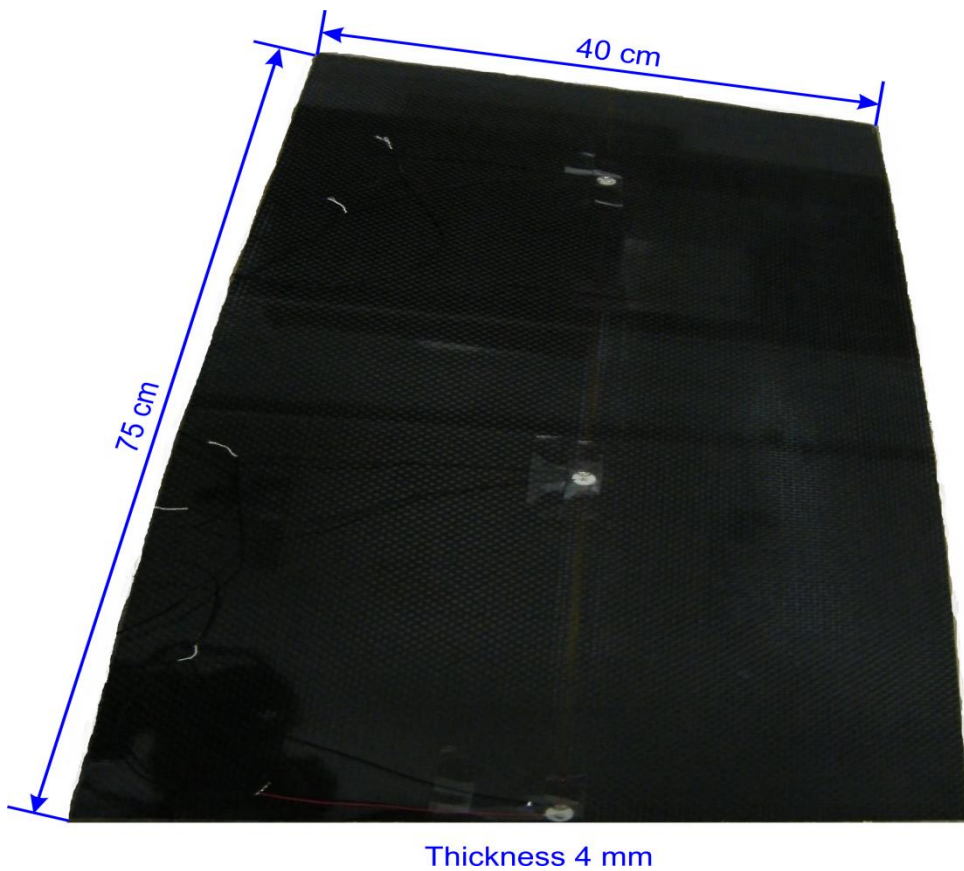


Figure 9.5 Demonstration of the dimensions of a laminated composite specimen used to validate damage identifications.

Table 9.1 Group layups for specimen 1

Location	Layup
Plate body	$[0^\circ, 90^\circ]_w/[0^\circ/90^\circ]_s/[0^\circ, 90^\circ]_w$

Table 9.2 Group layups for specimen 2

Ply Group	Location	Layup
1	Cap	$[0^\circ/45^\circ/-45^\circ/90^\circ]_3$
2, 3	Connection Part	$[0^\circ/90^\circ]_s$
4	Base	$[0^\circ/45^\circ/-45^\circ/90^\circ/0^\circ/45^\circ/-45^\circ/90^\circ]_s$

9.2 Experimental Setup

Three CFRP panel structures were impacted using a hand-held, instrumented hammer manufactured by PCB Piezotronics [100]. Both the impact force signals from the impact hammer and the sensors output signals from the structural responses were collected by a computer data acquisition (DAQ) system manufactured by Labortechnik Tasler. Also, a function/arbitrary waveform generator and a power amplifier were utilized to generate a series of repetitive random interfering noises. Since all impact cases considered were designed as low-velocity impact experiments, the sampling rates from 25 kHz to 50 kHz were thus collected, and all collected sensor response data were in the range of ± 15 V.

Meanwhile, specimen 1 was clamped and fixed on one side and the other side was free, which was built as a cantilever structure shown in Figures 9.6 and 9.7. Specimen 2 was supported by 4 columns at the corresponding 4 corners separately, as illustrated in Figure 9.8. And as for specimen 3, it was structured same as the support method of specimen 1, the configuration of the experimental setup is presented in Figure 9.9.

Moreover, specimen 1 was used to verify the different forward models constructed from the built FEM training and experimental training approaches, to evaluate the impact location estimations, and to assess the impact identification applicability of the ensemble impact monitoring and identification approach, which can be competent to the variety of external disturbed conditions such as random noises resulting from mechanical vibration actions. Specimen 2 was used to validate and evaluate the performance of the ensemble IMI approach through varying composite layup groups, various structure configurations and diverse types of

impactors. Then, specimen 3 was also used to verify and assess the performance of the ensemble impact monitoring and identification approach from the viewpoint of an inhomogeneous structure such as a cantilever composite structure with a cutout hole in its structural body.

The three laminated composite specimens were instrumented with the designed piezoelectric wafer transducer arrays (PWTAs), of which each transducer array was composed of a specified PZT actuator and the remaining PZT sensors. In the used PZT transducer arrays, the profile of each transducer is a circular wafer, and its diameter is 6 mm. On the three experimental specimens, a transducer was always specified as the actuator and was mounted at the bottom edge on the surface of the composite specimens. The function of an actuator is to excite the tested composite specimens with the defined interrogating Lamb waves.

It is illustrated in Figure 9.10 that the instrumented laminated composite plate with the three delaminations of 1.0 cm, 1.9 cm, 3.0 cm diameters was bonded with the designed PZT wafer transducer array. And a zoomed-in ultrasonic phased image for the multiple delaminations region in the tested composite plate is also shown in Figure 9.10b, which is captured partially from the full-scale phased image of the ultrasonic scan.

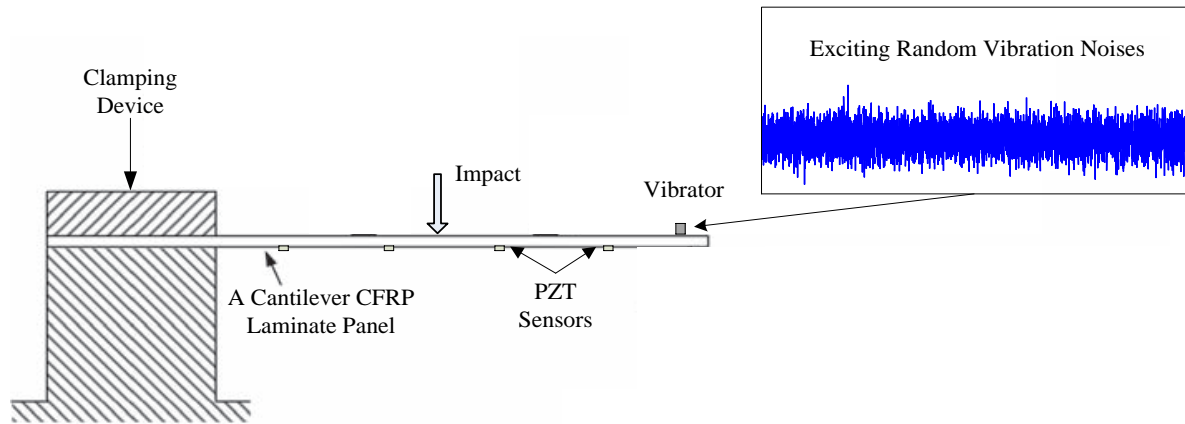


Figure 9.6 Schematic diagram of impact tests on specimen 1



Figure 9.7 Experimental setup of vibration configuration on specimen 1

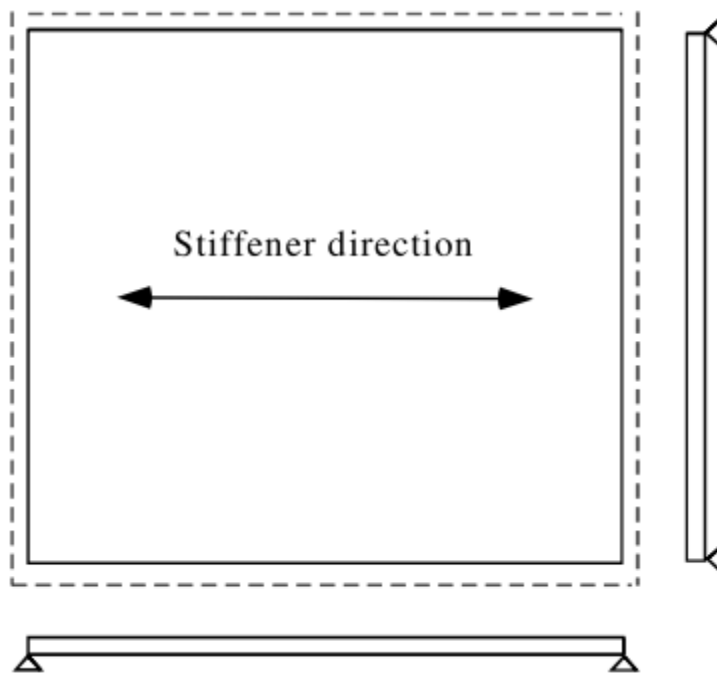


Figure 9.8 Configuration for Boundary conditions on specimen 2

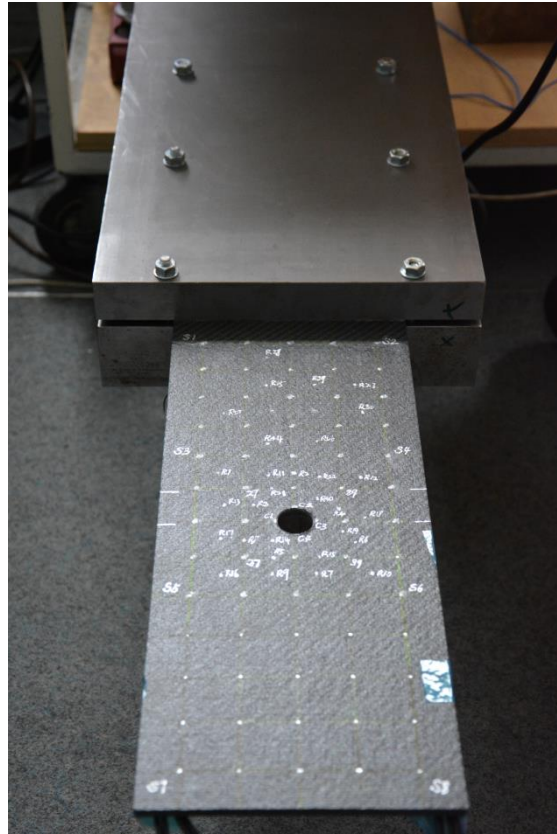


Figure 9.9 Experimental setup configuration for specimen 3

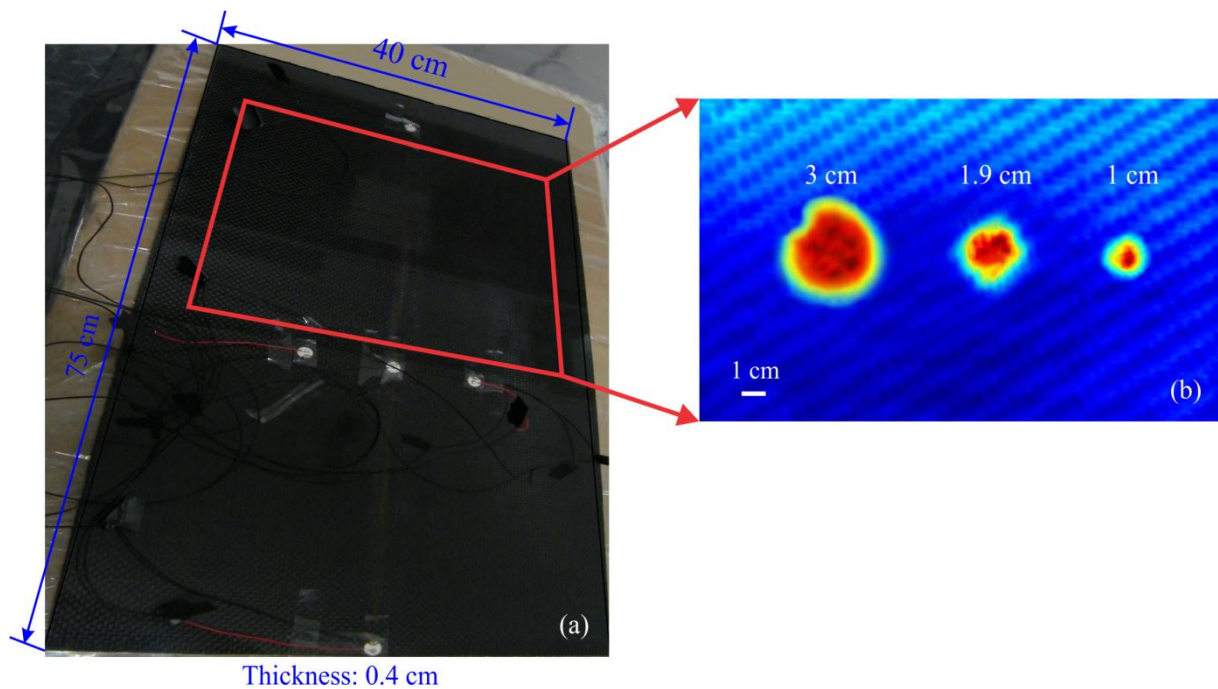


Figure 9.10 An instrumented laminated composite specimen with three seeded-in delaminations: (a) the instrumented composite plate with the designed piezoelectric wafer transducer array, (b) a zoomed-in ultrasonic phased image of the multi-delaminations region.

In addition, from Figure 9.10, it can be seen that the actuator creates a moment on the tested composite plate. This moment loading produces bending waves used to locate and quantify the multi-damage in the composite plate structure. The three sensors in the designed PZT transducer array were bonded in the middle zone between the actuator and the multiple delaminations, and the remaining sensor was then laid out in the behind zone of the three delaminations. The designed piezoelectric wafer transducer array on the validated composite plate made up of four circular sensor elements and an actuation element.

9.3 Experimental Tests

Before unknown random impact events were implemented, a little training work of impacts on a structure had to be performed to obtain the experimental functional-network of impulse response function matrix cover the whole panel structure. Once the corresponding network made up of the IRF nodes to a structure was found individually, various impact experimental tests could be made on any arbitrary location on the structure. A demonstration with an unknown impact event on specimen 1 is illustrated in Figure 9.11 to indicate the ensemble IMI approach online visualization and automation.

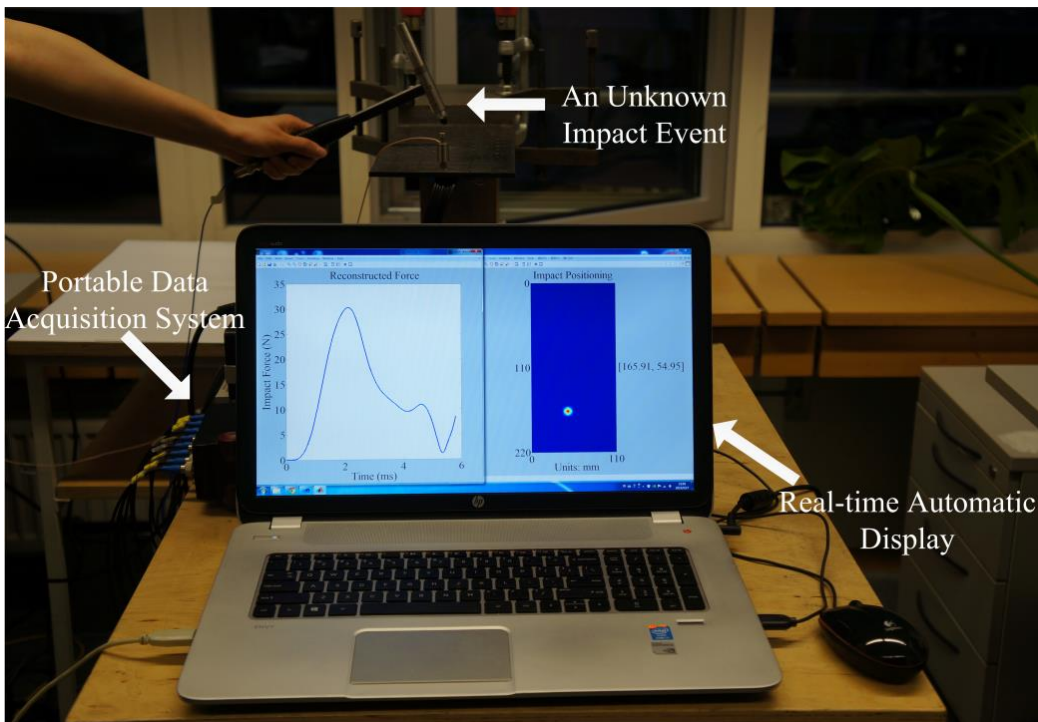


Figure 9.11 Real-time visualization inspection for an unknown impact event

However, in order to obtain the various functional-network of IRF matrices, the training work of impacts was implemented on all tested composite structures. And the details will be described in the following subsections.

9.3.1 Specimen 1 – A Normal Panel

In order to obtain the experimental impulse response functions network, a series of the point-contact impact tests were performed cover the whole panel structure.

Furthermore, to make up the network nodes of the IRFs and validate the qualities of the corresponding impulse response functions, impact force signals and sensor signals from the structural responses were collected from 65 positions of impact training on specimen 1 as shown in Figure 9.12, where the experimental impact points were laid at uniformly spaced positions, and random force magnitude was applied at each position.

Once the corresponding network made up of the IRF nodes to specimen 1 is found, various impact cases with unknown force magnitudes can be implemented on any arbitrary (unknown) location on specimen 1. Also, a series of verifications on impact identifications can be implemented effectively.

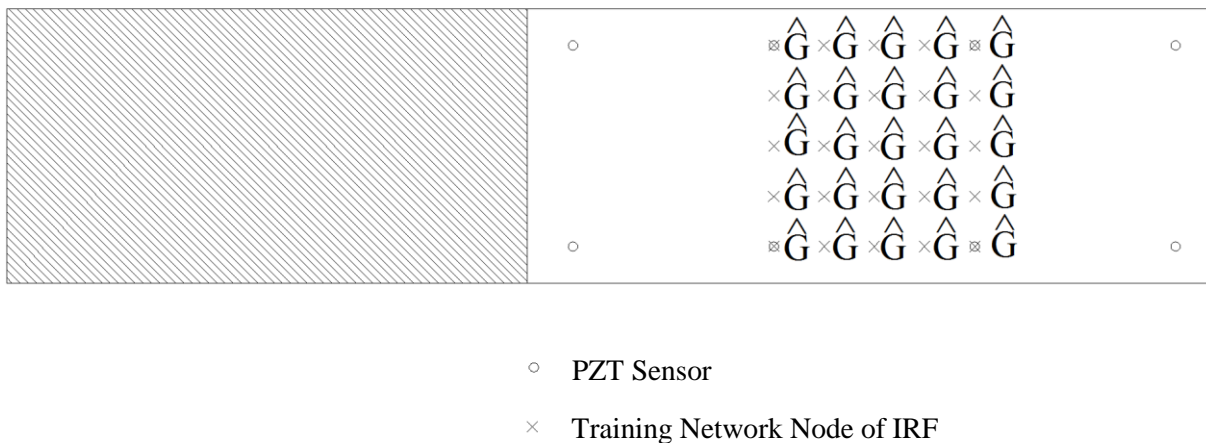


Figure 9.12 Demonstration for the formation of IRFs network on specimen 1

9.3.2 Specimen 2 – A Stiffened Panel

A stiffened panel as specimen 2 can be divided into two different identification regions for generation of an accurate network of impulse response functions, where they are one stiffener region and two bay regions. Each region needs at least four points of impulse response functions to reconstruct a real impact force using Gauss-Newton Optimization and Interpolation method as Eq. (6.13). Due to the structural symmetry property of this panel, the entire impulse response functions network sets of two different identification parts that are 1) the stiffener section and 2) the bay part could overlay the entire panel structure including the boundary region, where the bay section adopted one of two bay regions to build up the

impulse response functions. Furthermore, because of the structural symmetry property in any direction that is x-axis or y-axis, thus, we simplify to consider that only estimated results for the bottom right side of specimen 2 are analyzed in the evaluation procedures of impact localization and identification, and which can represent of the dynamic responses of the whole panel. All in all, the integrated network of impulse response functions for a stiffened structure was obtained from the numerical results calculated at 40 location points, and their impact locations are shown in Figure 9.13.

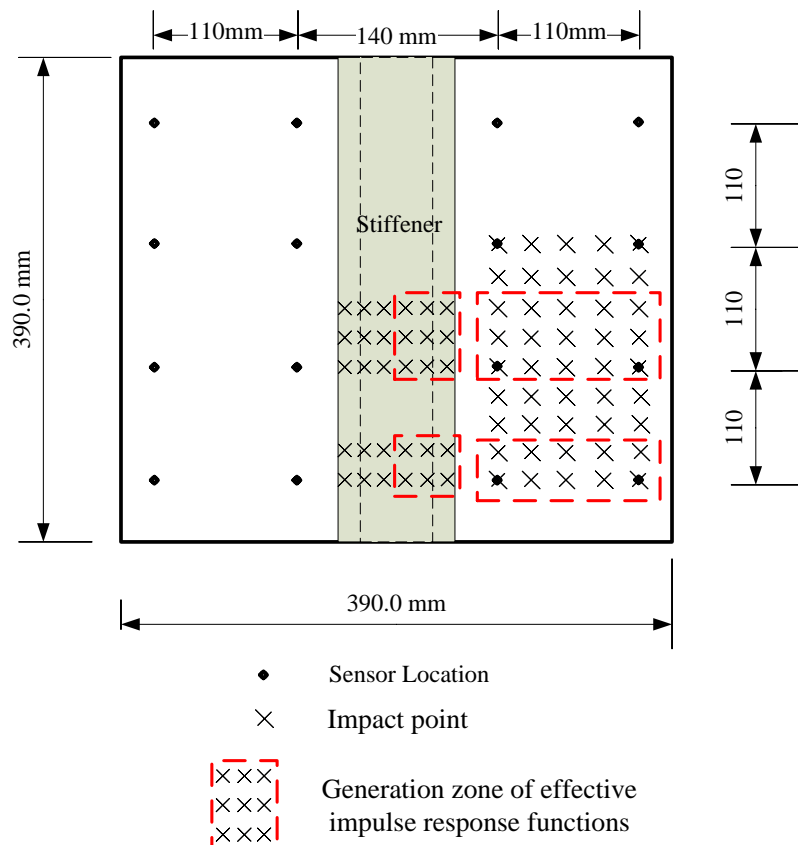


Figure 9.13 Illustration for the formation of IRFs network on specimen 2

Once the functional network of impulse response functions was obtained successfully, unknown impact cases could be performed at any location that is in the stiffener region or two bay regions.

Additionally, the validation experiments were executed to verify the impact monitoring and identification methodology effectiveness for various impactors. Because that the weight, material and velocity of an impactor determine the amplitude and frequency content of the force impulse, the wave shapes of the structural responses are thus dependent on the impactor. Therefore, by changing the tip of the impact hammer, different material impactors with various weights were tested. There are three different types of the tips used, and they are

rubber, plastic and steel tips which represented of soft, medium and hard materials. Using the various types of impactors in materials and masses, the functional network of impulse response functions established was verified for identifying various impact forces effectively, where any unknown impact event could be positioned and reconstructed its magnitude of force in real time mode.

9.3.3 Specimen 3 – A Cutout Panel

Regarding specimen 3, it is an inhomogeneous structure with the surfaces of orange peel, where it owns a circular cutout hole in the plate. This kind of composite structure tends to be more practical structure components from a real aircraft.

For this kind of special structure, a specialized network of impulse response functions need to be established, which is presented in Figure 9.14. Thus, the required number of IRF points for specimen 3 are naturally more of 3 than that of specimen 1, that is, the entire network of impulse response functions was formed from the 68 location points calculated numerically. Through the adaptive IRFs network of 48 Honeycomb grids per sensor found, random impact tests with unknown contents could be implemented to evaluate the performance of the smart impact monitoring and identification system proposed.

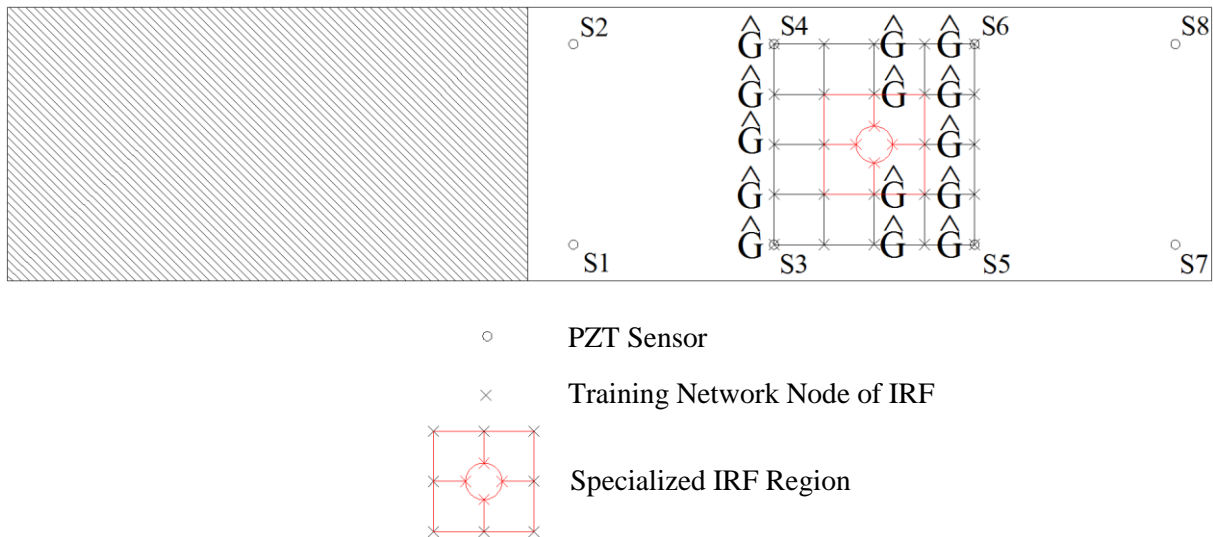


Figure 9.14 Demonstration for the formation of IRFs network on specimen 3

9.3.4 The Laminated Composite Specimens of Damage Identifications

A 5-peaks narrow-band sine tone burst wave signal with the amplitude of 50 V was defined and employed as a probing actuation wave. This probing wave was excited repetitively from the specified actuator using an actuation mode of the sweep frequencies from 60 kHz to 200 kHz, and the sweep interval is 20 kHz. In the meantime, the resulting response signals were observed and recorded at each sensor location of the designed PWT array.

The three instrumented laminated composite specimens were examined by means of acousto-ultrasonics. Figure 9.15 demonstrates the overview execution of the experimental validation tests for damage identifications. Figure 9.15a presents that one of the examined composite specimens seeded with a single delamination of 1.9 cm diameter was tested by the setup PZT wafer transducer array. Figure 9.15c presents that another one of the instrumented composite specimens seeded with the multiple delaminations of increasing 1.0, 1.9 and 3.0 cm diameters was examined using a type of designed PWT array.

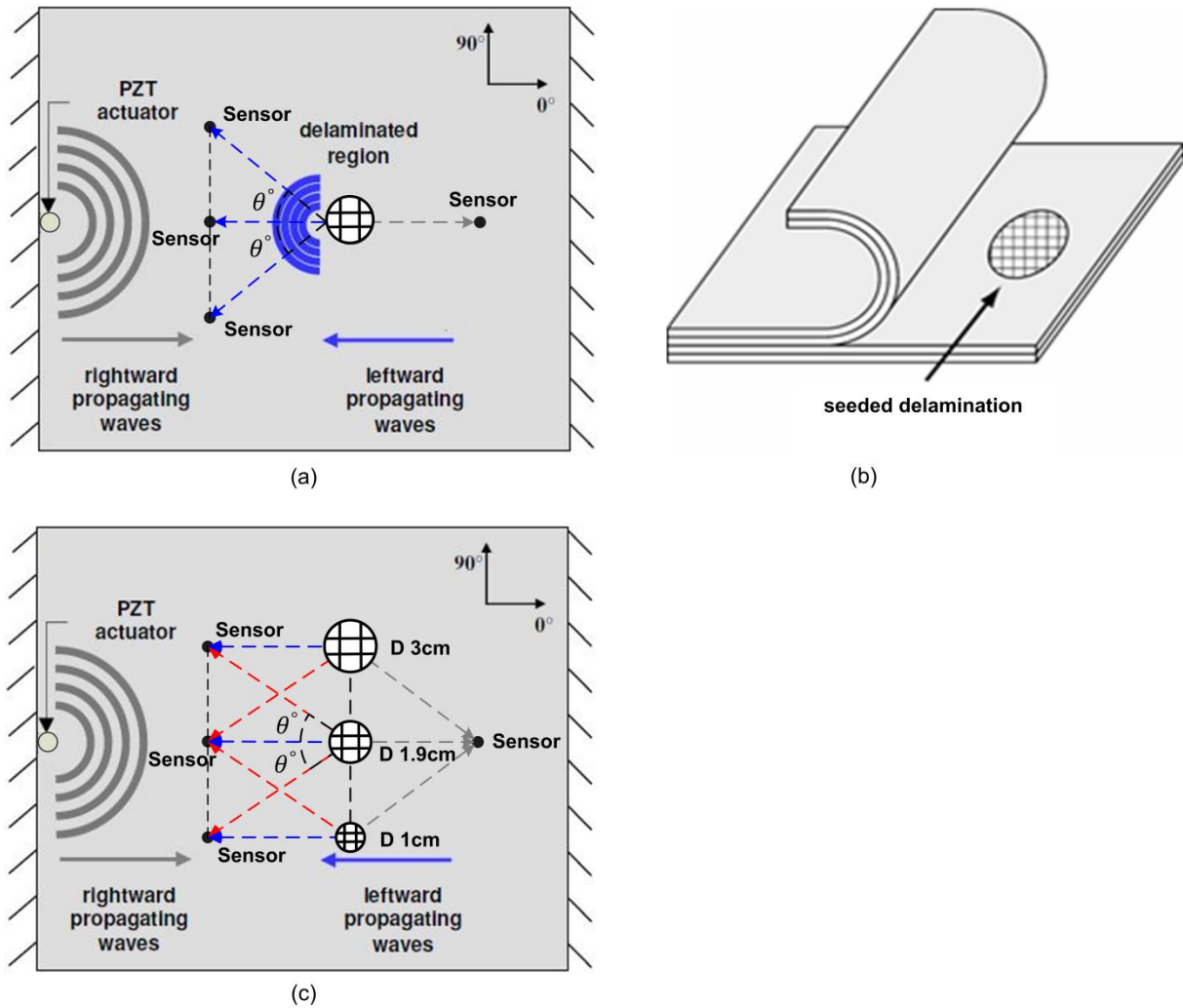


Figure 9.15 Experimental validation tests for the single and multiple damage identifications: (a) the identification of single delamination in a laminated composite specimen, (b) Teflon patches used as the seeded-in delaminations, (c) the identification of multiple delaminations in another laminated composite specimen.

From Figure 9.15, it presents respectively the frameworks of two damage identification cases: (1) the identification of a single delamination seeded in a laminated composite plate structure and (2) the identification case of multiple delaminations in another laminated composite plate structure, where the three delaminations of progressive diameters were seeded in the same layer and their center points were in a same vertical line. The delaminations invisible to the naked eyes were detected in the leftward propagating waves as well as in the selected sensor responses.

9.3.4.1 Determination of Wave Velocity Distribution to Propagating Angles in Laminated Composites

To locate accurately any damage in a laminated composite, the group velocities distribution depending upon wave propagation angles need to be learned and calculated by estimating the TOF information of the excited Lamb waves propagating along different directions in the examined laminated composite.

Due to the dispersion feature of Lamb waves propagating in a laminated composite, the group velocities of the fundamental antisymmetric A_0 Lamb mode need to be estimated in terms of the map of the discrete group velocities varying with the alteration of the propagation angles. The group velocity profile takes the average values $\bar{C}_g(\theta)$ of group velocities at the twenty-four propagation angles, which is obtained from the varied excitation frequencies from 60 kHz to 200 kHz repeated in six measurement times. The map of group velocities distribution depending on wave propagation angles is presented in Figure 9.16.

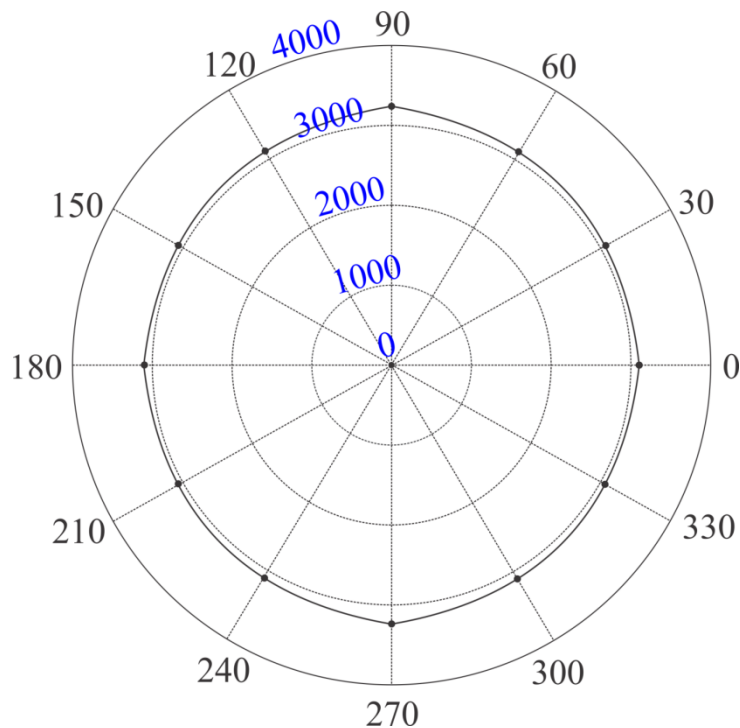


Figure 9.16 A map of group velocity distribution varying with wave propagation angles, units: m/s.

The more details on the determination of propagating Lamb wave velocity is described in Si's damage identification paper.

9.4 Validation of Forward Model of Structural Response

As a very vital part of the construction of an effective and robust forward model, one always validates the chosen forward model by comparing it with the real output of structural response. Actually, it is impossible to establish a forward model that completely describes the true structure response. Meanwhile, some features will always exist in the real structure response, but which the forward model cannot describe. Hence, the model verification addresses an important question of finding out whether the simulated response outputs from the determined forward model match well with the real response outputs from a structure.

To validate the forward model, firstly the optimal model order is necessary to be determined. However, it has been described in detail in Section 5.1.5 to how to select the optimal model order. Here, to interpret briefly, there presents a histogram as shown in Figure 9.17 to indicate the procedure of model order selection.

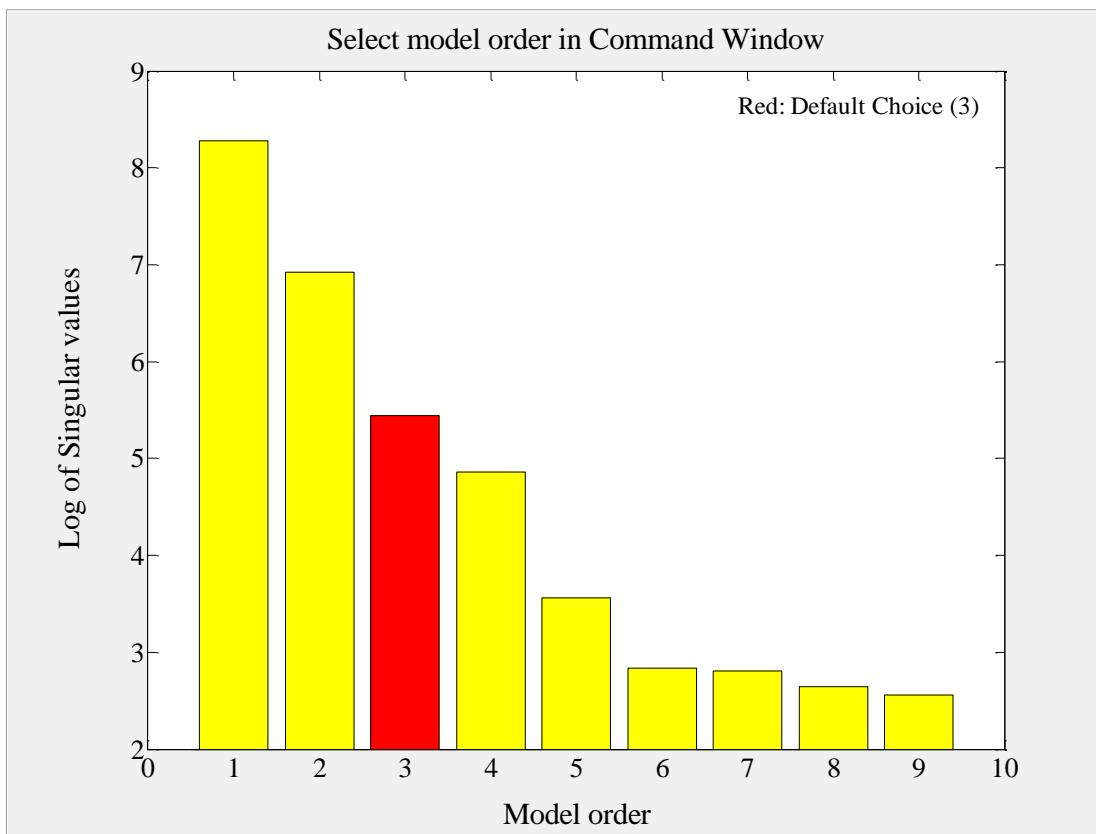


Figure 9.17 Histogram of model order selection

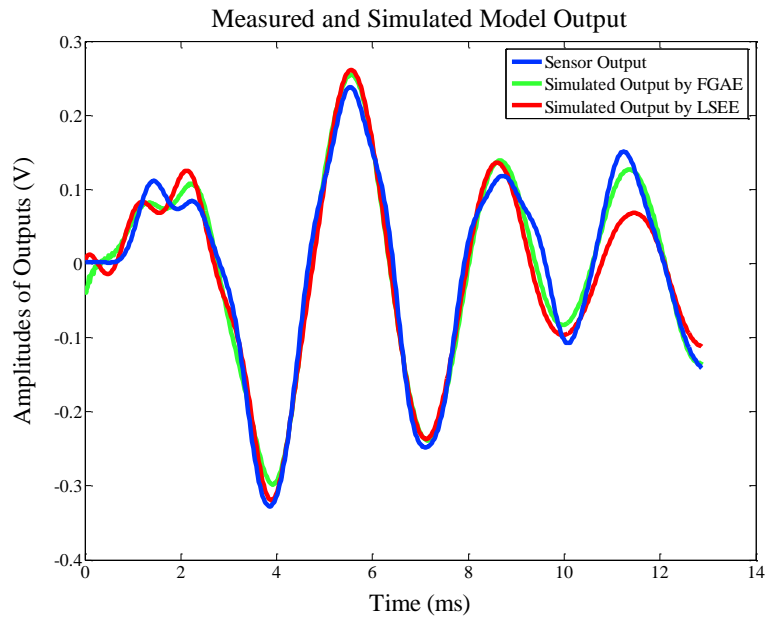
Secondly, the forward model validation is done with a set of new input data produced from an instrumental impact hammer. Meanwhile, every new input sequence is generated by the impact hammer with different tips and is multiplied by the built IR function G_f^S to obtain the

corresponding simulated response outputs. Subsequently, the simulated response outputs are compared with the recorded signals from sensor outputs, and where it gives an indication of how good the forward model is.

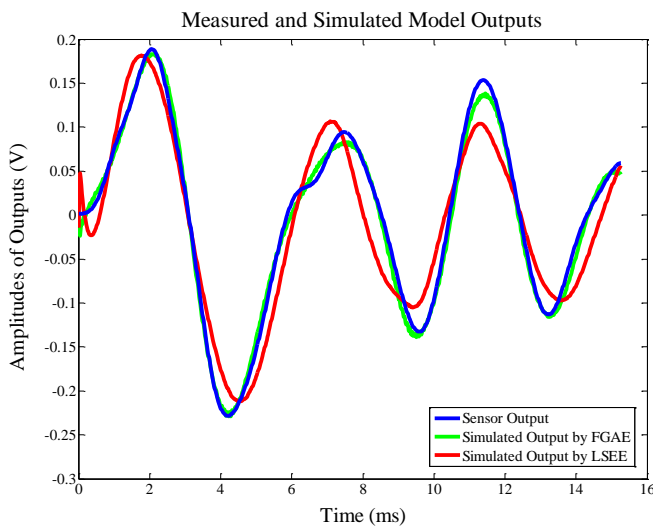
However, a universal impulse response functions matrix G_f^s should be firstly constructed through the developed ensemble impact monitoring and identification technique using the impact hammer with a medium hardness tip – a plastic tip. And a simulated response output from the forward model found is plotted with the corresponding real output recorded from a specific sensor in Figure 9.18*b*. Then, using the same impulse response function G_f^s and different hammer tips, the simulated response outputs from the corresponding forward models are compared with the sensor output signals recorded, respectively. For the soft material property of rubber tip and the high hardness material of steel tip, their simulated response outputs match well with the recorded output signals, which are shown in Figures 9.18*c* and 9.18*d*, separately. Therefore, it can be said that the universal IR function G_f^s is capable to reproduce the responses of the structure.



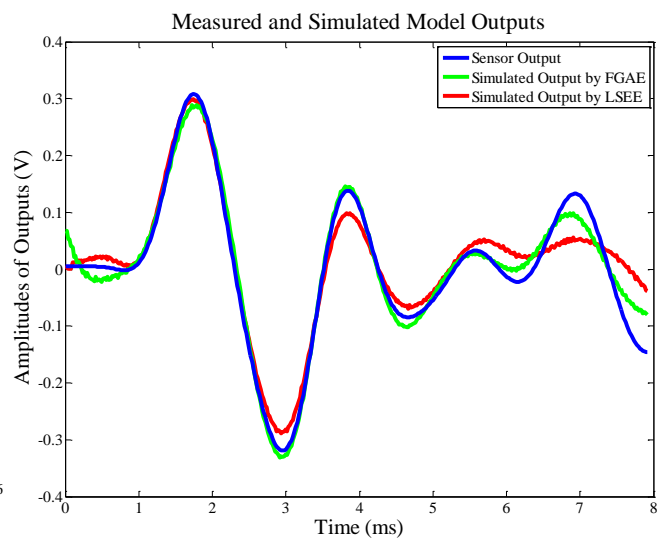
(a)



(b)



(c)



(d)

Figure 9.18 Forward model validations through different hammer tips: (a) three different hammer tips, (b) model validation by the plastic tip, (c) model validation by the rubber tip, (d) model validation by the steel tip.

10. Results and Discussion

The estimated and reconstructed results are illustrated to validate the dependability and robustness of the ensemble SHMI technique for impact source identification. Here, it needs to point out two issues that are 1) the experimental results on actual impact forces were collected directly from the instrumented hammer to the DAQ system, thus the results of the real forces were not affected from any disturbance; 2) when the experimental data were collected using the DAQ system, the two work modes of trigger and online were utilized respectively. For the trigger mode, a minimum threshold value for impacts needs to be set to record the data, but it does not need to do for the online mode. Then, the relevant issues will be also discussed in detail in this chapter, which include the impact positioning and assessments of their estimated locations under diverse structure configurations and random mechanical vibration disturbances; the effects of force reconstructions resulting from various anisotropic structure configurations, different impact conditions, and random vibration noise contamination. Moreover, the structural state assessments were also applied in structural damage cases, which includes the structural damage localizations, quantifications and structural state prognosis based on the damage prediction functions (curves) for the structural damage expansion, and so on.

10.1 Estimations of Impact Locations

In order to assess the estimated impact locations, the location error (LE) evaluated is defined in Equations (10.1-10.3), which is expressed as the distance from the estimated impact location to the actual impact location. Here, for specimens 1 and 3, the x -directions are defined as the length directions of the CFRP plates; for specimen 2, the y -direction is defined as the direction of the stiffener.

$$\Delta x = x_{calc} - x_{act} \quad (10.1)$$

$$\Delta y = y_{calc} - y_{act} \quad (10.2)$$

$$\zeta_e = \sqrt{\Delta x^2 + \Delta y^2} \quad (10.3)$$

The average positioning error ratio (APER) e_p still needs to be defined as,

$$e_p = \frac{1}{N} \sum_1^n \frac{\zeta_e}{I_s} \times 100\% \quad (10.4)$$

where I_s is referred to the interval between the sensors.

10.1.1 Specimen 1 – A Normal Condition

To illustrate the proposed performance of impact positioning and its accuracy under various impact conditions, two representative impact conditions were selected from a series of impact validation tests, where an unknown impact event acted in the boundary vicinity of the cantilever structure, and the other unknown impact event acted in the middle region of the structure. Hence, a set of estimation results of impact locations on specimen 1 are shown in Figures 10.2a and 10.2b.

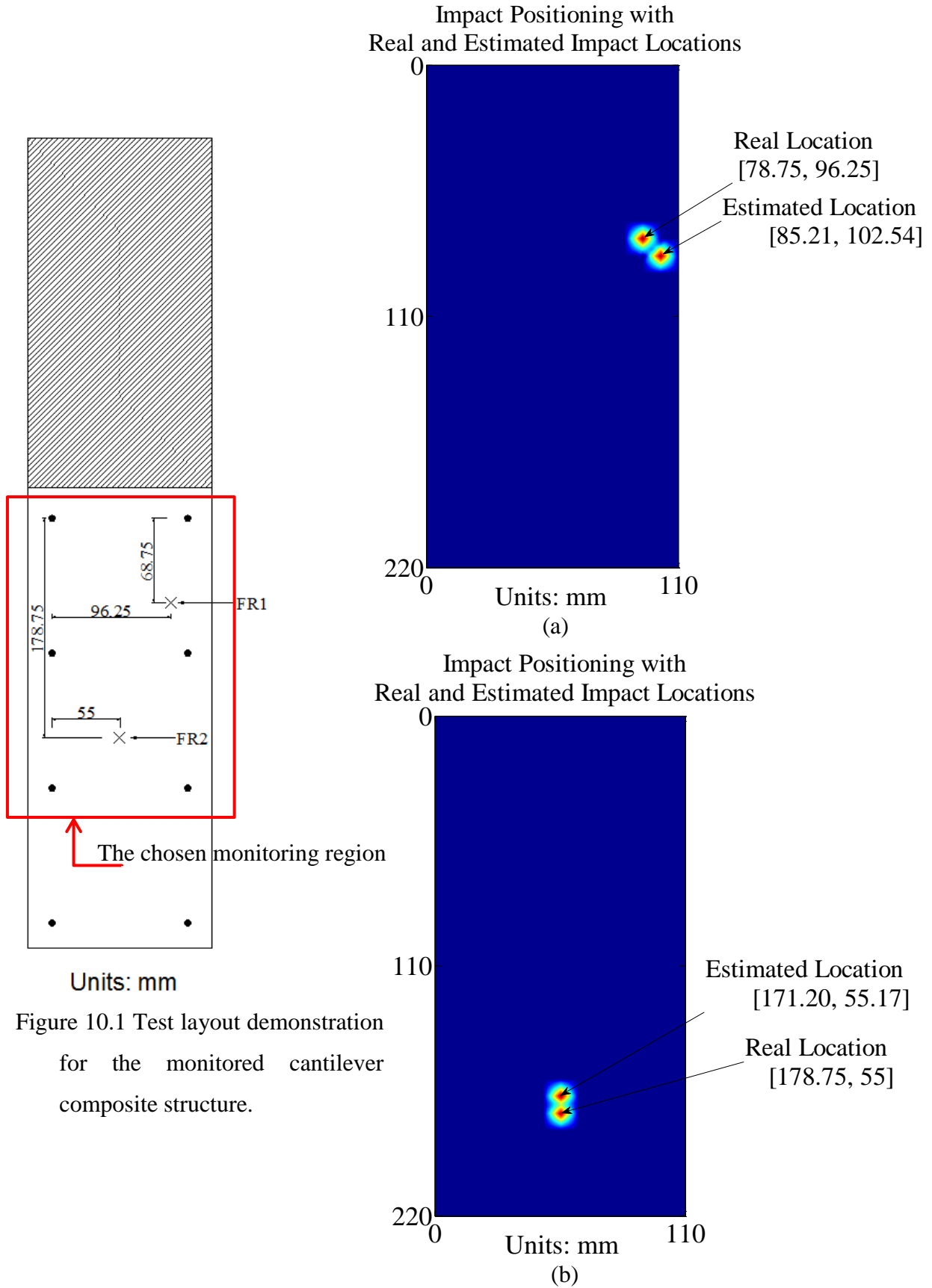


Figure 10.2 Location estimations for two unknown impact events on the structure: (a) impact FR1 localization, (b) impact FR2 localization.

Through a series of impact verification tests on specimen 1, the average positioning error ratio is mostly in the range of 10.3% of the corresponding sensor interval laid, which is shown in Figure 10.3.

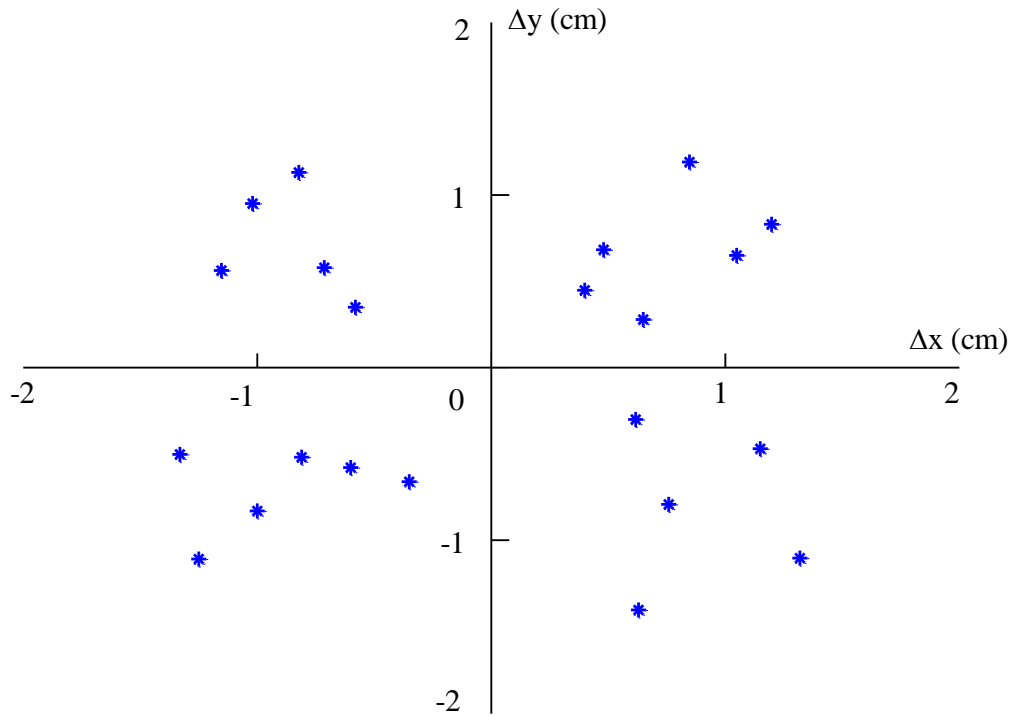
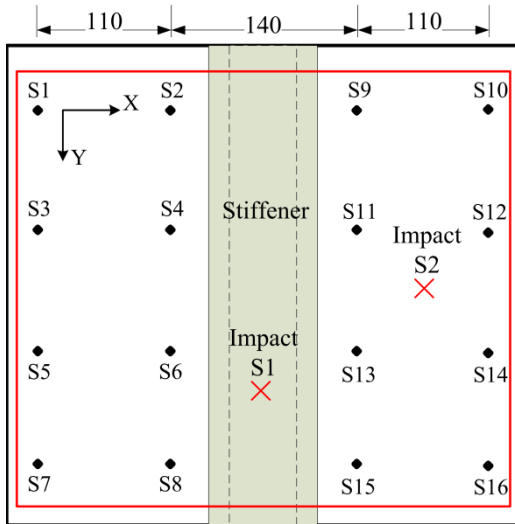


Figure 10.3 Location estimation errors for unknown impact events on Specimen 1

10.1.2 Specimen 2 – Structural Complexity Consideration

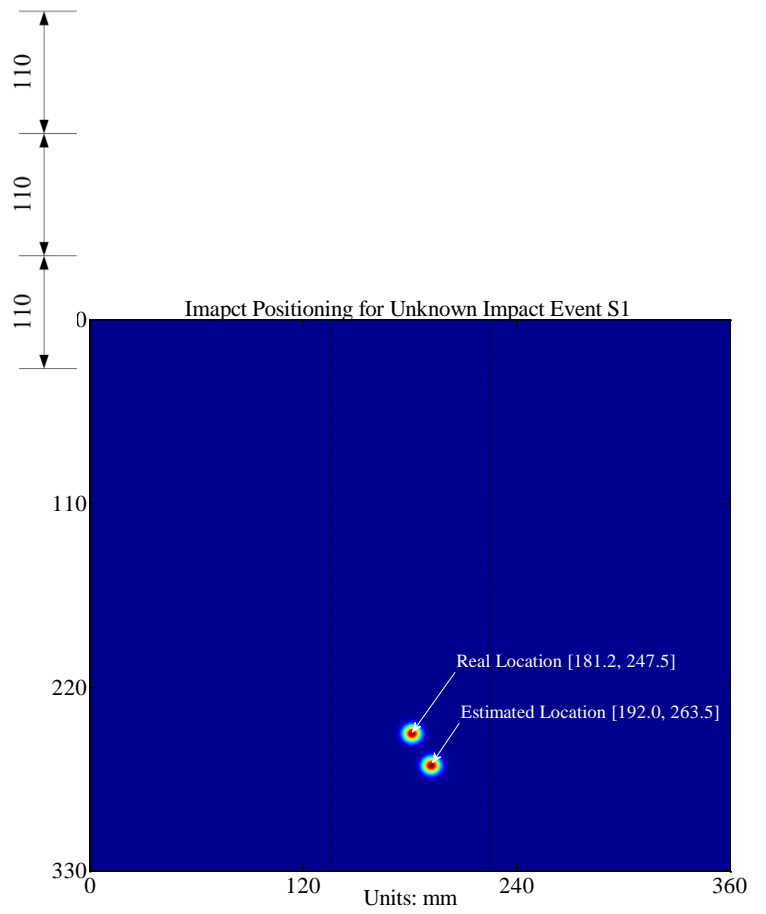
In order to interpret the universal performance of the IMI approach, two representative impact conditions were also selected from a series of impact validation tests, where one impact event acted in the stiffener area of the stiffened panel, and the other impact event acted in the right bay area of the stiffened panel. Because of the symmetry of the stiffened panel structure, only one side of the bay areas is considered here. The location estimation results of two unknown impact events on specimen 2 are illustrated in Figures 10.5a and 10.5b.

The estimation errors of impact locations on the stiffened CFRP panel are divided into two corresponding different areas, respectively. The location estimation error in the right bay area is shown in Figure 10.6a, and the location estimation error in the stiffener area is shown in Figure 10.6b. As well, the overall average errors of the location estimations for impacts are both lower than 13 mm in the whole structure region.

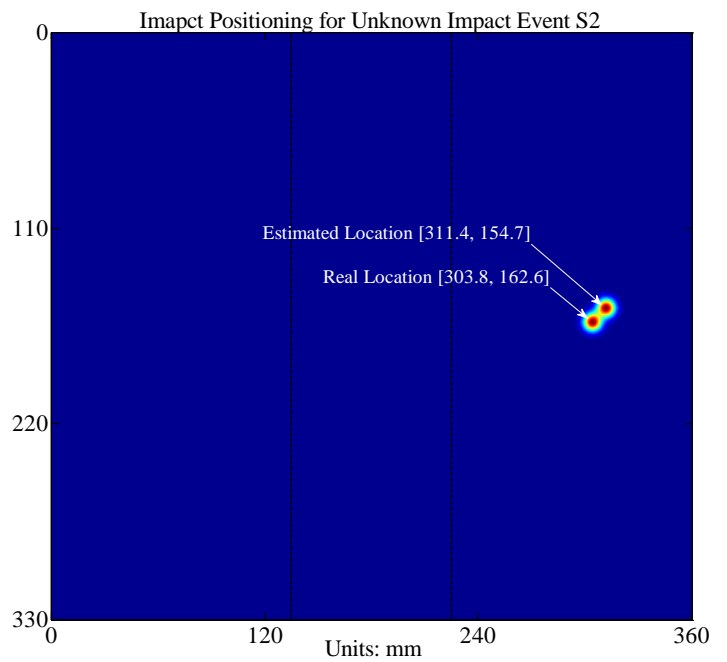


The monitoring region Units: mm

Figure 10.4 Test layout for the monitored stiffened composite structure.

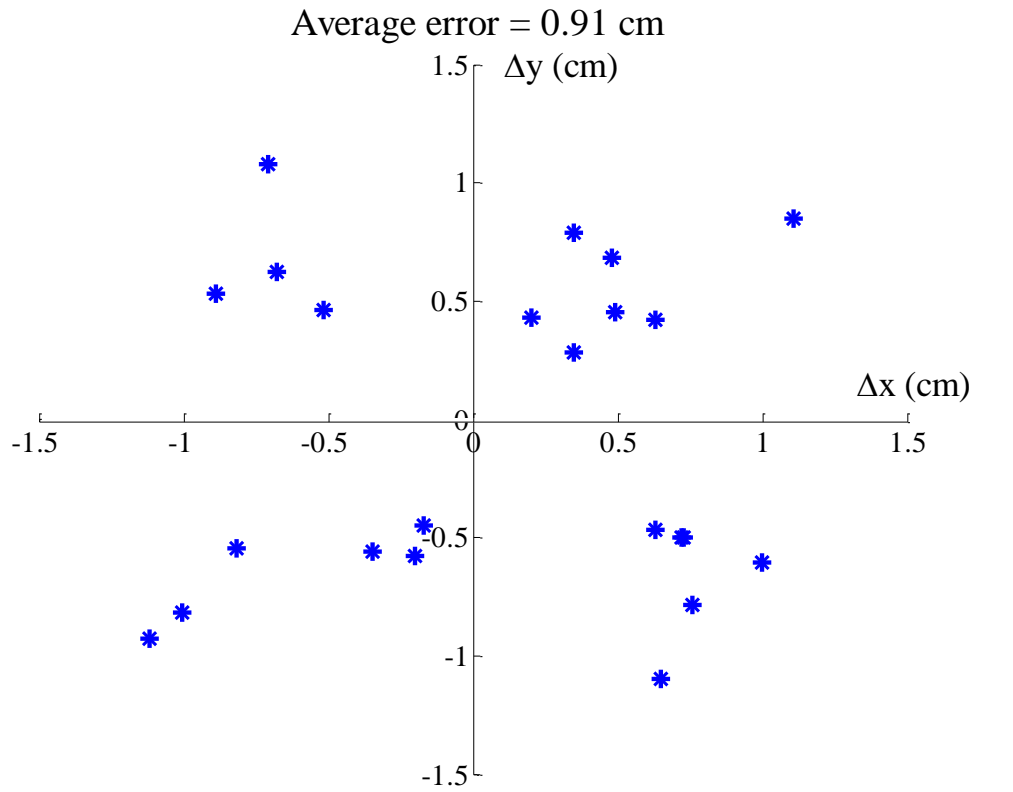


(a)

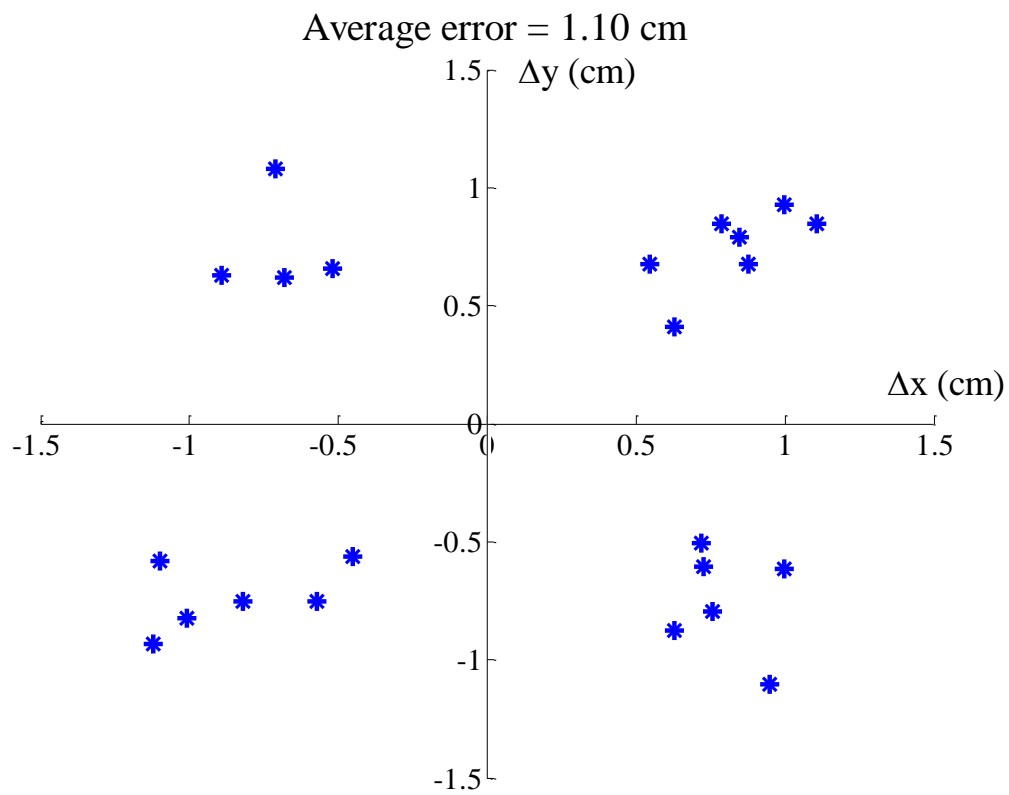


(b)

Figure 10.5 Location estimations for two unknown impact events on the structure:
 (a) impact S1 on the stiffener area, (b) impact S2 on the right bay area.



a) The right bay area



b) The stiffener area

Figure 10.6 Location estimation errors for unknown impact events on the stiffened panel.

10.1.3 Specimen 3 – Structural Discontinuity Consideration

A particular structure with rough surfaces or cutout holes can affect the wave propagation resulting from an impact force, such as a cutout panel structure. This is because the stress waves induced by an external force will generate complex diffraction phenomenon when the waves encounter a discontinuity such as a cutout hole in a structure, from which the wave propagation is affected, and lead to obvious changes and differences from traveling in a normal intact structure. In other words, it means that there may be changes in the phase velocities of the propagating waves, compared to the waves traveling in a normal structure without any discontinuity.

As a result, in the case of impact monitoring and localization, it is difficult to locate an unknown impact force, especially when the impact occurred in the region surrounding the cutout hole. Accordingly, the sensor signals recorded need to be preprocessed so as to facilitate the numerical calculation of impact positioning effectively.

However, two representatively unknown impact examples around the cutout hole were selected to illustrate the effects in the following Figure 10.7. Furthermore, through a series of impact verification tests on specimen 3, the average positioning error ratio is mostly in the range of 12.3% of the corresponding sensor interval laid, which is shown in Figure 10.8.

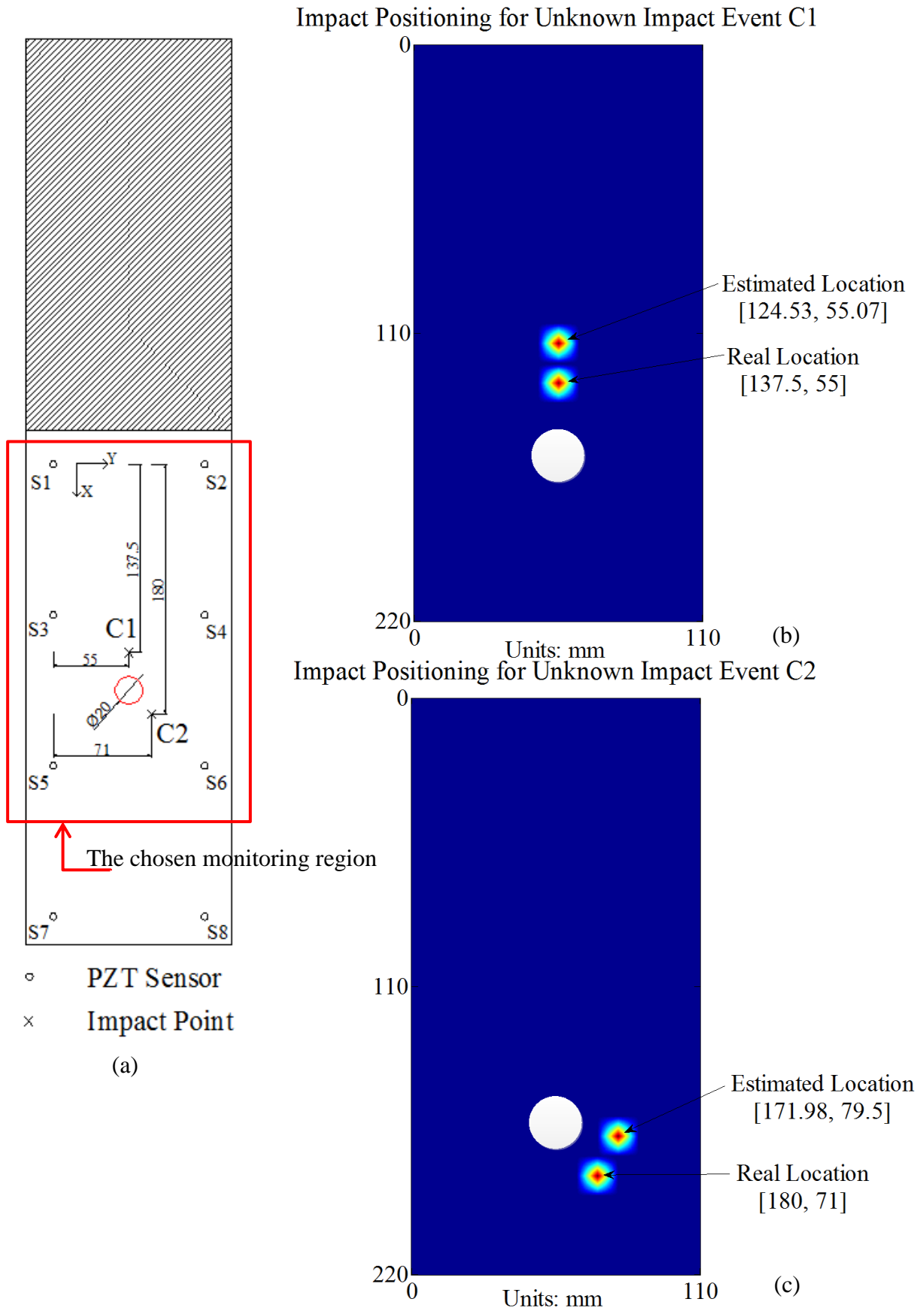


Figure 10.7 Location estimations for two unknown impact events on Specimen 3: (a) the test layout, (b) impact C1 localization, and (c) impact C2 localization.

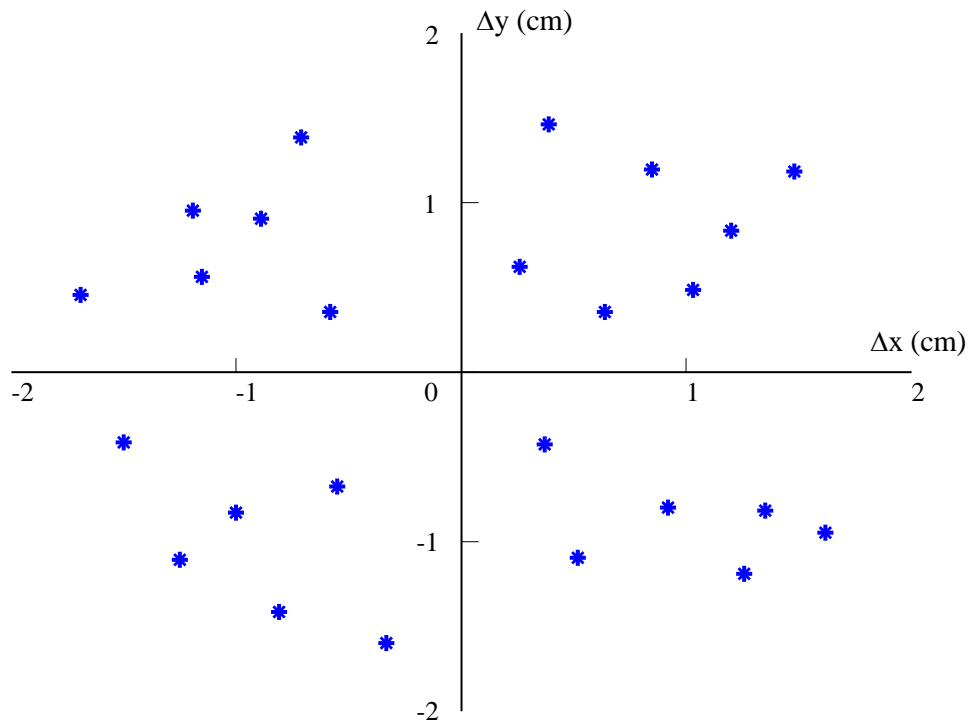


Figure 10.8 Location estimation errors for the unknown random impact events on Specimen 3

10.1.4 Comparison of the Location Estimation Methods

To contrast the two impact positioning methods (IPMs) described in Chapter 7, which are 1) the time-of-flight based quadrilateral centroid positioning method (TOF-b-QCPM) and 2) the cost function based positioning method (CF-b-PM), the relationship between the average positioning error ratio (APER) and the sensor interval needs to be applied to reveal their individual accuracies of impact positioning.

Hence, the following Figure 10.9 shows distinctly that the average positioning error ratios change with the variation of the sensor interval, and further that the average positioning error ratios increase proportionally as the sensor interval increases. And also, throughout the variation of the sensor interval from Fig. 10.9, the positioning precision using the time-of-flight based quadrilateral centroid positioning method is always better than that using the cost function based positioning method, because the coordinates of an impact location can be calculated by the time-of-flight based quadrilateral centroid positioning method based on certain physical significances, which are the wave propagation property and the corresponding phase velocity computation from the propagating wave dynamic model detailed in Appendix B.

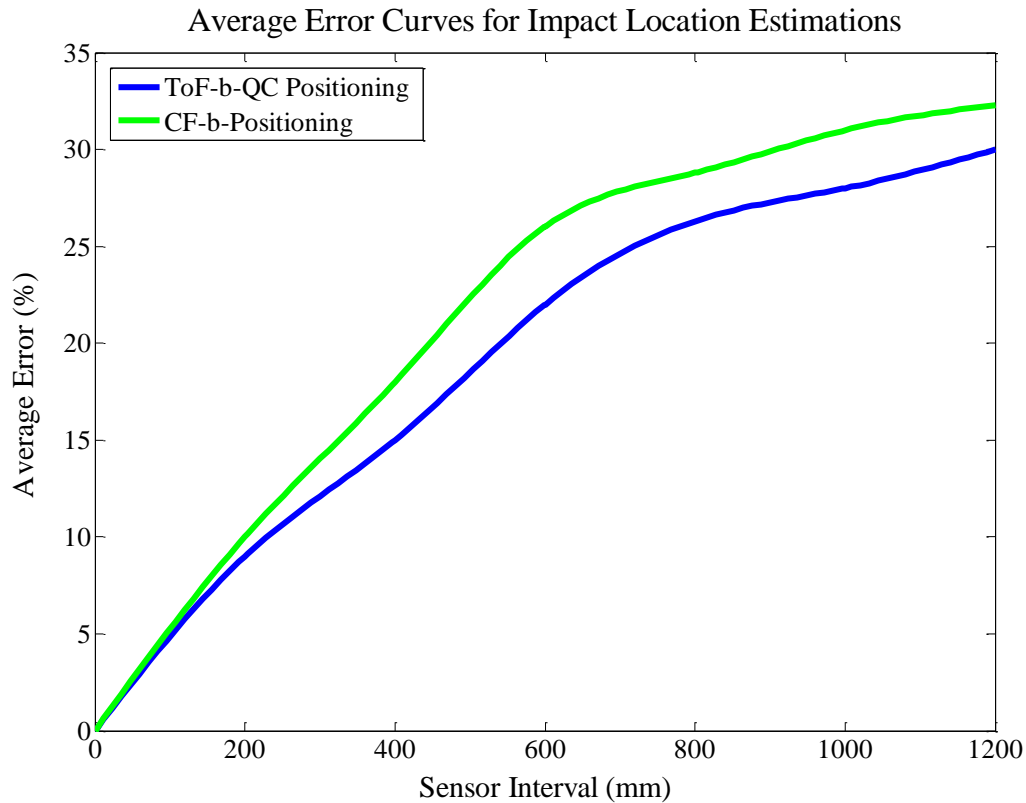


Figure 10.9 Comparison of the accuracies of the two impact positioning methods

10.2 Impact Force Reconstructions

Typical impact identification tests were executed to validate the performance of force reconstructions with respect to various composite structure configurations. First, various impulse response function matrix networks for various types of composite structures such as specimens 1 and 2 were obtained from two different approaches, which are that the one utilizes the simulated output data from the built FE models and the other one adopts the output data from a series of corresponding impact training. Nevertheless, for specimen 3, we directly adopted the means of the experimental measurements. Hence, using the various IRF matrix networks found, the procedure of force reconstructions can be implemented easily for unforeseen impacts on diverse types of composite structures.

An impact force was reconstructed using the selected sensor signals and the corresponding impulse response functions that can be obtained through the proposed impact identification algorithm. Then, to validate the dependability and robustness of the reconstructed force, three eigenparameters of impacts were considered to evaluate for the performance, as follows:

- 1) maximum force amplitude;

2) force duration;

3) impulse (integral of force against time).

Furthermore, in order to assess the accuracies of the reconstructed forces, the relative average errors e_a corresponding to the above three parameters are needed for comparison, where the relative average error is defined as,

$$e_a = \frac{1}{n} \sum_{i=1}^n \frac{\text{calculated value} - \text{actual value}}{\text{actual value}} \times 100\% \quad n = 1, 2, \dots \quad (10.5)$$

However, in order to interpret the universal performance of the ensemble impact monitoring and identification technique comprehensively, some representative impact cases were selected with respect to the three experimental specimens.

10.2.1 Specimen 1 – A Normal Condition

In order to indicate the efficacy of the ensemble impact monitoring and identification technique representatively, the evaluation results for unknown impacts of FR1 and FR2 on specimen 1 are presented in Table 10.1. In view of all of cases considered, for force reconstructions using the IRF matrix networks obtained from the training response data of the FEM simulations, the corresponding average error of maximum amplitude is 6%, the corresponding average error of force duration is 10.6%, and the corresponding average error of impulse is 10.1%; and for force reconstructions using the IRF matrix networks obtained from the training output data of the sensor measurements, the corresponding average error of maximum amplitude is 8%, the corresponding average error of force duration is 12.8%, and the corresponding average error of impulse is 11.3%.

For specimen 1, the impact location FR1 was selected due to the consideration of boundary performance validation for the ensemble impact monitoring and identification technique, and the evaluation result of force reconstruction is presented in Figure 10.11. The impact location FR2 was selected due to the consideration of generality performance validation for the EIMI approach, and its reconstruction result is demonstrated in Figure 10.12.

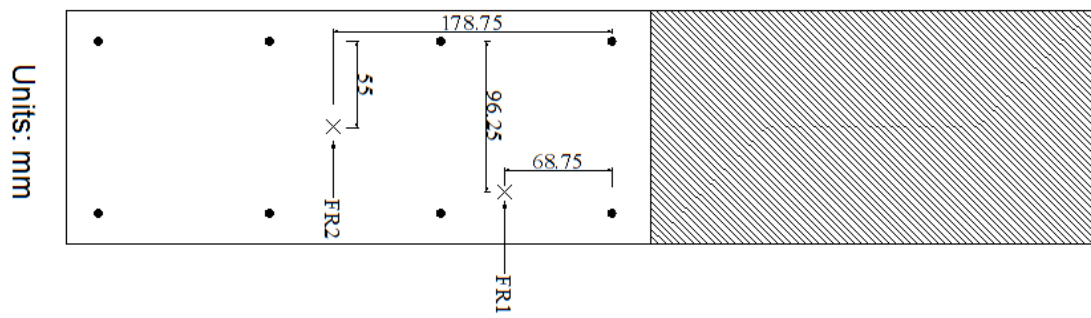


Figure 10.10 Two unknown impact events on Specimen 1

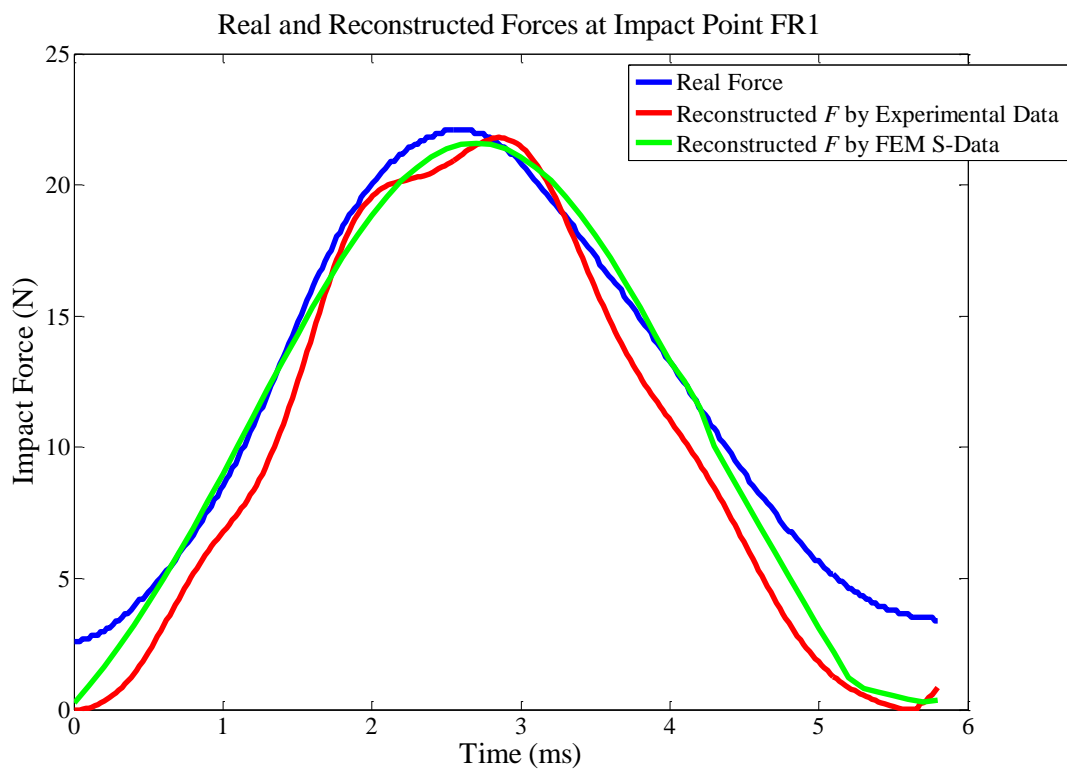


Figure 10.11 Force reconstruction for an unknown impact event at point FR1

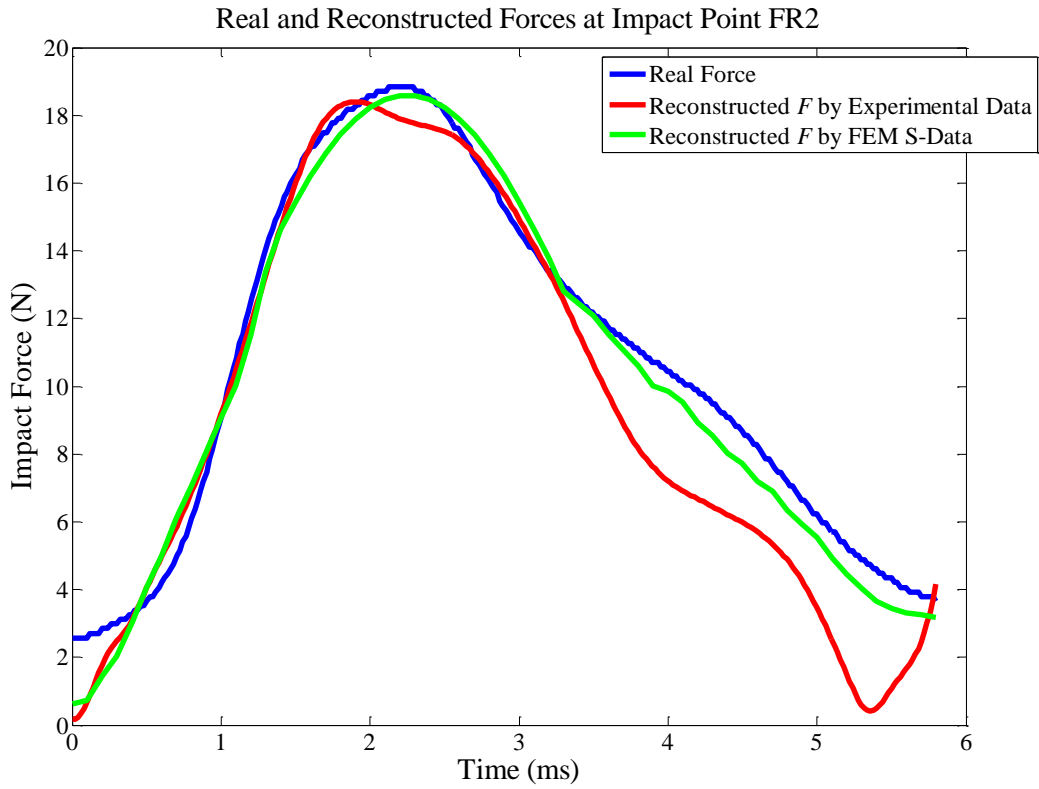


Figure 10.12 Force reconstruction for an unknown impact event at point FR2

Table 10.1 Evaluation results for unknown impacts of FR1 and FR2

Impact Event		Real	Estimations by experimental data	Estimations by FEM data
FR1	Maximum amplitude (Unit: N)	22.11	21.75	21.70
	Impulse (Unit: N·s)	0.07	0.06	0.07
FR2	Maximum amplitude (Unit: N)	18.84	18.37	18.68
	Impulse (Unit: N·s)	0.06	0.05	0.06

10.2.2 Specimen 2 – Structural Complexity Consideration

For specimen 2, the impact locations of A, B and C were selected to correspondingly verify anti-sensitivity capability, anti-inhomogeneous capability and generality capability of the ensemble impact monitoring and identification technique due to the composite structure with inconstant structural properties. The impact position A is located at the vertical top of a specific sensor; the impact position B is located at an arbitrary position in the stiffened region; and the impact position C is located at an arbitrary position in the right bay region.

The evaluated results of force reconstructions are well matched with the original impulse signals arising from random impact acting anywhere on the whole panel, such as in the right bay area, as shown in Figure 10.16; in the stiffened area, as illustrated in Figure 10.15; or even the top of the sensors, as shown in Figure 10.14.

For specimen 2, from the three evaluation parameters that are maximum amplitude, impact duration and impulse, the corresponding average errors are all lower than 12.2%.

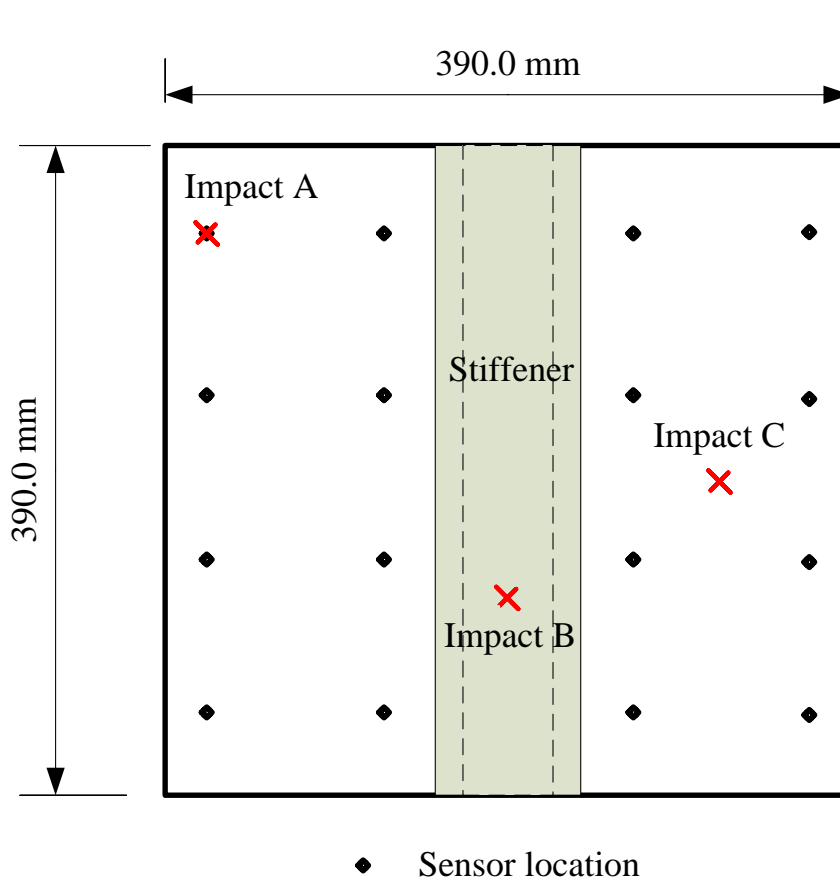


Figure 10.13 Demonstration of random impact locations

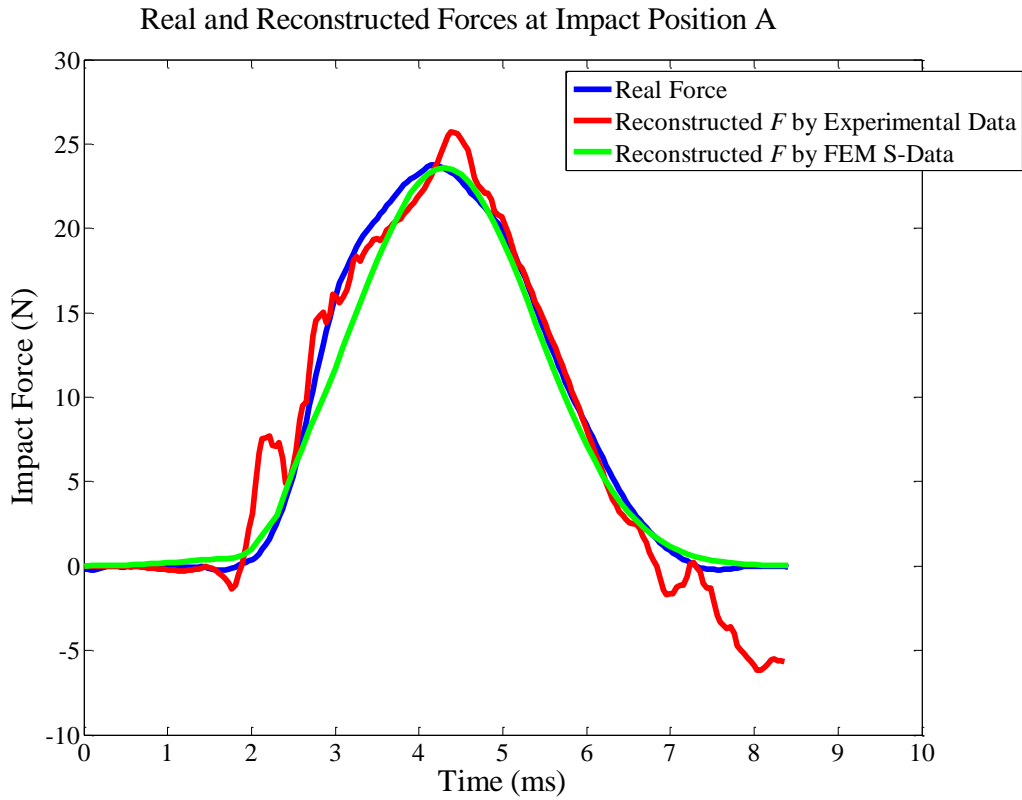


Figure 10.14 Force reconstruction for a random impact at point *A*

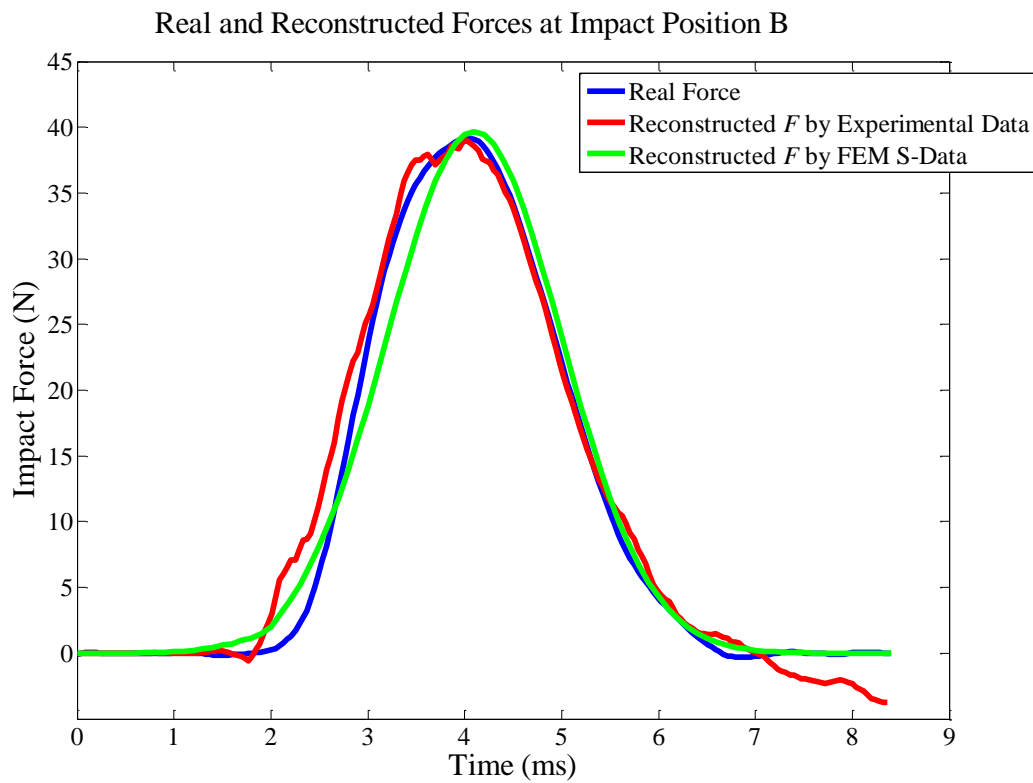


Figure 10.15 Force reconstruction for a random impact at point *B*

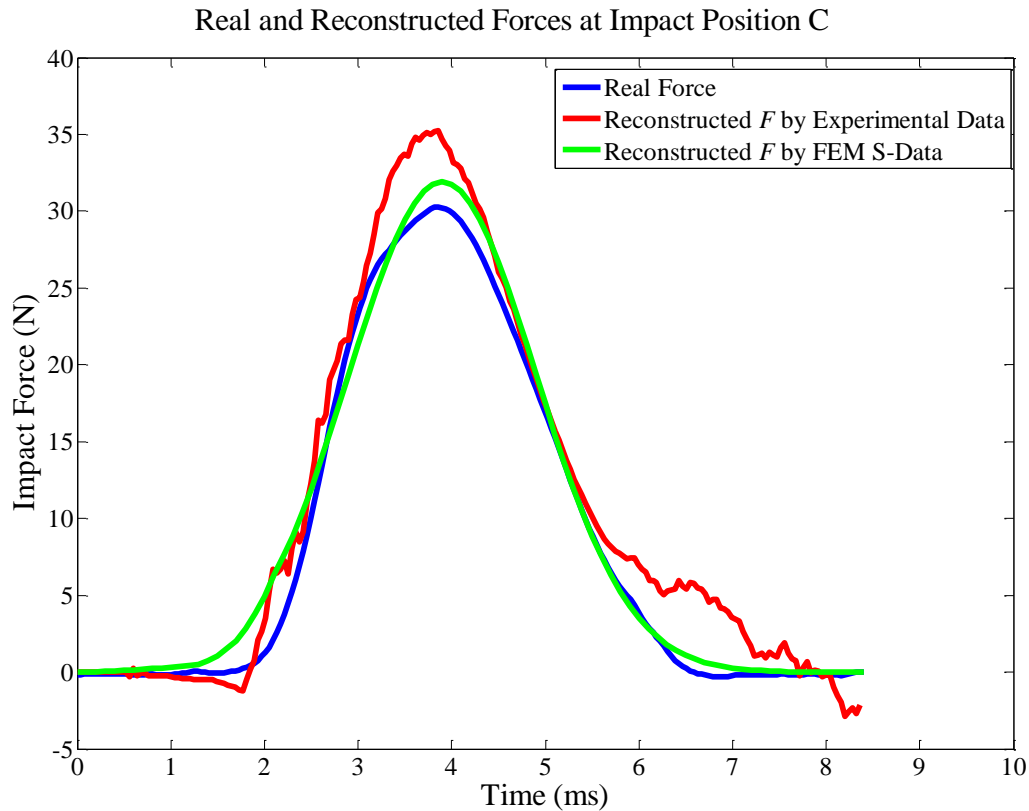


Figure 10.16 Force reconstruction for a random impact at point *C*

10.2.3 Specimen 3 – Structural Discontinuity Consideration

A particular structure can affect the wave propagation resulting from an impact force, for instance, typically a panel structure with a cutout hole. It is because the stress waves induced by an external force will generate complex diffraction phenomenon when the waves encounter a discontinuity such as a cutout hole in a structure, which will lead to evident changes and differences in wave propagation. In other words, it means that the time delays may occur when the waves arrive at the sensors furnished on the structure, compared to the waves traveling in a normal intact structure without any discontinuity.

Therefore, for impact identification, it is also very difficult to identify an unknown impact force especially when the impact occurred close to the cutout hole. Accordingly, the sensor signals collected need to be preprocessed so as to assist the numerical calculation of impact identification efficiently.

Through a series of impact tests on specimen 3, two representatively unknown impact examples around the cutout hole were selected, of which the force reconstruction results are illustrated in the following Figures 10.18 and 10.19. Meanwhile, from the three evaluation

parameters, which are maximum amplitude, force duration, and impulse, the corresponding average errors can be all controlled in the range of 14.0%. From the values of the average errors, they are all a little higher than that of the normal structure Specimen 1, because of the result of a structural discontinuity property.

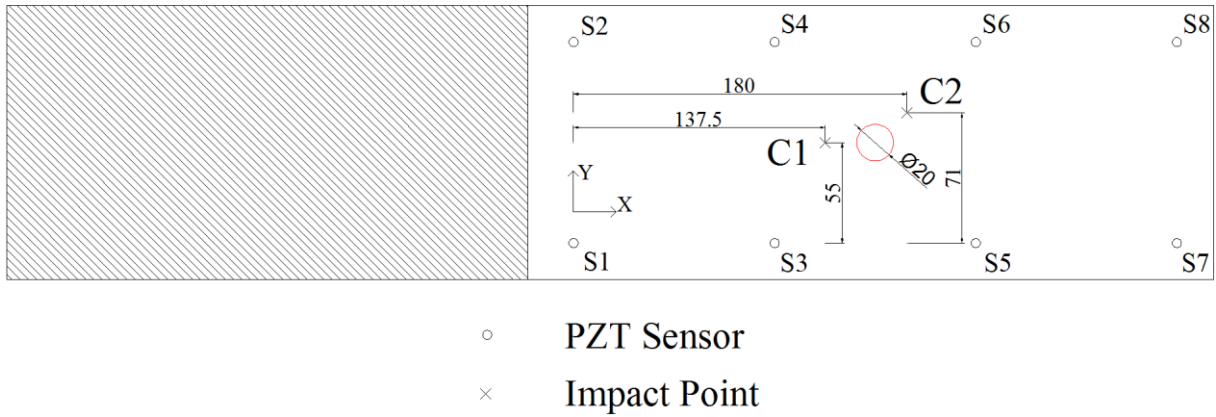


Figure 10.17 Two unknown impact events on Specimen 3

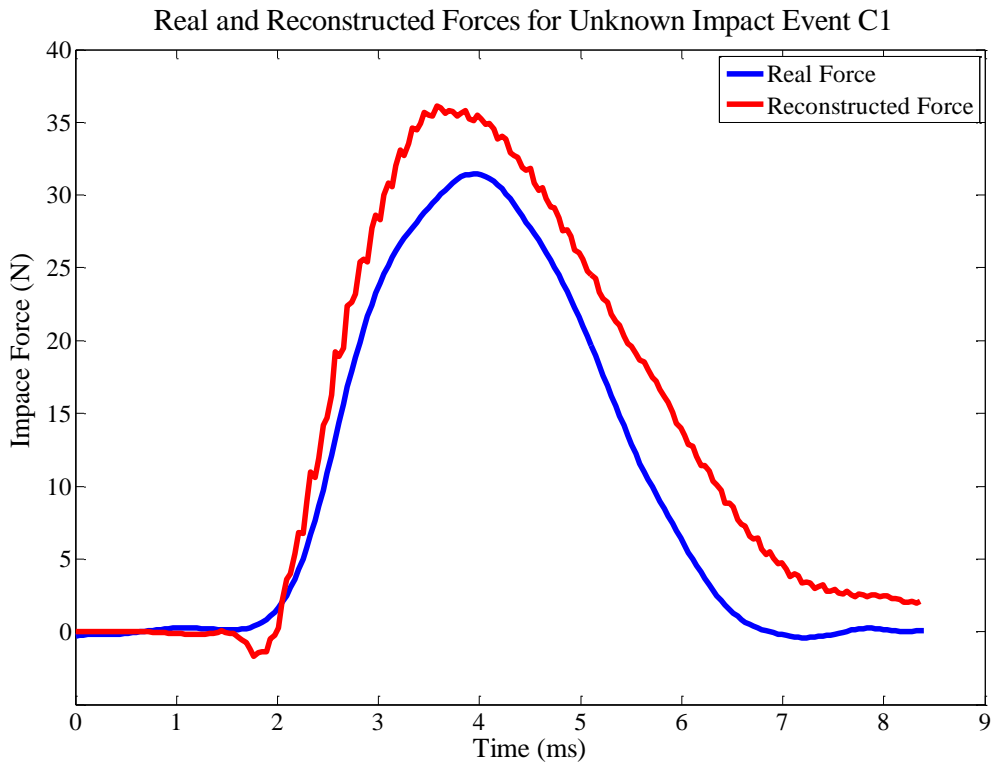


Figure 10.18 Force reconstruction at impact location C1 on the cutout panel

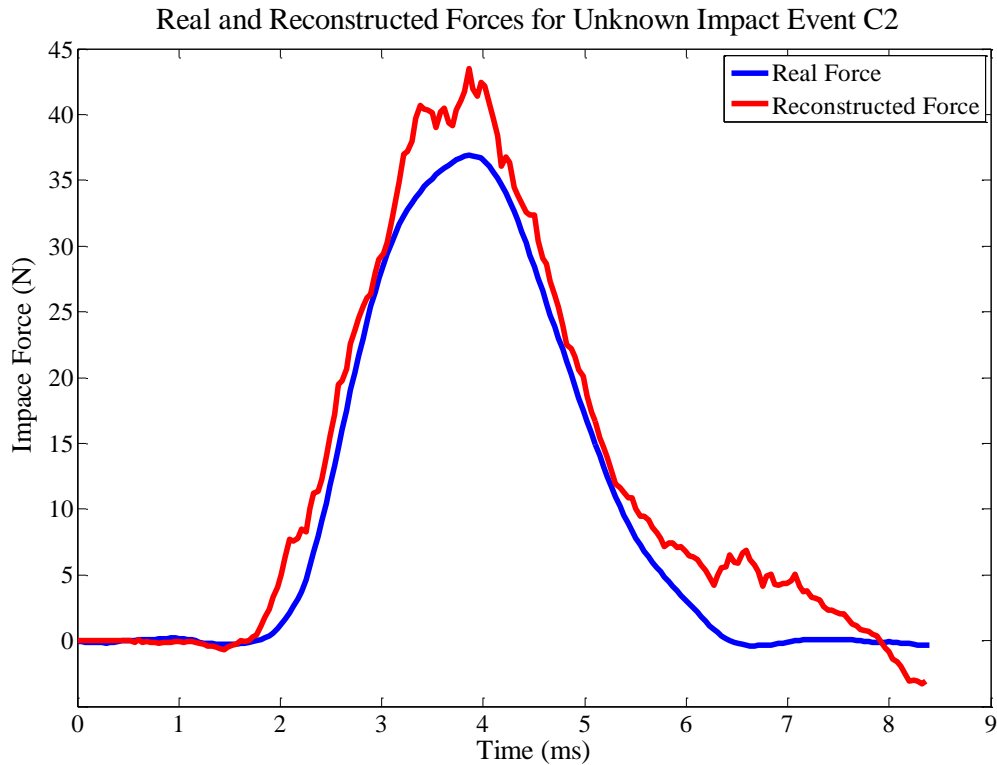


Figure 10.19 Force reconstruction at impact location C2 on the cutout panel

10.2.4 Conclusion

From the previous force reconstruction results and comparisons to the two approaches, it is easy to see that the force reconstructions using the training data from the FEM simulation can obtain better results than the reconstructions using the training data from the experimental measurements. However, this leads to the situation of different errors discovered in all the impact cases, mainly caused by several disturbed and unstable factors that may be known or unknown, for instance, from the constitutive property of CFRP material structure, there are 1) the deviations of material property of a carbon fiber prepreg laminates from the technical data sheets and manufacturing process, and 2) the inconsistency of the structural property (e.g. stiffness) of a CFRP structure between the FEM calculation and actual CFRP product, because of possible defects inside of the real structure; from in-situ impact experimental tests, there are also 1) accuracy of beating the training network nodes, and 2) unpredictable impact conditions acting on the structures, etc..

10.3 Structural Condition Awareness Based on Signal Energy Distribution

What happens in the structure when impact events occur unexpectedly on a structure? How does the structural condition alter? And what of effects are produced in the structure? With a series of the problems mentioned, an approach of the signal energy distribution provides a better solution to solve the intractable problems for a structure, which result from unforeseen impact events. The signal energy distribution (SED) method applies the structural response data to analyze and evaluate the distribution of the energy in the structure resulting from an impact, as described in Section 7.1. Using Eq. 7.1, the distributed energies collected by sensors can be obtained from the meaningful time windows that are corresponding to the impact duration. Moreover, the energies distributed in a structure are generated from the kinetic energy transformation of an impact; in other words, the distributed signal energies evaluated from the measurements are produced through the energy transmission to the impacted structure from the impact. The evaluated energies don't affect the goal of the structural condition awareness on getting the information of the structural dynamic responses. And then the evaluated energy is defined as the signal energy E_s , which is not the conventional notion of physical energy E_p . However, the two kinds of energies are closely related, and they can be converted each other, as given by this equation $E_p = \frac{E_s}{z}$, where z represents the magnitude of the characteristic impedance of the transmission line. Through the signal energy distribution method, the structural condition can be monitored in real-time mode. Also, the SED method can use the output data from the structural responses to evaluate the distribution of the energies in the structure, and then from the energy distribution, the manifestation of the structural condition is supplied to determine the corresponding FE model order generated by any impact event. And the combination with the simulation results from FEM, it is possible to provide an effective basis for the optimization design of composites.

Accordingly, Specimen 1 was only used as this demonstration to illustrate the synthesized performance of the signal energy distribution method, which is presented in Figures 10.21 and 10.22. When the impact events of FR1 and FR2 occurred on the structure, the energies distributed in the structure are evidently higher in the corresponding impact regions. In this case, the energy distribution supplies a powerful indication for the initial localization of impact regions. Additionally, the appearance of shear effects due to impacts can also be observed intuitively. What is more, an intuitive visualization can be provided using the SED method, which is used to determine which FE model order is generated due to impacts. Because the energies resulting from the impacts of FR1 and FR2 are not high, both are first model orders produced in the cantilever composite structure as Figure 10.20.

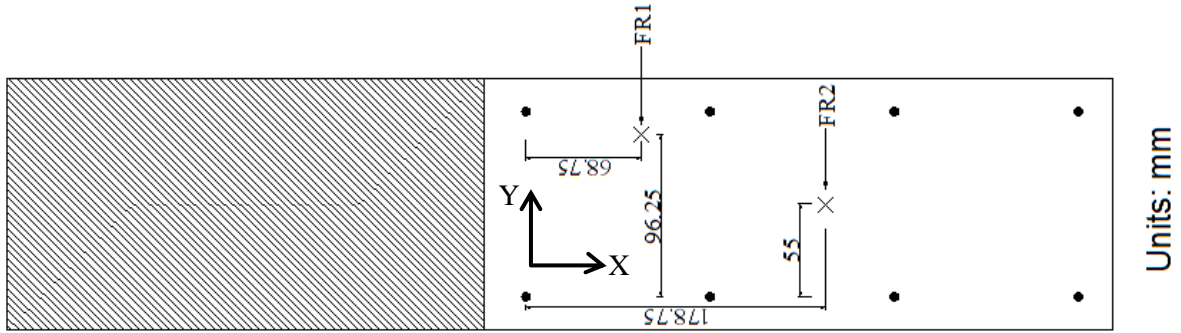


Figure 10.20 Two random impacts on the cantilever composite structure

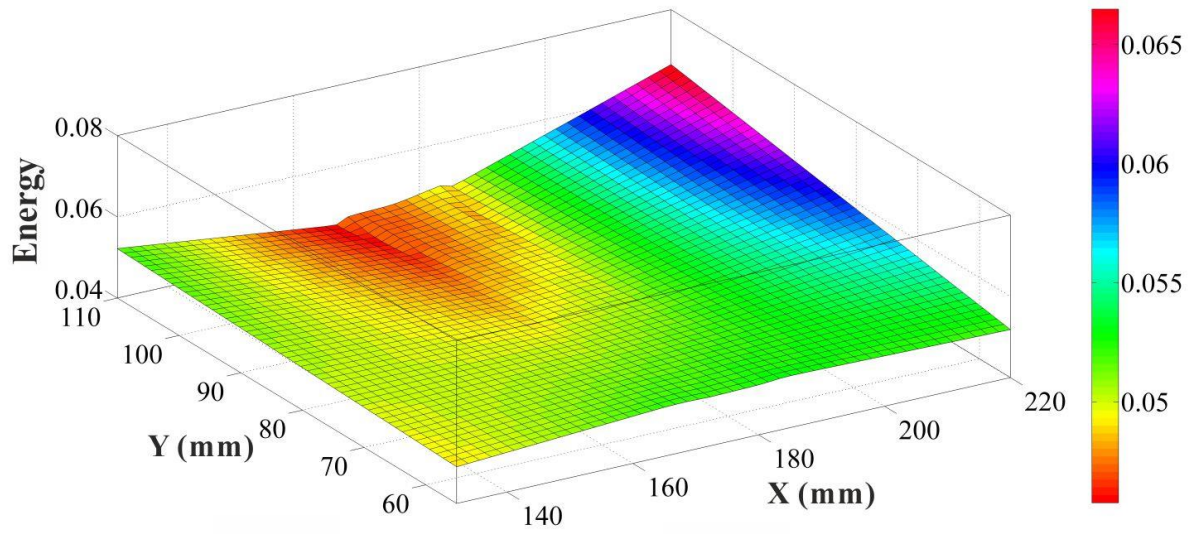


Figure 10.21 Structural condition awareness when impact at location FR1

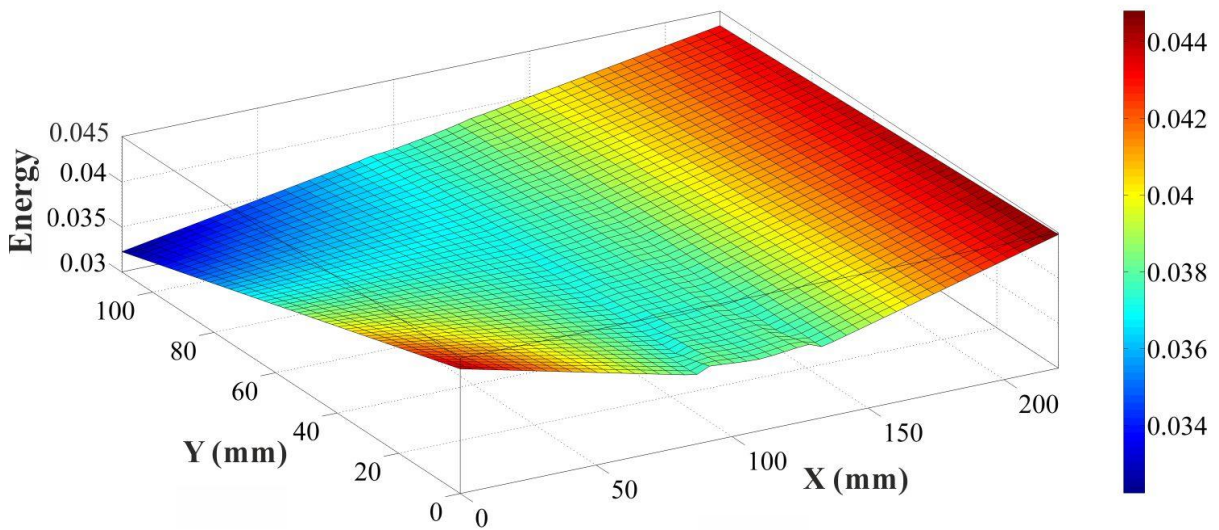


Figure 10.22 Structural condition awareness when impact at location FR2

10.4 Impact Monitoring Under Vibration Noise Contamination

To reveal the anti-disturbance performance of the developed EIMI approach in a fully convincing way, changeable vibration conditions were applied to the impact verification tests. In the impact verification tests, a set of original multi-sensor response signals due to an impact event were recorded under random vibration environments, as presented in Figure 10.23. Subsequently in this section, two major aspects are still discussed, which are impact positionings and their error evaluations, and impact identifications and relevant error assessments.

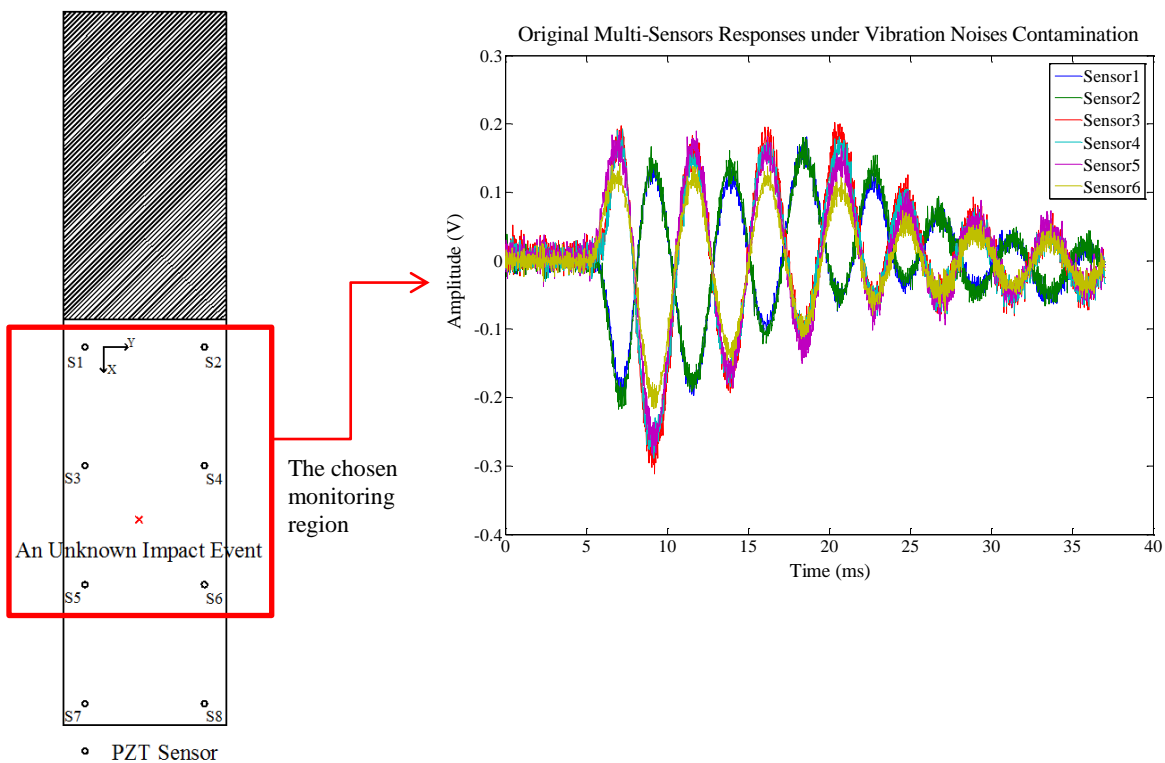


Figure 10.23 Original multi-sensor response signals under vibration noises contamination.

10.4.1 Estimations of Impact Locations

To illustrate the anti-disturbance performance of the proposed monitoring and identification technique, a set of estimated results for impact locations on specimen 1 are presented in Figure 10.24. And two cases of impact positioning were both implemented under vibration disturbance.

Furthermore, through a series of impact verification tests under random vibration conditions, the average positioning error ratio (APER) e_p that is defined in Function (10.4) under vibration disturbance is a little more 3% than the APER e_p of a normal condition.

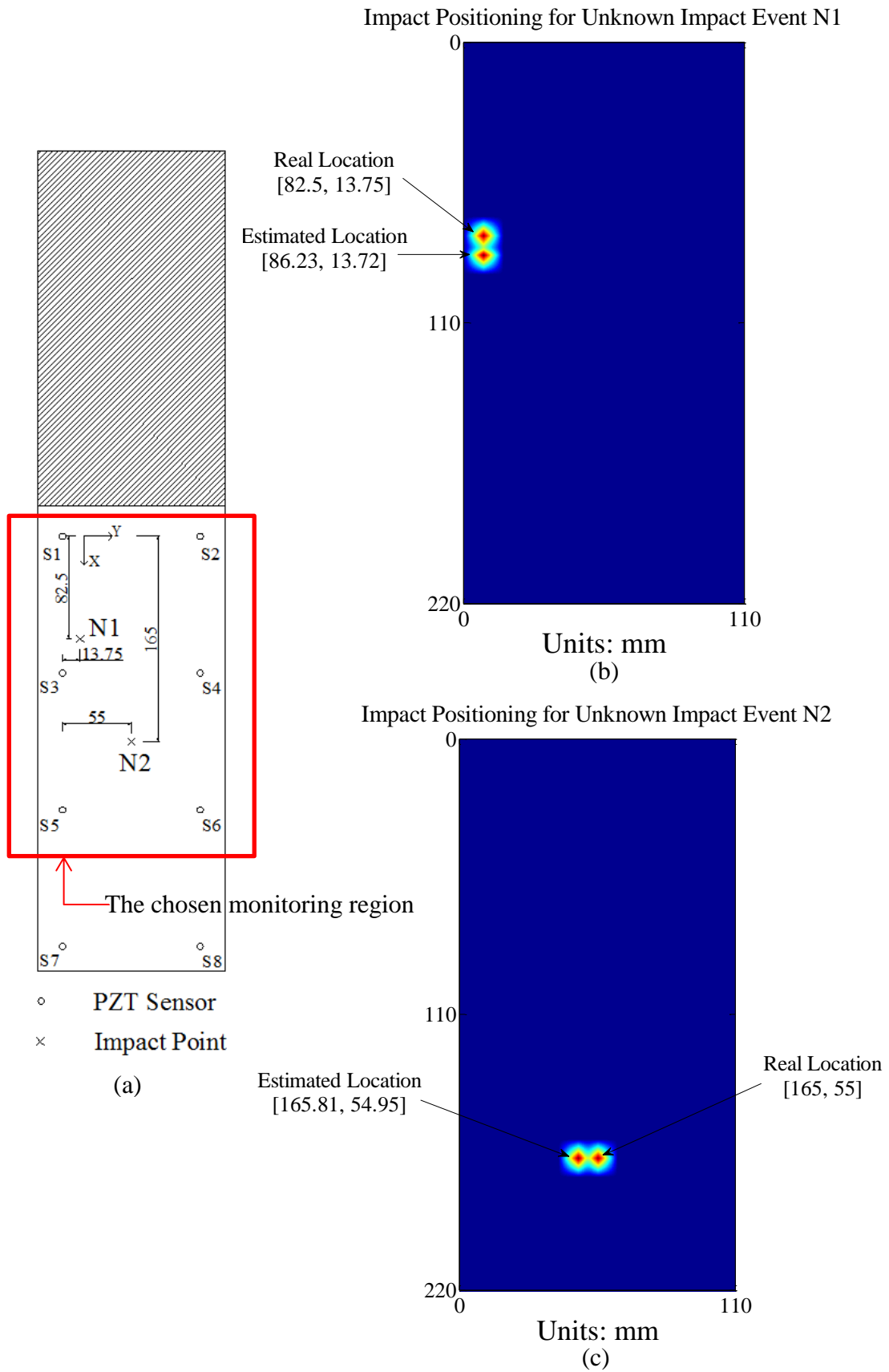


Figure 10.24 Location estimations for two unknown impact events under random vibration conditions: (a) the test layout, (b) impact N1 localization, and (c) impact N2 localization.

10.4.2 Impact Force Reconstructions

To verify the performance of the ensemble impact monitoring and identification approach against vibration noise effects, unpredictable random vibration disturbance conditions were added to impact experiment tests. Then, through identification processing using the EIMI approach, the different results of force reconstructions are compared as shown in Figures 10.25 and 10.26, where they indicate that the impact forces are reconstructed under de-noising, within vibration noises of SNR of 20 and within vibration noises of SNR of 10. Furthermore, three representative disturbance conditions were selected from changeable random vibrations, where one is under the noise condition of SNR of 10, another one is under the noise condition of SNR of 15, and the third one is under the noise condition of SNR=20. The average errors of force reconstructions within various noise contaminations are calculated out, which are all a little more than the results of de-noising implementation. The different results of impact identifications are indicated in Table 10.2. In general, in the condition of original output response signals of SNR=10 (within noise contamination), the overall average error in force reconstruction is approximately 8.6% more than that of the de-noising implementation; in the condition of original output response signals of SNR=15 (within noise contamination), the overall average error in force reconstruction is approximately 6.9% more than that of the de-noising implementation; and in the condition of original output response signals of SNR=20 (within noise contamination), the overall average error in force reconstruction is approximately 5% more than that of the de-noising implementation.

Through comparing with the two vibration noise conditions, it becomes evident that the ensemble impact monitoring and identification approach developed can be competent to do the significant task of structural impact monitoring and real-time structural state analysis and assessment under some intractable practical-engineering requirements and conditions, of which a significant indication is uncorrelated random vibration noise interferences. Here, it is worth noting that the signal data preprocessing (SDP) function block from the ensemble impact monitoring and identification approach plays a key filtering role in eliminating any possible uncorrelated random disturbances from existing engineering conditions.

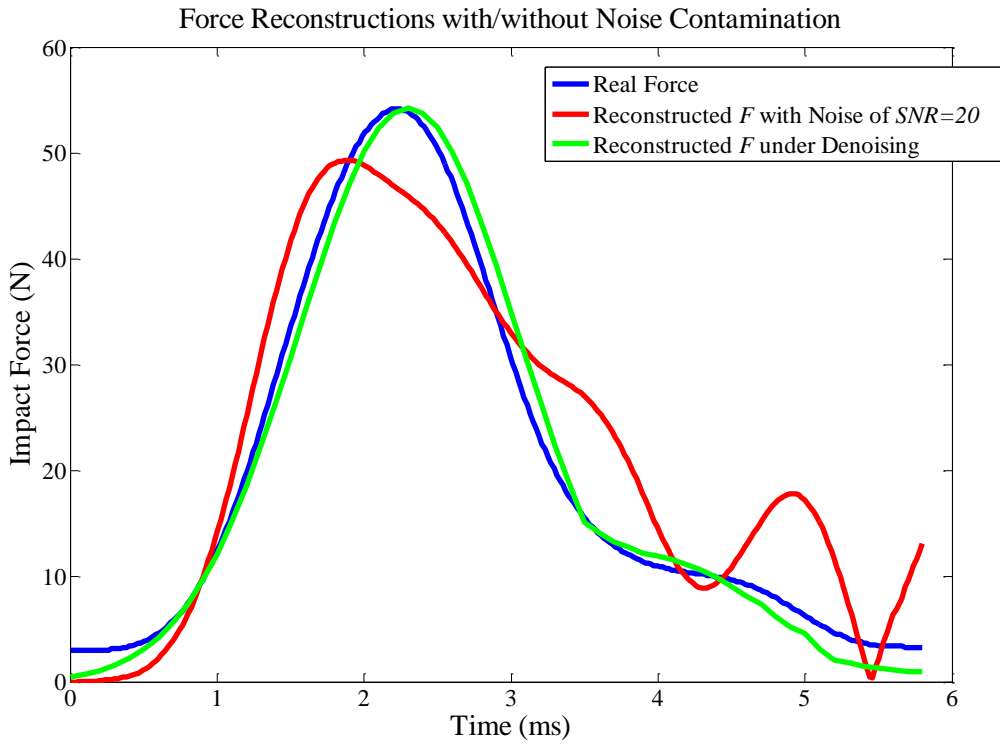


Figure 10.25 Force reconstruction with and without vibration noises of $SNR=20$

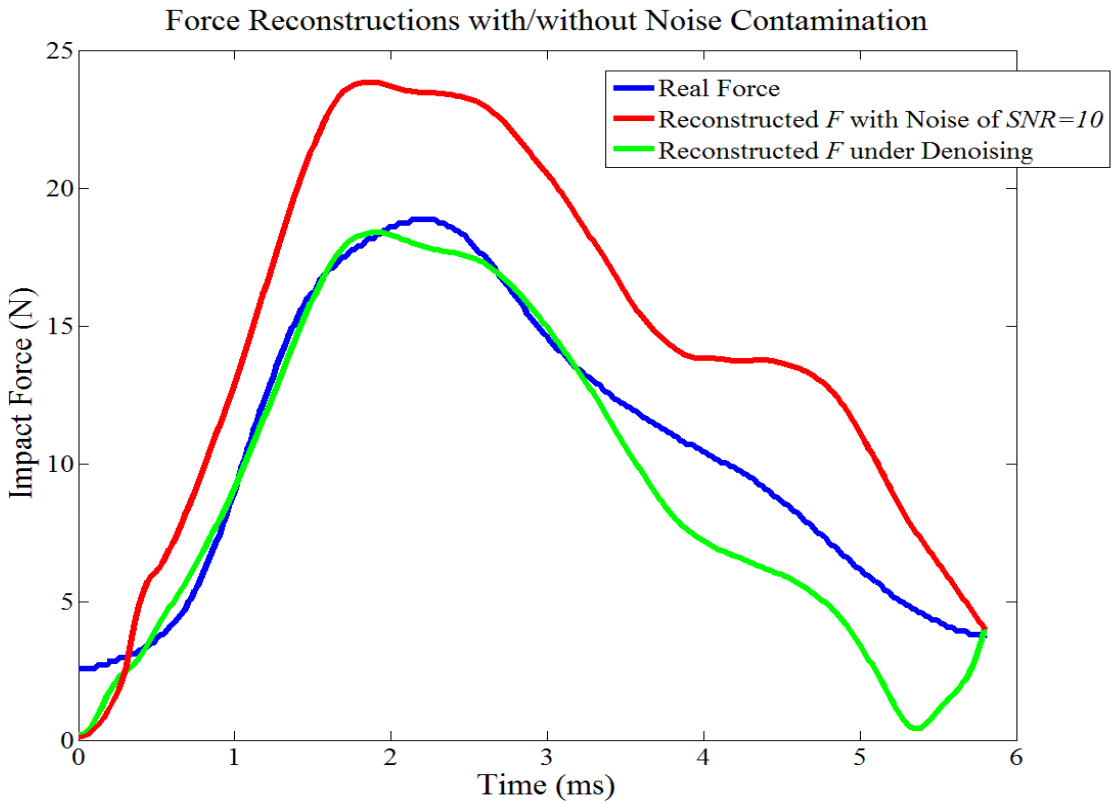


Figure 10.26 Force reconstruction with and without vibration noises of $SNR=10$

Table 10.2 Impact evaluation results within vibration noises of SNR=10, 15 and 20

Impact Event		Real	Estimations by Denoising	Estimations within Noises
SNR10	Maximum amplitude (Unit: N)	18.84	18.38	23.83
	Impulse (Unit: N·s)	0.06	0.05	0.09
SNR15	Maximum amplitude (Unit: N)	43.28	44.35	49.62
	Impulse (Unit: N·s)	0.09	0.11	0.13
SNR20	Maximum amplitude (Unit: N)	54.12	54.26	49.35
	Impulse (Unit: N·s)	0.11	0.12	0.14

10.5 Validation for Various Types of Impactors

In this section, three kinds of impactors were used to implement impact tests on specimen 2. As for the three types of impactors, three impact balls with different materials and masses were adopted separately in impact tests. They were a rubber ball, a plastic ball, and a steel ball. The three different balls have different hardnesses and weights, which are presented in Figure 10.28. Further, for the hardness, the balls stand for soft, medium and hard, respectively. As mentioned in the previous Chapter 5, the relation is considered to be linearly dependent, between which are the structural dynamic (impulse) responses resulting from a random impact and the impact force. Thus, by using the various impactors, random impact experiments were executed to verify the robustness and efficacy of force reconstruction for the impact monitoring and identification methodology developed, and to analyze the effects of force reconstructions due to different impactors.

Consequently, a network of the inverse impulse response function matrix \hat{G}_s^f needed to be built from a series of impact tests using the impact hammer with a kind of hammer tip. The plastic hammer tip was selected as a standard reference to generalize various impact conditions, and the weight of the hammer was 239.15 g. Then, using the inverse IRF matrix

network obtained from the impact of the plastic tip, force reconstructions could be implemented in various impact tests with different impactors.

The evaluated results of force reconstructions with different impact balls are presented in Figures 10.29, 10.30 and 10.31. With the universal inverse IRF matrix network obtained, the reconstructed results from the computation model of impact identification match well with the actual impact forces recorded concerning both maximum amplitude and force duration. Moreover, using the three evaluation parameters that are maximum amplitude, force duration, and impulse, it is concluded that the corresponding average errors are mostly less than 12.7%.

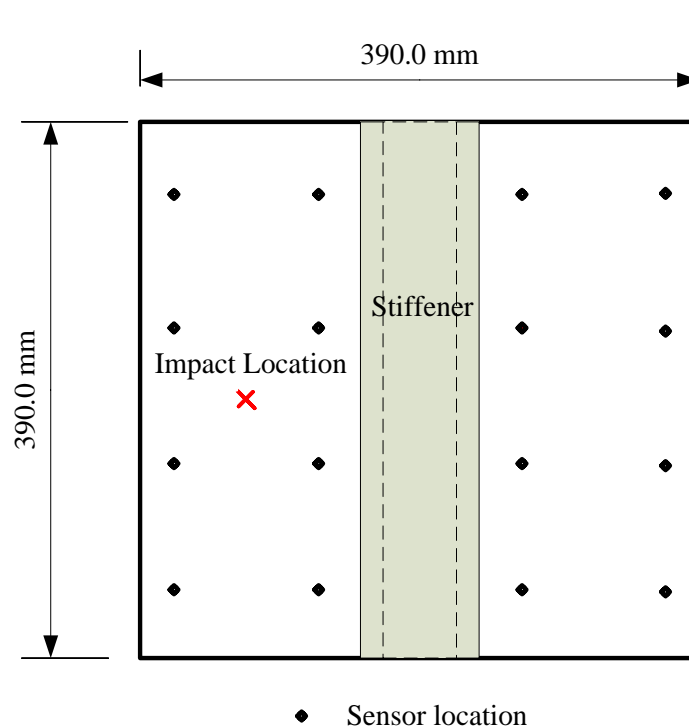


Figure 10.27 Validation tests at a same location for various impactors




Diameter (mm)	15	20	25
			
	Steel	Rubber	Plastic
Weight (g)	163.9	96.5	79.3

Figure 10.28 Three types of impactors used to impact tests on Specimen 2

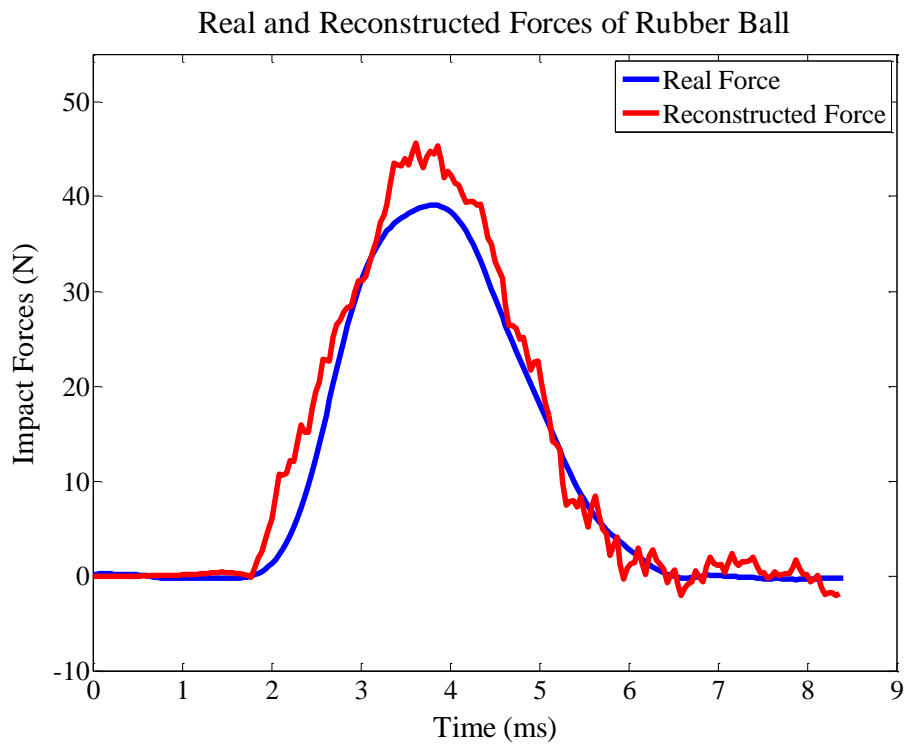


Figure 10.29 A force reconstruction due to impact from the rubber ball

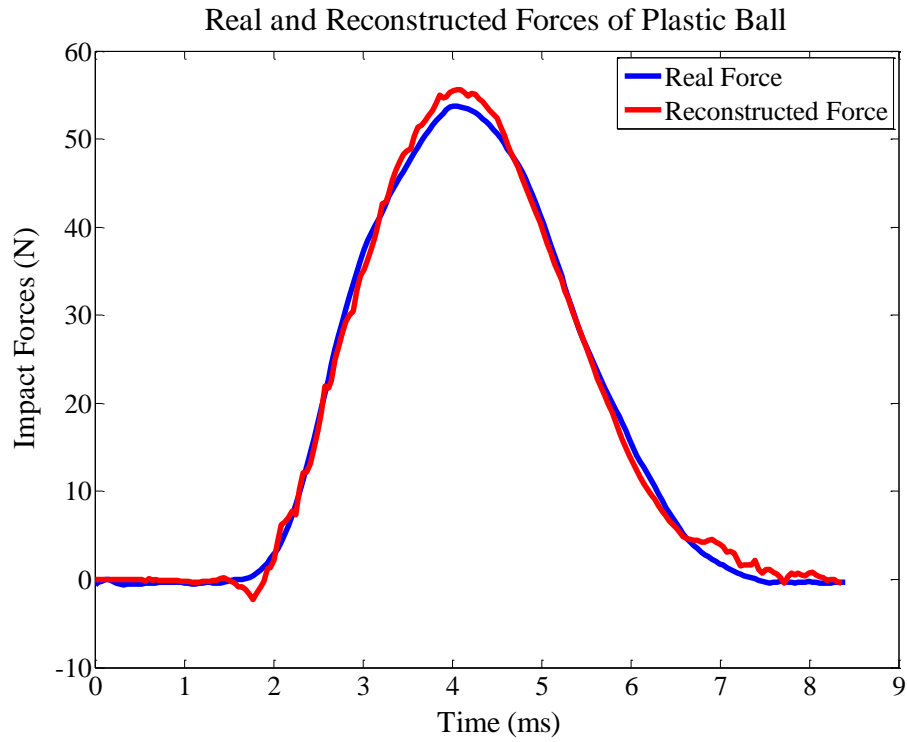


Figure 10.30 A force reconstruction due to impact from the plastic ball

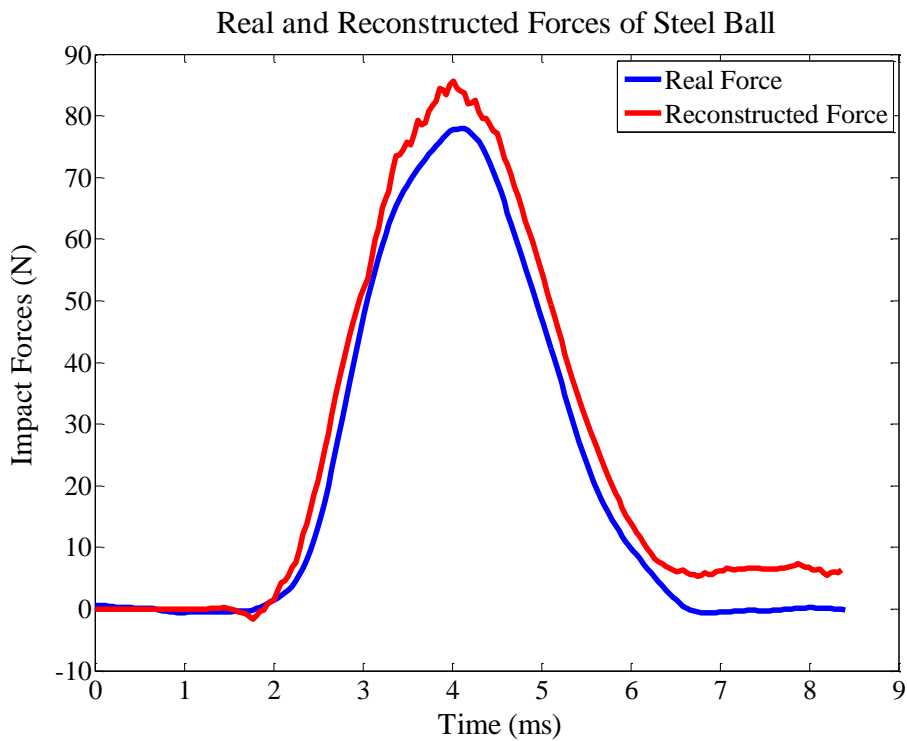


Figure 10.31 A force reconstruction due to impact from the steel ball

10.6 Structural State Assessment – Damage Identifications

In this section, a series of the evaluation results of multiple damage identifications are presented, using the developed damage index parameters that are the energy density metric, the energy time-phase shift metric and phase divergence metric. From the damage assessment results, the developed rapid multi-damage identification approach offers a great opportunity to apply in the practical inspection and maintenance for engineering structures. Thereby, to achieve the goal of the SHM based structural design criteria, the ensemble structural health monitoring and identification technique makes a significant and steady progress, and provides an opportune platform.

10.6.1 Judgment of the Damage Presence by the Transient Analysis Based on

FEEMD

A transient analysis and judgment (TAAJ) method based on FEEMD was developed and executed to determine the presence of any damage in a laminated composite. The details on the methodology, advantages and validation of the TAAJ method have been described completely in Si' paper [66]. Here, it is only presented that the evaluation results for the judgment of single or multiple damage presence using the developed TAAJ method were validated. And an interpretation on the merits of the TAAJ method is also supplemented.

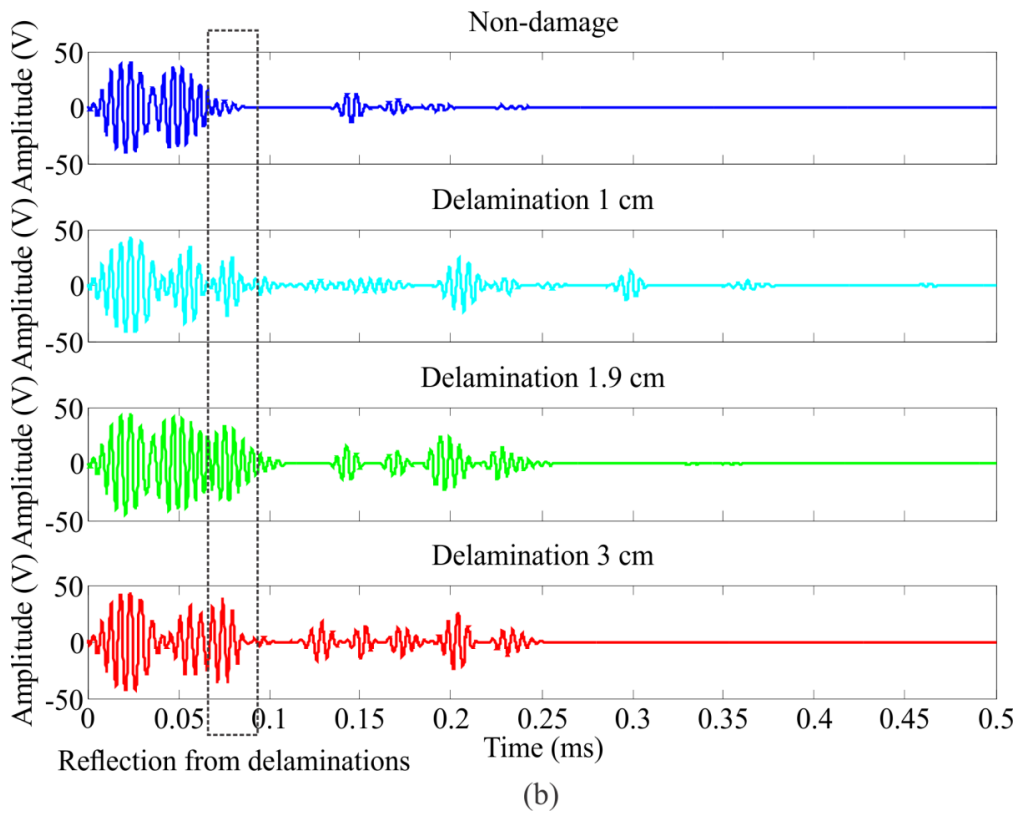
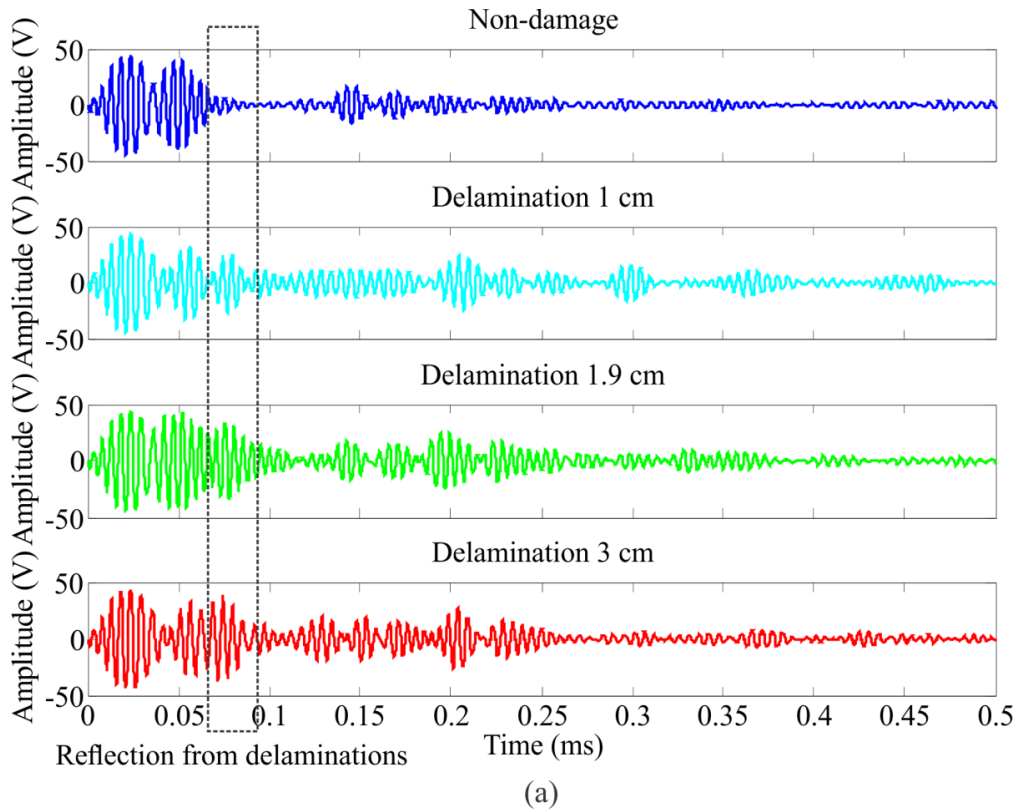


Figure 10.32 Comparison for the judgments of damage presence using two different baseline methods: (a) the conventional baseline method based on original response signals, (b) the new proposed baseline method based on decomposed IMF components.

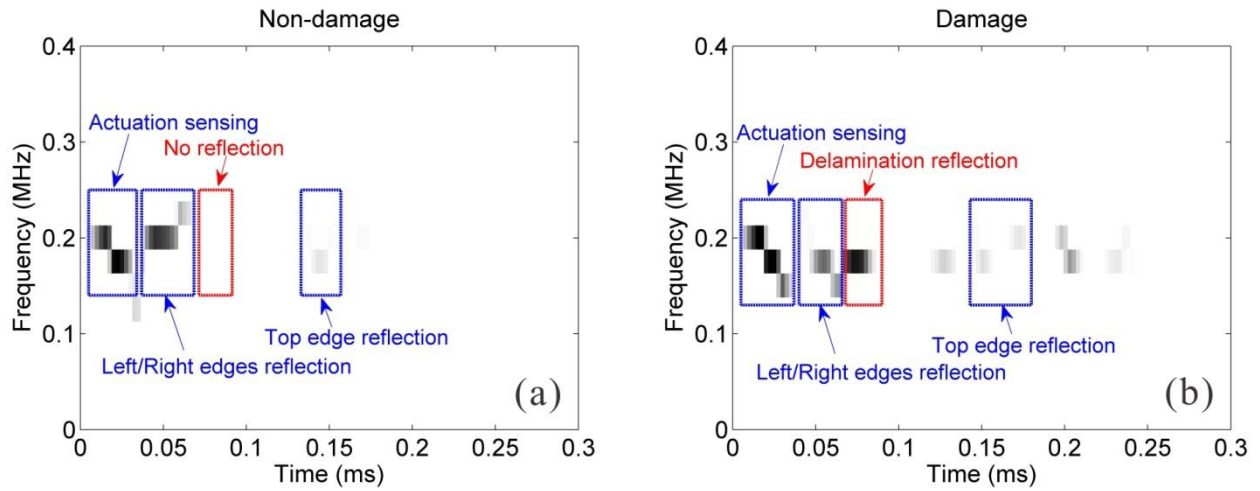


Figure 10.33 Judgement of damage presence using the energy density metric: (a) no reflection no damage, (b) reflection appearance damage presence.

Here, to reveal the merits of the new IMF based baseline method to determine damage presence, the two instantaneous phases resulting from an original response signal and the corresponding decomposed IMF components are shown in Figure 10.34.

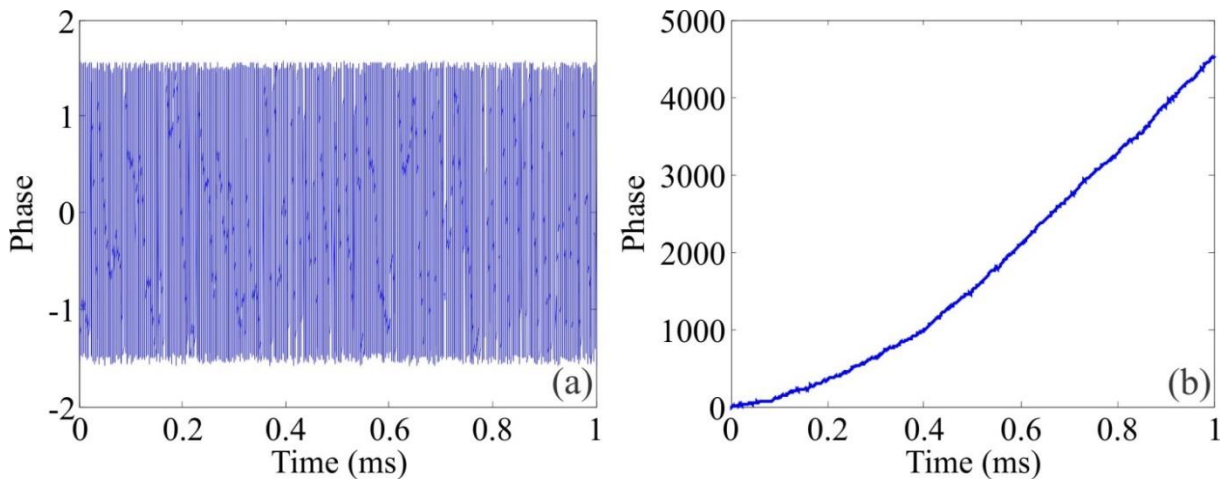


Figure 10.34 The unwrapped instantaneous phases with the delamination of 1.9 cm diameter computed from the original signal (a) and from the IMF components obtained using FEEMD (b).

10.6.2 Multiple Delaminations Quantification and Track by Energy Density Metric

The primary validation to how the energy density metric (EDM) utilizes the time-frequency spectra to quantify multiple delaminations and trace the increasing delaminations has been presented in detail in Si's paper. Here, the evaluation results of multiple delaminations quantification using the energy density metric are only shown in Figure 10.35, where the energy density E can be visualized through the color intensity. Furthermore, a linear damage prediction trend curve is constructed to predict the possible growth of damage, which is illustrated in Figure 10.36. This proposed damage prediction trend curve achieves the rapid damage identification for a laminated composite easily.

In the meantime, with the use of its confidence value as P-value, the reliability and accuracy of the EDM thereby get the improvement on identifying any damage in a structure. In this case, it provides a higher possibility for the energy density metric to employ in the actual engineering applications.

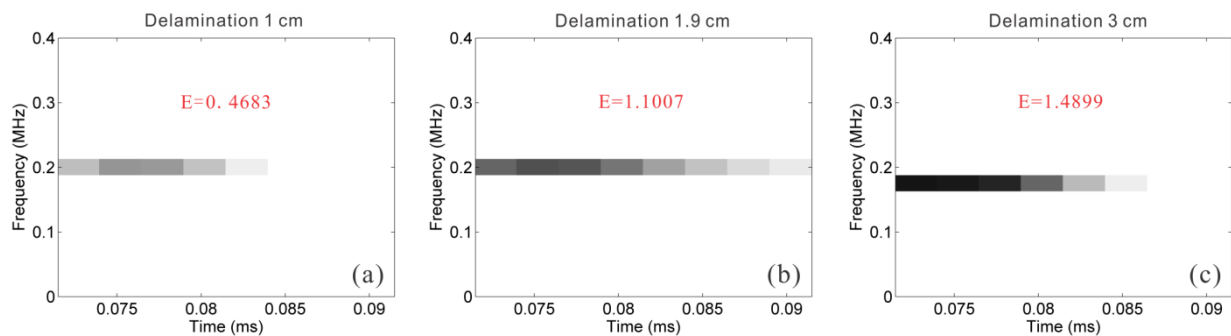


Figure 10.35 Energy density metrics used to quantify multiple delaminations in an examined laminated composite: (a) a delamination of the 1.0 cm diameter, (b) another delamination of the 1.9 cm diameter, (c) the other delamination of the 3.0 cm diameter.

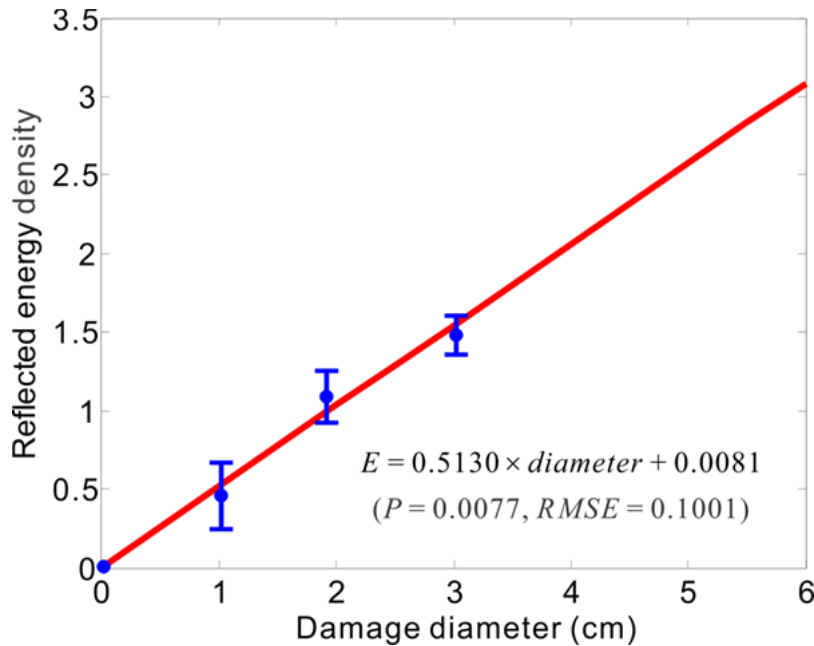


Figure 10.36 Damage prediction trend curve provided by the energy density metrics to trace damage growth.

10.6.3 Multiple Delaminations Identification and Track by Energy Time-Phase

Shift Metric

The significant validation has also been presented systematically in Si's paper. It interprets comprehensively how the energy time-phase shift metric (ETPSM) uses the energy time spectrum to determine the useful time-of-flight (TOF, or time-of-arrival (TOA)), and to locate accurately multiple delaminations using the obtained TOF information, and further to trace the progressive delaminations using the damage index TOF. Here, the evaluation results of the localization and quantification of multiple delaminations are only presented in Figure 10.37, where the sufficient TOF information are used and obtained from the constructed energy time-phase shift metric.

Meanwhile, a rapid damage prediction trend function (curve) is linearly established to predict the possible growth of damage, as shown in Figure 10.38. This developed damage prediction trend function realizes the combination of damage localization and quantification for a laminated composite easily. At the same time, with the use of its confidence P-value, the robustness and accuracy of the ETPSM thus gain the enhancement on assessing any damage state in a structure. In this case, it also offers a great opportunity for the energy time-phase shift metric to apply to the real engineering structural inspections.

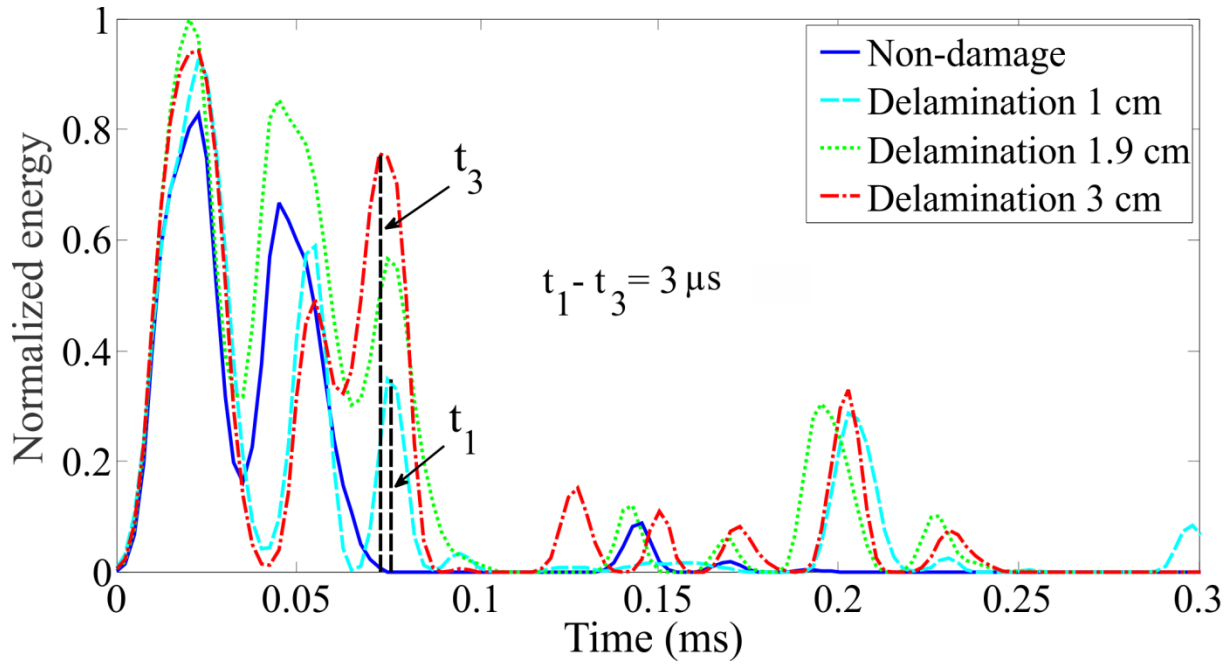


Figure 10.37 Energy time-phase shift metric used to quantify multiple delaminations and extract the required TOF information for locating the delaminations.

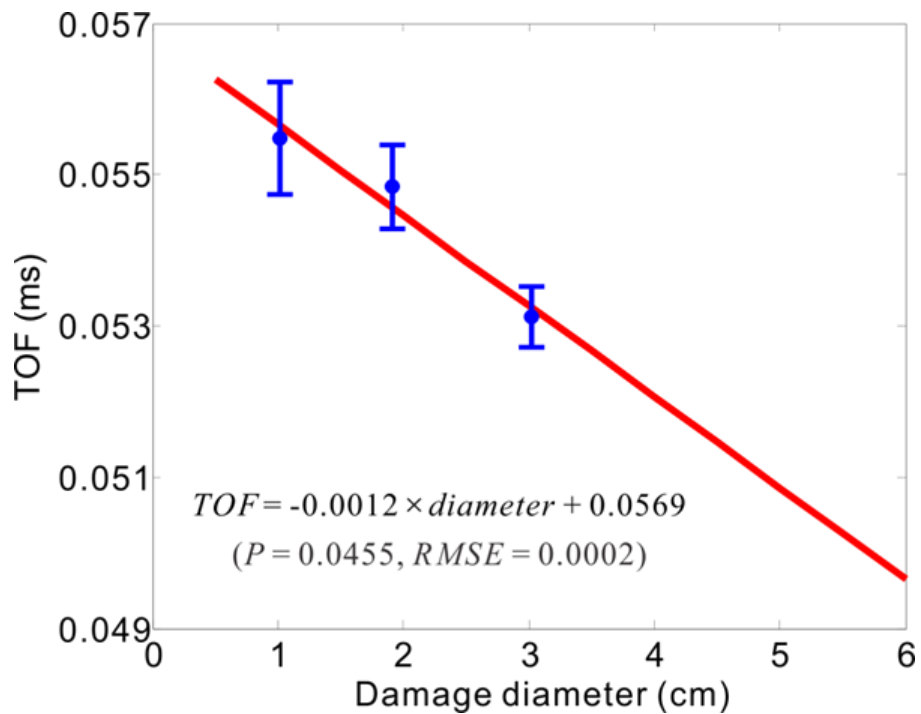


Figure 10.38 Damage prediction trend curve based on the TOF variables to trace the increasing damage.

10.6.4 Multiple Delaminations Identification and Track by Phase Divergence

Metric

A new damage index parameter – the phase divergence metric (PDM) is proposed and utilized to execute the localization and quantification of multiple delaminations in a laminated composite using the phase divergence with regard to time variation. What's more, as any damage in a structure grows possibly, it can be traced by the root-mean-square phase deviation (PDrms) between the phase functions of the damaged case and undamaged case. The theoretical basis of the phase divergence metric has been interpreted detailedly in Section 6.2.2.3.

The instantaneous unwrapped phase is represented as the generalized phase radian of propagating Lamb waves associated with the time evolution. The unwrapped phases as the function of time are presented in Figure 10.39, where the phase curves of the four cases that are the undamaged, damage of 1.0 cm, damage of 1.9 cm and damage of 3.0 cm indicate the individual changing slopes with time alteration. Actually, the multi-damage identification capability of the phase divergence metric has been validated through the experimental tests with the progressive delamination patches of 1.0, 1.9 and 3.0 cm. To obtain an appropriate phase function curve of Lamb waves traveling in a laminated composite, the phase function curve is unwrapped once, and the value of the phase is added 2π when the absolute value of the phase difference between two consecutive time points satisfies $\frac{3}{5}\pi$ in radian, depending on demands.

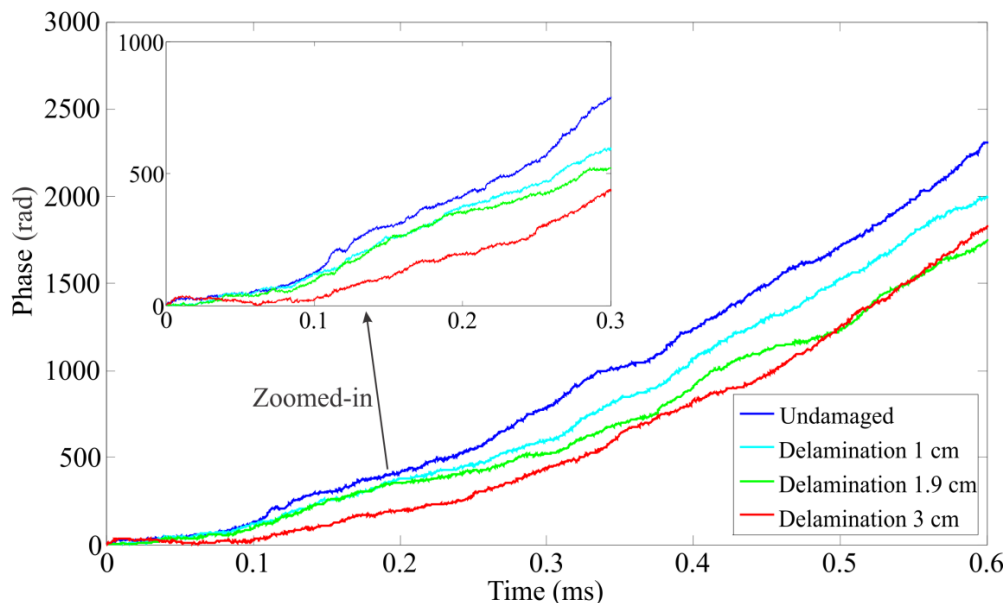


Figure 10.39 Phase divergence metric to identify multiple delaminations in an examined laminated composite.

To verify the stability and dependability of the new damage index parameter to identify multiple damage in a laminated composite, the phase divergence metric is obtained from the different frequencies of pitch-catch wave signals through the means of acousto-ultrasonics. As shown in Fig. 10.40, the evaluation results of multiple delaminations identification using the PDM damage index are compared in the frequencies of 160 kHz, 180 kHz and 200 kHz. Through the comparison result, it is not difficult to conclude that the new PDM damage index can be applicable to quantify robustly multiple damage, and to locate multiple damage in a laminated composite by using the required TOA information in cooperation with the corresponding wave group velocity.

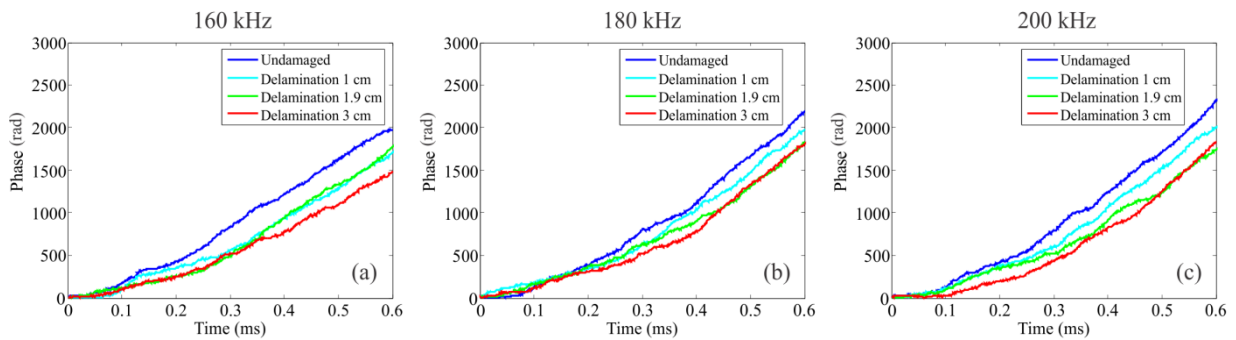


Figure 10.40 Phase divergence metrics in different frequencies to indicate the reliability and stability of the PDM to identify multiple delaminations: (a) phase divergences due to delaminations in 160 kHz frequency, (b) phase divergences due to delaminations in 180 kHz frequency, (c) phase divergences due to delaminations in 200 kHz frequency.

The root-mean-square phase deviations of the three sizes of delaminations were estimated using Equation (6.7), and the phase in the undamaged case was taken as the reference. The estimated values of the PD_{rms} for the delaminations of 1.0, 1.9 and 3.0 cm are 0.1360, 0.2593 and 0.3152, respectively. From Fig. 10.41, it can be seen that the alteration in the PD_{rms} values is positively proportional to the increment the damage sizes, in other words, the damage sizes grow as the PD_{rms} values increase. In addition, the damage predictive trend curve based on the PD_{rms} indicates comparative perfectly the linear relationship between the PD_{rms} and damage sizes, which satisfies then the linear regression function: $PD_{rms} = 0.0882 \times d + 0.0634$, where d means damage diameter, as represented in Figure 10.41. The damage predictive trend curve based on the PD_{rms} presented in Figure 10.41 actually provides a rapid way of damage assessment for a laminated composite using the FEEMD based Hilbert spectral analysis of noninvasive signal data processing method. To validate the credibility of the PD_{rms} based damage prediction trend curve to the demanded structural damage (state) assessments, it is essential to estimate the two regression parameters that are the confidence P value and the root-mean-square error (RMSE) of the linear damage

prediction curve. Through the evaluation of the two regression parameters, the estimated confidence P value is 0.0418 falling within the required confidence range $P < 0.05$, and the RMSE of the damage prediction curve is obtained at the value of 0.0201. Accordingly, the PD_{rms} based damage prediction trend curve constructed is sufficient to the demand of actual structural state assessment.

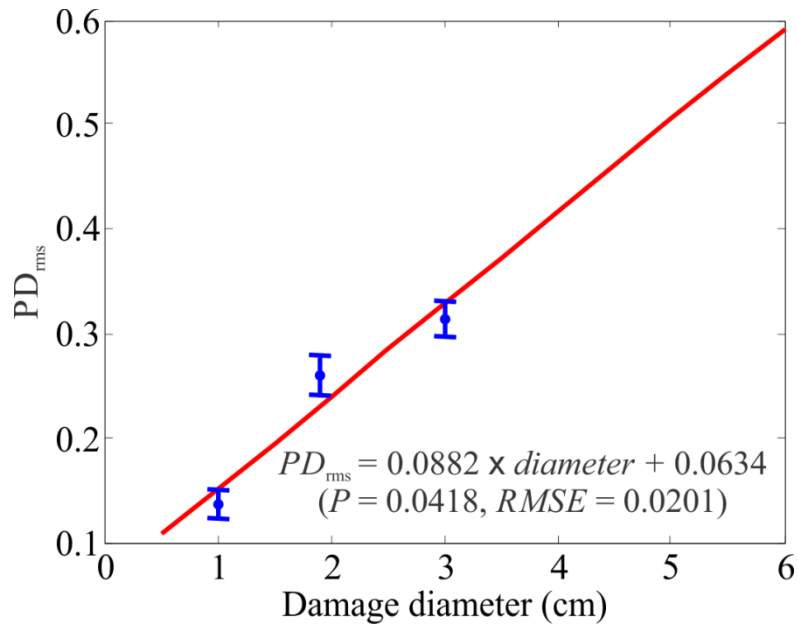


Figure 10.41 Damage prediction trend curve constructed by the RMS phase deviation for damage growth prognosis.

From the above validation results, the phase divergence metric is also enabled to offer a great opportunity for the phase divergence metric to apply to the online health state inspections for engineering structures.

10.7 Discussion

It is worth noting that the requirement for the high accuracy of impact identification relies on the determination of the network of impulse response functions. However, to construct the appropriate network of IRFs for a given structure, it is concluded from two essential prerequisites:

1) More training data sets are perhaps indispensable once one needs to build a finer network of IRFs for a composite structure that has complex geometry and varying mechanical properties within the whole structure. Therefore, to achieve this demand easily, the impact identification module based on FE models can be fast to obtain any grid network from a practical requirement, through the simulating computations.

2) In view of the applicability of actual engineering, the transient dynamic responses due to impacts are duplicated at the symmetrical locations within a symmetric structure. But in case the location of each sensor was laid out individually due to the practical demand, it may result in a challenge in the application of large-scale structures. The response data from sensors might still need to be gathered even if similar areas are at symmetrical locations in a complex composite structure. Nevertheless, the FE model based impact identification module can be adaptive and fast to obtain the database from structural responses and overcome the above shortcoming completely, but also, it can obtain any required response data set easily from any complex structure. Consequently, it could be qualified for applying the ensemble SHMI technique to monitor in real-time any accidental impact event that causes possible damage in a large-scale aerospace composite structure.

In addition, the other important point needs to be mentioned that when the strain waves are propagating in an anisotropic laminated composites, the wave velocities are variable as the propagation angles of the waves are diverse, which is resulting from the complex anisotropic material structures of the composites. Furthermore, the material anisotropy of a structure does also affect the accuracy of the TOA (TOF) computation due to the variations of wave propagations such as the propagation path variations resulting from the structural discontinuous configurations of anisotropic composites. However, the consequences of the anisotropic property of composites on the impact monitoring and damage identification have been taken into consideration in the proposed SHMI method, as the map of wave velocity distribution with the variation of the propagation angles is described in Section 9.3.4.1. A variety of composite structural configurations were employed in the validation tests, and the corresponding evaluation results on the impact and damage identifications are presented in Chapters 9 and 10. Meanwhile, the proposed advanced spectral analysis method described in Section 6.2.2 indicates its capability to access the accurate TOF information under the disturbance of a structural anisotropy. With taking into account the anisotropic material

property of composites, the developed SHMI method has been validated to its performance of robustness and reliability through a series of experimental tests using the different structural configurations of composites, as described in this chapter. Actually, using the SHMI method, the effect on the evaluation (identification) accuracy due to the material anisotropy of a laminated composite structure is usually small, unless the structural anisotropy is extremely high. However, in the performed experimental tests as described in Chapter 10, the effect on the evaluation accuracy due to the structural anisotropy such as with a $[0^\circ / 90^\circ]_s$ laminate and also with a stiffener is controlled in the average error ratio of 3% less, in contrast to that of a quasi-isotropic structure where the error is even lower.

10.7.1 Discussion for the Interval of Impulse Response Function Points

After the sensor interval is determined, the network of impulse response functions should be established through a certain training procedure, which can be implemented conveniently in the FEM simulation using the FE model built. As discussed in Chapter 5.2, the accuracy of the impact identification in Eq. (5.62) depends mainly on the interval of impulse response function points. Generally, the accuracy of impact identification increases as the interval of IRF points decreases. However, the interval of impulse response function points can be determined in accordance with the demanded accuracy, which can be achieved through a set of impact verification tests.

To reveal the effect of the selected interval points, a set of impact verification tests were conducted. The piezoelectric sensors were attached to a laminated composite panel with the uniform interval that was 110 by 110 mm². And then, impulse response functions were obtained firstly at the four points with a particular interval. Subsequently, a set of impact evaluation tests were implemented at the evaluation points that are all inside of the region composed of the four impulse response function points. The impact forces at the set evaluation points were reconstructed using Eq. (5.62) combining with the four impulse response function matrices found. An example of the evaluations of impact identifications with a specified interval of IRF points is demonstrated in Figure 10.42. Nevertheless, the impact forces that need to be evaluated were reconstructed at the selected 21 evaluation points evenly distributed inside of the specified IRF region; wherein three representative evaluation points were only chosen to indicate their results of force reconstructions in Figure 10.42.

From Figure 10.43, it is not difficult to see that the average error with a certain interval increases as the interval increases. In this case, if the mean error is required to be less than 10%, the interval should not be more than 200 mm; and if the demanded accuracy is admitted to 20%, then the interval can be increased to 430 mm. For any demand accuracy of impact identification, the interval of IRF points can thus be determined through a set of impact verification tests.

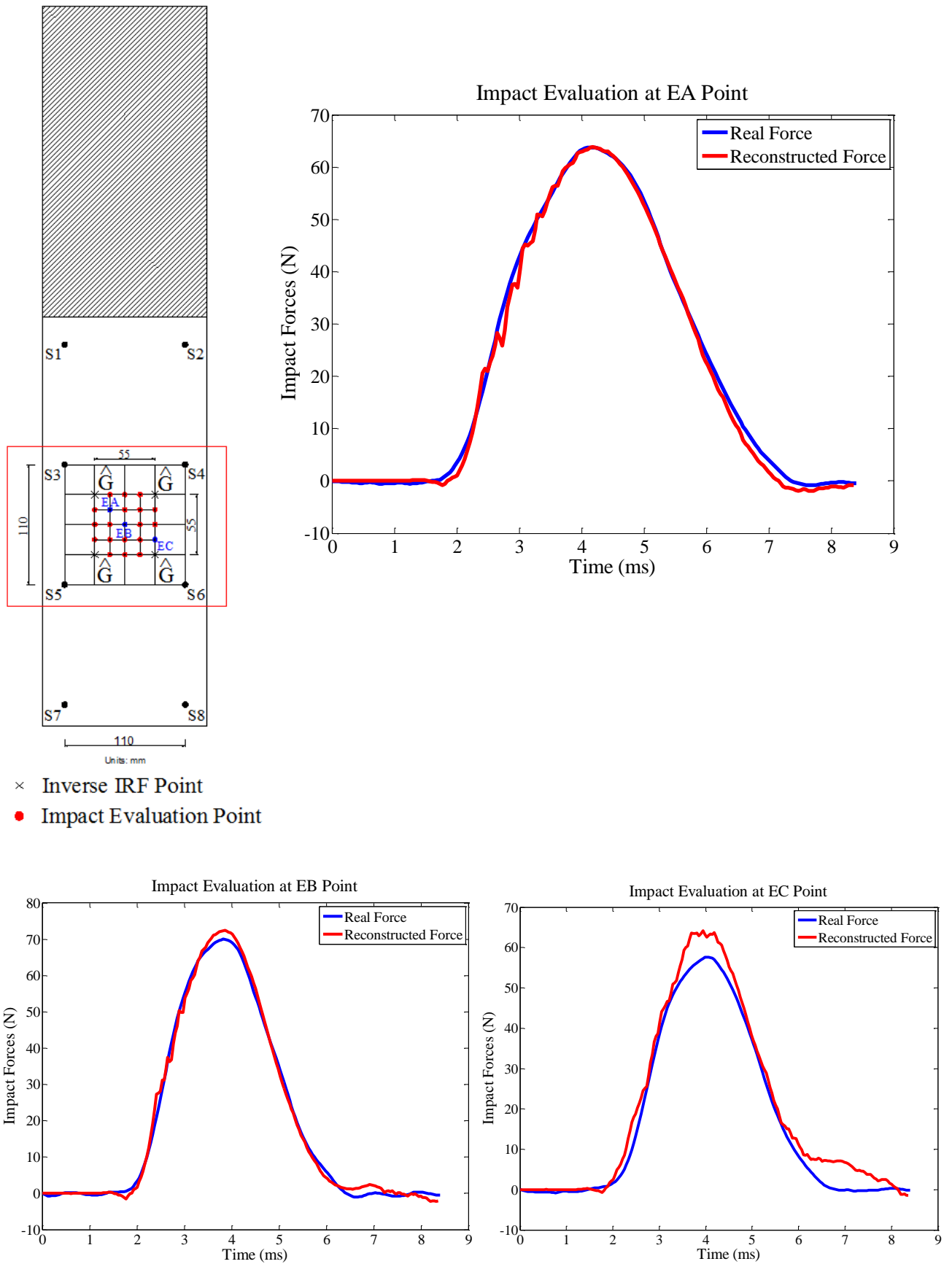


Figure 10.42 Evaluations of impact identifications with a specified IRF interval

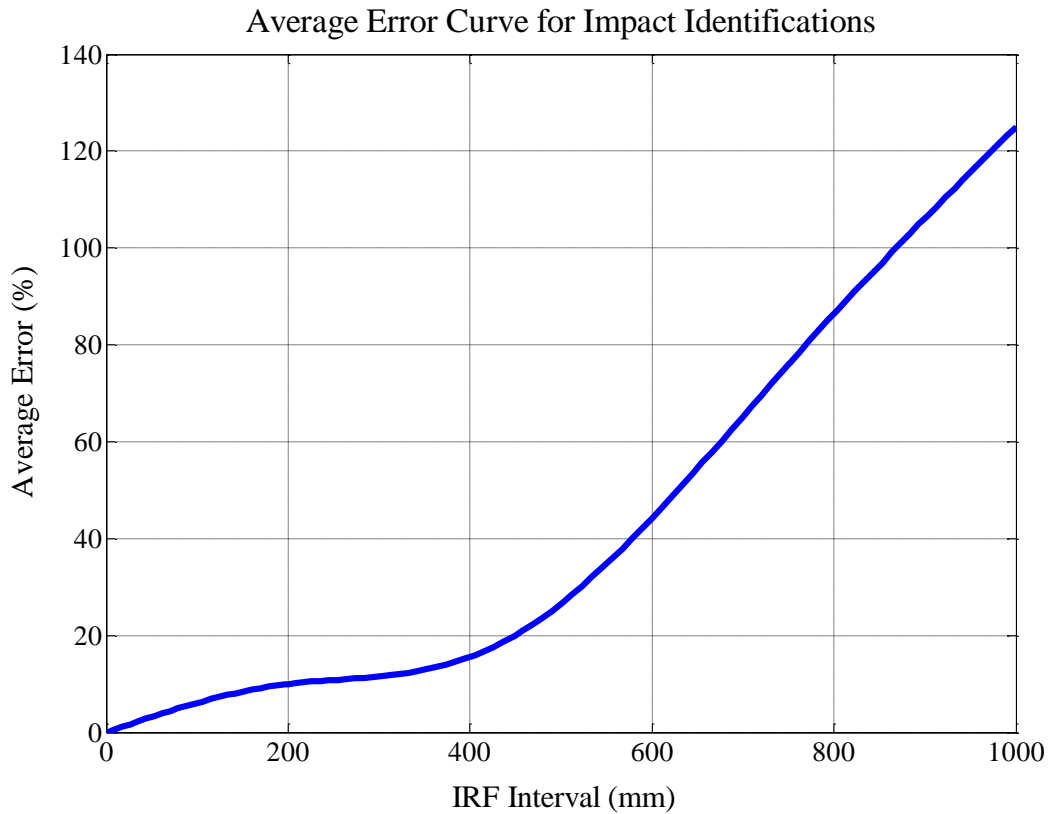


Figure 10.43 Variation of the average errors for impact identifications versus to the IRF intervals

10.7.2 The Discrimination of Damage Identification Using the RMDI Approach

The discrimination of damage identifications is a significant research focus in many developed damage identification methods. The damage discrimination (DD) capability is the sensitivity performance of a damage identification method to the damage severity. Thus, the damage discrimination is an important criterion to measure a damage identification method. Due to the significance of the damage discrimination, the following discussion is presented from Si's paper [66]:

Actually, in our validation experiments of damage identifications, the PZT sensors that were laid out between the PZT actuator and delaminations region didn't affect the damage identification results evaluated by the developed RMDI approach. The reasons are as follows:

It is small enough to be negligible that the sensors affect the analysis and estimation of the collected signals. Since the diameter of a sensor is 0.6 cm, then the minimum size of which a probing wave is sensitive to a discontinuity is 1.0 cm. Thus, the propagation of a probing wave including wave velocity, propagation direction and so on isn't affected by the sensors,

most of the rightward propagation waves all diffract across the sensors, because the size of a sensor is much less than the minimal sensitivity size. Secondly, due to the delaminations seeded in the middle of the tested composite panel, they didn't emerge on the surface of the panel. As the laid sensors were affixed to the surface of the panel, wave propagation should not be affected much with the consideration of the boundary condition when the Lamb waves were actuated from the actuator. This has been proven by the experimental validations as well. Therefore, the influence of the sensors' reflection is negligible and isn't taken into account for the implementation of the developed RMDI approach.

10.7.3 Time Resolution for the Time-Of-Flight

The time resolution of the time-of-flight (TOF) for damage identifications is a difficulty and research hotspot in the online in-situ damage inspection (DI) applications. It is a challenge to select an efficient estimation method of the time-of-flight, as the accurate extraction of the time of arrival of the instantaneous waveform is very difficult under complex and adverse engineering environmental conditions such as recorded sensor signals having low signal-to-noise ratio [66]. Actually, the developed RMDI approach based on the FEEMD decomposition effectively overcomes the difficulty. The more merits of the RMDI approach have also been discussed in Si's paper. Here, the time resolution problem of the TOF for the dead zones of damage identifications will be discussed. The following discussion on the time resolution of the TOF is also presented from Si's article [66]:

The RMDI approach meets a challenge that the reflections from boundaries mix with the reflections from the delaminations. And the issue of the reflections from the left/right and top boundaries had been addressed in Subsection 10.6.1, of which two estimation results have been shown in Fig. 10.33. Although the boundary reflections may increase the difficulty of damage inspection and identification, it doesn't affect the implement of the developed ETPSM to damage identifications. The proposed ETPSM can be applied in a more extensive condition as the time of arrival (TOA) for a delamination is determined by the peak of the reflection energy of a probing wave using the Hilbert spectral analysis, rather than the direct information of wave packets. If the peaks of the two energy reflections during the wave propagation can be distinguished, the time of arrival of each energy reflection can be evaluated and thereby the corresponding damage can be located and identified. Since the reflected energy is defined as the overall energy accumulated within the time period of full width at half maximum (FWHM) of the energy peak, the reflected energy from a delamination may be overestimated if the wave reflections from diverse discontinuities or wave packets overlapped overmuch, and then the estimation of damage dimension may not be accurate either. In this case, Gaussian curves are used to fit the energy curves of peaks and each reflected energy is approximated as the integration of the Gaussian function over the period of full width at half maximum of the Gaussian peak. In summary, the ETPSM

proposed in this study can also be applied in the case scenario of wave packets overlapping. However, the ETPSM may not work in the case when two peaks of the energy reflections completely overlap. As shown in Fig. 10.44, the minimum time resolution of arbitrary two energy peaks of reflected wave packets that can be differentiated is around $5.7 \mu\text{s}$, which corresponds to 1 cm in wave propagation distance. The dead zone is defined as the region within 1 cm from a structural boundary. But actually in real engineering cases, damage within the range of 1 cm from a structural boundary may not exist.

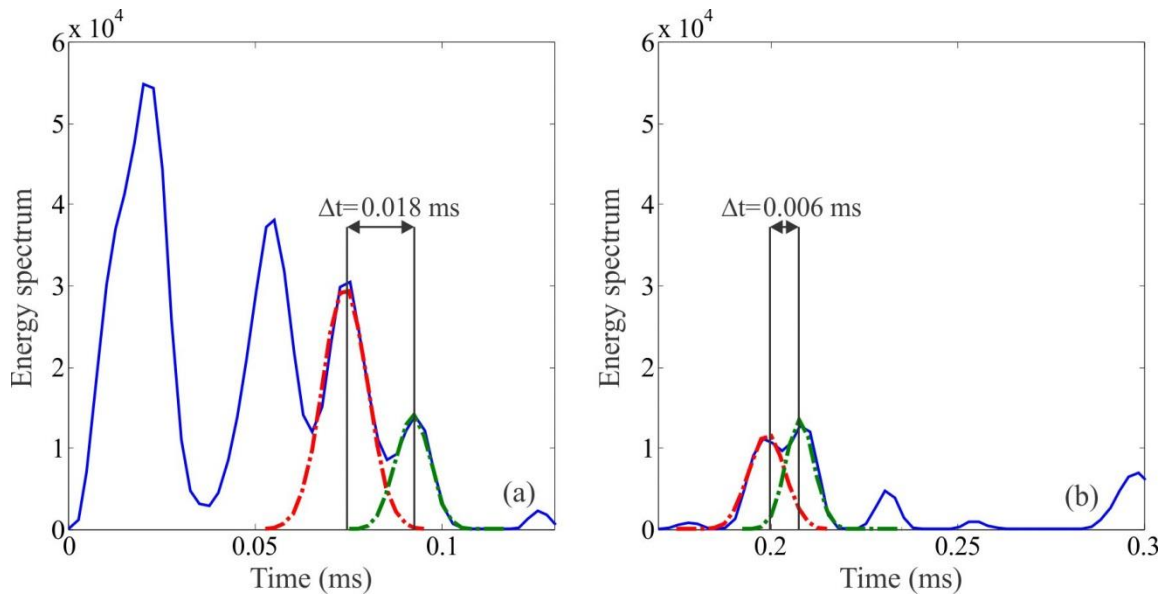


Figure 10.44 Time resolution instructions for the problem of dead zones: (a) the medium overlap of the energy reflection spectra from reflected wave packets, (b) the strong overlap of the other energy reflection spectra from reflected wave packets.

11. Conclusions and Outlook

The last chapter is interpreted synoptically as two parts, which are 1) the conclusions that summarize the reliable and robust performance of the developed ensemble structural health monitoring and identification technique on the capability of impact monitoring and damage identifications; and 2) the outlook that forecasts further expansive work in this research direction.

11.1 Conclusions

In this dissertation, a systematic structural health monitoring and identification scheme is presented. By using the adaptive distributed sensors networks designed, a robust in-situ ensemble structural health monitoring and identification technique is proposed and developed to estimate the impact locations, the force histories including the information of the force magnitudes, and to evaluate the structural conditions by calculating the signal energy distributions so as to determine the corresponding model orders caused by the impacts, what's more, to assess the structural states by identifying the severity of damage including the number of damage, the extent and location of each damage, furthermore by the damage prediction trend functions (curves) constructed using the three damage index parameters – the multi-functional multi-metrics, which is able to trace the progressive damage in a laminated composite structure.

For the entire automatic identification procedure, owing to the fact that an accurate (or called robust) forward model is essential and crucial to impact identification, in other words, it affects the accuracy of impact identification whether the forward model is precise or robust enough, even an incorrect or unstable forward model may lead to the failure of impact identification. Nevertheless, the accurate forward model for a given structure can be established rapidly using the function module of the forward model generator from the proposed ensemble structural health monitoring and identification technique. Meanwhile, by incorporating the dynamic state-space model, the impact forces can be reconstructed with few number of impulse response functions derived from the optimal model parameters (a_i, b_j) calculated using the proposed fast genetic algorithm parameters estimation during the modeling of the dynamic prediction model, which eliminates the need of numerous impact training for constructing the network of impulse response functions grids for a structure. Nevertheless, in the impact positioning and evaluation procedure, the initial impact locations can be estimated using the developed smoothed energy distribution method; afterwards, on the basis of the results from the initial location estimations, each recognized region due to an impact made up of four sensors can be determined. Subsequently, the accurate location coordinates of each impact can be updated further using two different localization methods

that are 1) the proposed time-of-flight (TOF) based quadrilateral sensor network positioning method, and 2) the defined cost-function based positioning method. Moreover, the other significant aspect of the ensemble SHMI technique is able to assess the state of a monitored composite structure through the developed integral multi-damage identification approach. Once damage is generated in a structure due to impacts or other objects, the multi-damage identification approach can execute rapidly the damage judgment, the damage localization and quantification, furthermore evaluate the possible damage growth using the damage prediction trend functions. Here, it needs to indicate that the above damage identification issues are implemented all by using the proposed and developed damage indices – the MFMMs, which are separately the energy density metric, the energy time-phase shift metric and phase divergence metric. This dependable in-situ ensemble SHMI technique shows satisfactory success in predicting impact locations and estimating force histories for various types of structure configurations and under varying vibration environmental conditions, and its capability of structural condition monitoring and real-time structural state assessment using the rapid multi-damage identification approach is also verified. Throughout all the validation cases of relevant experimental tests considered, the ensemble structural health monitoring and identification technique shows its potential as an online on-board diagnosis and assessment tool of accidental impact events and possible damage caused by the impacts in an aerospace composite structure. The performance of the ensemble SHMI technique can be revealed in the following detailed aspects:

1. Positioning and evaluating in real-time the locations of unknown impact events with the prospective error range;
2. Reconstructing in real-time the force histories from unforeseen impact events within the prespecified error limit;
3. Reporting the magnitudes of impact forces in real time mode;
4. Evaluating the structural condition of a fiber composite structure online;
5. Estimating the locations of multi-damage;
6. Quantifying the extents of multi-damage;
7. Assessing the structural state using the damage prediction functions or trend curves;
8. Maybe applicable for large-scale fiber composite structures, typically aerospace vehicle structures.

It is not difficult to conclude from the above eight statements that the developed ensemble SHMI technique can be competent in the aim of impact monitoring of diverse composite structure configurations, even encountering complex adverse environments; also in the objective of the structural state assessment through damage identifications. This technique owns its highly reliable and highly robust performance on impact monitoring and identifications, structural condition evaluations and structural state assessments. In the meantime, the ensemble SHMI technique can overcome the obvious shortcoming of most research investigations on impact monitoring, as it can achieve successfully impact monitoring and identification in complex changeable disturbance environments, particularly in random vibration conditions. Moreover, this investigation with regard to revealing the effects of random mechanical vibrations on impact monitoring and identification has been implemented successfully in our research. In the performance of structural state assessments, the ensemble SHMI technique proposed the rapid multi-damage identification approach to integrally conduct the structural damage awareness, localization and quantification, furthermore to predict and evaluate possible damage growth. Through a series of the executions of structural damage assessments, the technique shows a more comprehensive superiority on damage identifications than other developed damage inspection methods, and it realizes the prospective goal of structural state assessments.

From all of the validation results of the experimental tests, it can be said that the ensemble structural health monitoring and identification technique has a great potential as an on-board monitoring and rapid diagnostic tool of unforeseen impacts and multiple damage for laminated composite structures, even possibly serves for large-scale laminated composite structures.

11.2 Outlook

Based on our existing research achievements that are online monitoring unforeseen impact events, and autonomously connecting and launching the rapid diagnosis and real-time assessment for possible damage induced by the impacts or other adverse objects such as lightning, in the near future, a highly-intelligent and highly-integrated SHM system will be developed, which can implement more significant engineering functions and purposes, such as identifying possible types of damage, prognosis for structural lifecycle, maintenance and operation recommendations while an aerospace vehicle is operating, and even SHM based structural design optimization.

Nevertheless, as our ensemble structural health monitoring and identification technique is concerned, it is referred as a combination of active-passive SHM technique, which does integrate the multi-functional sensor network including both the actuating function and sensing function to bond on/embed in the demanded structures distributively. When a sudden impact occurs, the response signals are recorded by the sensors, and simultaneously the response data are processed and diagnosed to determine the location and force magnitude of the impact applied to the structures, and to evaluate the structural conditions through the energy distribution method; as well as, using the guided Lamb waves excited from the configured sensing network, the structural state evaluation can be implemented through multi-damage identification approach, and then possible structural damage expansions can be predicted by using the damage prediction trend curves.

As for the estimated parameters of impact forces, they can be utilized to correlate with the extents of damages due to impacts in the structures. Thus, an intensive intelligent SHM system that saves time, is low-cost, and doesn't require an aerospace structure system to be out of service will be developed soon and its conceptual systematic frame is presented in Figure 11.1. It is composed of two main parts: impact monitoring and identification (IMI) and autonomous damage identification/inspection (ADI). Then, the smart SHM system requires the deployment of a multi-functional sensor network, where it is necessary to define and configure some sensors as actuators for actively identifying damages in the structures. Further, the locations and magnitudes of multiple impact forces on complex aerospace structures can be estimated accurately by starting up the subsystem of IMI, and then the IMI subsystem determines if any impact force is greater than a set threshold or not, which can be used to determine whether there has been any damage available due to the corresponding impact; subsequently, according to the above result of the determination from the IMI subsystem, the second subsystem of ADI is activated, or not. When the value of any impact force exceeds the set threshold, the ADI subsystem will implement automatically to locate and quantify the various damages which are caused by impacts, such as, delamination, matrix cracking and broken carbon fibers in aerospace structures.

Finally, the multi-functional integrative SHMI system is able to report the structural state with a set of detailed data parameters information automatically, especially, resulting from unknown impact events. Nevertheless, for damage identification actions, the integrative SHMI system can perform the localization and quantification of multiple damage, which are directly (or indirectly) caused by impacts or other objects such as the fabricating process and lightning. The smart integral SHMI system will indicate the evaluated results, as follows:

1. Locations of multi-impacts;
2. Magnitudes of impact forces;
3. Distributed locations of multi-damage such as debonds, matrix breakages and delaminations, which are probably induced by impacts;
4. Severities of multi-damage;
5. Possible types of damage; (Future research focus)
6. Prognosis for structural lifecycle; (Future research focus)
7. Maintenance (or sustainment) and operation recommendations. (Future research focus)

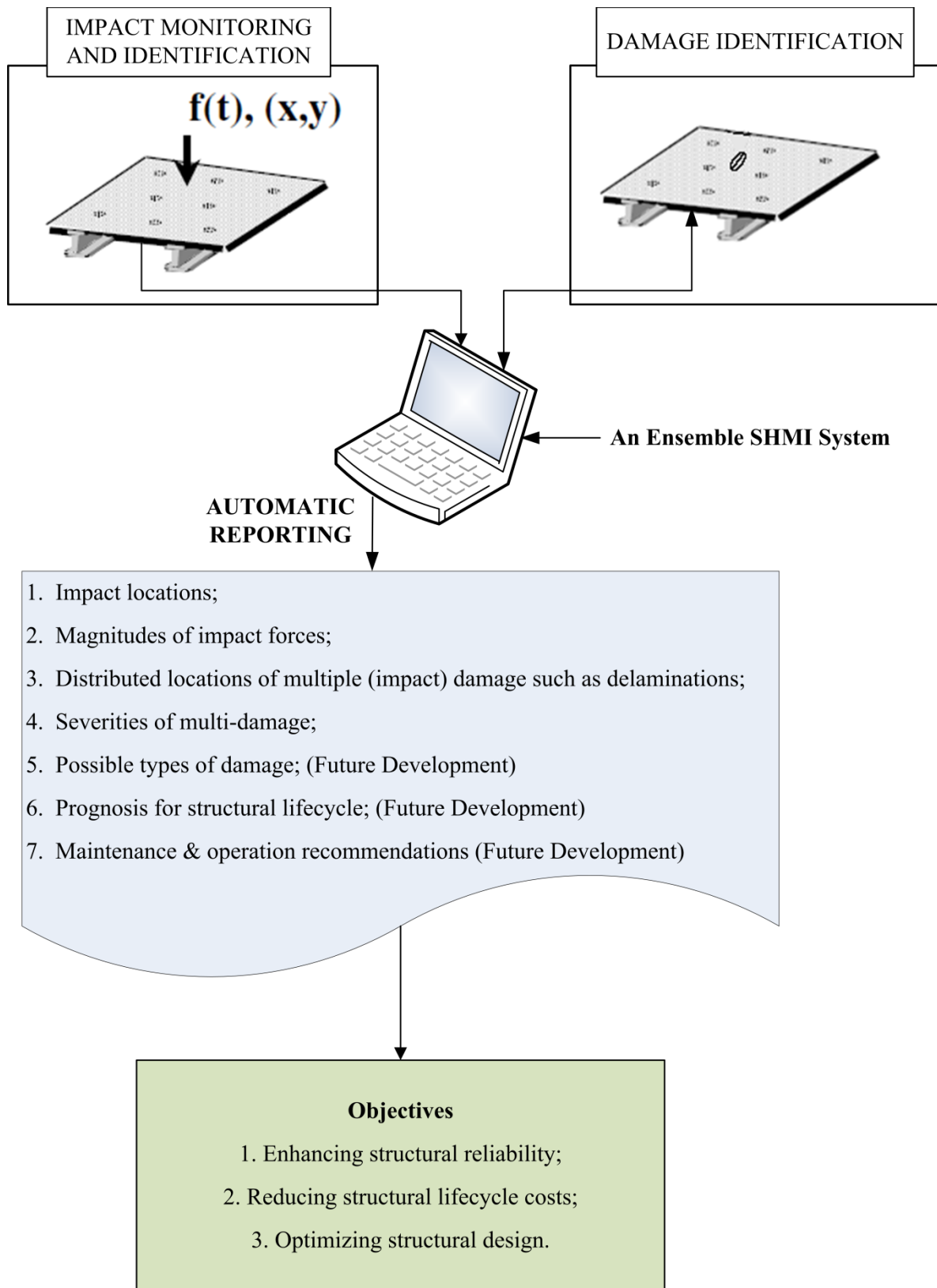


Figure 11.1 A smart multi-functional integrative structural health monitoring and identification system

Bibliography

1. Chang, F.-K., *Structural health monitoring 2000*. 1999: CRC Press.
2. Si, L. and H. Baier, *Real-Time Impact Visualization Inspection of Aerospace Composite Structures with Distributed Sensors*. *Sensors*, 2015. **15**(7): p. 16536-16556.
3. Renshaw, J., et al., *The sources of heat generation in vibrothermography*. *NDT & E International*, 2011. **44**(8): p. 736-739.
4. Genest, M., et al., *Pulsed thermography for non-destructive evaluation and damage growth monitoring of bonded repairs*. *Composite Structures*, 2009. **88**(1): p. 112-120.
5. Lee, B., *Review of the present status of optical fiber sensors*. *Optical fiber technology*, 2003. **9**(2): p. 57-79.
6. López-Higuera, J.M., et al., *Fiber optic sensors in structural health monitoring*. *Journal of Lightwave Technology*, 2011. **29**(4): p. 587-608.
7. Kuang, K., et al., *Plastic optical fibre sensors for structural health monitoring: a review of recent progress*. *Journal of Sensors*, 2009. **2009**.
8. Zhou, Z., et al., *Techniques of Advanced FBG Sensors: Fabrication, Demodulation, Encapsulation, and Their Application in the Structural Health Monitoring of Bridges*. *Pacific Science Review*, 2003. **5**(1): p. 116-121.
9. Schroeder, K., et al., *A fibre Bragg grating sensor system monitors operational load in a wind turbine rotor blade*. *Measurement Science and Technology*, 2006. **17**(5): p. 1167.
10. Majumder, M., et al., *Fibre Bragg gratings in structural health monitoring—present status and applications*. *Sensors and Actuators A: Physical*, 2008. **147**(1): p. 150-164.
11. Dai, Y., et al., *A novel time-division multiplexing fiber Bragg grating sensor interrogator for structural health monitoring*. *Optics and Lasers in Engineering*, 2009. **47**(10): p. 1028-1033.
12. Van Steenkiste, R.J. and L.P. Kollár, *Effect of the coating on the stresses and strains in an embedded fiber optic sensor*. *Journal of composite materials*, 1998. **32**(18): p. 1680-1711.
13. Pohl, R., et al., *NDT techniques for railroad wheel and gauge corner inspection*. *NDT & E International*, 2004. **37**(2): p. 89-94.
14. Barton, D., *Comparative vacuum monitoring: a new method of in-situ real-time crack detection and monitoring*. *Structural Monitoring Systems Ltd., Perth, WA*, 2004.
15. Wishaw, M. and D. Barton. *Comparative vacuum monitoring: a new method of in-situ real-time crack detection and monitoring*. in *Proceeding of 10th Asia-Pacific Conference On Nondestructive Testing*. 2001.

16. Structural Monitoring Systems Ltd. Australia. Available from: <http://www.smsystems.com.au/>.
17. Barton, D.P., *Comparative vacuum monitoring (CVM™)*. Encyclopedia of Structural Health Monitoring, 2009.
18. Roach, D., *Real time crack detection using mountable comparative vacuum monitoring sensors*. Smart structures and systems, 2009. **5**(4): p. 317-328.
19. Lin, M., et al., *Built-in structural diagnostic with the SMART Layer TM and SMART Suitcase TM*. Smart Materials Bulletin, 2001. **2001**(4): p. 7-11.
20. Beard, S., et al. *Multifunctional software suite for structural health monitoring using SMART technology*. in *Proceedings of the 2nd European Workshop on Structural Health Monitoring*. 2004.
21. Qing, X.P., et al., *Advances in the development of built-in diagnostic system for filament wound composite structures*. Composites science and technology, 2006. **66**(11): p. 1694-1702.
22. Kumar, A., et al. *A Self-Diagnostic Structural Health Monitoring System for Composite Structures*. in *SEM X International Conference, California*. 2004.
23. Scott, M., et al. *Structural health monitoring—the future of advanced composite structures*. in *Proc. 5th Workshop on Structural Health Monitoring*. Sept. 2005. Stanford, USA.
24. Kousourakis, A., *Mechanical properties and damage tolerance of aerospace composite materials containing CVM sensors*. 2008, RMIT University.
25. Hussain, N. *Structural Health Monitoring and Its Role in Affordability*. in *10th International Workshop on Structural Health Monitoring*. 2015. Stanford.
26. Speckmann, H. and C. Brousset. *Structural Health Monitoring (SHM) a future alternative to conventional NDT*. in *2006 49th Annual NDT Forum-Fort Worth, Texas*. 2006.
27. Giurgiutiu, V. and C. Soutis, *Enhanced composites integrity through structural health monitoring*. Applied Composite Materials, 2012. **19**(5): p. 813-829.
28. Jones, R.T., J.S. Sirkis, and E. Friebele, *Detection of impact location and magnitude for isotropic plates using neural networks*. Journal of intelligent material systems and structures, 1997. **8**(1): p. 90-99.
29. De Marchi, L., et al., *A passive monitoring technique based on dispersion compensation to locate impacts in plate-like structures*. Smart Materials and Structures, 2011. **20**(3): p. 035021.
30. Niri, E.D. and S. Salamone, *A probabilistic framework for acoustic emission source localization in plate-like structures*. Smart Materials and Structures, 2012. **21**(3): p. 035009.

31. Ciampa, F., M. Meo, and E. Barbieri, *Impact localization in composite structures of arbitrary cross section*. Structural Health Monitoring, 2012. **11**(6): p. 643-655.
32. Ahmari, S. and M. Yang, *Impact location and load identification through inverse analysis with bounded uncertain measurements*. Smart Materials and Structures, 2013. **22**(8): p. 085024.
33. Fink, M., *Time reversal of ultrasonic fields. I. Basic principles*. Ultrasonics, Ferroelectrics, and Frequency Control, IEEE Transactions on, 1992. **39**(5): p. 555-566.
34. Wu, F., J.-L. Thomas, and M. Fink, *Time reversal of ultrasonic fields. II. Experimental results*. Ultrasonics, Ferroelectrics, and Frequency Control, IEEE Transactions on, 1992. **39**(5): p. 567-578.
35. Ribay, G., et al., *Acoustic impact localization in plates: properties and stability to temperature variation*. Ultrasonics, Ferroelectrics, and Frequency Control, IEEE Transactions on, 2007. **54**(2): p. 378-385.
36. Chen, C., Y. Li, and F.-G. Yuan, *Impact source identification in finite isotropic plates using a time-reversal method: experimental study*. Smart Materials and Structures, 2012. **21**(10): p. 105025.
37. Ciampa, F. and M. Meo, *Impact detection in anisotropic materials using a time reversal approach*. Structural Health Monitoring, 2012. **11**(1): p. 43-49.
38. Park, B., et al., *Impact localization in complex structures using laser-based time reversal*. Structural Health Monitoring, 2012. **11**(5): p. 577-588.
39. Qiu, L., et al., *A time reversal focusing based impact imaging method and its evaluation on complex composite structures*. Smart Materials and Structures, 2011. **20**(10): p. 105014.
40. Qiu, L., et al., *Digital sequences and a time reversal-based impact region imaging and localization method*. Sensors, 2013. **13**(10): p. 13356-13381.
41. Seydel, R. and F.-K. Chang, *Impact identification of stiffened composite panels: I. System development*. Smart Materials and Structures, 2001. **10**(2): p. 354-369.
42. Seydel, R. and F.-K. Chang, *Impact identification of stiffened composite panels: II. Implementation studies*. Smart Materials and Structures, 2001. **10**(2): p. 370-379.
43. Sharif-Khodaei, Z., M. Ghajari, and M. Aliabadi, *Determination of impact location on composite stiffened panels*. Smart Materials and Structures, 2012. **21**(10): p. 105026.
44. LeClerc, J., et al., *Impact detection in an aircraft composite panel—A neural-network approach*. Journal of Sound and Vibration, 2007. **299**(3): p. 672-682.
45. Ghajari, M., et al., *Identification of impact force for smart composite stiffened panels*. Smart Materials and Structures, 2013. **22**(8): p. 085014.

46. Mallardo, V., M. Aliabadi, and Z.S. Khodaei, *Optimal sensor positioning for impact localization in smart composite panels*. Journal of intelligent material systems and structures, 2012. **24**(5): p. 559-573.
47. Tracy, M. and F.-K. Chang, *Identifying impacts in composite plates with piezoelectric strain sensors, part I: theory*. Journal of Intelligent Material Systems and Structures, 1998. **9**(11): p. 920-928.
48. Tracy, M. and F.-K. Chang, *Identifying impacts in composite plates with piezoelectric strain sensors, Part II: Experiment*. Journal of intelligent material systems and structures, 1998. **9**(11): p. 929-937.
49. Herszberg, I., et al. *Structural health monitoring for advanced composite structures*. in *Proceedings of the Sixteenth International Conference on Composite Materials*. Kyoto, Japan. 2007.
50. Hu, N., et al., *An efficient approach for identifying impact force using embedded piezoelectric sensors*. International journal of impact engineering, 2007. **34**(7): p. 1258-1271.
51. Yen, C.-S. and E. Wu, *On the inverse problem of rectangular plates subjected to elastic impact, Part I: Method development and numerical verification*. Journal of applied Mechanics, 1995. **62**(3): p. 692-698.
52. Yen, C.-S. and E. Wu, *On the inverse problem of rectangular plates subjected to elastic impact, Part II: Experimental verification and further applications*. Journal of applied mechanics, 1995. **62**(3): p. 699-705.
53. Worden, K. and W. Staszewski, *Impact location and quantification on a composite panel using neural networks and a genetic algorithm*. Strain, 2000. **36**(2): p. 61-68.
54. Park, J., *Impact identification in structures using a sensor network: The system identification approach*. 2005, Stanford University. p. 113.
55. Gaul, L. and S. Hurlebaus, *Determination of the impact force on a plate by piezoelectric film sensors*. Archive of Applied Mechanics, 1999. **69**(9-10): p. 691-701.
56. Guyomar, D., et al., *Passive impact location estimation using piezoelectric sensors*. Structural Health Monitoring, 2009. **8**(5): p. 357-367.
57. Zhang, C., et al., *An imaging method for impact localization using metal-core piezoelectric fiber rosettes*. Journal of Intelligent Material Systems and Structures, 2015. **26**(16): p. 2205-2215.
58. Moon, Y.-S., et al., *Identification of Multiple Impacts on a Plate Using the Time-Frequency Analysis and the Kalman Filter*. Journal of Intelligent Material Systems and Structures, 2011. **22**(12): p. 1283-1291.
59. Park, C., et al. *Low velocity impact monitoring for composite sandwich panels using PVDF sensors*. in *Proceedings of 2nd European Workshop on Structure Health Monitoring*. 2004.

60. Peelamedu, S.M., C. Ciocanel, and N.G. Naganathan, *Impact detection for smart automotive damage mitigation systems*. Smart materials and structures, 2004. **13**(5): p. 990.
61. Hiche, C., C.K. Coelho, and A. Chattopadhyay, *A strain amplitude-based algorithm for impact localization on composite laminates*. Journal of Intelligent Material Systems and Structures, 2011. **22**(17): p. 2061-2067.
62. Ma, C.-K., J.-M. Chang, and D.-C. Lin, *Input forces estimation of beam structures by an inverse method*. Journal of sound and vibration, 2003. **259**(2): p. 387-407.
63. Park, C.Y. and I.-G. Kim, *Prediction of impact forces on an aircraft composite wing*. Journal of Intelligent Material Systems and Structures, 2008. **19**(3): p. 319-324.
64. Speckmann, H. and R. Henrich. *Structural health monitoring (SHM)–overview on technologies under development*. in *Proc. of the World Conference on NDT, Montreal-Canada*. 2004.
65. Meo, M., et al., *Impact identification on a sandwich plate from wave propagation responses*. Composite structures, 2005. **71**(3): p. 302-306.
66. Si, L. and Q. Wang, *Rapid Multi-Damage Identification for Health Monitoring of Laminated Composites Using Piezoelectric Wafer Sensor Arrays*. Sensors, 2016. **16**(5): p. 638.
67. Huang, N.E. and S.S. Shen, *Hilbert-Huang transform and its applications*. 2005: World Scientific.
68. Donoho, D.L., *De-noising by soft-thresholding*. Information Theory, IEEE Transactions on, 1995. **41**(3): p. 613-627.
69. Donoho, D.L. and J.M. Johnstone, *Ideal spatial adaptation by wavelet shrinkage*. Biometrika, 1994. **81**(3): p. 425-455.
70. Huang, N.E., et al., *The empirical mode decomposition and the Hilbert spectrum for nonlinear and non-stationary time series analysis*. Proceedings of the Royal Society of London. Series A: Mathematical, Physical and Engineering Sciences, 1998. **454**(1971): p. 903-995.
71. Rilling, G., P. Flandrin, and P. Goncalves. *On empirical mode decomposition and its algorithms*. in *IEEE-EURASIP workshop on nonlinear signal and image processing*. 2003. NSIP-03, Grado (I).
72. Markmiller, J.F. and F.-K. Chang, *Sensor network optimization for a passive sensing impact detection technique*. Structural Health Monitoring, 2010. **9**(1): p. 25-39.
73. Jacquelin, E., A. Bennani, and P. Hamelin, *Force reconstruction: analysis and regularization of a deconvolution problem*. Journal of Sound and Vibration, 2003. **265**(1): p. 81-107.

74. Qiu, L., et al., *Design of an all-digital impact monitoring system for large-scale composite structures*. Instrumentation and Measurement, IEEE Transactions on, 2013. **62**(7): p. 1990-2002.
75. Chen, C. and F.-G. Yuan, *Impact source identification in finite isotropic plates using a time-reversal method: theoretical study*. Smart Materials and Structures, 2010. **19**(10): p. 105028.
76. Wu, Z., et al., *Impact energy identification on a composite plate using basis vectors*. Smart Materials and Structures, 2015. **24**(9): p. 095007.
77. Si, L., Z. Chen, and H. Baier. *Real-time health monitoring on impact identification of composite structures with distributed built-in sensor network*. in *SPIE Smart Structures and Materials+ Nondestructive Evaluation and Health Monitoring*. 2013. International Society for Optics and Photonics.
78. Lennart, L., *System identification: theory for the user*. 1999, Prentice Hall PTR, USA.
79. Goldberg, D., *Genetic Algorithms in Search, Optimization, and Machine Learning*, Addison-Wesley, Reading, MA. 1990.
80. Juang, J.-N., *Applied system identification*. 1994.
81. Kammer, D.C., *Estimation of structural response using remote sensor locations*. Journal of guidance, control, and dynamics, 1997. **20**(3): p. 501-508.
82. Larrosa, C., K. Lonkar, and F.-K. Chang, *In situ damage classification for composite laminates using Gaussian discriminant analysis*. Structural Health Monitoring, 2014. **13**(2): p. 190-204.
83. Wang, C.S., F. Wu, and F.-K. Chang, *Structural health monitoring from fiber-reinforced composites to steel-reinforced concrete*. Smart materials and Structures, 2001. **10**(3): p. 548.
84. Qiu, L., et al., *A quantitative multidamage monitoring method for large-scale complex composite*. Structural Health Monitoring, 2013. **12**(3): p. 183-196.
85. Wu, Z., et al., *Validation and evaluation of damage identification using probability-based diagnostic imaging on a stiffened composite panel*. Journal of Intelligent Material Systems and Structures, 2014: p. 1045389X14549873.
86. Wang, L. and F. Yuan, *Active damage localization technique based on energy propagation of Lamb waves*. Smart Structures and Systems, 2007. **3**(2): p. 201-217.
87. An, J., et al., *Experimental study on identifying cracks of increasing size using ultrasonic excitation*. Structural Health Monitoring, 2012. **11**(1): p. 95-108.
88. Giurgiutiu, V., A. Zagrai, and J. Jing Bao, *Piezoelectric wafer embedded active sensors for aging aircraft structural health monitoring*. Structural Health Monitoring, 2002. **1**(1): p. 41-61.

89. Cortes, D.H., S.K. Datta, and O.M. Mukdadi, *Dispersion of elastic guided waves in piezoelectric infinite plates with inversion layers*. International Journal of Solids and Structures, 2008. **45**(18): p. 5088-5102.
90. Frieden, J., et al., *Low energy impact damage monitoring of composites using dynamic strain signals from FBG sensors—Part I: Impact detection and localization*. Composite structures, 2012. **94**(2): p. 438-445.
91. Guyomar, D., et al., *Impact localization and energy quantification based on the power flow: A low-power requirement approach*. Journal of Sound and Vibration, 2011. **330**(13): p. 3270-3283.
92. Jones, R.M., *Mechanics of composite materials*. 1998, New York: CRC Press.
93. Achenbach, J., *Wave propagation in elastic solids*. 1984: Elsevier.
94. Ye, L., et al., *Functionalized composite structures for new generation airframes: a review*. Composites Science and Technology, 2005. **65**(9): p. 1436-1446.
95. Gibson, R.F., *A review of recent research on mechanics of multifunctional composite materials and structures*. Composite structures, 2010. **92**(12): p. 2793-2810.
96. Tracy, M.J., *Identifying impacts in composite plates with piezoelectric sensors*. 1996, Stanford University. p. 115.
97. Giurgiutiu, V., *Structural health monitoring: with piezoelectric wafer active sensors*. 2007: Academic Press.
98. LIU, G., *A modified electro-mechanical impedance model of piezoelectric actuator-sensor for debonding detection of composite patches*. Journal of Intelligent Material Systems and Structures, 2002. **13**(4): p. 389-396.
99. Giurgiutiu, V. and A.N. Zagari, *Characterization of piezoelectric wafer active sensors*. Journal of Intelligent Material Systems and Structures, 2000. **11**(12): p. 959-976.
100. *ICP Impulse Force Test Hammers Operating Manual*. 1996: PCB Piezotronics.
101. Graff, K.F., *Wave motion in elastic solids*. 1975: Courier Dover Publications.
102. Purekar, A.S., *Piezoelectric phased array acousto-ultrasonic interrogation of damage in thin plates*. 2006.
103. Reddy, J.N., *Mechanics of laminated composite plates and shells: theory and analysis*. 2004: CRC press.
104. Nayfeh, A.H., *Wave propagation in layered anisotropic media: With application to composites*. Vol. 39. 1995: Elsevier.
105. Kollár, L.P. and G.S. Springer, *Mechanics of composite structures*. 2003: Cambridge university press.
106. Kessler, S.S., S.M. Spearing, and C. Soutis, *Damage detection in composite materials using Lamb wave methods*. Smart Materials and Structures, 2002. **11**(2): p. 269-278.

Appendix A. Piezoelectric Sensor Discs

A.1 Sensor Dynamics Theory

Piezoelectric materials (e.g. Piezoceramics, etc.) are popular as either sensors or actuators for smart materials and structures, for instance, aerospace materials and structures. In this subsection, the sensor dynamics theory will describe the relations among the external forces and electromechanical response of the structure system through a set of equations derived out.

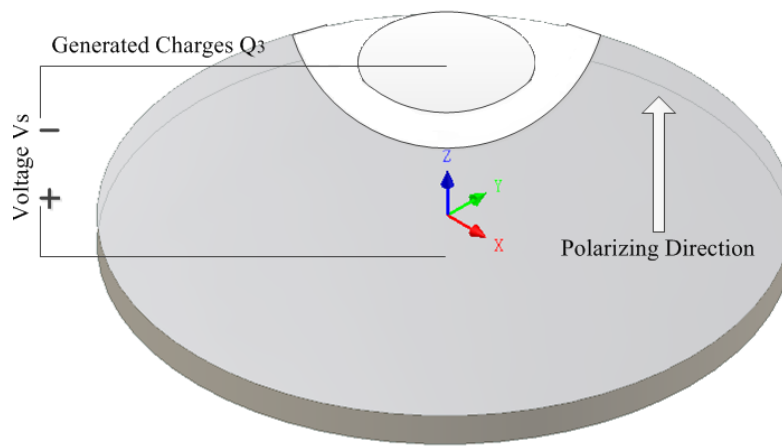


Figure A.1 Schematic for the electromechanical response and the coordinate system of a circular piezoelectric sensor

For the coordinate system shown in figure A.1, the matrices of the constitutive model for a piezoceramic sensor can be expressed as

$$\epsilon^S = \begin{bmatrix} \epsilon_1^S & 0 & 0 \\ 0 & \epsilon_2^S & 0 \\ 0 & 0 & \epsilon_3^S \end{bmatrix}$$

ϵ^S is electrical permittivity;

$$e = \begin{bmatrix} 0 & 0 & 0 & 0 & e_{15} & 0 \\ 0 & 0 & 0 & e_{15} & 0 & 0 \\ e_{31} & e_{32} & e_{33} & 0 & 0 & 0 \end{bmatrix}$$

here, e is defined as $e = c^E \cdot d$.

For elastic stiffness coefficient c^E ,

$$c^E = \begin{bmatrix} c_{11}^E & c_{12}^E & c_{13}^E & 0 & 0 & 0 \\ c_{12}^E & c_{11}^E & c_{13}^E & 0 & 0 & 0 \\ c_{13}^E & c_{13}^E & c_{33}^E & 0 & 0 & 0 \\ 0 & 0 & 0 & c_{55}^E & 0 & 0 \\ 0 & 0 & 0 & 0 & c_{55}^E & 0 \\ 0 & 0 & 0 & 0 & 0 & c_{66}^E \end{bmatrix}$$

Piezoelectric charge coefficient d ,

$$d = \begin{bmatrix} 0 & 0 & 0 & 0 & d_{15} & 0 \\ 0 & 0 & 0 & d_{15} & 0 & 0 \\ d_{31} & d_{32} & d_{33} & 0 & 0 & 0 \end{bmatrix}$$

where the superscripts that $(\dots)^E$ means the values are measured at constant electrical field, and $(\dots)^S$ means the values are measured at constant strain.

For a simply supported structure, the displacement field can be expressed as the following form,

$$u = \Phi_\gamma \gamma = a \begin{bmatrix} 0 & 0 & \Lambda & 0 \\ 0 & 0 & \Lambda & 0 \\ \sin(\beta_1 x) & \sin(\beta_2 x) & \Lambda & \sin(\beta_n x) \end{bmatrix} \gamma$$

where, $\beta_i = \frac{i\pi}{bL}$ and $a = \sqrt{\frac{2}{m}}$

m is the total mass of the structure, and is defined as $m = \rho b h L$.

The strain field is represented as

$$S = \begin{bmatrix} 0 & 0 & -z \frac{\partial^2}{\partial z^2} \\ 0 & 0 & 0 \\ 0 & 0 & 0 \\ 0 & 0 & 0 \\ 0 & 0 & 0 \\ 0 & 0 & 0 \end{bmatrix} u = \begin{bmatrix} -z \frac{\partial^2}{\partial x^2} \Phi_\gamma \end{bmatrix} \gamma = N_\gamma \gamma$$

For the voltage, it can be expressed as

$$E = \begin{bmatrix} 0 \\ 0 \\ -\frac{\partial}{\partial z} \end{bmatrix} \quad \varphi = \begin{bmatrix} 0 \\ 0 \\ -\frac{\partial}{\partial z} \Phi_v \end{bmatrix} \quad \nu = N_v \nu$$

$$\text{where } \Phi_v = \begin{cases} \frac{z-t_p}{t_s} & z > t_p \\ 0 & \text{elsewhere} \end{cases}$$

t_p is a half of a plate thickness and t_s is the thickness of a piezoelectric sensor.

Because all the piezoelectric sensors are electrically disconnected from each other, C_s is a diagonal matrix of which the size equal to the number of sensors. Each element can be calculated as follows:

$$C_{sij} = \frac{\epsilon_{33}}{t_s} \cdot d \cdot b$$

where the subscript j is the piezoelectric index and d is the diameter of the j^{th} sensor. Using the formula defined above, Γ can be calculated as

$$\Gamma_i = \sqrt{\frac{2}{m}} e_{31} b \beta_i \frac{t_p^2 + 2t_p t_s}{2t_s} (\cos(\beta_i x_2) - \cos(\beta_i x_1))$$

Finally, the following form of system equations can be obtained as,

$$\dot{z} = Az + Bf$$

where

$$A = \begin{bmatrix} 0 & I \\ -H^2 & 0 \end{bmatrix}$$

$$B = \sqrt{\frac{2}{m}} \begin{bmatrix} 0 \\ M \\ \sin(\beta_1 x_0) \\ M \\ \sin(\beta_n x_0) \end{bmatrix}$$

where

$$H^2 = \frac{4Et_p^2}{\rho} \begin{bmatrix} \beta_1^4 & 0 & \Lambda & 0 \\ 0 & \beta_2^4 & \Lambda & 0 \\ M & M & O & M \\ 0 & 0 & \Lambda & \beta_n^4 \end{bmatrix}$$

The output sensor voltages are related with the state variables as

$$s = Cz$$

where

$$C = [C_s^{-1}\Gamma|0]$$

A.2 Design Criterion of Sensor Network

This discussion on the sensor network layout was mentioned in Si's article [77]. The interval of sensor locations or called the sensor density needs to be considered to overlay an entire large-scale structure. As an impulse response function matrix can be constructed from the dynamic relationship between the input force and the response (or sensor) output, the associated response (or sensor) outputs are much more concern for constructing the IR functions. In this research, the instantaneous responses of a structure subjected to low velocity impacts were concerned. In this case, the sensor output signal should represent the instantaneous mode of the structural responses, not vibration mode of that. Nevertheless, since the stress waves due to impacts decay both in time and space generally, there exists the limitation on spacing sensor positions. The limitation can be determined by the energy decay of the propagating stress wave within the distance between an impact location and the pertinent neighboring sensors of which the area include the impact location. For the force reconstruction, a quadrilateral (or triangular) sensor network is required to update the impact location. Therefore, as impacts need to be identified for the structures with different dimensions, the sensors interval should be considered so that the IRFs matrix can be constructed from the appropriate quadrilateral sensors grids.

Then, to select the proper sensors interval, an empirical linear approximation method was proposed. In the light of large amounts of experimental data and the outlined theoretical basis, the minimum number of acquired sensors can be evaluated by the following function (A.1) for a newly-used laminated composite structure. For instance, for the peak load of 100 N from an impact, the maximum sensors interval that induces the satisfactory error rate of impact identifications (in general, $\varepsilon < 20\%$) is about 40 cm. And then for the peak load of 300 N from another impact, the maximum sensors interval increases to about 70 cm. The above

evaluation results imply that the sensors interval can be determined approximately as a multiple of the square root of the peak value of an impact load, given by

$$d_{ss} = n\sqrt{F_p} \quad (\text{A.1})$$

where the correlation coefficient n is integer, and normally the values of n are not more than 4. Assumption that an impact force of 1000 N can be used as a lower limit for an actual aircraft composite component, once the force increases approximately by a multiple of four, the distance between sensors increases by about 2, until to 160 cm. In our study, a small sensors interval was determined to obtain more precise estimation results, of which the accuracy is on demand. The sensors intervals laid on the specimens were shown in Figures 9.1, 9.2 and 9.3.

Appendix B. Wave Propagation in Composite Laminates

B.1 Basic Wave Mechanics

Before introducing propagating wave model for laminated composites, the fundamental theory on wave mechanics of isotropic material [101] needs to be described firstly. A propagating wave can be characterized by a temporal angular frequency ω , as well as a spatial frequency k , which is called as the wavenumber. A wave propagating in one direction is commonly represented by $e^{i(\pm kz + \omega t)}$, where the sign of the wavenumber indicates the traveling direction of the wave. The propagation velocity of the constant phase is defined as the phase speed, which is expressed as,

$$V_p = \frac{\omega}{k} \quad (\text{B.1})$$

Then, a group of waves corresponding to a band of frequencies will travel at a speed differed from the phase speed. This group speed will be defined as the local slope of the frequency-wavenumber relationship, which is given by

$$V_g = \frac{\partial \omega}{\partial k}(\bar{\omega}) \quad (\text{B.2})$$

where the frequency $\bar{\omega}$ is the center frequency with a bandwidth of $\Delta\omega$, and a group wave is composed of a packet of frequencies centered around $\bar{\omega}$.

The relation between the wavenumber k and the temporal frequency ω describes the propagating modes of a wave. Supposing this relationship is linear, the phase velocity is then constant, and the waveform would be same during the wave propagates through the structure, and no dispersion thus occurred. Whereas the wavenumber-frequency relation is nonlinear, the frequency components of the wave will travel at different velocities and the waveform will not maintain its original shape, as the wave happened to be dispersive. The wavenumber becomes a crucial parameter in the wave propagation since it describes not only the spatial distribution of the wave but also affects the wave propagation velocity in a medium. The wavenumber-frequency relationships of a thin isotropic plate are expressed as equations (B.3) and (B.4) [102].

$$\text{Transverse direction:} \quad k = \sqrt{\omega^4 \frac{m}{D}} \quad (\text{B.3})$$

$$\text{Longitudinal direction:} \quad k = \pm \omega \sqrt{\frac{\rho}{E}} \sqrt{1 - \nu^2} \quad (\text{B.4})$$

where m is the mass per area of a plate and D the rigidity of the plate. It can be seen that the wavenumber-frequency relationship is nonlinear in the transverse direction and is linear in the longitudinal direction. These representations are valid based on the assumption that the wavelength should be much larger than the plate thickness and no shear effect considered. However, a more comprehensive representation of the wave propagation properties should be taken into account shear effect and be expressed by modeling propagating waves as described in the following section.

B.2 Propagating Wave Model

For constant temperature, the material recovers its initial shape after all loads are removed, where it shows linear elastic behaviour. Meanwhile, each ply of carbon fiber prepreg is a continuous medium [103]. Therefore, in these conditions, it is valid to describe the constitutive model for an individual lamina by the Generalized Hook's law, which is expressed in Eq. (B.5).

$$\sigma = C \varepsilon \quad (\text{B.5})$$

where the stress tensor σ is a linear function of the strain tensor ε and C , and C is a fourth order tensor with eighty-one material parameters. However, the C tensor can be simplified further if it is assumed that all the fibers within each lamina have the same orientation (unidirectional lamina), and that the material symmetry planes are parallel and transverse to the fiber direction. In this case, assume that a composite plate made up of orthotropic layers and each layer behaves as an orthotropic material, through the transfer matrix (TM) method, the constitutive model in equation (B.6) can be defined by the nine independent material parameters [104].

$$\begin{Bmatrix} \sigma_1 \\ \sigma_2 \\ \sigma_3 \\ \sigma_4 \\ \sigma_5 \\ \sigma_6 \end{Bmatrix} = \begin{bmatrix} C_{11} & C_{12} & C_{13} & 0 & 0 & 0 \\ C_{12} & C_{22} & C_{23} & 0 & 0 & 0 \\ C_{13} & C_{23} & C_{33} & 0 & 0 & 0 \\ 0 & 0 & 0 & C_{44} & 0 & 0 \\ 0 & 0 & 0 & 0 & C_{55} & 0 \\ 0 & 0 & 0 & 0 & 0 & C_{66} \end{bmatrix} \begin{Bmatrix} \varepsilon_1 \\ \varepsilon_2 \\ \varepsilon_3 \\ \varepsilon_4 \\ \varepsilon_5 \\ \varepsilon_6 \end{Bmatrix} \quad (\text{B.6})$$

In order to describe the behavior of a laminated composite, the next step is to take into account the interaction of all the layers through the CLPT theory.

In accordance with the CLPT theory, the basic premise is that a laminated composite plate can be treated as a thin body as long as its thickness is small compared to the in-plane dimensions. Therefore, a laminated composite is considered to be under a plane strain state. In the CLPT theory, the constitutive model for the i^{th} orthotropic lamina with respect to the local material coordinate system in (B.6) can be simplified into equation (B.7) [105],

$$\begin{Bmatrix} \sigma_1 \\ \sigma_2 \\ \sigma_6 \end{Bmatrix}^{(i)} = \begin{bmatrix} C_{11} & C_{12} & 0 \\ C_{12} & C_{22} & 0 \\ 0 & 0 & C_{66} \end{bmatrix}^{(i)} \begin{Bmatrix} \varepsilon_1 \\ \varepsilon_2 \\ \varepsilon_6 \end{Bmatrix}^{(i)} \quad (\text{B.7})$$

Then the details of the stress-strain relation for the i^{th} orthotropic lamina with respect to the global coordinate system is described in [103]. Owing to the fact that the compliance coefficients are written directly in terms of engineering constants which are expressed in $[S] = [C]^{-1}$, the derivation in (B.8) is performed in order to write the global extensional S tensor. In a word, it is possible to write the laminate constitutive model if the contribution of the layers is integrated along the entire thickness h .

$$\text{Thus,} \quad \begin{Bmatrix} \varepsilon_{xx}^{(0)} \\ \varepsilon_{yy}^{(0)} \\ \gamma_{xy}^{(0)} \end{Bmatrix} = \begin{bmatrix} \frac{1}{E_x} & \frac{-\nu_{yx}}{E_y} & \frac{-\eta_{xy}}{G_{xy}} \\ \frac{-\nu_{xy}}{E_x} & \frac{1}{E_y} & \frac{-\mu_{xy}}{G_{xy}} \\ \frac{-\eta_x}{E_x} & \frac{-\mu_y}{E_y} & \frac{1}{G_{xy}} \end{bmatrix} \begin{Bmatrix} \sigma_{xx} \\ \sigma_{yy} \\ \sigma_{xy} \end{Bmatrix} \quad (\text{B.8})$$

A composite plate is inherently an anisotropic body, since the material properties are direction-dependent. However, it is possible to design a stacking sequence with many angle

changes such that E_x and E_y are sufficiently close. In this case, the laminate can be treated as quasi-isotropic.

As for a quasi-isotropic laminate, c_t and c_l are the transverse and longitudinal wave velocities respectively, and are defined in equation (B.9). c_p is the phase velocity, ω is the angular frequency. The velocities c_t and c_l depend on the density ρ , and the Lamé's constants μ and λ , which are expressed in terms of material properties such as the Young's modulus E , and the Poisson's ratio ν , as shown in expressions (B.11) and (B.12) [97, 106].

$$c_t^2 = \frac{\mu}{\rho}; \quad c_l^2 = \frac{(\lambda + 2\mu)}{\rho} \quad (\text{B.9})$$

$$c_p = \lambda_w f; \quad k = \frac{2\pi}{\lambda_w}; \quad \omega = 2\pi f \quad (\text{B.10})$$

$$\mu = \frac{E}{2(1+\nu)} \quad (\text{B.11})$$

$$\lambda = \frac{E\nu}{(1-2\nu)(1+\nu)} \quad (\text{B.12})$$

Phase velocity c_p is the velocity for each individual frequency within a sinusoidal wave. However, if a wave signal is a bandwidth signal with more than one frequency component, in each frequency component the wave propagates with a different velocity. The wave signal includes certain wave packets, thus they characterize the wave with a beat pattern, and thereby the multiple different frequencies can alternate in and out of phase as the wave's dispersion property in the frequency-thickness product. Therefore, each wave packet propagates with a group velocity c_g different from the phase velocity, as defined in Eq. (B.13) [104].

$$c_g = c_p - \lambda_w \frac{\partial c_p}{\partial \lambda_w} \Leftrightarrow c_g = \frac{c_p}{1 - \frac{f}{c_p} \frac{\partial c_p}{\partial f}} \quad (\text{B.13})$$

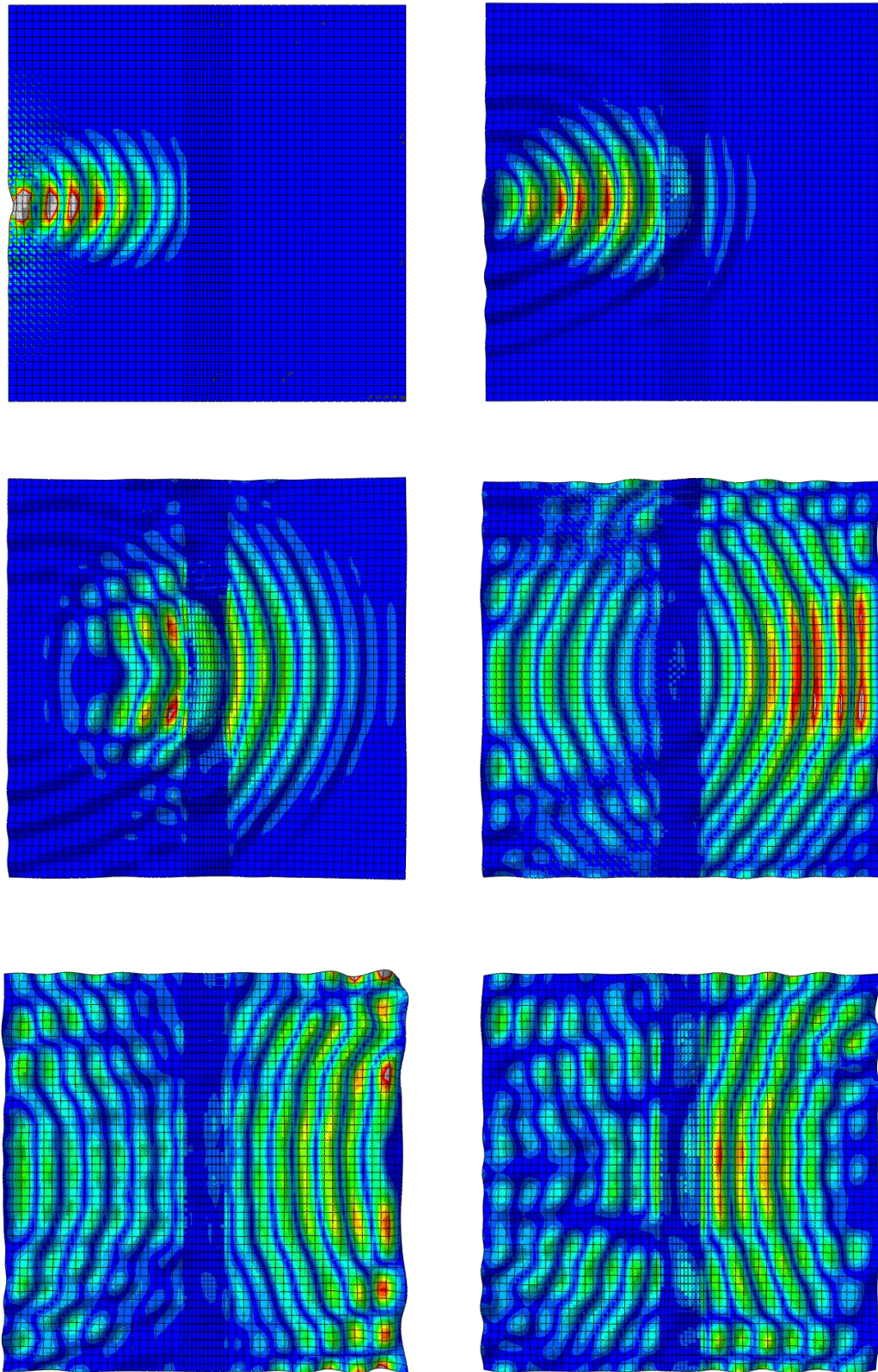


Figure B.1 Demonstration of a wave propagation in a stiffened CFRP panel during 8 *ms*

Appendix C. Computer Programs

The developed structural health monitoring and identification technique was implemented with the computer code to achieve impact localization and quantification, structural condition awareness based on impacts, and structural state assessment including structural damage localization and quantification.

The computer code is broken into two components, which are the IMPACT IDENT and DAMAGE ASSESS both shown in Figure C.1. In the IMPACT IDENT processing, any unforeseen unknown impact event can achieve to be located and quantified in real time; furthermore, the structural conditions can be identified and analyzed by the proposed signal energy distribution method. In the DAMAGE ASSESS processing, it performs to locate and quantify for possible structural damage resulting from the adverse impacts. Meanwhile, three multi-functional multi-metrics were proposed and applied as the damage index parameters to provide the damage identification information such as the energy densities, the TOF values and the phase slope variations corresponding to multiple damage in a structure.

The IMPACT IDENT utilizes the proposed FGA parameter estimation method to find the optimal prediction model that could match well with the real response output, and further to obtain the optimal model parameters from the optimized output model. Using the model parameters (a_i, b_j) , the IRF matrix can be computed and built. Then, through the reversion and generalization procedure, the force history resulting from an unknown impact can implement to be reconstructed and estimated quantitatively. The details on the methodology and implementation of impact forces estimations can be found in Chapter 5 and Section 10.3. Moreover, the localization implementation for unknown impacts is described in detail in Chapter 7.

The primary task of the DAMAGE ASSESS is to realize the structural state (damage) assessment that includes the structural damage localization and quantification, especially for the invisible multiple damage case such as internal delaminations hidden in a laminated composite structure. Its implementation is interpreted systematically in Chapter 6.

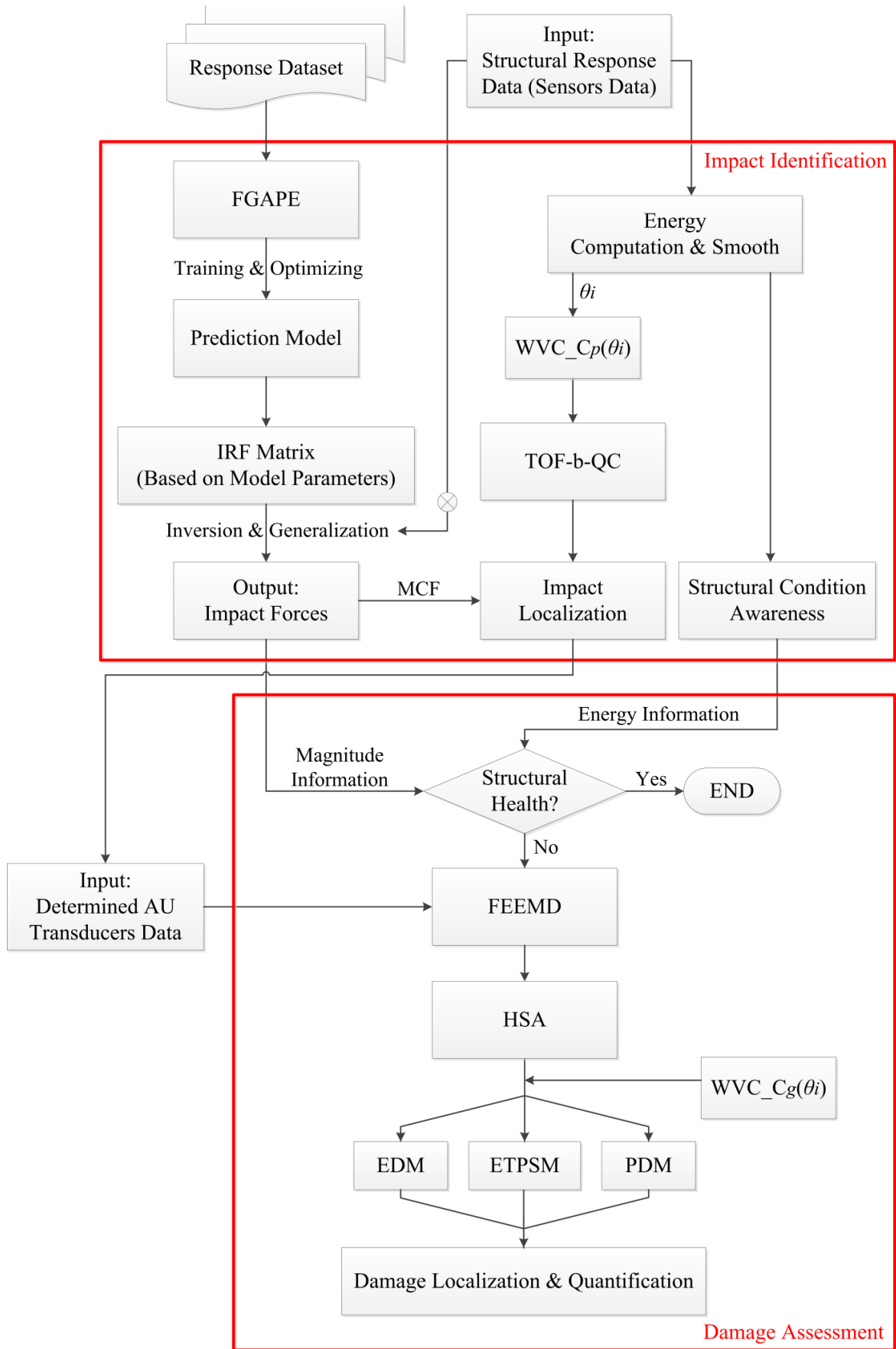


Figure C.1 Overview of the process of the developed in-situ SHMI computer program

The main program of the impact identification:

```
function [XX,YY,Fmax,fitresult,gof]=
main(x,y,z,revise,dataPath,fs,gridmatrixPath,na,nb,nc,nd,nn,mm)
% x, y      sensors locations
% s         sensors signals
% z         communication channels
% fs        sampling frequency
% na        sensors intervals in x or y axis
% nb        sensors intervals in y or x axis
% nc        IRFs grids lengths in x or y axis
% nd        IRFs grids lengths in y or x axis
% nn        numbers of used sensors in x or y axis
% mm        numbers of used sensors in y or x axis
% gridmatrix matrix of IRFs grids

%=====one example: compensation coefficients, if need=====
ss(:,1)=1.4115*dataPath(1023:1313,2); %
ss(:,2)=0.9915*dataPath(1023:1313,3); %
ss(:,3)=0.8885*dataPath(1023:1313,4); %
ss(:,4)=dataPath(1023:1313,5); %
ss(:,5)=1.2596*dataPath(1023:1313,6); %
ss(:,6)=1.6066*dataPath(1023:1313,7); %
data=ss;

%=====Contribution of sensors network=====
[sensorgrid,x1,y1,xn,yn]=getsensor_num(x,y,z,nn,mm);

tic;
N = length(x);
if N~=length(y), error('The number of the coordinates x and y of sensors
must keep same!'); end
x = reshape(x,N,1);
y = reshape(y,N,1);
z = reshape(z,N,1);
s=data; %s=importdata(dataPath);
[row,column]=size(s);
for i=1:N
    s(:,i)= s(:,i)*revise(i);
end
% original response signals processing including filtering
[s]=getright_signal(s,fs);
% main estimations
% initial localization
[Prms_tw,E_tw]=SourceLocation(x,y,z,s,fs);
t_arrive=[1 1 1 1 1 1]';
[sensor_turn]=get_sensor_sig(t_arrive,z,x,y,s,fs,na);
[Xc,Yc]=position_zone(x,y,z,s,fs,nn,sensor_turn);
%
[sensorgrid,x1,y1,xn,yn]=getsensor_num(x,y,z,nn,mm);
%
a=round(max(x)-min(x));
b=round(max(y)-min(y));

gridmatrix=gridmatrixPath; % gridmatrix=importdata(gridmatrixPath);
% precise localization and force reconstruction
[XX,YY,F,Fa,Fb,Fc]=force_position(Xc,Yc,fs,gridmatrix,a,b,na,nb,nc,nd,s,sen
sorgrid,x1,y1,xn,yn,mm,z,x,y);
F1=sort(F,'descend');
```

```
Fmax=sum(F1(1:10,1))/10;
toc;
% structural condition awareness
[fitresult, gof] = PlotEnergyDistribution(XX,YY,fs,dataPath,nn,mm,na,nb);

end
```

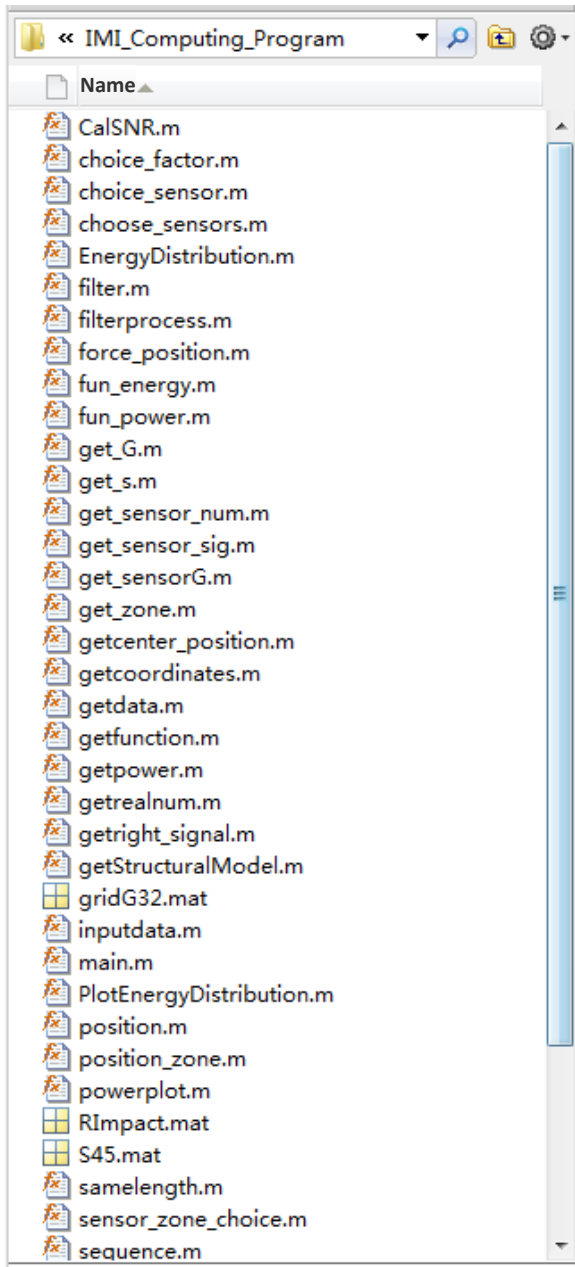


Figure C.2 Computer program for the impact monitoring and identification



Figure C.3 Rapid computation implementation of the impact identification in real time